Local control of strain in La0.7Sr0.3Mn03 (LSMO) thin films : application to MEMS

Laryssa Carvalho de Araujo

Normandie Université

THÈSE

Pour obtenir le diplôme de doctorat

Spécialité ELECTRONIQUE, MICROELECTRONIQUE, OPTIQUE ET LASERS, OPTOELECTRONIQUE MICROONDES

Préparée au sein de l'Université de Caen Normandie

Local control of strain in La0.7Sr0.3Mn03 (LSMO) thin films - application to MEMS

Présentée et soutenue par
LARYSSA CARVALHO DE ARAUJO

Thèse soutenue le 17/12/2021 devant le jury composé de		
M. MARC FAUCHER	Chargé de recherche HDR, IEMN - Inst. d'Elec, de MIcro et de Nano	Rapporteur du jury
MME SILVANA MERCONE	Professeur des universités, Université de Tours François Rabelais	Rapporteur du jury
M. GUILLAUME AGNUS	Maître de conférences, Université Paris Saclay	Membre du jury
M. BERTRAND VILQUIN	Maître de conférences HDR, École Centrale Lyon	Membre du jury
M. STEPHANE FLAMENT	Professeur des universités, Université Caen Normandie	Président du jury
MME LAURENCE MECHIN	Directeur de recherche au CNRS, ENSICAEN	Directeur de thèse

Thèse dirigée par LAURENCE MECHIN, Groupe de recherche en informatique, image, automatique et instrumentation

UNIVERSITÉ CAEN NORMANDIE

ENSI CAEN
ÉCOLE PUBLIQUE D'INGÉNIEURS
CENTRE DE RECHERCHE

MIIS

GREYC
Laboratoire de recherche en sciences du numérique

UNIVERSITÉ DE CAEN

DOCTORAL THESIS

Local control of strain in LSMO thin films – application to MEMS

Author:
Laryssa Mirelly CARVALHO DE ARAÚJO

Supervisor:
Dr. Laurence MÉCHIN

A thesis submitted in fulfillment of the requirements for the degree of Doctor of Electronics Engineering

in the

GREYC Laboratoire
Mathematique, Information, Ingénierie des Systèmes

November 13, 2021

"Men build too many walls and not enough bridges."

Isaac Newton

Acknowledgements

First, I would like to express my sincerest gratitude to Laurence Méchin, my thesis directrice, who have guided and motivated me, altogether with sharing her expertise and passion for research. Not only is she patient and responsible but also supportive to help me overcome the obstacles and keep the research always exciting. It has been a pleasure working with such an inspiring researcher whose instructions were essential not only for the conclusion of this thesis, but her kind advices have also helped me shape the path of my career.

I highly appreciate also all the help I received throughout these years from several other members of the laboratory, Victor Pierron, for all the assistance in clean room, Stéphane Flament, for his guidance since the day of my interview for the PhD, for helping me go through the paper work and for sharing his knowledge and experience to the best interest of my research, Bruno Guillet, for supplying great materials whenever in possession that I could benefit from and even directing me during the requests for vacancies for TP and TD at Unicaen. Furthermore, I'd like to express my profound appreciation to Chantal Gunther who I had the pleasure to have great conversations, who made me feel so welcome in the group from the beginning with her great portuguese and inestimable experiences from Brazil to share, always with great advices to facilitate my life in France. Luiz Enger for his support in and outside the laboratory, Vanuza Marques for passing on some of her knowledge on the processes I came to need in the thesis and Yoann Lechaux for the great times and talks when sharing the office.

Many thanks go to Sophie Rastello, Arielle Perrette and Gaëlle Lenogue, for assisting me so many times with every administrative detail during these years and Philippe Poupard, for the uncountable times that he come to my rescue with IT solutions.

I am also grateful for the interesting discussions with the several interlocutors I had the chance to work with during this thesis development. Bertrand Vilquin, from INL, who performed PZT depositions and some XRD measurements for me. Gilles Poullain and Cristhophe Cibert from CRISMAT who not only performed the PZT depositions in high temperature and P(E) measurements but also kindly had me over their laboratory to participate on the measurements along with providing me some interesting bibliography.

Bernadette Domengès for all the time allocated to instruct me about the Digital Holographic Microscopy, Darrell Schlom for providing the substrates I used in my fabrication processes and Valerie Ruaux for providing me access to the X-Ray diffractometer in her laboratory for this work. I also acknowledge the members of my CSI, Guillaume Agnus and Arnaud Fouchet, for the great discussions about my

research and the enlightenments on it.

To my family, who have always supported me even from the distance, always with kind words and great advices and my fiancé who has always been there for me and who encouraged me even in the difficult moments, my highest esteem. Not only have they been essential to keep the perfect balance between my PhD and personal life but also my strength in these difficult pandemic times.

Finally, I acknowledge the financial support of Normandy Region for financing the research.

Contents

List of Figures

List of Tables

List of Abbreviations

AFM	**A**tomic **F**orce **M**icroscopy
CMOS	**C**omplementary **M**etal **O**xide **S**emiconductor
DHM	**D**igital **H**olographic **M**icroscopy
FWHM	**F**ull-**W**idth **H**alf **M**aximum
IBE	**I**on **B**eam **E**tching
MBE	**M**olecular **B**eam **E**pitaxy
MEMS	**M**icro-**E**lectro-**M**echanical **S**ystems
MPB	**M**orphotropic **P**hase **B**oundary
PFM	**P**iezoresponse **F**orce **M**icroscopy
PLD	**P**ulsed **L**aser **D**eposition
RHEED	**R**eflective **H**igh-**E**nergy **E**lectron **D**iffraction
RIE	**R**eactive **I**on **E**tching
RT	**R**oom **T**emperature
RTA	**R**apid **T**hermal **A**nnealing
SOI	**S**ilicon-**O**n-**I**nsulator
SOS	**S**ilicon-**O**n-**S**apphire
SG	**S**ol-**G**el
ST	**S**awyer-**T**ower
UHV	**U**ltra **H**igh **V**acuum
XRD	**X**-**R**ay **D**iffraction

Chapter 1

Introduction

Microelectromechanical Systems (MEMS) devices combining sensors, actuators and electrical interface on a single structure is a current trend and it has been widely studied because of their remarkable potential for new application as vibrational sensors, lab-on-chip for medical applications, micromachined ultrasonic transducers, droplet ejectors, energy harvesters, etc. Many are the advantages in fabricating micro and nano-sensors as well as MEMS such as the use of silicon microtechnology, the devices small size and low weight, the possibility of batch production and performance improvement by integration of electronics and actuators. However, a few difficulties can be faced to achieve these devices like process incompatibility between materials, major packaging problems, some device deficiencies like offset, drift, non-linearity, cross-sensitivity, temperature, etc.

Piezoelectric materials have shown to scale very favourably upon miniaturization which led to an increasing growing interest in using piezoelectric films for MEMS applications. The deposition and integration of high-performance piezoelectric films to drive these devices' actuators such as lead zirconate titanate with the morphotropic phase boundary composition, i.e., $PbZr_{0.52}Ti_{0.48}O_3$ (PZT), have received wide attention because they can potentially outperform other MEMS actuators due to their exceptionally high ferroelectric polarization and piezoelectric coefficients. The integration of high quality piezoelectric materials enables the design of novel piezoelectric MEMS products and provides greater consolidation with CMOS circuitry and into advanced low-power applications.

Lead-free piezoelectric materials like aluminium nitride, AlN, also display high piezoelectric responses useful for MEMS fabrications, however there is still great difficulty in growing thin films of these materials with similar piezoelectric response as in their ceramic form. For this reason, PZT is still widely used in piezoelectric MEMS in research and development and also in commercial products. AlN, however, displays great chemical stability upon some acid attacks showing up as a good candidate for protection material, so although a smaller piezoelectric effect is

expected, AlN is compatible with fabrication processes where PZT would be completely etched away.

The performance of piezoelectric MEMS is however strongly dependent on the film quality since the surface nature onto which the piezoelectric material is grown plays a crucial role as it can lead to degradation of its piezoelectric properties. To achieve enhanced performance of the final devices, epitaxial piezoelectric films growth was envisaged in this thesis due to greater piezoelectric coefficients, polarization and dielectric constants, compared to polycrystalline films.

PZT deposited on top of conductive oxide electrodes exhibits better performance than on typical platinum-coated Si wafers such as better fatigue properties and suppression of dead-layers, as a result of the *oxygen sink* effect of oxide electrodes that fills the oxygen vacancies during switching cycles which can still be improved by the use of symmetrical oxide/ ferroelectric/ oxide electrodes compared to a single one.

In addition to conductive and superconductive oxides as electrode materials, conductive perovskites have gained importance as they enable heteroepitaxial growth with PZT, like $SrRuO_3$, $(La,Sr)CoO_3$, $Sr(Ti,Sb)O_3$ (SSTO), $LaNiO_3$, $(La,Sr)SnO_3$ (LSSO) and $(La,Sr)MnO_3$ (LSMO). The possibility to epitaxially grow high-quality single-crystalline STO onto Si(001) enables the integration of LSMO on silicon.

Among the large choices for perovskites bottom electrode, $La_{2/3}Sr_{1/3}\,MnO_3$ (LSMO), a ferromagnetic oxide with strong magnetoelastic coupling thus potentially allowing for high magnetoelectric effects via a piezoelectric- magnetoelastic coupling, is presented as a promising choice not only because of its good lattice parameters matching with PZT but also for its majority of charge carriers, since a p-type conducting oxide steer clear of surface charge accumulation at the interface PZT/oxide during the polarization cycle, effect that would be observed if a n-type electrode were employed due to PZT's characteristic of a wide bandgap p-type semiconductor. With no carrier injection leading to accumulation of oxygen vacancies at the interface, the fatigue problems are again minimized.

In addition, the outstanding properties of rare-earth manganese oxides materials such as LSMO that presents a high electrical resistance variation as a function of temperature around its transition metal-insulating, that takes place close to room temperature, is attracting considerable interest due to its possible applications as uncooled sensors, such as anisotropic magnetoresistances or infrared bolometers, taking advantage of its low-noise level compared with other resistive materials such as semiconductors (a-Si, a-Si:H, aGe, poly SiGe) and other oxide materials (semiconducting $YBa_2Cu_3O_{7-\delta}$, VOx, etc.) and the utilisation of classical silicon microfabrication techniques.

This enables applications such as micro-electromechanical systems (MEMS) based on epitaxial piezoelectric layers integrated to LSMO thin films that can find applications in spectroscopy sensing or in terahertz imaging devices for military or health sensors or magnetoelectric sensors. In an inverted manner, one can also profit from the understanding on resonant frequency shift in the LSMO beams to define a device that is not limited to room-temperature usage but that can be also used in higher temperatures through the control of strain to compensate for the shift in frequency and maintain the device under resonance to reduce energy dissipation.

This thesis is the result of a multidisciplinary work where the objective was focused in developing a fabrication process in clean room allowing the realization of suspended structures of LSMO integrated with piezoelectric materials.

To develop resonant MEMS based on such innovative materials, a series of steps are needed, namely the understanding and use of physics of the properties used for converting the physical quantities into electrical ones in order to propose innovative devices and understand its principle of operation, comprehension on materials science to grow epitaxial films, use of micro-(nano-)technology to fabricate devices, some mechanical engineering for the dynamic measurements and electronics for the general assembly of samples tests and characterization. This work includes three main parts:

- A comprehensive study of piezoelectric thin-film that has been carried out to propose the best method compatible with a room-temperature fabrication process achieving full epitaxy with our LSMO thin films. This was followed by the deposition and characterization of hetero-epitaxial thin-film multilayer;
- Establishment of a reliable microfabrication process to produce piezoelectric epitaxial MEMS with micrometer resolution;
- Mechanical study of the fabricated devices, both static and dynamic.

The definitions of main concepts on epitaxy and strain application in thin films are presented in chapter 2. A general overview on piezoelectric and epitaxial MEMS are shown, as well as applications found in literature and our own proposition of device.

The materials that are going to constitute the final actuator-integrated resonant device, namely, the perovskite LSMO and also the piezoelectric materials PZT and AlN, are studied in details in chapter 3. The methods of deposition together with the characterization ones focused on the thin films quality are described and the results examined in the end of the chapter. The properties of LSMO layers on different substrates are studied as well as different deposition methods for the piezoelectric films integration onto LSMO.

Chapter 4 is dedicated to discuss the fabrication process of the suspended clamped-clamped beams on silicon and silicon-on-sapphire substrates as means to verify the epitaxial strain effects on the structural and dynamic properties of such bridges. All the steps are shown with the respective calculated parameters, such as dose tests for direct-write lithographies of different layers and etch rates for each material. And the validation of all the steps is done by comparing the electrical resistivity of the films before and after the etching stages as well as the comparison of electrical resistivity for the as-grown films and the suspended bridges' ones. The dynamic evaluation of the suspended structures are presented. The performance under air for simple bridges are evaluated and a value of *apparent Young's modulus* for our used heterostructures is given in comparison with the expected theoretical resonance frequencies.

Finally the full device process is presented for two different cases: either on Si or silicon-on-sapphire substrates or using silicon-on-insulator ones but it was not possible to arrive up to a successful functional device before the end of writing this manuscript. A conclusion including perspectives to continue the work is given in chapter 5.

Chapter 2

Piezoelectric MEMS

To achieve heteroepitaxy, the deposition of a crystalline layer on a crystalline substrate, the mismatch between lattice parameters in the interface cannot be ignored and should even be considered as a true technique to control the desirable properties of functional oxide materials by the application of residual stresses due to their sensitivity to external disturbances.

Strain, as one of the most important external factors along with oxygen vacancies, defects, thickness and deposition conditions, and one of the key parameters for improving conductivity and performance of devices in the CMOS technology, can be applied by the so called *strain engineering*, either by strain due to lattice mismatch (in compression or in tension), by substrate bending (semi-flexible type of substrates) or by Micro-Electro-Mechanical Systems (MEMS), as shown in figure 2.1. It can also be used to tune the functional properties of thin films.

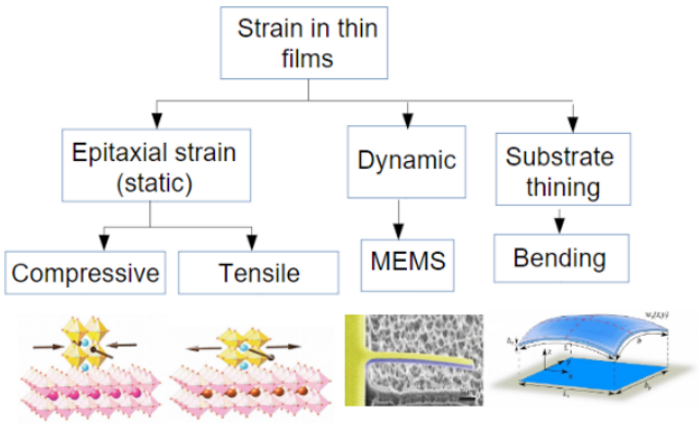

FIGURE 2.1: Methods of strain application in thin films. Extracted from (Chaluvadi, 2017a)

In this chapter the main concepts in the development of piezoelectric and

epitaxial MEMS are presented. After a brief introduction on strain engineering, basic concepts from epitaxy itself to the aforementioned different methods of strain application in thin films are described. Relevant aspects of our main objective are discussed as well as the main fabrication associated challenges and the applications possibilities for the proposed full process integration development.

2.1 Strain engineering

The mechanical strains developed in micro and nanolayers or heterostructures under the influence of external controlling fields, result in physical effects in solids such as changes of the band structure, electric, magnetic, optic, and other materials properties that are of interest for development of innovative sensor devices. The technology that produces materials with desired properties by means of mechanical stresses control is called *strain engineering*. This is not restricted, however, to such controlled change of materials properties in semiconductor technologies (Banerjee, 1997), but also extended to magnetic and ferroelectric films (Haeni et al., 2004) (Collins and Saslow, 1996) as well as graphene (Pereira and Castro Neto, 2009) and several 2D materials (Heine, 2015) (Zibouche et al., 2014) (Wei, Dai, and Huang, 2017).

Two branches of this recent area of study, are seen in figure 2.2. The first one considers massless relativistic electrons in two-dimensional media with the uncertainty principle of Heisenberg taken into account and the General Relativity. This approach is explained in (Atanasov and Saxena, 2011) and is based considering two-dimensional materials such as corrugated graphene sheets to simulate the motion of relativistic particles in curved spacetime, but also hexagonal boron nitride, ZnO, ultra-thin layers of transition metal chalcogenides: MoS_2, WSe_2, PdS_2, WTe_2, semiconductors monolayers and planar heterostructures of them. The innovations in this branch aim the strain-mediated manipulation of semiconductor electronic structures (Bukharaev et al., 2018) where the mechanical stresses actuate as an elastic gauge field interacting with fermions as an electromagnetic field.

The second branch treats the linkage between mechanical stresses and magnetic or ferroelectric subsystems in crystals for strain control. It has as main element heterostructures of magnetic layer with anisotropy produced by substrate deformation in the framework of magnetic sensors.

Such non-volatile magnetic strain engineered devices (maintain the steady state in the absence of an energy supply) are fit for state-of-the-art technologies such as read-only and random-access memory elements combination in a single device. In addition, envisaging such applications, their switching energy as memory units has been estimated to be below 1 aJ (Roy, Bandyopadhyay, and Atulasimha, 2011) (Roy, 2014), very close to the limits of fundamental thermodynamic principles, such

as the Landauer limit $k_B T ln2$ which is the minimal energy dissipated during the erasure of an information bit.

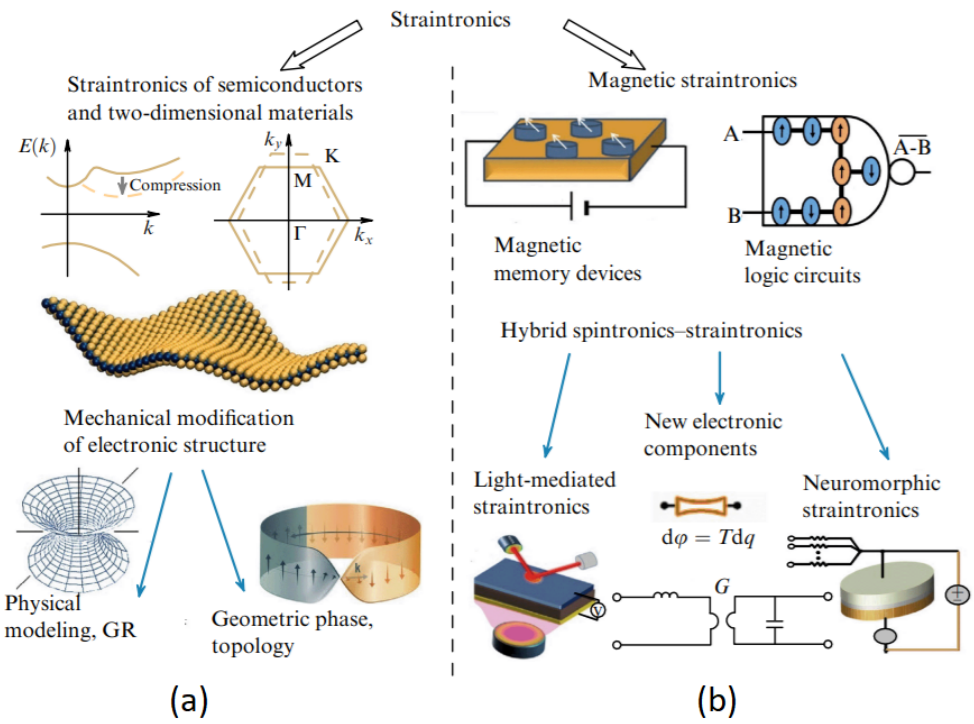

FIGURE 2.2: The two branches of *straintronics*/strain engineering (a) strain-mediated manipulation of the electronic structure with mechanically induced transition from direct- to indirect-band structure in silicon nanotubes and modification of the Brillouin zone in graphene and (b) the main magnetic straintronic devices, namely magnetic memory and logic, in particular, as well as some newly emerging kinds of straintronics: neuromorphic straintronics and light-mediated straintronics). Extracted from (Bukharaev et al., 2018)

Mechanical stresses are incorporated to thin films during epitaxial growth as a result of their lattice constants difference in comparison with the substrate's ones. Such relative deformation in oxide epitaxial thin films may go up to several percent. Stress may also be applied to a material by a mechanical deformation of the structure where it is deposited, leading to the interest in developing MEMS structures.

2.1.1 Epitaxial growth

In 1928, Royer established the conditions for oriented overgrowth, defining the term epitaxy[1] and determining a rule that says epitaxy only occurs when it involves the parallelism of two lattice planes that have networks of identical or quasi-identical form and of closely similar spacings (Herman, Richter, and Sitter, 2004a). It is a

[1]Greek word meaning "above in an ordered manner" and possible to be translated as "arrangement on".

well-controlled phase transition that leads to a single crystalline solid, accomplished through nucleation, making it possible for a crystalline phase to grow in a structure-dependent manner onto another (Herman, Richter, and Sitter, 2004a). It designs the arrangement of atomic particles on the surface of a crystalline substrate preserving preferred orientations of the substrate into the film so that both crystallinities match even if the composition of the materials may differ. It is widely aimed to grow *high-quality functional films* for electronics applications.

Based on experimental results it was determined that the lattice misfit, given by $(a_s - a_f)/a_s$, where a_s and a_f are the corresponding network spacings (lattice constants) in the substrate and film, respectively, should be limited to 15% for epitaxial growth to occur. Since the growing layers follow the orientation of the substrate, a requirement for epitaxy is a clean substrate surface, otherwise, the information about orientation of the substrate is disordered or even destroyed, and the consequences are crystalline defects up to polycrystalline or amorphous growth (Vivien and Pavesi, 2013).

The processes involved in epitaxial growth are shown in figure 2.3 in which atomic species sublimated from effusion cells arrive at the substrate surface in high vacuum and condense either by chemical or physical adsorption. Once in the substrate surface, the adsorbed atoms diffuse thermally to jump to the sites of minimal energy, such periodical adsorbing sites for bonding and nucleation of adsorbed atoms that migrate colliding with crystalline nuclei are provided by the crystalline substrate. On the other hand, surface defects on the substrate surface due to slight misorientation behave as preferential nucleation centres since displaying a relatively small bonding energy. Hence, epitaxial growth of high-quality thin films requires compatible crystalline structures of both film and substrate as well as low lattice mismatch between them.

The epitaxial film starts to grow pseudomorphically imposing its lattice parameter to adapt to the substrate one and thus accumulating elastic strain energy as the deposited thickness is increased. However, beyond a critical thickness a relaxation of the elastic strain takes place either by plastic relaxation through dislocations formation at the interface or by elastic relaxation through formation of coherent 3D islands. Small lattice mismatch is important then not only to avoid defects but also to decrease interface strain in order to obtain high-quality crystalline films, leading to a cube-on-cube growth for similar cubic lattice structures. In other cases, though, a large mismatch can be accommodated by a re-orientation of the crystalline structure, i. e., a lattice mismatch can be decreased if the unit cell of the film is rotated by some angle relative to the substrate, as is the case of STO (3.905 Å) buffered on Si (5.432 Å) that when rotated by 45 degrees provides a lattice mismatch of only 1.65%. Other structures can still be seen as pseudo-cubic cells with lattice constants close to those one aims to match.

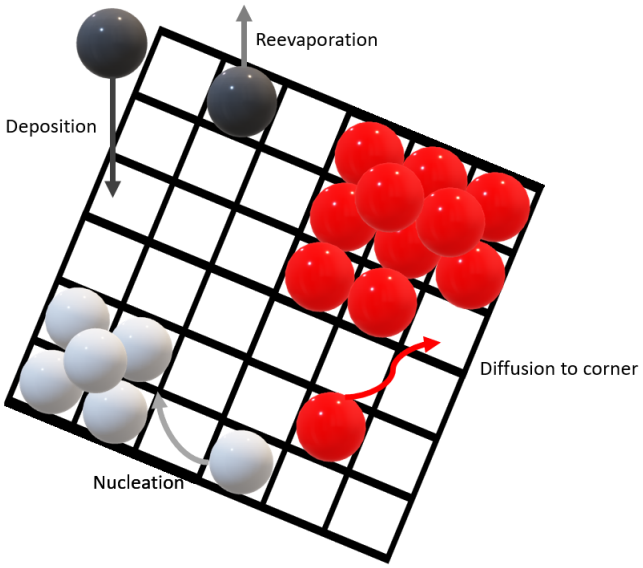

FIGURE 2.3: Atomistic process of the epitaxial growth (Yin, 2013a)

The epilayer grown on the substrate crystal surface may be formed from amorphous solid deposits, a liquid phase (a solution or a melt), vapour or gas (consisting of neutral or ionized particles) and from atomic or molecular beams (in a high or ultra high vacuum environment) (Herman, Richter, and Sitter, 2004a).

With respect to the modes of crystal growth, (Herman, Richter, and Sitter, 2004a) defines five of them, shown in figure 2.4, that are possible to be distinguished in epitaxy:

- **Volmer-Weber mode (VW-mode):** also called island growth mode, it is a mode where small clusters are nucleated directly on the substrate surface and then grow into islands of the condensed phase. It happens when the atoms, or molecules, of the deposit are more strongly bound to each other than to the substrate. This mode can be observed in many systems of metals growing on insulators.

- **Frank-van der Merwe mode (FM-mode):** this mode displays the opposite characteristics of the previous one because the atoms are more strongly bound to the substrate than to each other, so the first atoms to condense form a complete monolayer on the surface, which becomes covered with a somewhat less tightly bound second layer. This growth mode is observed in the case of adsorbed gases, such as several rare gases on graphite and on several metals, in some metal-metal systems and in semiconductor growth on semiconductors.

- **Stranski Krastanov mode (SK-mode):** also known as layer plus island growth mode, it is an "intermediate" case in which after forming the first monolayer, or a few monolayers, subsequent layer growth is unfavourable and islands are

formed on top of this intermediate layer due to factors that disturb the monotonic decrease in binding energy characteristic for layer-by-layer growth. It occurs especially in cases when both the interface energy and the strain energy of the film are high.

- **Columnar growth mode (CG-mode):** in this mode, when the film thickens, the condensed phase islands characteristic to these modes tend to cover the whole substrate surface without the merging of columns. As a result, columns usually remain separated throughout the growth process of the film, and the films grown in this way are easily fractured. It occurs when low atomic mobility over the substrate surface leads to the formation of highly defective atomic columns of the deposited material on this surface.

- **Step flow mode (SF-mode):** this mode is observed when the substrate wafer is cut slightly misoriented from a low-index plane in a specific direction, so its surface breaks up into monoatomic steps with precisely oriented low-index terraces and edges.

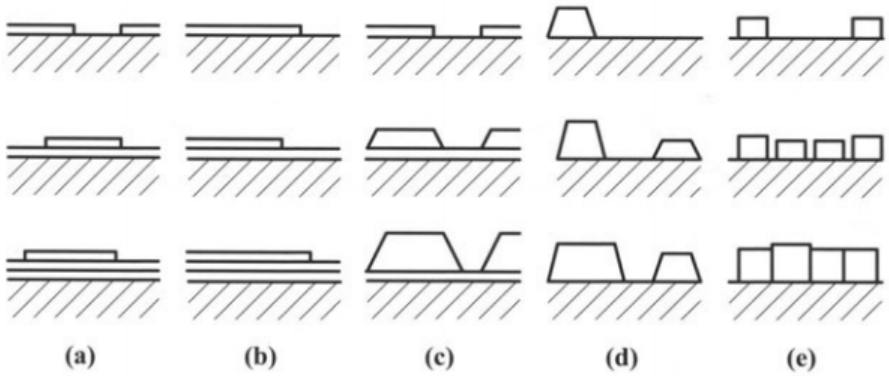

FIGURE 2.4: Schematic representation of the five crystal growth modes occurring on flat surfaces of substrate crystals: (a)F-M mode; (b) SF-mode; (c) SK-mode; (d) VW-mode; (e) CG-mode. Extracted from Herman *et. al*, 2004 (Herman, Richter, and Sitter, 2004a).

The prerequisite for a macroscopic phase transformation, seen in figure 2.5, to take place, is the nucleation process which is the spontaneous formation of small embryonic clusters – also called nuclei –, with some critical size determined by the equilibrium between their vapour pressure and the environmental pressure (Herman, Richter, and Sitter, 2004b). The critical nucleus is defined by a size where growth by capture of adatoms[2] is more probable than decay of the nucleus Vivien and Pavesi, 2013. These clusters exhibit increased surface/volume ratio having more energy than the bulk phases of the same mass, and hence a chance to survive and to produce macroscopic entities of the new stable phase (phase B) only within the supersaturated/undercooled homogeneous medium (Herman, Richter, and Sitter, 2004b).

[2]Adsorbed atoms in a precursor state for later incorporation in the lattice (Vivien and Pavesi, 2013).

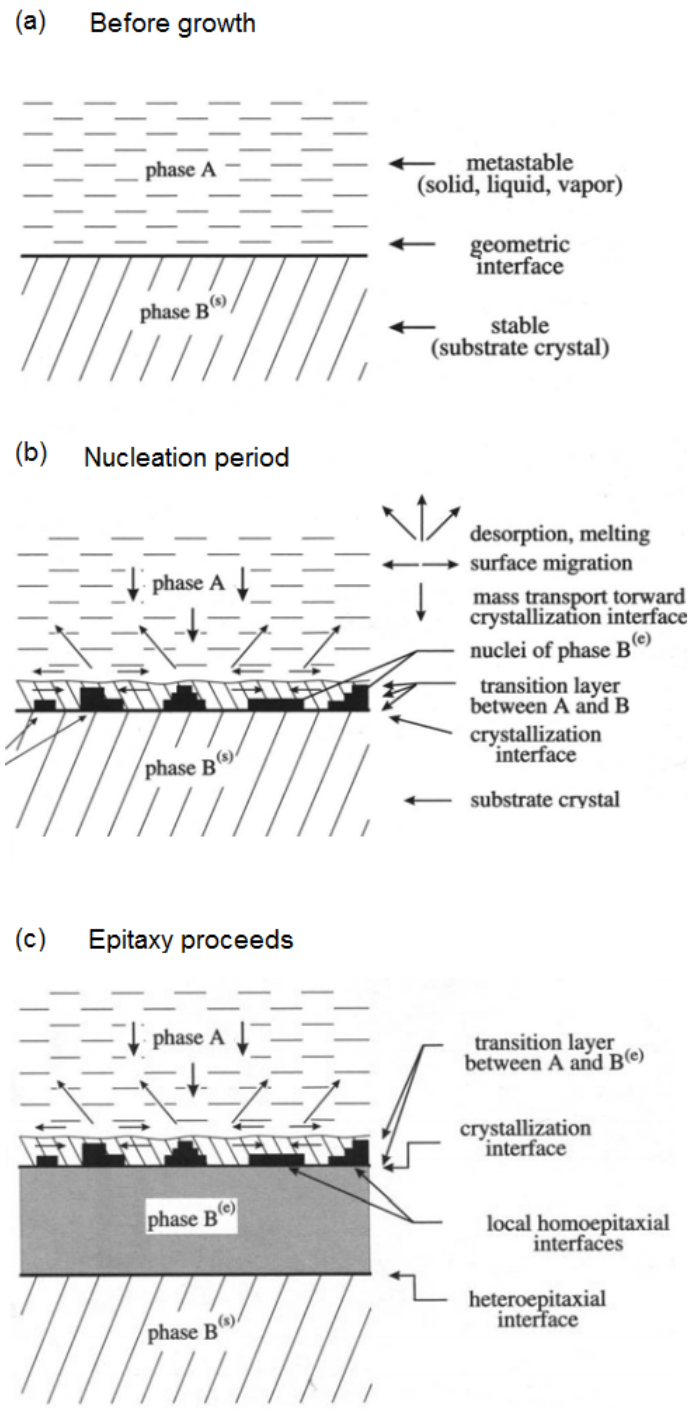

FIGURE 2.5: Schematic illustration of the geometrical configuration of the epitaxial growth system in different time periods of crystallization: (a) before the growth started, (b) in the nucleation period related to growth of the first monolayer, (c) at the stage of epitaxial growth, when an epilayer has already been grown and a fairly thick epilayer is exhibited. Extracted from Herman *et. al*, 2004 (Herman, Richter, and Sitter, 2004a).

In the case of heterogeneous nucleation, the particle clusters forming the critical nuclei of phase A do not occur in the homogeneous medium A but within the

matrix of adsorbed particles of medium A on the substrate crystal, i.e., on the phase B (Herman, Richter, and Sitter, 2004b). It happens as a sequence of two processes:

- Formation of adsorbed material of the phase A on the surface of substrate B, which is in sufficiently long-lasting contact with the surrounding phase A;
- Formation of a critical nucleus from the adsorbed particles and its subsequent growth to a supercritical size.

The orientation behaviour of the growing layer on a substrate single crystal may not only be influenced by nucleation of the deposited phase A, but also by the subsequent growth of the phase A on the crystalline surface of the phase B. When the deposit crystallites and the crystallites of the substrate show both the textural and azimuthal orientation towards one another then it is said to have epitaxial orientation relationships (Herman, Richter, and Sitter, 2004b).

The importance of nucleation to epitaxy for the production of high quality epilayers concerns the island growth (VW-mode and CG-mode) and layer growth (FM-mode and SK-mode) cases, whereas the step-flow growth mode (SF-mode) does not have this requirement (Herman, Richter, and Sitter, 2004b). In the island growth case, for example, since critical nuclei are quite stable, can reorient themselves and move over the substrate, one can conclude that it is largely the migration, rotation and coalescence of small stable crystallites that eventually produce an epitaxial layer (Herman, Richter, and Sitter, 2004b). These processes must be going on during deposition when it is carried out at high temperatures which is why clusters are often seen to be in epitaxial orientation at all stages of the deposition.

In the layer-growth regime, the substrate has a very strong influence on the form of the thin layer produced, and the growing layer has little option but to choose the best orientation in which to grow (Herman, Richter, and Sitter, 2004b).

2.1.2 Heteroepitaxial layers

The growth process in heteroepitaxy depends strongly on whether the interface between the epitaxial overgrowth and the substrate is crystallographically perfect or not, that is, on whether the grown epilayer is coherent – free to adopt any in-plane lattice constant that minimizes its free energy – or incoherent with the substrate – the energy minimization is achieved by adopting the in-plane lattice constant of the substrate (Herman, Richter, and Sitter, 2004b).

From the point of view of the mutual relation between the substrate and the heteroepilayer, three factors must be taken into account:

1. Lattice constant matching or mismatch, which constitutes the crucial problem of heteroepitaxy;

2. Crystallographic orientation of the substrate;

3. Surface geometry, or surface reconstruction, of the substrate.

If the misfit between a substrate and a growing layer is sufficiently small, the first atomic monolayers which are deposited will be strained to match the substrate and a coherent epilayer will be formed (Herman, Richter, and Sitter, 2004b). However, as the layer thickness increases, the homogeneous strain energy E_H becomes so large that a thickness is reached when it is energetically favourable for misfit dislocations to be introduced. The overall strain will then be reduced but at the same time the dislocation energy E_D will increase from zero to a value determined by the misfits defined by $(a_s - a_f)/a_s$ (Herman, Richter, and Sitter, 2004b).

2.1.3 Epitaxial strain induced by substrates

One possible way to induce strain in epitaxial thin films is to use the lattice mismatch between the film and the chosen substrate. Before I start my PhD thesis, a previous PhD student, Sandeep Kumar Chaluvadi (Chaluvadi, 2017a), had studied the effect of the strain induced by a selected list of substrate materials, as shown in figure 2.6, to evaluate its effects on the magnetic properties of LSMO and more precisely on its magnetic anisotropy (Chaluvadi et al., 2020).

Depending on the substrate materials and on the LSMO film thickness, it was shown that the magnetic anisotropy could be tuned from in-plane uniaxial to in-plane biaxial, including a mix of them or traces of out-of-plane anisotropy in some cases. It was then discussed that the choice of the appropriate substrate can be a way to tune the magnetic anisotropy as required for different applications such as AMR sensors or memory devices for examples (figure 2.7).

Works by other groups can be found in different references. One can cite (Mandal, Choudhary, and Das, 2020) who tuned the magnetotransport properties of epitaxial $Sm_{0.5}Ca_{0.25}Sr_{0.25}MnO_3$ thin films via strain engineering due to different film thicknesses and (Adamo et al., 2009) who studied the electrical and magnetic properties of LSMO thin films deposited on different single crystalline substrates, thus varying the substrate-induced biaxial strain from -2.3% to +3.2%. It was shown that the dependence of the Curie temperature on biaxial strain was in very good agreement with the theoretical predictions of (Millis, Darling, and Migliori, 1998).

2.1.4 Thin flexible substrates

Magnetic thin films deposited on polymer substrate show tremendous potentialities in new flexible spintronics based-applications, such as magnetic sensors adaptable to non-flat surfaces. In the case of flexible sample made of polymers coated by a very

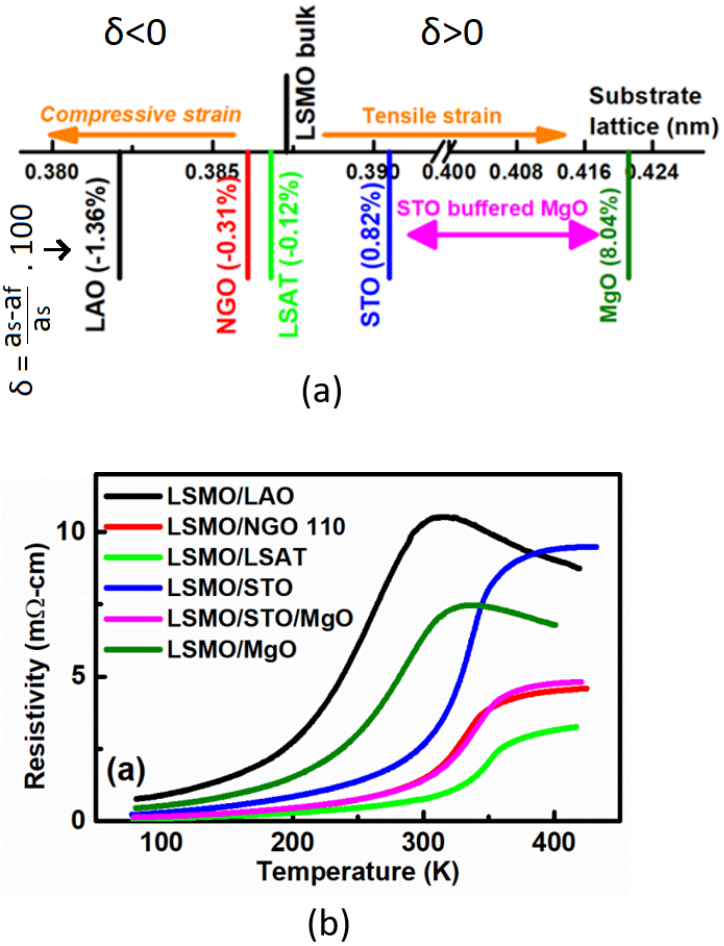

FIGURE 2.6: (a) Lattice parameters of different single crystal substrates used during Chaluvadi's PhD thesis along with the calculated lattice misfit strain by considering the pseudocubic bulk lattice parameter of LSMO (0.389 nm); (b) Electrical resistivity versus temperature characteristics of the 50 nm LSMO film deposited on various substrates. Extracted from (Chaluvadi et al., 2020)

Table 1. Thickness and substrate-dependent in-plane magnetic anisotropy, dominant effects that contribute to magnetic anisotropy, anisotropic field and applications are tabulated.

Substrates	LSMO thickness	*In-plane* magnetic anisotropy	Dominant effect	$\mu_o H_k$ (mT)	Applications
NGO (110)	12 – 50 nm	Uniaxial	Magneto-elastic	3.4–8.4	AMR sensors
LSAT (001)	50 nm	Uniaxial + OOP	Compressive strain,	17	AMR sensors
	12 nm	Uniaxial	interface effects	20	
STO (001)	50 nm	Biaxial (almost isotropic)	Magneto-crystalline + step-induced	3.3	User choice by inducing shape effects
	12 nm	Uniaxial	Steps, miscut angle of STO	2	AMR sensors
STO/MgO (001)	50 nm	Pure Biaxial	Magneto-crystalline	5.47	Four-state memory devices

FIGURE 2.7: Thickness and substrate-dependent in-plane magnetic anisotropy, its possible origins, anisotropic field and applications are tabulated (Chaluvadi et al., 2020)

thin layer, a very small bending effort can lead to relatively high stress in the layer (Gueye et al., 2014).

Structures based on a 200 nm-thick Nickel film deposited by radio frequency sputtering at room temperature on a flexible substrate (KaptonVR 24) of 125 μm were used by (Zighem et al., 2013) to study the voltage induced in-plane magnetic anisotropy in a magnetostrictive film deposited on a flexible substrate and glued onto a piezoelectric actuator.

The use of flexible compliant substrate with a much smaller Young's modulus than a rigid substrate such as silicon, for example, with $E = 180\ GPa$ can be chosen in order to avoid clamping effects with the substrate to obtain maximum strain transmission in between a piezoelectric actuator and the film as done by (Zighem et al., 2013). The stress applicable to the magnetization by the piezoelectric environment is limited by the clamping effect which may reducing perspective on applications.

A significant strained induced magnetoelectric coupling is obtained in this kind of bilayers (piezoelectric/magnetostrictive) only in the presence of non negligible in-plane strains (Zighem et al., 2013). The strains ϵ_{xx} and ϵ_{yy} were observed to be transmitted onto the proposed structures homogeneously in the thickness, i. e., the transmission of the in-plane strains between the actuator and the surface of the film was close to 100%.

The magnetization in 20 nm thick Co_2FeAl, CFA Heusler alloy, deposited on Kapton flexible substrate was also studied by (Gueye et al., 2014) and shown to be easily manipulated by bending the sample. The bending strain effect was experimentally studied by microstripline ferromagnetic resonance (MS-FMR).

2.1.5 Strain application

MicroElectroMechanical Systems (MEMS)

MEMS devices are miniaturized mechanical systems produced using microfabrication techniques widely explored in the electronics industry. Some of its advantages are the use of silicon microtechnology, small size, low weight, batch production and performance improvement by integration of electronics/actuators. However, some difficulties can be found when dealing with such microstructures fabrication as process incompatibility between materials and major packing problems, the devices may also present some deficiencies (offset, drift, non-linearity, cross-sensitivity, temperature) that must be considered for each application.

Such structures offer the possibility of taking into account the defects, microstructure and even compositions which can change with strain in thin film samples in contrast with stress-dependent properties studies based on films subjected to

static stresses, that simply derive the effects of the deformation from the comparison of samples subjected to different stresses. Reversibly controllable stress using piezoelectric material, for example, helps overcome this problem and allows direct measurements of strain-dependent ferroic properties to be made (Dörr et al., 2009). Compared to electrostatic MEMS, piezoelectric devices also offer advantages in larger actuation amplitude, faster response time and lower operation voltage (Banerjee et al., 2014).

Use of piezoelectric substrates

Controlled deformation of the crystal lattice is a desirable tool for exploring the influence of deformation in thin films.

The basic idea of a piezoelectric substrate is as follows: an electric field applied perpendicular to the plane of the substrate causes a biaxial deformation in this plane by the inverse piezoelectric effect (coefficient d_{31}), and a thin film deposited on the substrate will be continuously strained with the substrate, as shown by figure 2.8 for insulating and conductive films, respectively. The film thickness limit is dependent on the force that the piezoelectric surface must exert to apply stress in the film (Dörr et al., 2009). This force increases in proportion to the thickness of the film, ultimately leading to cracking on the surface of the piezo material, assuming the film does not crack earlier.

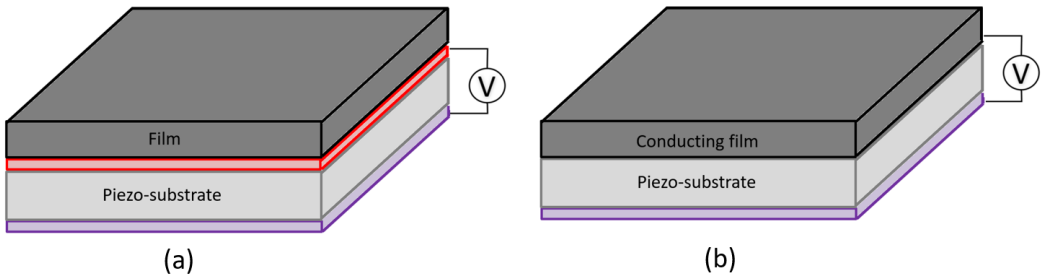

FIGURE 2.8: Piezoelectric actuation principle. Extracted from (Dörr et al., 2009)

(Thiele et al., 2005) proposed to use 0.72Pb $(Mg_{1/3}Nb_{2/3})O_3$–$0.28PbTiO_3$ PMN-PT substrates with oriented surfaces (001) to provide deformation in the biaxial plane so as to be electrically controllable, due to some important advantages, like the fact that it is almost cubic even in the ferroelectric state - this composition of PMN-PT is rhombohedral with $a_{PMN-PT} = 4.022$ Åand $\alpha = 89.90°$ at 300 K, which is close to a cubic structure -, reaching extremely high strain levels (above 0.6%) and low hysteresis can be achieved in addition.

Electrical transport measurements under the reversible strain in the plane of the substrate for LSMO and LCMO thin films deposited on top of STO/PMN-PT

(001) were analyzed by (Bilani-Zeneli et al., 2008) by applying a voltage between a lower Au/NiCr electrode and the conductive manganite film - this is possible due to the much larger resistance of the piezoelectric crystal ($> 10^9$ ohms), compared to the resistance in the kilo-ohm range of the manganite film, leading to a low leakage current which can, however, have all its contributions avoided if the resistance measurements of the films use alternating signs of source current (Thiele et al., 2005).

The importance of using a buffer layer such as STO comes from the fact that many properties depend nonlinearly on strain, so that in order to properly assess the observed change in a property X depends on strain as developed from the film, one must first know a predetermined lattice parameter a_0 (the pseudocubic film lattice parameter at E = 0) to determine the influence of the reversible strain in the dX/da derivative, as underlined by (Dörr et al., 2009). Otherwise, this can give very different values of dX/da depending on the state of deformation in the state of strain during the growth of the film (static strain).

Strain transfer from substrate to films can be revealed in strain-dependent electrical resistance measurements, which must present a reversible hysteresis loop. The butterfly-like format is a typical behavior of the change in resistivity due to the deformation induced by the reversal of the direction of polarization in the PMN – PT substrate (Zheng et al., 2010). If the ferroelectric field effect played a dominant role in the influence of resistivity, we would observe a rectangular hysteresis loop $\rho - E$ with the change in resistivity showing opposite signs for opposite directions of the applied electric field. It is still important to note that butterfly-like cycles involve the danger of cracking due to the repeated switching of the substrate (P) polarization, therefore, the safer type of measurement avoids a P inversion when working in a unipolar mode of the substrate.

The resistance of the films was seen to be proportional to the strain, because its loop follows the strain hysteresis curve and the R maxima are at the coercive fields of the substrate recorded in the polarization measurements, P (E). The resistance at room temperature increases under application of stress and is roughly proportional to V_{piezo}. The electrical resistance varies appreciably with the state of deformation of the films; therefore thinner films can be passed from a thermal dependence of the insulating type to a metallization by stress relaxation obtained from a thermal treatment.

The decrease in the resistivity of the thin film is explained, according to (Zheng et al., 2010), by the decrease in the tensile stress in the plane leading to the reduction of the tetragonal distortion of the MnO_6 octahedra of the film - revealed by an angularly resolved X-ray absorption spectroscopy study of thin films of $La_{0.7}Sr_{0.3}MnO_3$ subjected to epitaxial strain - and thus weakening the electron-lattice coupling force. As a result, this improves the hopping amplitude of electrons.

One way to quantify the contraction in the plane is to first evaluate the 2-theta value of the film reflection shifts and its corresponding increase in the cell constant c and then assume an approximate volume conservation after measuring the expansion out of plan. This means that an increase in $\epsilon_{zz} = (c_{film} - c_{bulk})/c_{bulk}$ (outside the constrained plane) would be accompanied by a decrease in the tensile stress in the plane ϵ_{xx}, the two quantities of which are related using the expression $\delta\epsilon_{zz} = -2\nu/((1-\nu)\delta\epsilon_{xx})$ - where ν is the Possion coefficient (Zheng et al., 2010).

A decrease in Curie temperature, T_C, was also verified on the LCMO/ STO/ PMN-PT (001) sample studied by (Bilani-Zeneli et al., 2008) - this was attributed to the effect of tension tensile strength in the manganite film -, as shown by (Angeloni et al., 2004) whose ferromagnetic temperature Curie, T_C, of $La_{0.7}Sr_{0.3}MnO_3$ was reduced by 365 K for unconstrained films/bulk at 270 K in 16 nm thick LSMO/ $LaAlO_3$ (001) structures under compression. (Thiele et al., 2005) also showed an increase of 6 K on T_C when applying a voltage $V_{piezo} = 400V$ leading to strain relaxation on the LSMO layer. A reduction in the transition temperature of the insulating-metal type was also provided by (Zheng et al., 2010) of about 9 K by applying an electric field of 10 kV/cm for $La_{7/8}Ba_{1/8}MnO_3$ structures on $0.67Pb(Mg_{1/3}Nb_{2/3})O_3$–$0.33PbTiO_3$ (LBMO/ PMN-PT).

Associated with the dependence of Curie temperature on stress, remanent (MR) and saturating (MS) magnetization also show both strain-related changes as a consequence as reported by (Dörr et al., 2009), using a basic model system for a strain-coupled two-phase magnetoelectric multiferroic composed by a magnetic film of $La_{0.7}A_{0.3}MnO_3$ (A = Sr or Ca) on a PMN-PT piezoelectric substrate, epitaxially deposited, so that the film-substrate sample is also well suited to theoretical modeling - for which a tetragonal approximation has been widely used with success for strained films, due to the distortions being small enough for a cubic reference cell, even though the structure of bulk lattice of materials is either rhombohedral or orthorhombic -, since the orientations and crystallographic deformations are well defined. No significant change in the coercive field, H_C, in these strain-dependent studies was observed, which is attributed to the low level of reversible strain (0.1%), which does not significantly change the total tensile strain and leaves the easy axes of the film unchanged.

It was still observed by (Dörr et al., 2009) that the dT_C/da increases with decreasing thickness, while no significant difference between the Sr or Ca doping was found. The T_C of near cubic ferromagnetic manganites has been described as quadratic strain dependent, described by

$$T_C = T_{C_0}(1 - \frac{1}{3\alpha\epsilon_a} - \frac{\delta}{2\epsilon_a^2}) \tag{2.1}$$

With the T_{C_0} *unconstrained*, the total strain in the plane ϵ_a and the positive volume and tetragonal strain coefficients α and δ, respectively, and under the assumption of a Poisson number of $\nu \approx 0.33$.

Actuation in MEMS

The actuation in MEMS devices, however, can be performed by different solutions used to apply deformation to suspended structures by mechanical bending, such as lateral gates (Biasotti et al., 2013), Lorentz force actuation (Remaggi et al., 2016), Atomic Force Microscopy (AFM) tip strain application and, finally, piezoelectric layers. Each one of these first three methods are briefly discussed in the following topics. Piezoelectric actuation will be presented in a separate section (2.2).

Coplanar electrodes actuation: Cantilever-type structures with an actuation by applying an electric field between side pads (lateral gates) instead of using typical top-bottom electrodes have been demonstrated by (Biasotti et al., 2013), as shown in figure 2.9. The structures were fabricated using Pulsed Laser Deposition (PLD) deposited STO/LSMO on STO substrates (001). Controlled bending of the beam was carried out under quasi-static electric fields applied according to the image below, using different values of tensions on the side pads, without any conductive layer deposit on top of the structure (the tension is applied to the lower LSMO by perforating the insulating STO support layer).

This actuation is based in the the voltage potential gradual drop over the domain of the substrate and the electric field lines gradually bending in the air and inside the STO substrate towards the ground pads. The electric field polarizes the dielectric beam mainly in its longitudinal (y) direction, and the non-uniform electric field bends it down.

The geometry of the side pads has a weaker electromechanical coupling, but a stronger relative dependence on the dielectric constant of the dielectric film, in particular at high values compared to the configuration of the top-bottom pads.

Such coplanar actuation has also been verified in the fabrication of resonant high-electron-mobility transistors (R-HEMT) in (Faucher et al., 2009). Instead of using a passive piezoelectric sandwich for detection, an $Al_{0.26}Ga_{0.74}N/GaN$ 100 nm long, 5 μm large, doubly clamped beam heterostructure was fabricated on a silicon, Si (111), substrate. The actuation was performed by a Schottky diode and the two-dimensional electron gas (2-DEG) as a bottom electrode (which is electrically

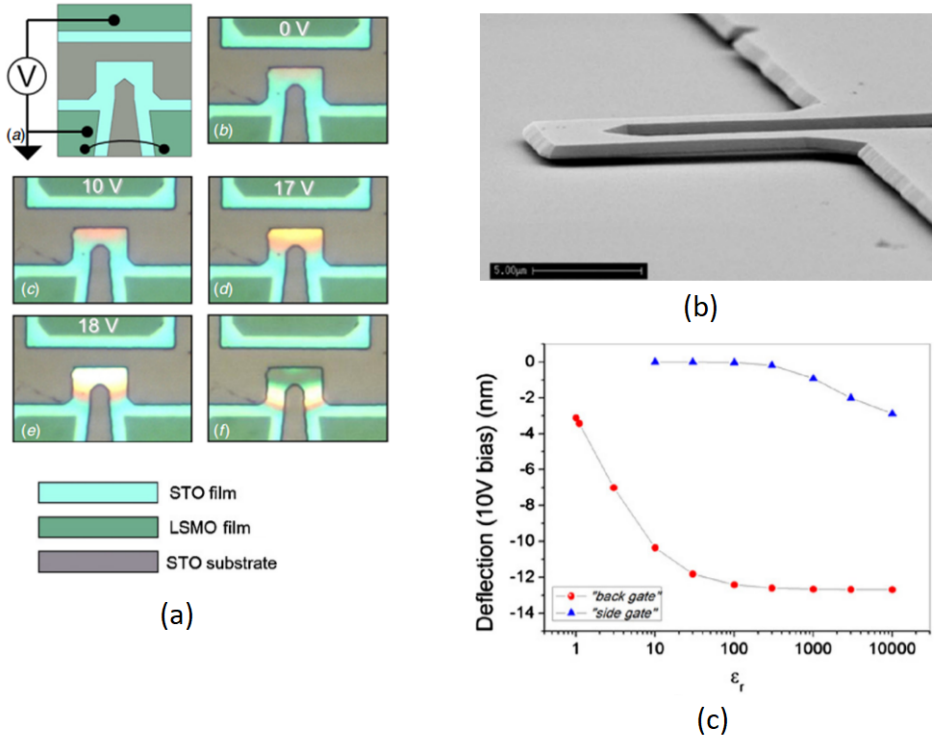

FIGURE 2.9: LSMO/STO cantilever (a) optical image upon different voltage bias applied to a lateral gate design structure actuation, showing the scheme of electrical contacts and color map with change of colours in the microcantilever reflecting its bending until stiction with substrate when pull-in voltage is achieved, (b) Scanning Electron Microscope (SEM) micrograph and (c) endpoint tip deflection with its normalized as a function of the dielectric constant of the STO film for the side gate and back gate configurations. Extracted from (Biasotti et al., 2013)

linked to coplanar guide by an ohmic contact at its termination it also defines a path between the ohmic contact located on the beam and two other ones below the clamping point). Hence, it defines a structure where coplanar electrodes laterally connect both the source and bridge over the gate to connect the drain.

Lorentz force actuation: Resonant structures which exploit the Lorentz force principle to detect magnetic fields by measuring the displacement of such structures exposed to external magnetic fields by capacitive, piezoresistive or optical detection techniques, have their operating principle based on an amplified response to the applied excitation source with a frequency equal to the resonant frequency (s) of the structure - amplification caused by the efficient transfer of energy from the excitation source to the structure. The use of sensors based on resonant structures can produce larger output signals, increasing its sensitivity. MEMS magnetometers are potentially compatible with CMOS manufacturing, without magnetic hysteresis, an advantage over Hall effect sensors with their higher power consumption for

better resolutions or even magnetoresistive sensors which require special magnetic materials in the process of manufacturing; On the other hand, they present generally low resonant frequencies and therefore limited by the flicker noise (S.Ghosh and J.E.Y.Lee, 2016).

The idea, as proposed by (Herrera-May et al., 2009) and graphically explained in figure 2.10, is based on an aluminium loop placed on the surface of the bridge: the excitation current flows inside with a frequency equal to the first frequency resonance of the structure. When exposed to an external magnetic field B_x, a Lorentz force, $F_L = lB_xL_y$, is generated. Where L_y is the length of the Al loop while the amplitude of the deflection of the beam depends on the amplitude of the Lorentz force, which is directly proportional to I and B_x. Such deflections lead to a deformation linked to the elastic modulus of the material structure, to the geometric characteristics of the resonant structures and to the quality factor (Q) (Todaro et al., 2012).

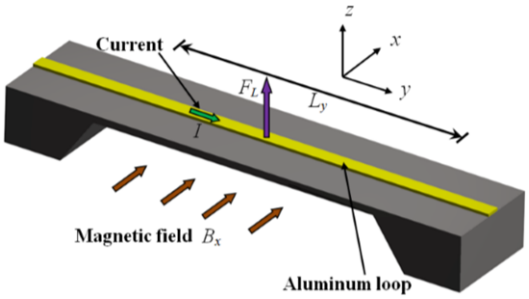

FIGURE 2.10: Bridge-type structure actuated by Lorentz force. Extracted from (Herrera-May et al., 2009)

Most of these structures are fabricated on Si substrates, which have an elastic modulus dependent on temperature in such a way that T affects the performance of a resonant sensor (it influences the properties of the material and creates stresses inside the structure). The resonance frequencies are affected by the residual stresses on the structure: the deformation causes a shift in f_R (Todaro et al., 2012). For bridge and beam structures, if the internal stresses are compressive then they reduce the resonant frequency of the beams; on the other hand, if the internal stresses are such of traction, they increase the resonant frequency of structures (Herrera-May et al., 2009).

Tip induced actuation: Local actions can be performed by using a mechanical profilometer or a scanning probe microscopy in order to suject a MEMS device to an external force application. A mechanical pressure can be exerted to such structures with the cantilever of an atomic-force microscopy (AFM) (Pellegrino et al., 2009) or optomechanically with the probe of a near-field microscope (Salary et al., 2016).

2.2 Piezoelectric MEMS

Piezoelectric MEMS are based on the intrinsic electromechanical coupling effect of the piezoelectric materials, which is a physical quantity related to the materials ability to convert electrical energy into the mechanical form or vice-versa. A direct effect is visualized when electric charges appear on the surfaces of a piezoelectric material upon an elastic stress application and it configures the base for piezoelectric sensors, i. e. direct mechanical transducers, whereas an inverse effect takes place by the application of an electric field inducing elastic strain which is the case for actuators such as resonator for which the resonance parameters, frequency and amplitude, are influenced by the input physical quantities.

Common piezoelectric actuators are either based on bimorph or expansion structure to obtain the elastic displacement: the former is based in the in-plain piezoelectric strain e_{31} which is to be measured as beam deflection while in the later, it's the longitudinal electric-field-induced strain, d_{33}, that is responsible for mechanical displacement, a simpler design at the cost of a less important variation.

Piezoelectric thin films offer several significant applications in microelectronics and microelectromechanical systems (MEMS) such as microsensors, microactuators, non-volatile memories, printheads, etc. Due to large piezoelectric coefficients of many ferroelectric materials, such as lead zirconate titanate, $Pb(Zr,Ti)O_3$ (PZT), large actuation force and displacements can be generated and also thin films actuators can be driven by high-frequency signals with high contact and restoring forces at low voltages. The use of such piezoelectric materials in MEMS scale allows the exchange of minimal amount of energy to achieve improved performances in terms of resonance frequency reach as well as sensitivities, hence high efficiency and quality factor, Q. The performance of piezoelectric MEMS is, however, strongly dependent on the film quality since the surface nature onto which PZT is grown plays a crucial role as it can lead to degradation of its piezoelectric properties (Isarakorn, 2011) since it affects leakage current, dielectric properties and the growth and crystalline structure of the grown ferroelectric films.

The actuation behaviour of MEMS devices is a result of the intrinsic and extrinsic contributions of the aforementioned material's piezoelectric response. These contributions originate from the stretching/contracting of the unit cell dipoles in the piezoelectric material and the contributions due to domain wall movements, respectively. In this sense, a thermal poling procedure is imperative for proper operation of MEMS actuators devices to eliminate a decrease in deflection of the actuator due to reduction of extrinsic contributions and/or re-poling ones after a few actuation cycles. This characterizes a typical procedure where the use of thermal energy in combination with an electric field is used to align defect dipole complexes and create an internal electric field aligned with the polarization direction and lock in the

domain configuration (Funakubo et al., 2012).

Conventionally, PZT is deposited onto platinum-coated Si wafers and coated also with platinum for top contacts, in order to form a capacitor structure of the type Metal-Ferroelectric-Metal (MFM) (Vilquin, B. et al., 2001).

2.3 Epitaxial MEMS

The development of epitaxial MEMS allows a way to promote an enhancement in the piezoelectric properties to the typical growth of piezoelectric materials. However, it requires optimization of growth process for achieving better quality films for such improved performances. Additionally, the high-frequency losses of films may be smaller than those of bulk materials and sensitivity can be increased.

So far, few realisation of epitaxial MEMS using oxides can be found in literature and very few of them integrate piezoelectric materials.

- (Banerjee et al., 2014) has used yttria stabilized zirconia (YSZ)as buffer layer to epitaxially grow by PLD at high temperatures a multilayer of sandwiched $PbZr_{0.52}Ti0.48O_3$ (PZT) between $SrRuO_3$ (SRO) electrodes on a silicon (001) substrate. The structures were patterned by lift-off with a AlO_x sacrificial mask followed by anisotropic substrate etching (hot KOH-etching) to obtain a cantilever configuration to be operated in bending mode actuated by an external voltage that induces a lateral extension/ contraction in the active piezoelectric layer causing a bimorph actuation due to the clamping with substrate. This can be seen in figure 2.11. Epitaxy was confirmed by X-ray diffraction measurements and the electromechanical response of the PZT cantilevers well-behaved ferro and piezoelectric responses was investigated employing laser Doppler vibrometry, and the dependence of frequency versus cantilever length can be verified in figure 2.11(c).

- The enhanced piezoresponse in relaxor ferroelectrics with engineered domain states and associated possibility to improve performance of piezoelectric MEMS by incorporating these materials has led (Baek et al., 2011) to study the use of $Pb(Mg_{1/3}Nb_{2/3})O_3$-$PbTiO_3$ (PMN-PT), a lead-based relaxor ferroelectric with piezoelectric coefficients that can be 5 to 10 times those of bulk PZT ceramics and a large electromechanical coupling coefficient of $k_{33} \approx 0.9$. A composition 0.67PMN-0.33PT was used due to maximized physical properties in ferroelectric solid solutions morphotropic phase boundary (33% PT in the PMNPT solid solution system). Problems with the appearance of pyrochlore phase, one of the major processing difficulties, were bypassed by the careful control

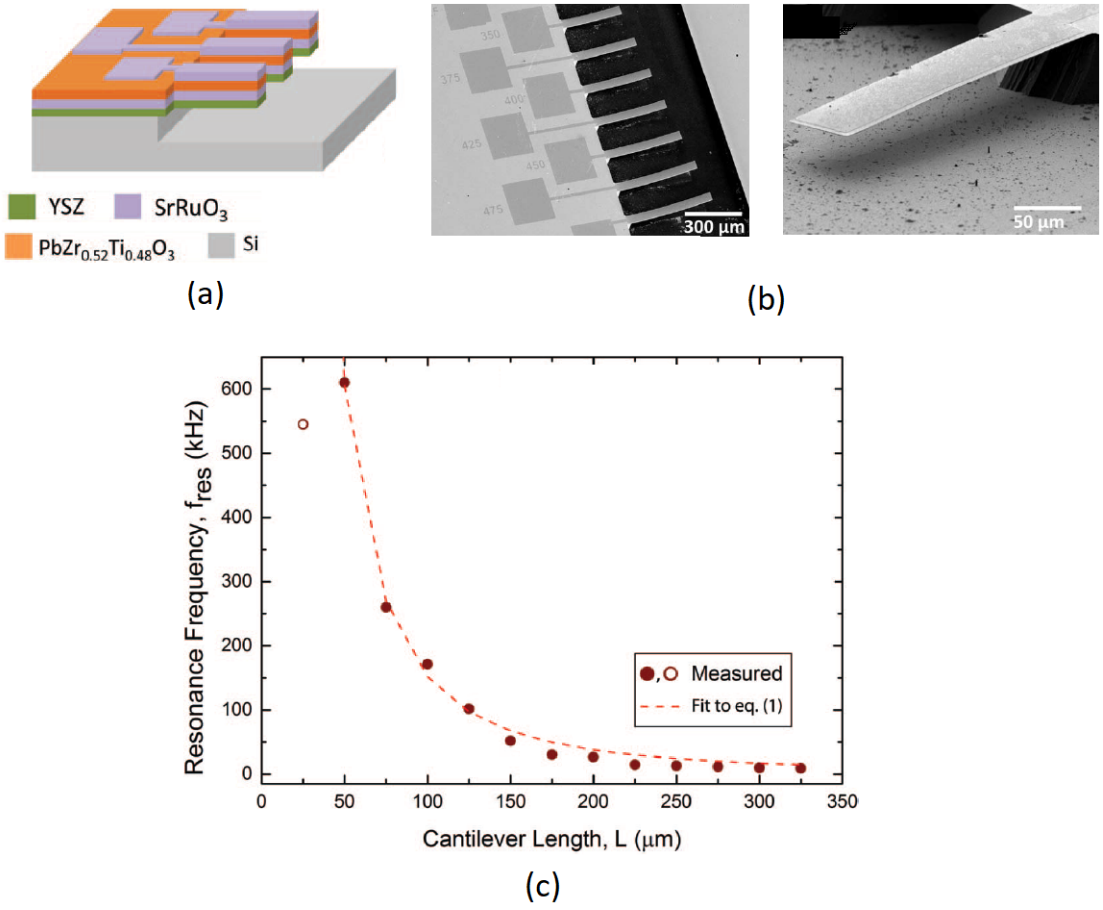

FIGURE 2.11: (a) Schematic representation of freestanding piezo-MEMS devices, (b) Scanning Electron Microscopy (SEM) overview of a series of cantilevers with different lengths and (c) measured resonance frequency of dominant vibrational mode versus the length of the freestanding heteroepitaxial cantilevers; Equation (1) to which it refers determines the bending resonance frequencies as a function of numerical factors α_n, the length of the cantilever L, its width W, thickness t, effective Young's modulus E and beam mass per length m_L: $f_n = \frac{\alpha_n^2}{2\pi L^2}\sqrt{\frac{E(Wt^3/12)}{m_L}}$; Extracted from (Banerjee et al., 2014)

of thin-film growth conditions to achieve $(001)_{pc}$ oriented single-crystal PMN-PT films. To achieve this, an epitaxial $SrTiO_3$ buffer layer was used as well as a 4 miscut Si substrate, since the effect of high density of steps on the surface of miscut substrates is to maintain film stoichiometry by effectively incorporating volatile constituents, as PbO, into the film, suppressing formation of lead-deficient pyrochlore. The PMN-PT film on 4° miscut Si have shown dramatic improvement in both phase purity and epitaxy of perovskite phase in comparison with exact Si.

The polarization–versus–electric field (P-E) hysteresis loops measured for 1 μm thick PMN-PT films were seen to be negatively imprinted indicating the existence of a built-in bias which decreased the permittivity at zero field, resulting in an improvement of the figure of merit for sensors operating in a voltage-sensing mode. A further study replacing randomly oriented PZT actuators in radio frequency MEMS switches with these highly oriented PMN-PT films decreased the voltage required to minimize contact resistance from $10V$ to $< 2.5V$.

All the cantilevers are bent downward, as shown in figure 2.12, after release from the Si substrate due to the relaxation of the epitaxial strain between PMN-PT ($a_{pc} = 0.402$ nm) and $SrRuO_3$ ($a_{pc} = 0.393$ nm).

- Magnetoelectric (ME) sensors use the mechanical coupling between a ferromagnetic material and a piezoelectric (PZT) one in a multiferroic laminated composite to convert directly a magnetic signal into an electrical one with remarkably high sensitivity compared to other different magnetometers for resonant AC fields (Kiser et al., 2013), (Robisch et al., 2015). The heterostructures grown epitaxially enhance mechanical coupling and, hence, the stress transfer between the functional layers. The self-excitation capability provided by integration of piezoelectric materials allows the avoidance of solenoid coils in microdesign (Ngoc et al., 2021).

  The operation principle of such devices is based on the resultant stress in the magnetic layer subjected to an external magnetic fields that is transferred to the piezoelectric layer due to the mechanical coupling between them and leading to a shift in the resonant frequency of the system. Such change in the resonant frequency is measurable through an impedance measurement.

  Doubly clamped magnetoelectric micro-electromechanical systems have been proposed using AlN (750 nm) as piezoelectric material and FeCo (200 nm) as magnetic field sensing layer in resonators with a magnetic field sensitivity of about 5000 Hz/T in a bias magnetic field of up to 0.2 T (Bennett et al., 2017). The sensitivity in such sensors is calculated by the ratio of the shift in the resonant frequency over the range of external DC magnetic field, i. e., df/dB.

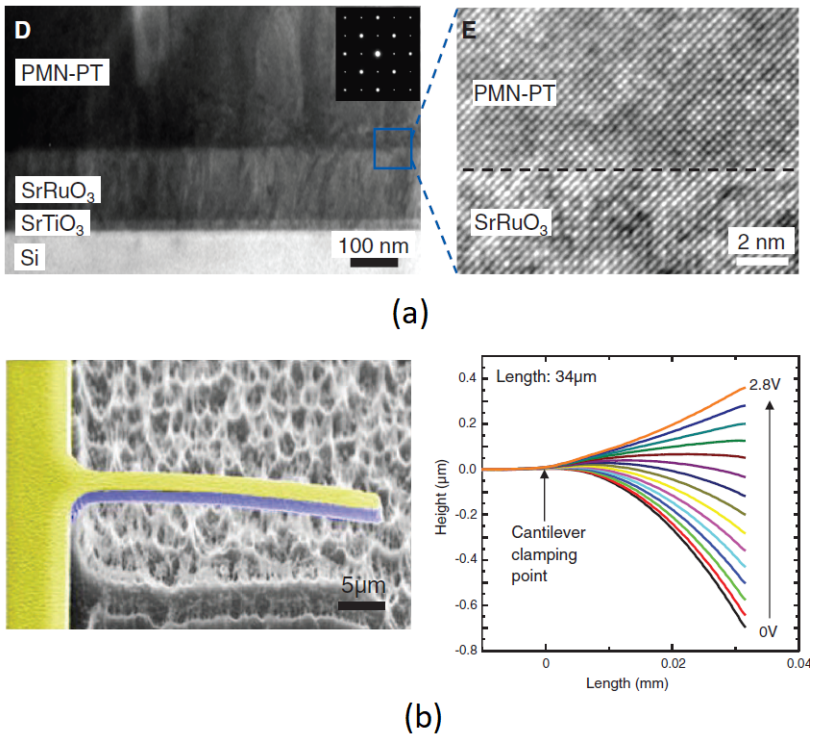

FIGURE 2.12: (a) Bright-field cross-sectional (Transmission Electron Microscopy) TEM image at the interface between PMN-PT and $SrRuO_3$, the inset is a selected-area electron diffraction (SAED) image of PMN-PT along the [100] zone axis with atomically sharp interface between the $SrRuO_3$ and PMN-PT layers exhibiting clear epitaxial match between the layers (b) SEM image of a PMN-PT cantilever and its profile as a function of dc voltage. Extracted from (Baek et al., 2011)

- (Ngoc et al., 2021) have shown the use of resonant cantilever structures based on freestanding multi-ferroic PZT/Tb–Fe–Co thin film multilayers as magnetic sensors where the Tb–Fe–Co layer (150nm) acts both as a magnetic field sensing and top electrode and the PZT one (150 nm) as a micro-transducer to obtain an electrical signal to estimate the magnetic signal by the shift of the device resonant frequency. A $SrRuO_3$ (SRO) layer is employed as bottom electrode for the complete heterostructure grown on silicon substrate as shown in figure 2.13. The devices are patterned as 40 μm long, 20 μm large cantilevers.

  The deflection curve follows the conventional butterfly shape of the C-E curve, in this case with a total variation of 6 μm, as well as the shift of the resonant frequency, which is consistent with the deformation of the cantilever under the application of the electric field, exhibiting the same butterfly shape.

  A DC magnetic field can be sensed by such devices through the the impedance phase angle frequency peak of the magnetoelectric PZT/ Tb–Fe–Co cantilever resonators as shown in figure 2.13(d). It has exhibited sensitivities of around 487 Hz/T at low field ($< 0.2T$) and 249 Hz/T at high field ($> 0.2T$).

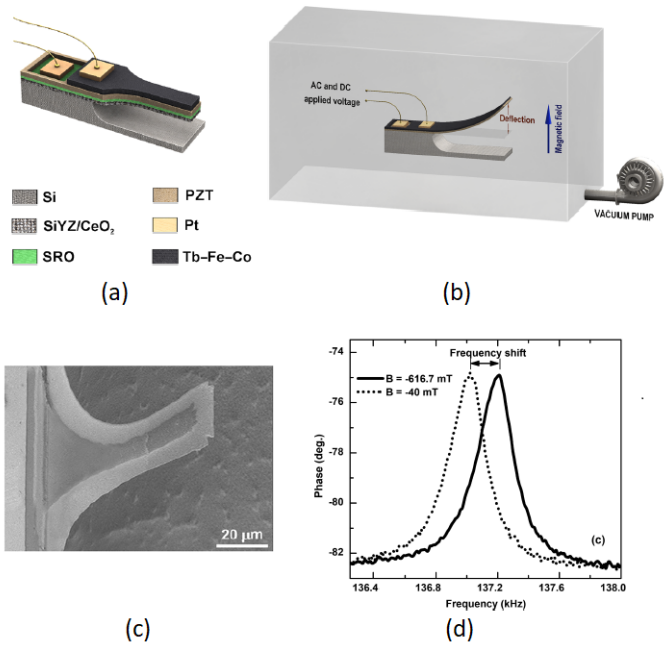

FIGURE 2.13: (a) Schematics of the proposed PZT/Tb–Fe–Co microresonators, (b) its experimental setup for resonance characterization, (c) the scanning electron microscopy image of the fabricated structure and (d) an impedance phase plotted as a function of frequency at two different values of the out-of-plane DC magnetic field. Extracted from (Ngoc et al., 2021)

- (Pellegrino et al., 2009) have shown the fabrication of an all-oxide micro-electromechanical structure based on suspended bridge devices made of an epitaxial heterostructure composed of a $La_{0.7}Sr_{0.3}MnO_3$ (LSMO) sacrificial layer and

STO supporting layer to study the strain effects in oxide compounds.

The fabricated geometries are designed in order to measure the resistance of the microbridge region during its bending by a four-wire electrical configuration. The bending was performed either mechanically through the use of a stiff AFM tip leading to linear increase of the electrical resistance until contact with substrate enabling the experimental value of the elastic constant of the bridge to be calculated from the slope of the force–distance curve, or through the application of a bias voltage between the gate and substrate region (that is also covered by a conducting LSMO film) to increase the electromechanical coupling. Both cases are shown in figure 2.14. Small deflection of the bridge is verified up to -21V seen by a slight change of color at the bridge edge, accompanied by the occurrence of subtle increase of the film resistance due to small strains. At -22V, however, an abrupt change in the optical image linked to a jump toward a high-resistance state is observed. The reduction in voltage keeps the bridge's position between states C and D remaining in contact with the substrate where the induced strain and film resistance approximately stand constant at their maximum value.

From the AFM tip actuation, values of k in the range of 10–15 N m^{-1} were extracted, in accordance with estimations for cantilever theory and a Young's modulus for STO films of approximately 100 GPa. The LSMO resistance modulation achieved is about 0.6–1.6% either bending with the AFM tip or by electric fields and its increase is explained in the framework of a reduced bandwidth and higher localization effect due to an increased Jahn-Teller splitting. Strain distribution along the bridge was concluded to be non-uniform, with a maximum value reached at the joints and the device performed mainly uniaxial stresses along the bridge length. A maximum surface tensile strain at the joint along the bridge length was calculated to be 0.26%.

- Epitaxial all-oxide nanocantilevers composed of a strontium titanate ($SrTiO_3$) active layer sandwiched between two layers of strontium ruthenate ($SrRuO_3$) were studied as flexoelectric devices in comparison with MEMS based on the piezoelectric effect by (Bhaskar et al., 2016). Flexoelectricity defines the linear coupling between the mechanical strain gradient with the electric polarization (or inversely, or the mechanical response under the electric field gradient) and it is a property that all high-k dielectric materials used in CMOS circuitry should possess, since it is not restricted by material symmetry, extending the possibilities of materials likely to be suitable for nanoscale electromechanical device applications, providing a route to integrating *more than Moore* electromechanical functionalities within transistor technology since flexoelectric curvature/voltage scales as the inverse of the cube of the thickness

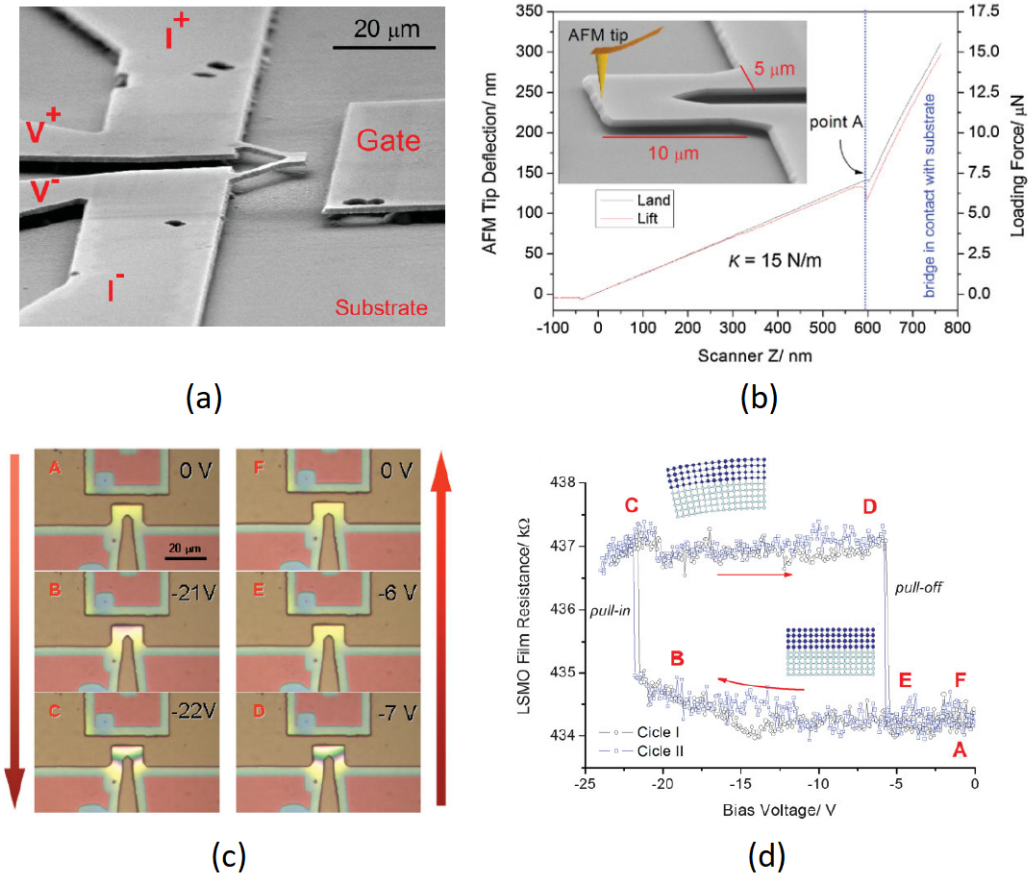

FIGURE 2.14: (a) SEM image of the proposed triangular STO microbridge with electrical contacts indicated,(b) AFM-tip deflection versus Scanner Z extension, showing the two regimes of bridge bending and bridge in contact with the substrate, (c) optical images of the bridge at different biasing states as indicated by capital letters and (d) LSMO film resistance as a function of the applied voltage, measurement reports two voltage-ramp cycles. The resistance discontinuities are associated with jumps in the bridge deflection and in the strain of the overgrown LSMO film. Extracted from (Pellegrino et al., 2009)

and it could be expected to exceed the performance of even the best piezoelectric and ferroelectric devices reported in the literature to date (Bhaskar et al., 2016). The device was tested in resonant mode showing an observed resonance frequency of 310 kHz, as displayed in figure 2.15, which corresponded to the analytical estimate based on the geometry and the value of the effective flexoelectric coefficient was calculated from the slope of the curvature versus voltage. Finally the analysis of the flexocoupling ratio $f = \mu/\epsilon$ was made showing good agreement with the estimated values for ionic solids and comparable to the value found for other perovskites such as lead magnesium niobate–lead titanate (PMN-PT).

The coefficients were measured by inverse and direct methods leading to similar values validating that flexoelectric devices display the same coupling constant for operation as a sensor and actuator.

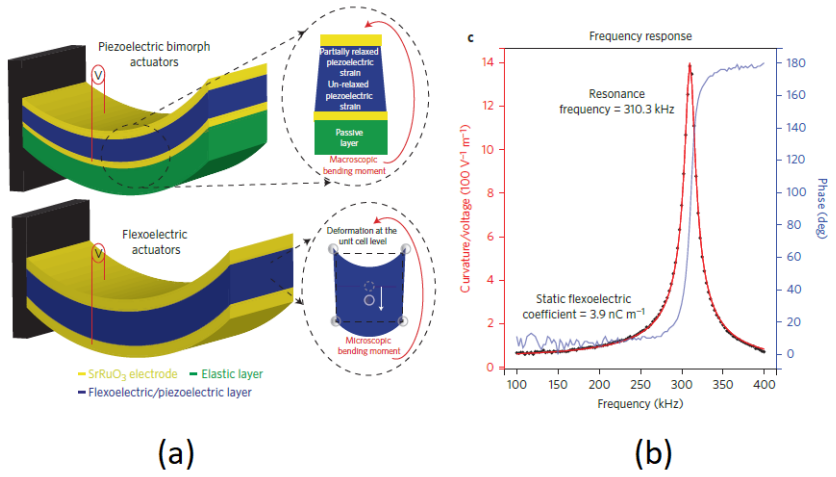

FIGURE 2.15: (a) Schematic comparing flexoelectric actuation and piezoelectric bimorph actuation in nanoscale actuators and (b) curvature/voltage ratio as a function of frequency for the $SrTiO_3$ nanocantilever at 1 V excitation, showing the resonant peak at 310 kHz confirmed by the 180° phase change, with quality factor Q of 25. Extracted from (Bhaskar et al., 2016)

(Guillet et al., 2019) have developed the process of using LSMO thin films into sensors in order to obtain very low electrical noise. This was used in two high signal-to-noise ratio sensors based on LSMO thin films: uncooled bolometers on STO buffered silicon substrates (in order to allow the use of standard micromachining techniques of silicon) and uncooled low-field magnetic sensors (anisotropic magnetoresistances) on STO substrates. To minimize parasitic effects on the electrical contacts due to non-homogeneity in the current density distribution the mask designs were made to avoid any deviation of the current lines. Such designs were used as a base for the masks with integrated piezoelectric actuation for suspended beams designed in this thesis. The importance in the geometry design is to avoid an increase of up to 3 orders of magnitude difference in the noise spectral density ($V^2 Hz^{-1}$) that

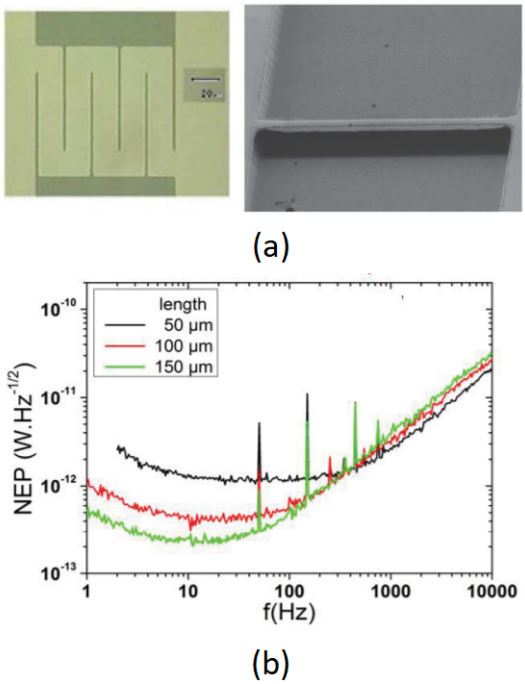

FIGURE 2.16: (a) Examples of LSMO bolometers, first a non-suspended meander of 18 μm width and second a 50 μm long free-standing beam with 4 μm width, and the (b) NEP of 50-150 μm long, 2 μm width, suspended 75 nm thick LSMO thin films bolometers. Extracted from (Guillet et al., 2019)

were measured in the same sample by (Guillet et al., 2019) when the design was not well chosen.

The effect of the LSMO films thickness was evaluated and it was verified that in the 20-80 nm range the films are generally relaxed and therefore exhibit low noise values, whereas beyond this range (close to the critical thickness value for epitaxial films on STO) an increase of the noise levels is observed and it can be related to the presence of inhomogeneous strain or even cracks for these higher thickness values. When the structures are released from the substrate the thermal conductance was shown to be reduced by 3 orders of magnitude (down to $10^{-7}W \cdot K^{-1}$), increasing the sensitivity by a factor of 1000.

Thanks to the very low $1/f$ noise and the use of adequate geometries ultra low Noise Equivalent Power (NEP) values, expressing the minimum detectable power per square root bandwidth of a given detector, in the order of $pW \cdot Hz^{-1/2}$ could be obtained at 300 K. The large Temperature Coefficient of Resistance (TCR) (around 2-3 % K-1) has showed that LSMO is a promising candidate for fabricating uncooled bolometers in addition to the low-noise level compared with other resistive materials such as semiconductors (a-Si, aSi:H, a-Ge, poly SiGe) and other oxide materials (semiconducting YBCO, VOx, etc.). This also enables the use of LSMO in applications in magnetoresistive sensors.

The observed magnetoresistance is due to anisotropic effect in ferromagnetic LSMO films on STO (001) film showing uniaxial anisotropy. The Anisotropic MagnetoResistive effect (AMR) led to a measurement of sensitivity of about $400\% \cdot T^{-1}$ and the magnetic noise was estimated to be in the order of $200pT \cdot Hz^{-1/2}$ at 310 K.

In the sense of $La_{0.7}Sr_{0.3}MnO_3$ (LSMO) thin film based bolometers, (Nascimento et al., 2021) have shown the electro-thermal and optical properties of such devices with a detection area of $100 \times 100\ \mu m^2$. The thermal conductance was evaluated through the voltage-current (V-I) characteristics measured in vacuum from 240 to 415 K and the electrical responsivity was determined and compared to the optical responsivity measured with a laser diode at 635 nm. A NEP value, obtained without any absorbing layer or antenna, as low as $2.3\times10^{-11}\ W \cdot Hz^{-1/2}$ was obtained at 300 K and a bias current of 80 μA, in the 20-200 Hz modulation frequency range and the response time was 1.3 ms. This have shown a promising path into fabricating LSMO-based bolometers for IR or THz detection.

(Bourdais et al., 2015) have proved the interest of using epitaxial LSMO films in sensors field, more specifically, integrated in a Pirani gauge configuration, as a low-power oxide-based pressure sensor, due to their high stability under extreme conditions (temperature and oxidation), an advantage over p-doped silicon, despite having the same order of magnitude of Temperature Coefficient of Resistance (TCR) in the linear approximation (an important parameter directly correlated to the pressure sensitivity) in room temperature. LSMO provides to the device endurance under high temperature or oxidizing conditions and very low electrical noise level, making them suitable for high sensitivity sensors. The chemical stability of this material as hot filament allows its operability in various environments, increasing the possible applications in comparison to traditional materials.

The structures were patterned with two different clamping configurations: circular and at 90° to prove that the strain is more spatially distributed in the case of circular clamping configuration leading to a reduced value of the maximum strain level and a higher yield of fabrication (95% vs 35%).

Characterization of LSMO-based Pirani pressure sensors has shown the typical Pirani S-shaped curve (while sweeping the pressure, resistance remains constant at low pressure, then drops due to the modification of wire temperature to become constant again at high pressure), however, exhibiting a more-than-twice higher sensitivity with respect to a standard metal-based one with the same geometry with a power consumption reduced by a factor of 10000 (Bourdais et al., 2015).

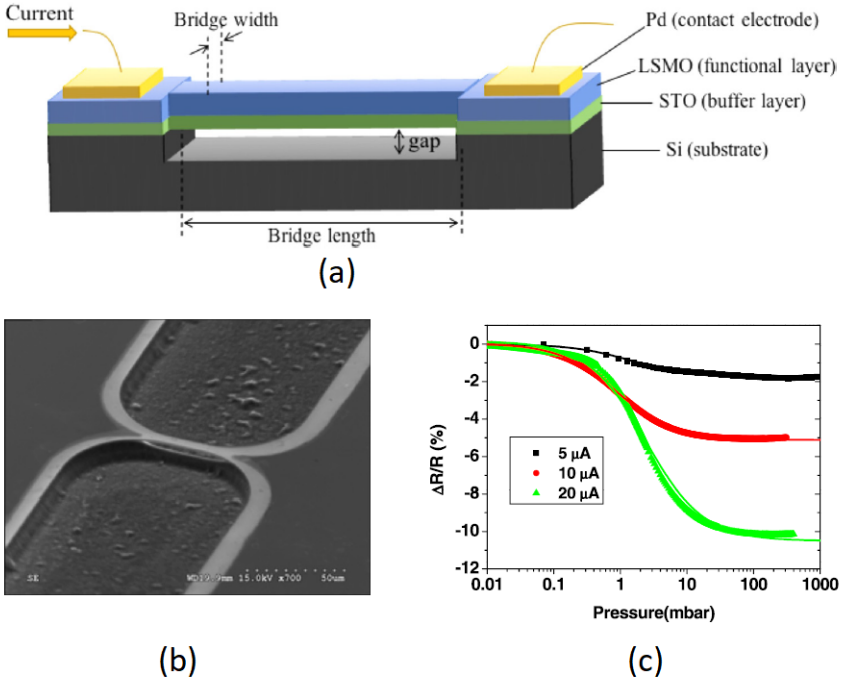

FIGURE 2.17: (a) Schematic view of the LSMO/STO bilayer bridge where the LSMO is the active conductive film and Pd pads are used to minimize its contact resistance, (b) secondary electron microscopy image of the free standing bridges with optimized circular geometry and (c) resistivity variation versus pressure of a LSMO (50 $\times$ 20) μm^2 freestanding bridge for several heating currents normalized to the resistivity at low pressure. Extracted from (Bourdais et al., 2015)

2.4 My thesis objectives: resonant LSMO MEMS clamped-clamped beams

My thesis project consisted in developing the fabrication process of piezoelectrically actuated LSMO doubly clamped bridges. This was done by incorporating active piezoelectric layers to offer actuation and sensing capabilities to the LSMO suspended bridge structures that were object of study of a previous PhD student, Vanuza Nascimento, to achieve a fully integrated resonant device based on LSMO clamped-clamped beams. The implementation of such integrated MEMS requires the ability to integrate thin-films of high-quality materials with good electromechanical coupling while guaranteeing the maintenance of the LSMO's electrical characteristics' quality during all fabrication steps.

The growth of epitaxial LSMO in Si-based substrates is possible when a perovskite such as $SrTiO_3$ (STO) with compatible crystal structures is primarily epitaxially grown on the substrate. The use of such epitaxial heterostructures composed of a Au/(PZT or AlN)/LSMO/STO/Si-based substrates in the fabrication of Micro-Electro-Mechanical Systems (MEMS) impose some technological difficulties linked to finding the ideal etching processes for each layer without damaging or inadvertently etching the others and also concerning the release of such layers subjected to epitaxial strain.

LSMO's rich phase diagram, as will be shown in chapter 3 is determined by coupling of spin, charge, and lattice degrees of freedom, whose interplay can be modified by doping, external fields and lattice strain. The latter consists of one of the most powerful parameters to achieve control of Transition-Metal Oxides (TMO) functionalities (Pellegrino et al., 2009).

Resonant MEMS bolometers are thermal radiation detectors, disposing an active area sensible to electromagnetic radiation, capable of displaying a measurable temperature rise when absorbing such radiation. Such innovative devices have been proposed by few groups, but not with oxides (Laurent et al., 2018) (Piller et al., 2021) (Zhang et al., 2019) (Zhang et al., 2016) .

Since LSMO is an absorbent material (up to 80%) in the infrared radiation range and qualifies as a promising material to be used as a light sensitive material, its usage for resonant MEMS is envisaged since it also exhibits excellent sensitivity to strain, hence, to mechanical effects and under optimized current conditions it can reach the phonon noise limit. It presents a ferromagnetic-to-paramagnetic at 360 K accompanied by a metal-to-insulator transition above room temperature, being ideal for uncooled sensors such as anisotropic magnetoresistances and infrared bolometers. Therefore, its use has been shown and well established as resistive bolometers, where the temperature rise in the thermally insulated material ($G \approx 10^{-7} W.K^{-1/2}$)

is measured as an increment in its electrical resistance.

Its use on vibrating structures proposes to measure a variation on the resonant frequency via a change in voltage on the detector side as a result of the increased temperature, as displayed in Figure 2.18 through the active modulation by epitaxial locking with piezoelectric thin films in the resonant beam structure, allowing such strain manipulation of oxides as well as the mechanical coupling between them and the piezoelectric material by the bending of the suspended bridges. The surface strain caused by the application of voltage in the the piezoelectric layer is mechanically transferred through epitaxial lock to the LSMO thin film. The mechanical clamping induced by the non-piezoelectric layer (LSMO/STO) creates a strain gradient across the structure, converting the piezoelectric strain into a flexural motion that is to be sensed in the other extremity of the beam by a change of voltage measured in the same type of piezoelectric material. A modulation of its electrical conductivity should also be verified. Such devices can find applications in resonant MEMS bolometers as terahertz imaging devices for military or health sensors, in spectroscopy sensing but also in magnetoelectric magnetic sensors.

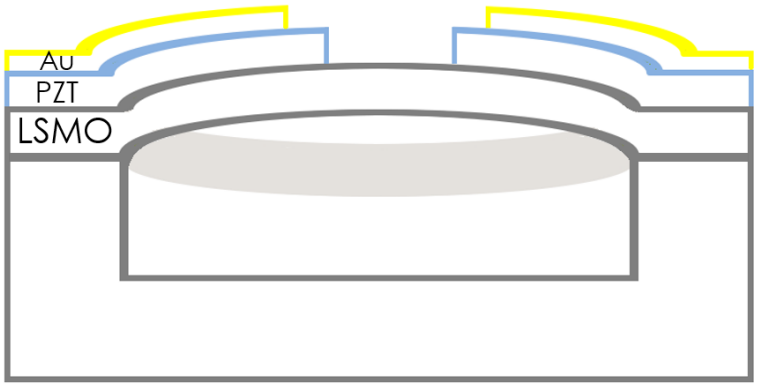

FIGURE 2.18: Integrated resonant clamped-clamped LSMO suspended bridge

The process was optimized for three different types of substrates, namely silicon (Si), silicon-on-insulator (SOI) and silicon-on-sapphire (SOS). The choice of SOI substrates were motivated by the possibility of keeping the topmost silicon of the wafer as a part of the vibrating micro-bridge, in order to retain the epitaxial strain between LSMO/STO films and Si. This is important to keep the structures as flat as possible once released and allow a lower resonant frequency, within the range of measurement of typical equipments. The choice of the SOS ones was mainly induced by the possibility of achieving deposited LSMO/STO thin films with smaller residual strain onto these substrates. Significant mosaic broadening of the top Si peak on such substrates, attributed to a higher density of defects, is replicated in the epitaxial layers grown onto SOS, resulting in a slightly smaller epitaxial strain.

Therefore this thesis is focused on the development of the complete process fabrication of the aforementioned devices by using AlN/LSMO/STO/SOI and PZT/LSMO/STO/Si heterostructures aiming a trade-off between the material's quality and optimal yield. The choice of materials and their deposition methods and characterization techniques are detailed in 3. The complete fabrication process steps, lithography mask designs, UV lithography dose tests and etching procedures are discussed in chapter 4, as well as the dynamic measurements for the fabricated suspended structures. Finally, chapter 5 discusses the obtained results and proposes a path for continuation of this work.

Chapter 3

Materials

High performance microelectromechanical systems brought the interest in the conception of devices employing new and multifunctional materials.

This chapter presents the fundamental properties and applicabilities on the main materials used in the final device, i.e. LSMO, PZT and AlN, necessary for the understanding of its general functioning. It also includes the fabrication technologies involved such as the deposition techniques used for each thin film as well as the respective characterization techniques and our results achieved in this sense for the choice of materials.

3.1 $La_{0.7}Sr_{0.3}MnO_3$

Oxides are very interesting materials because they provide the possibility of playing with their structural richness since they can arrange in many structures in the crystallographic sense because of the oxygen atom. We work with perovskites because not only they are very good for epitaxy but they also show a wide range of functional properties. Such properties originate from metal-oxygen bonds and very strong electronic correlations (colossal magnetoresistance, superconductivity, magnetism, piezoelectric and ferroelectricity, multiferroics) leading to interactions like Coulomb repulsion, constraint, orbital bandwidth, structural change and Hund exchange coupling which appear in a sense of competing energies leading, therefore, to the ordering of spins, charge and degrees of orbital freedom. Perovskite-type magnetic oxides are also known for their sensitivity to many external parameters, including distortions of the mesh structure.

The doped lanthanum manganites, exhibiting a general formula expressed by $R_{1-x}A_xMnO_3$ (R = La, Pr... A = Sr, Ca...), present a rare-earth ion substituted by an alkaline earth one creating a mixed valence Mn^{3+}/Mn^{4+} that is responsible for structural, magnetic and electric properties finely linked. As the substitution rate x of the alkaline earth ions leads to great change in the the physicochemical properties of such materials, they present a large variety of phase diagrams.

The doping x in $La_{1-x}Sr_xMnO_3$ (LSMO) manganite controls the nature and numbers of carriers at its Fermi level: the charge carriers are holes when x < 0.5 and the conduction band is filled beyond half and electrons when x > 0.5, in the opposite case; at the optimal substitution rate, i. e., x = 1/3, LSMO is a ferromagnet and present an electric transition at T_P (insulating/metal) combined with a magnetic transition at Curie temperature, T_C (paramagnetic/ferromagnetic) at its highest value. The maximum Curie temperature in accordance with this model can be confirmed by the LSMO phase diagram to be well above room temperature, enabling its use for uncooled sensors.

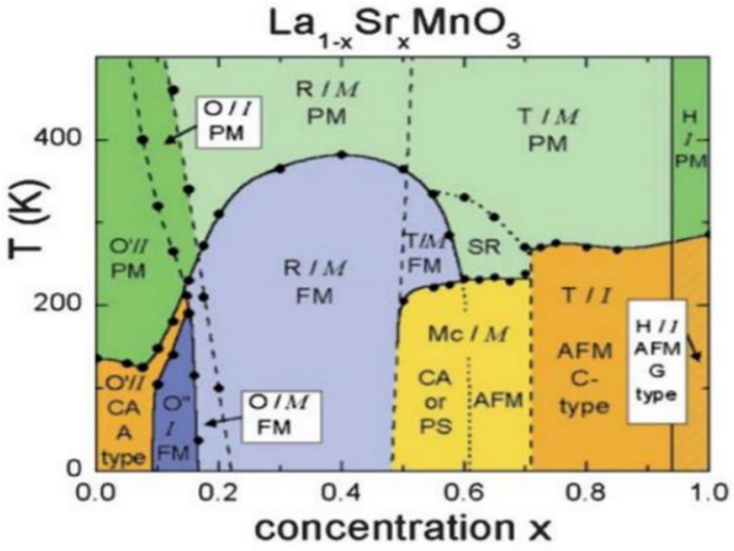

FIGURE 3.1: LSMO phase diagram with Sr doping concentration x. Extracted from (Hemberger et al., 2002)

The changeable x influences directly in the electric transitions that are visible in temperature:

1. for $x = 0$ the compound $LaMnO_3$ is insulating and anti-ferromagnetic;

2. for $x \geqslant 0.17$ a transition metal-insulator is observed around the temperature of magnetic order, T_c, at which a pic of resistivity is verified.

At the Fermi level, mostly all charge carriers in the conduction band for these materials have the same spin, which makes LSMO an almost perfect half metal: an approximately 100% polarization neighbour spin that makes these oxides interesting also for spin electronics applications.

3.1.1 LSMO properties

Electronic structure

An isolated 3d manganese ion possesses five degenerated orbital states splitted by the cubic crystal field into three t_{2g} orbitals and two e_g orbitals. The MnO_6 octahedrons exhibit a 1.5 eV separation between the lowest t_{2g} level and the highest e_g one,a crystal field splitting smaller than the exchange energy of about 2.5 eV ensuring the parallel alignment of the electron spins of the Mn^{3+} and Mn^{4+} ions, i. e., the first Hund's rule.

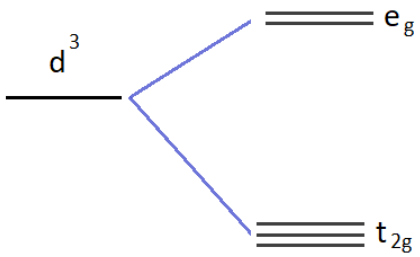

FIGURE 3.2: Electronic structure of an isolated 3d Mg ion degenerance

The $La_{1-x}Sr_xMnO_3$ manganites have a mixed valence state with both Mn^{3+} and Mn^{4+}. The latter, with three electrons d occupying the levels t_{2g} (that do not participate in the transport process because the level is strongly localized) and the e_g orbitals left empty; whereas the former, corresponding to the configuration $3d^4$, have the t_{2g} occupied by the three electrons with parallel spins and the e_g orbital, doubly degenerated, with a single electron.

Deformations of the MnO_6 octahedron can be verified by the Jahn-Teller effect for the Mn^{3+} ions, as a result of either orbitals occupation: z^2 or $x^2 - y^2$. In the case of the configuration $d^1_{z^2}d^0_{x^2-y^2}$, the occupation of the z^2 orbital leads to the greater separation of the anions on the z-axis while the ones in the x-y plane are pulled closer: a quadratic distortion. When the configuration is the inverse, $d^0_{z^2}d^1_{x^2-y^2}$, the anions in the plane x-y are the ones pushed away whereas the ones in the z-axes reproach the center of the structure. Since the Mn^{4+} ions do not have electrons in the e_g orbitals, they're not submitted to the Jahn-Teller effect (Coey, Viret, and Molnár, 1999).

Transport properties

The perovskite structure manifests its manganese ions quite far from each other such that the interactions are almost devoid of direct exchanges. In this sense, the magnetic coupling among the aforementioned ions is intermediated by oxygen nonmagnetic ones, that lay in between the manganese ions.

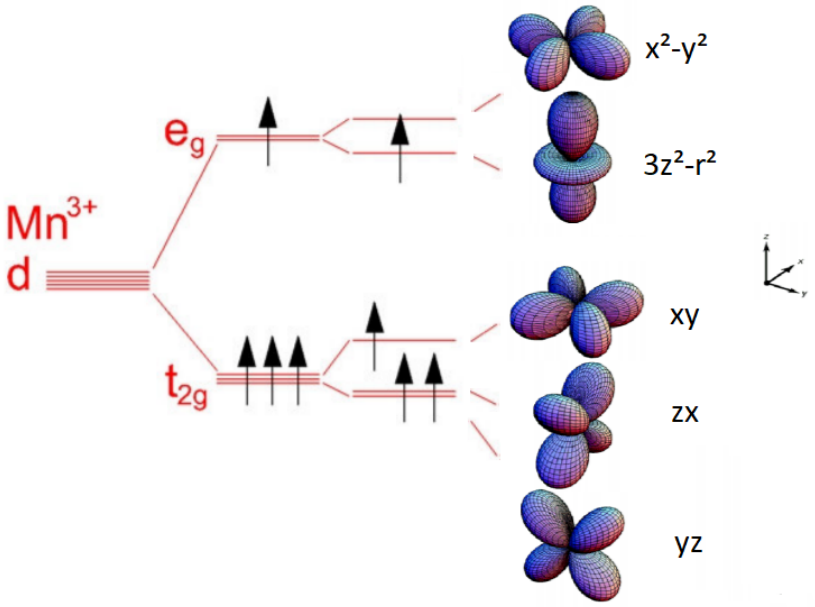

FIGURE 3.3: Field splitting of the atomic 3d levels of a Mn^{3+} ion and its five types of d orbitals degeneracy (Shirato, 2010)

The mixed valence composites with x=1/3 display negligible $Mn^{3+} - Mn^{3+}$ interactions compared to the $Mn^{4+} - Mn^{4+}$ (super-exchange of the antiferromagnetic type) and $Mn^{3+} - O - Mn^{4+}$ ones (double-exchange ferromagnetic).

The double-exchange (DE) mechanism produces a strong ferromagnetic interation through the simultaneous hopping of an electron e_g of the Mn^{3+} into the orbital O2p and from the orbital O2p into the empty level e_g of the Mn^{4+} ion. The hopping integral between two sites i and j of an electron is $t_{ij}cos\left(\frac{\theta_{ij}}{2}\right)$, where θ_{ij} is the angle between the spins S_i and S_j, in such a way that the itinerant electron spin must always be parallel to the local spin on each site, thus a conduction electron can only hop onto a site with its spin parallel to the local moment at that site.

We chose the doping of the LSMO equal to x = 1/3 in order to obtain the highest *double exchange* for this material, which allows the electrons to jump between the orbitals leading it in a ferromagnetic state. $La_{0.67}Sr_{0.33}MnO_3$ is, then, FM with the highest Curie temperature around 350 K and semi-metallic so that it can be used for room temperature applications.

Crystal structure

$La_{0.67}Sr_{0.33}MnO_3$ has a rhombohedral crystallographic structure with lattice constants equal to $a_r = b_r = c_r = 0.5471nm$ and angles $\alpha_r = \beta_r = \gamma_r = 60.43^o$, its space group is $R\bar{3}c$ Chaluvadi, 2017b. The crystal structure of LSMO can be seen in the Fig. 3.4. The rhombohedral unit cell (denoted by solid lines) can be seen as *pseudocubic* (dotted lines).

The pseudocubic (pc) lattice parameters are calculated by the following equation

$$a_{pc} = \frac{\sqrt{2}a_r}{1 + cos\alpha_{pc}}, \qquad \alpha_{pc} = acos(\frac{1 - 2cos\alpha_r}{2cos\alpha_r - 3}) \tag{3.1}$$

Where a_{pc}, a_r, α_{pc} and α_r are lattice constants and angles of pseudocubic and rhombohedral structures, respectively. This leads to a value of $a_{pc} = 0.3876$ nm for LSMO (Chaluvadi, 2017a).

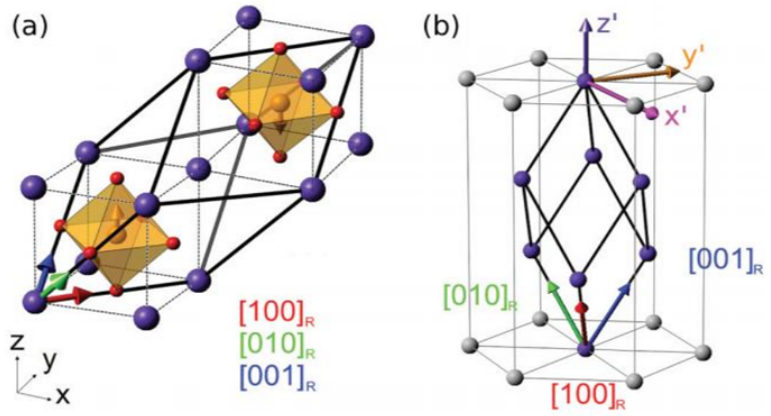

FIGURE 3.4: Crystal structure of LSMO. Extracted from Chaluvadi, 2017b

LSMO resistivity × temperature

The substitution rate x in manganites such as $La_{1-x}Sr_xMnO_3$ determines the nature of charge carriers that can be either holes if $x < 0.5$ or electrons if $x > 0.5$. The variation in x leads to many electrical transitions with temperature dependence as seen in figure 3.5. It shows the evolution of the resistivity and magnetic moment as a function of temperature for the material $La_{0.7}Sr_{0.3}MnO_3$. The reduction in temperature at $T < T_P$ coincides, at $T_C = T_P$ with the increase in magnetic moment of the ferromagnetic phase (Urushibara et al., 1995).

Mechanical Characteristics

Young's modulus represents the stiffness of the material that correlates with its atomic structure. The microstructure of thin films can deviate from the bulk materials and depend on deposition conditions such as ion energy, angle of incidence of plasma plume, substrate temperature, and atom:ion ratio (Schneider and Schultrich, 1998).

The effects of epitaxial strain to the elastic parameters of $La_{0.67}Ca_{0.33}MnO_3$ thin films were studied by (So et al., 2003) using resonant ultrasound spectroscopy where two characteristics of the elastic behaviour common to the strained films were observed near the resistance peak temperatures: a number of features in the elastic properties is observed as the temperature is swept monotonically which do

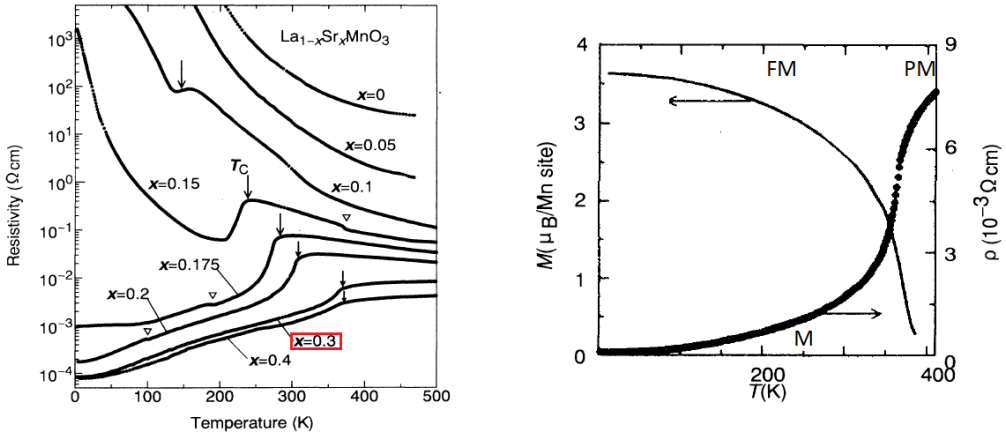

FIGURE 3.5: Temperature dependence of $La_{1-x}Sr_xMnO_3$ resistivity and the resistivity and magnetic moment for $La_{0.7}Sr_{0.3}MnO_3$ versus temperature. Extracted from Urushibara et al., 1995

not repeat if the sample is thermally cycled (due to thermal-stress induced, irreversible changes in the fine-scale structure of the as deposited films) and some features which do occur reproducibly at two temperatures, and these are indicated by jumps and/or, in nearly all cases, by changes in slope.

The elastic (longitudinal, L, shear, G, bulk, K, and Young's, Y) moduli of a bulk $La_{0.67}Sr_{0.33}MnO_3$ perovskite sample has been analysed by (Rajendran et al., 2003), where anomalies were observed both in all the moduli L, G, K and Y at the Curie temperature, T_C, and attributed to the transition from the PM to FMM state. The four moduli have been computed over wide range of temperatures from 298 to 460 K. A minimum in longitudinal and shear velocities at T_C was noticed and peaks in G and Y were larger in magnitude than the anomaly observed in L and K.

LSMO at room temperature has a Young modulus that can vary from 130 GPa from polycrystal ceramics to 562 GPa for epitaxial thin films (Huang et al., 2006). The usual Poisson ratio considered for the material is generally taken as 0.43 and the mass density 6.28 g/cm^3. From (Yang, Kim, and Takamura, 2011) the thermal dilatation coefficient was extracted as $13.4 \cdot 10^{-6} C^{-1}$.

Epitaxial LSMO

Epitaxial LSMO presents a ferromagnetic-to-paramagnetic transition at about 360 K that is accompanied by a metal-to-insulator transition above room temperature, which is very promising for uncooled sensors, such as anisotropic magnetoresistances or infrared bolometers (Nascimento et al., 2020). In addition, its high sensitivity of epitaxial oxides to strain, hence to mechanical effects, can be exploited for MEMS resonators (Giang et al., 2016) in addition to the lower voltage actuation and higher sensitivity detection, through inverse and direct piezoelectric effects,

expected from epitaxial growth due to the larger electro-mechanical coupling than with polycrystalline films (Yin et al., 2012a).

3.1.2 Oxides integration on Si-based substrates

Silicon substrates are not well adapted to the epitaxial growth of oxides due to a major roadblock to achievement of a sharp and chemically stable Si/oxide interface which is the formation of an amorphous silica layer as a result of surface reactivity of silicon. In addition, the interdiffusion of oxide with Si at the high temperature needed for growing epitaxial oxide films, and finally the large difference in the thermal expansion coefficients between oxides and Si are other problems found. These problems can be overcome by introducing single or multiple buffer layers.

3.1.3 Choice of substrate

SOI substrates, as seen in figure 3.6 are fabricated as shown in appendix E and for the achievement of our suspended beams, three different silicon-based substrates were used, accordingly to their advantages:

- **Silicon (Si)**, which allows the use of Si micromachining in a simpler and more direct way with reduction in number of steps to be followed, however, less robust to cope with the residual strain during the release of the suspended structures. To bypass this issue, other silicon-based substrates were used, still allowing the use of Si micromachining techniques but with a lower quality top Si that enables final suspended structures to be subjected to less residual stresses.

- **Silicon-on-Insulator (SOI)**, composed of an approximately $2\mu m$ large silicon dioxide, SiO_2, buried layer onto silicon, such that the topmost silicon layer can vary in thickness and in our cases were chosen as either 200 nm or 400 nm as it will be a part of the suspended bridge stack in order to retain the residual epitaxial strain with STO/LSMO and reduce the non-planarity of the beam while improving the mechanical properties of the suspended structure that becomes less prone to breakage.

- **Silicon-on-Sapphire (SOS)**, which is a part of the SOI class of CMOS technology and composed of a thin layer of silicon (typically up to 0.6 μm) grown on sapphire, Al_2O_3, and ideal substrate for our application, as sapphire presents itself as an excellent electrical insulator that prevents the incident radiation to lead to stray currents that spread to adjacent circuits. Its transmission window from 200 nm (ultraviolet) - 5000 nm (infrared) also allows backligthing of the beams while the actuation/detection and electrical measurements can all be made from the top. The SOS substrates show significant mosaic broadening of the top Si peak attributed to a higher density of defects that are replicated in the

following epitaxial layers because of the large lattice mismatch and differences in coefficient of thermal expansion (CTE) between Si and Sapphire.

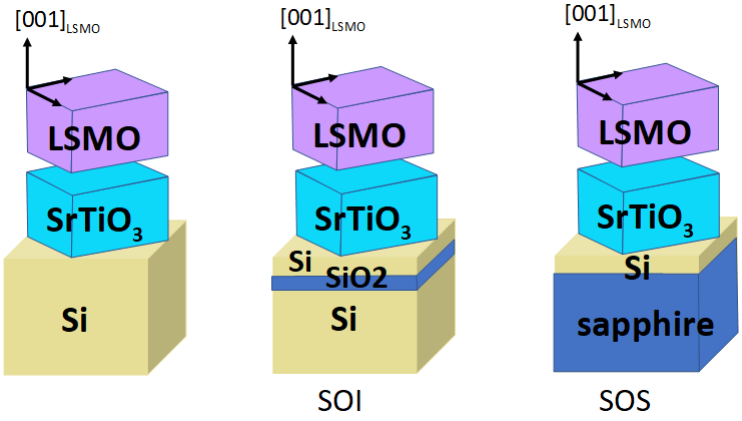

FIGURE 3.6: LSMO/STO thin films grown onto Si, SOI or SOS substrates. Extracted from (L. Méchin, Seminar)

Growth of STO buffer layer

STO is one of the most widely used monocrystalline oxide substrates with a cubic perovskite-like crystal structure at room temperature, with a mesh parameter equal to 3.905 Å, on which most transition metal oxides can be deposited epitaxially, including our LSMO. STO is a high bandgap (3.25 eV) dielectric material and its dielectric properties are affected by strong electric fields and largely determined by defects such as oxygen vacancies, structural defects or chemical doping. As thin film, it can also exhibit ferroelectric behaviour at low temperatures if the oxygen atoms O16 are changed to O18 (heavier) allowing the freezing of phonons at temperatures higher than zero Kelvin - otherwise it is *quantum paraelectric* (Nova et al., 2019) - and it can even be triggered ferroelectric at room temperature by a coherent stress (Biasotti et al., 2013). Regarding the mechanical properties of STO, its Young's modulus is $225GPa$, while the Poisson ratio is of 0.232. Below 105 K, its Young's modulus decreases and at 20 K it remains constant at less than 40% of the value measured at room temperature, which can also be further reduced by the application of an applied electric field Biasotti et al., 2013.

Therefore, the mechanical, dielectric and electronic properties of STO are correlated and influenced by crystal defects creating the need to obtain a good control of the crystalline quality of the layers and a general knowledge of the mechanical properties of the suspended structures. In addition, in the case of electrostatically actuated beams, the efficiency of the electromechanical coupling of the moving parts is crucial. STO films are very sensitive to biaxial stress and therefore ferroelectric under a tensile stress of the order of 1%, a reason which led (Bilani-Zeneli et al., 2008) to assess and qualitatively confirm the capability of using STO as buffer layer to transfer the stress of a piezoelectric substrate into a functional film deposited above.

During my PhD thesis I could use LSMO films deposited on 3 types of STO buffered Si-based wafers: (001) Si, SOS (Silicon on Sapphire) and SOI (Silicon on Insulator). Thanks to a long lasting collaboration with Prof. Darrell Schlom at Cornell University in the USA, all our 20 nm-thick STO grown on Si-based substrates were prepared by MBE by D. G. Schlom's group *Department of Materials Science and Engineering of Cornell's University, USA*. This way, I had the chance to work with either fully MBE grown LSMO/STO/Si stacks, which came from previous thesis on LSMO bolometers (Liu, 2013b) or PLD deposited LSMO on MBE grown STO on Si, SOS or SOI.

The details of the fully MBE grown LSMO/STO/Si can be found in (Méchin et al., 2012). LSMO films of thicknesses ranging from 10 to 100 nm were epitaxially grown and showed magnetic and electrical properties close to those deposited on STO substrates as shown in figure 3.7. The details on the PLD deposited LSMO can be seen in section 3.3.2 in this thesis.

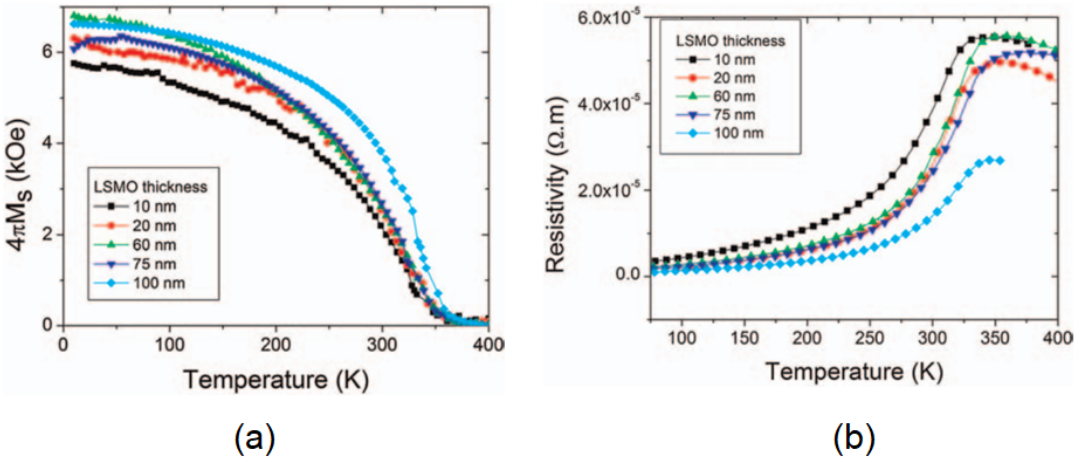

FIGURE 3.7: (a) Saturated magnetization as a function of temperature and LSMO thickness measured in LSMO/STO/Si heterostructures at an in-plane applied magnetic field of 5 kOe and (b) the electrical resistivity versus temperature characteristics for the same films. Extracted from (Méchin et al., 2012)

Unfortunately I could only use 2 pieces of 100 nm thick LSMO/STO/Si of this series. The Darrell Schlom's group did not grow anymore manganite materials these last years and could provide us only with STO/Si – based wafers. We received the following wafers deposited by Zhe Wang:

- ZW890: 20 nm thick STO/Si (001) - 3 inch wafer
- ZW602: 20 nm thick STO/SOS – 3 inch wafer
- ZW601: 20 nm thick STO/SOI1 – 2 inch wafer
- ZW600: 20 nm thick STO/SOI2 – 2 inch wafer

We asked the Murata company in Caen to cut the wafers into 10 mm $\times$10 mm or 5 mm $\times$10 mm pieces. V. Pierron, engineer at GREYC could grow 2 nm thick STO followed by 45 nm thick LSMO films at 750°C in 0.2 mbar of O_2. Properties will be described in 3.5.1.

3.2 Piezoelectric materials for MEMS actuation

The piezoelectric properties of a material can be predicted by its crystalline structure: opposite electric charges in centrosymmetric structures cannot be separated upon uniaxial deformation of the lattice, although a similar, but much weaker, effect may be verified, the electrostriction; it occurs in all dielectrics and produces a reduction in the dimension along the direction of applied electric field, due to electrostatic attraction between electric-field-induced dipoles but differs from piezoelectricity both in intensity and in lack of a reversal effect: the elastic stress is unable to induce polarization, hence, it presents always a compressive strain. Piezoelectricity is verified in non-centrosymmetric crystalline structures in which elastic stress can shift positive and negative charges along the opposite directions, leading to electric dipole formation in a linear way in both senses, i. e., inverting the direction of applied electric field also switches the sign of induced strain.

In MEMS application, the intrinsic electromechanical coupling effect of these materials, a physical quantity related to the materials' ability to convert electrical energy into the mechanical form or vice-versa, must be optimal for efficient device functioning. A direct effect is visualized when electric charges accumulate on the surfaces of a piezoelectric material that undergoes an elastic stress and it configures the base for piezoelectric sensors, i. e. direct mechanical transducers, whereas an inverse effect takes place upon application of an electric field inducing elastic strain which is the case for actuators such as resonators for which the resonance parameters, frequency and amplitude, are influenced by the input physical quantities.

Common piezoelectric actuators are either based on bimorph or expansion structure to obtain the elastic displacement; while the former is based in the in-plain piezoelectric strain which is to be measured as beam deflection, the later has as responsible for mechanical displacement the longitudinal electric-field-induced strain, d_{33}. We aim in the use of d_{31}, a simpler design and measurement at the cost of a less important variation (one third of d_{33} value) (Yin, 2013a). Evaluation of such piezoelectric coefficients is intrinsically complicated due to the lack of of standard methods, and commonly this is done by observing the response of voltage-deflection of a micro-cantilever made of PZT films (Wong et al., 2004) (Guirardel et al., 2004) (Park

et al., 2002). In addition, the transverse piezoelectric coefficient d_{31} leads to an important deformation along the perpendicular direction to the electric field if a longer lateral dimension in comparison with the piezoelectric thin film is verified. Our interest lies in the application of strain through the use of the piezoelectic material mainly in one of the clamped edges of the beam, as demonstrated in figure 3.8, taking advantage in the regions of the suspended beam that are subjected to the greater amounts of strain.

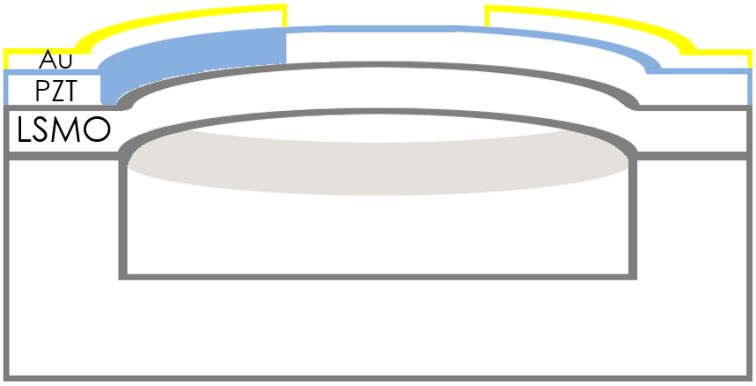

FIGURE 3.8: Piezoelectric actuation on one side of the clamped beam by use of transversal piezoelectric coefficient deformation through drive voltage application between top gold electrode and bottom LSMO thin film.

The use of piezoelectric materials in MEMS scale allows the exchange of minimal amount of energy to achieve improved performances in terms of resonance frequency reach as well as sensitivities, hence high efficiency and quality factor, Q.

It is therefore highly desired the use of a piezoelectric material with electromechanical properties stable through a wide range of temperature. Unlike Barium titanate, $BaTiO_3$, which becomes depolarized when heated to approximately 120^oC, its Curie temperature, both PZT and AlN exhibit good piezoelectric response with large piezoelectric coefficients - effective values respectively of 60-130 and 3.9 pm/V (largest among nitrides) (Yin, 2013a) - such that large actuation force and displacements can be generated and also thin films actuators can be driven by high-frequency signals with high contact and restoring forces at low voltages while meeting our envisaged fabrication processes requirements. The highest-performing piezoelectric MEMS heterostructures have been fabricated with PZT piezoelectric layers (Baek et al., 2011).

3.2.1 Lead Zirconium Titanate ($Pb(Zr,Ti)O_3$)

Lead Zirconium Titanate, $PbZr_xTi_{1-x}O_3$ (PZT), is a piezoelectic material with high electromechanical coupling, large piezoelectric coefficients (d_{33} and d_{31}) with more

than one order of magnitude larger than those of commonly used piezoelectric materials such as ZnO and quartz (Funakubo et al., 2012), reversible remanent polarization, reliable performances and ferroelectric properties. Such optimal piezoelectric response allows its use to achieve large-displacement actuators and high sensitivity sensors.

It is a ferroelectric material, i. e., it maintains a permanent electric dipole in crystalline lattice even in absence of external electrical field. Its properties can be, then, tuned by changes and switch of the applied electric field. Figure 3.9 shows a typical polarization versus electric field curve (P-E), for 500 nm PZT deposited by sputtering at high temperature. It demonstrates that polarization isn't exclusively determined by the electric field applied to the material but also by its own historical state which is why, before a P-E measurement, sometimes it may be needed to carry out a poling process, that may be thermal or electric in order to align the ferroelectric domains in a preferred direction. We performed our polings electrically before such measurements in order not to submit the metallic contacts to high temperatures.

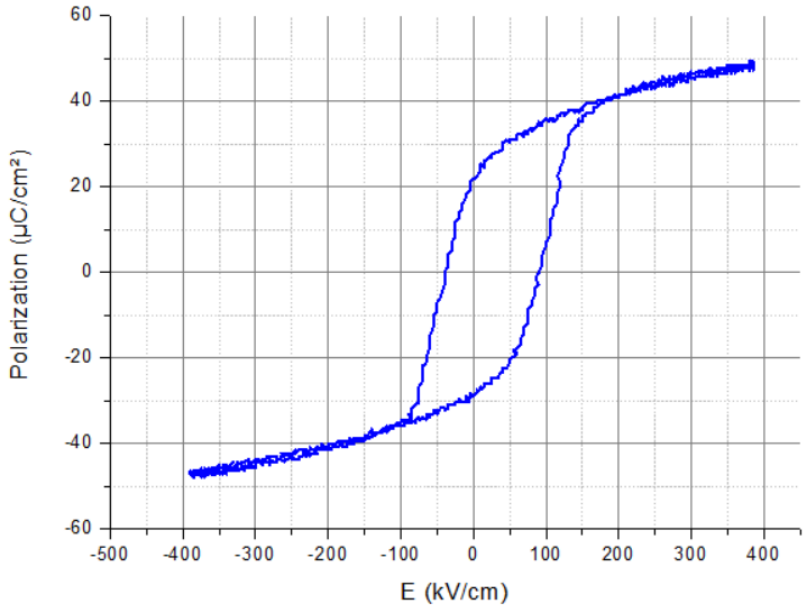

FIGURE 3.9: Typical hysteresis loop for ferroelectric material from our measurements of PZT thin films

The unit cell of PZT material is composed of eight Pb atoms forming a tetragonal structure, with Zr or Ti atom in its center surrounded by an octahedron of eight oxygen anions, as illustrated in figure 3.10. The size of Pb atoms radius (175 pm) being larger than that of Zr (160 pm) and Ti (147 pm) leads to a Goldschmidt tolerance factor greater than one. The large free space in oxygen octahedron enables the generation of permanent dipole by shifting the B cation away from the center of the lattice (Yin, 2013a).

(Jaffe, Roth, and Marzullo, 1954) have demonstrated, as illustrated in Fig.

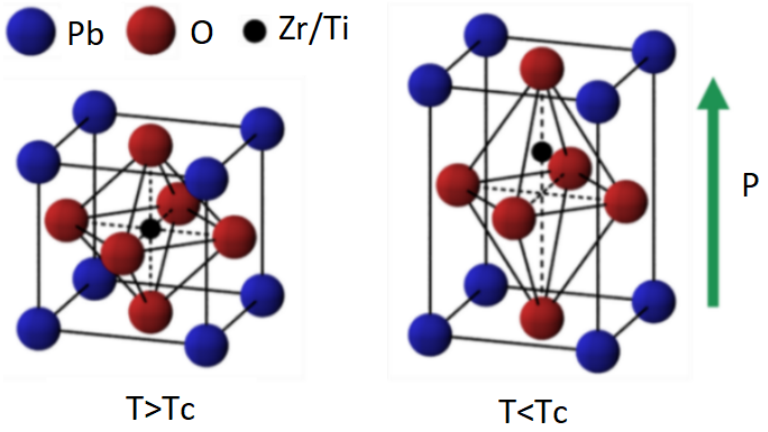

FIGURE 3.10: Schematic of perovskite structure of PZT and the origin of permanent dipole in tetragonal lattice. Extracted from (Yin, 2013a)

3.11, that for solid solution ceramics of $PbZrO_3$-$PbTiO_3$ combination, the electromechanical response of the rhombohedral specimens (Zr-rich) increases sharply as the transition composition at 45 mole percent $PbTiO_3$ is approached leading to tetragonal compositions near the boundary exhibiting strong piezoelectric response. Further substitution of more $PbTiO_3$, however, is accompanied by a noticeable decrease.

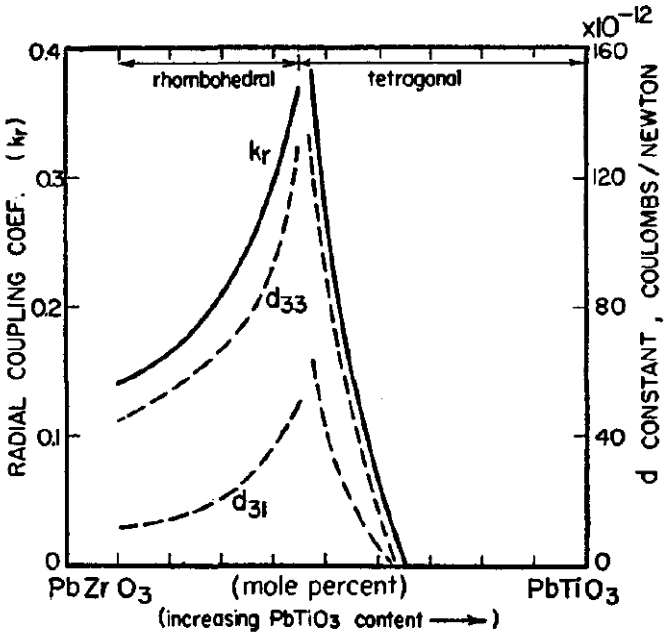

FIGURE 3.11: Dependence of the radial coupling coefficient as well as the d_{31} and d_{33} constants at room temperature on composition of PZT Jaffe, Roth, and Marzullo, 1954

Such abrupt change in crystalline structure in PZT's composition phase diagram is called the morphotropic phase boundary (MPB) and results in large piezoelectric response for compositions nearby (Funakubo et al., 2012). The MPB separates rhombohedral (pseudocubic with slight elongation along a cube diagonal)

Zr-rich with $0.1 < x < 0.5$ from tetragonal Ti-rich perovskite with the ferroelectric dipole oriented along c-axis with $x > 0.5$ and it's nearly vertical along the temperature scale as displayed in Fig. 3.12. The boundary is associate with a phase coexistence region whose width depends on the compositional homogeneity and on the sample processing conditions and for polycrystalline samples this width has been modelled based on free energy differences between tetragonal and rhombohedral phases by (Cao and Cross, 1993).

(Noheda et al., 1999) have identified tetragonal symmetry with space group P4mm and polar axis along [001] in room temperature and at low temperature a monoclinic phase with space group Cm in the PZT system at the composition with $x = 0.52$ presenting polar axis between [001] and [111], since it is a lower symmetry one that acts as a structural bridge between tetragonal and rhombohedral phases. Compared to single-phase tetragonal or rhombohedral films, the mixed phase films show larger orientation dependence of the various properties such as polarization, dielectric constant and piezoelectric coefficient (Funakubo et al., 2012). It is extensively used not only due to very large electro-mechanical coupling but also to its stable polarization response on external perturbations (Cross, 2004).

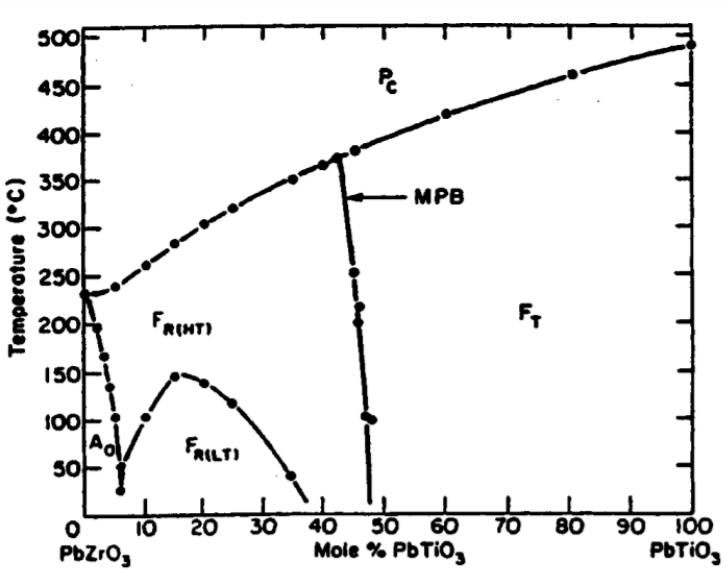

FIGURE 3.12: PZT phase diagram (Noheda et al., 1999)

Due to such enhanced piezoelectric response result of intrinsic PZT's characteristics, we have chosen, in this work, to employ $PbZr_{0.52}Ti_{0.48}O3$ in our structures.

The growth of single crystalline PZT films on silicon, displaying excellent electrical properties(large d_{33}, low leakage current and large coercive electrical field), requires a buffer layer such as strontium titanate ($SrTiO_3$) to reduce the lattice mismatch and avoid Pb and Si interdiffusion (Yin et al., 2012b).

Epitaxial PZT

The growth of high quality PZT films to enhance its performance faces several problems when realised on polycrystalline metallic electrodes due to possible generation of high-density defects which prevent ferroelectric domain walls motion effectively suppressing the electrically switchable nature of polarization resulting in a dead-layer; In addition, oxygen vacancies trapped near the metal/oxide interface lead to fatigue of the PZT film as well as an increase of leakage current. Such problems may be reduced through the use of a conductive oxide electrode which acts as an *oxygen sink* filling the oxygen vacancies during switching cycles dramatically decreasing the fatigue problem (Ramesh et al., 1992) (Eom et al., 1993) (Sama et al., 2008), that can still be improved by the use of symmetrical oxide/ferroelectric/oxide electrodes compared to a single one (Lee et al., 1993) (Chen, Wu, and Wu, 1996).

In addition to conductive and superconductive oxides such as IrO_2, ZnO and $YBa_2Cu_3O_{7-x}$ as electrode materials, conductive perovskites have gained importance as they enable heteroepitaxial growth with PZT, like $LaNiO_3$, $SrRuO_3$, $(La, Sr)CoO_3$, $Sr(Ti, Sb)O_3$ (SSTO), $(La, Sr)SnO_3$ (LSSO) and finally $(La, Sr)MnO_3$ (LSMO) (Eom et al., 1993) (Chen, Wu, and Wu, 1996) (Ramesh et al., 1993) (Chen et al., 2007) (Wu et al., 2000).

The integration of these various perovskite-structure functional oxides and lead-based ferroelectric on silicon is only possible, however, due to the possibility to epitaxially grow high-quality single-crystalline STO onto Si(001) that acts as structural template (with matching lattice parameters when rotated by 45 degrees and close thermal expansion coefficients) as well as a barrier for cation migration to avoid Pb cation interdiffusion into the Si substrate during growth stage at high temperatures that could lead to the formation of pyrochlore/fluorite phases which are not ferroelectric (Funakubo et al., 2012). As demonstrated by (Wang et al., 2002b) through a successful integration of epitaxial PZT films deposited by sol-gel technique onto $(La_{0,5}Sr_{0,5})CoO_3$ (LSCO)/ STO/ Si exhibiting clean and flat interfaces with minimum inter-diffusion. The aforementioned structure was compared with two other substrates, i. e., $Pt/TiO_2/SiO_2/Si$ and LSCO-buffered Pt-Si, revealing a dramatic influence on the bottom electrode on the orientation of the PZT film: polycrystalline PZT thin-films were verified in all but the LSCO/ STO/ Si structure, which displayed (00l)-peaks with much greater intensity due to the highly oriented nature. Epitaxial PZT also showed larger polarization and better fatigue properties. The small in-plane mismatch between PZT, electrode and template materials enables the epitaxial growth of PZT leading also to higher piezoelectric coefficients and smaller dielectric constants. In this sense, (Du et al., 1998) have evaluated the role of the same substrates, namely Pt/Si, LSCO/Pt/Si and LSCO/STO/Si, in the piezoelectric coefficient, d_{33}, verifying the improvement of its value as the crystalline quality of PZT films is increased: epitaxial PZT grown on LSCO/STO/Si exhibited

the highest d_{33}, namely 200pm/V for PZT (52:48).

Among the large choices for perovskites bottom electrode, $La_{2/3}Sr_{1/3}MnO_3$ (LSMO) – a ferromagnetic oxide with strong magnetoelastic coupling thus potentially allowing for high magnetoelectric effects via a piezoelectric- magnetoelastic coupling (Vrejoiu et al., 2008) – is presented as a promising choice not only because of its good lattice parameters matching with PZT (lattice mismatch of -6.8% given $a_{LSMO(pc)} = 0.3876$ nm and $a_{PZT(52/48)} = 0.405$ nm) but also for its majority of charge carriers, since a p-type conducting oxide steer clear of surface charge accumulation at the interface PZT/oxide during the polarization cycle (Leufke et al., 2012), effect that would be observed if a n-type electrode were employed due to PZT's characteristic of a wide bandgap p-type semiconductor (Auciello and Waser, 1995). With no formation of a forward biased p-n junction, thus no carrier injection leading to accumulation of oxygen vacancies at the interface, the fatigue problems are again minimized and the poling process gains effectiveness without being overshadowed by time dependent dielectric breakdown (TDDB) and subsequent failure of devices to field-driven redistribution of thermally activated oxygen vacancies in the PZT film as verified by several groups (Desu and Yoo, 1993) (Wouters et al., 1995). Therefore, the use of LSMO electrodes reduces some pressure on the poling procedure that can be made unnecessary if epitaxial PZT films are employed since it has been shown that epitaxial PZT films can be intrinsically stable without the need for the poling process (Funakubo et al., 2012). This can also lead to enhanced performances of the final devices as epitaxial piezoelectric films growth results in greater piezoelectric coefficients, polarization and dielectric constants, compared to polycrystalline films due to a well-defined polar axis orientation as well as high density and compositional uniformity (Akai et al., 2005) and lower leakage currents (Kondo, Maruyama, and Kurihara, 2002), (Kim et al., 1994).

PZT on LSMO thin films

Despite the great characteristics provided by PZT for microfabrication, the integration of epitaxial PZT on $La_xSr_{1-x}MnO_3$ have been demonstrated, however, by very few groups:

- (Wu et al., 2000) have grown 500nm-thick $Pb(Zr_{0.52}Ti_{0.48})O_3$ on 100 nm LSMO ($La_{0.7}Sr_{0.3}MnO_3$) on $LaAlO_3$ (001) substrates by pulsed laser deposition at 620^oC for demonstration of fatigue performance dependence with interface property at top electrode upon comparison of Pt deposited either on as-grown or in-situ annealed PZT, where the latter have exhibited rapid fatigue at about 10^6 cycles and high coercive electric field, E_c. This is a result of the lead loss at the surface layer of the PZT film, since local compositional variations induce point defects or space-charge layers at the top Pt/PZT interface leading to high E_c and rapid fatigue of the capacitor.

- (Chen et al., 2007) have deposited LSMO/PZT/LSMO capacitors epitaxially on (001) STO substrates to study the effects of highly-conductive p-type LSMO ($La_{0.7}Sr_{0.3}MnO_3$) electrodes in comparison with n-type perovskites, namely $La_{0.7}Sr_{0.93}MnO_3$, showing that the latter causes the ferroelectric hysteresis to broaden and the fatigue endurance to be dramatically reduced.

- (Tsuchiya et al., 2007) have grown epitaxial PZT onto 40 nm-thick $La_{0.7}Sr_{0.3}MnO_3$ on LAO substrate by excimer laser-assisted metal organic deposition (ELAMOD) in a low-temperature process, whose crystallinity and consequently lack of pyrochlore phases was found to be dependent on the combination of laser fluency and shot number; LSMO thickness also presented an influence in the intensity of the (002) PZT peaks in XRD analysis;

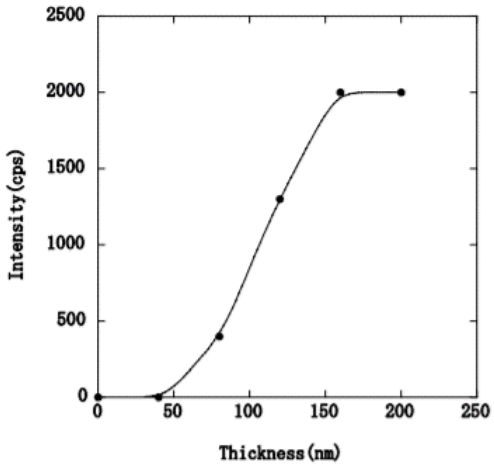

FIGURE 3.13: Relationship between LSMO film thickness and XRD intensity of PZT(002) peak. Extracted from Tsuchiya *et. al*, 2007 (Tsuchiya et al., 2007).

- 200 nm PZT was grown by Pulsed Laser Deposition on top of 40 nm LSMO ($La_{0.67}Sr_{0.33}MnO_3$) films on STO-buffered Si (001) by (Borowiak et al., 2012) with evidences of good ferroelectric properties.

- (Vrejoiu et al., 2008) have grown multiferroic epitaxial heterostructures based on 10 nm thick LSMO layers sandwiched by 30 nm PZT ones with Zr content in PZT increased over the epitaxial heterostructure as $Pb(Zr_{0.1}Ti_{0.9})O_3$/ $La_{0.7}Sr_{0.3}MnO_3$/$Pb(Zr_{0.2}Ti_{0.8})O_3$/$La_{0.7}Sr_{0.3}MnO_3$/$Pb(Zr_{0.3}Ti_{0.7})O_3$/$La_{0.7}Sr_{0.3}MnO_3$, and a second hybrid structure (HS) with 20 nm LSMO layers and 100 nm PZT of $Pb(Zr_{0.1}Ti_{0.9})O_3$ / $La_{0.7}Sr_{0.3}MnO_3$ / $Pb(Zr_{0.3}Ti_{0.7})O_3$ / $La_{0.7}Sr_{0.3}MnO_3$ / $Pb(Zr_{0.52}Ti_{0.48})O_3$ / $La_{0.7}Sr_{0.3}MnO_3$ to demonstrate the influence of interfacial biaxial strain exerted by thin PZT layers on the adjacent LSMO thin films locked by epitaxy. The HSs were deposited by PLD at a temperature of 600°C in 0.3 mbar oxygen and cooled down in 1 bar O_2. PZT was verified to be c-axis oriented and tetragonal, with its lattice parameters growing with the increase of Zr/Ti ratio ($a_{PZT(10/90)} = 3.93$Å, $a_{PZT(20/80)} = 3.954$Å, $a_{PZT(30/70)} = 3.98$Å,

$a_{PZT(52/48)} = 4.05$Å), leading to a gradually higher in-plane stress on the adjacent LSMO layers.

As a result of such strain, magnetization hysteresis in LSMO has shown steps indicating the values of the magnetic field at which independent magnetization switching occurs. This is due to the LSMO undergoes different in-plane stress values, affecting their structure and leading to slight differences in coercive field. For the HSs with thicker layers, H_c values are larger and better separated with a remnant and saturation magnetization values subtly smaller. This is a result of the LSMO layers in such HSs being subjected to larger tensile interfacial strain than the ones in the first HSs, leading to a higher magnetic disorder at the interfaces.

3.2.2 Aluminium Nitride (AlN)

Aluminium Nitride (AlN) is a III-V semiconductor, wide band gap (about 6.2 eV), with an hexagonal close packed non-centrosymmetric wurtzite structure possessing high piezoelectric coefficient that leads to the polarization of ions in a crystal. Its crystal structure space group is P63mc with polar in nature and it shows spontaneous polarization (Sivadasan et al., 2016) as high as 130 μCcm^{-2} that cannot be switched reversibly by the electric field once its coercive field is higher than the typical breakdown field (Ye et al., 2021). Moreover, it is a lead-free piezoelectric material, and since lead toxicity poses serious problems for the integration of devices in biomedical applications, AlN is highly promising for integration in such applications.

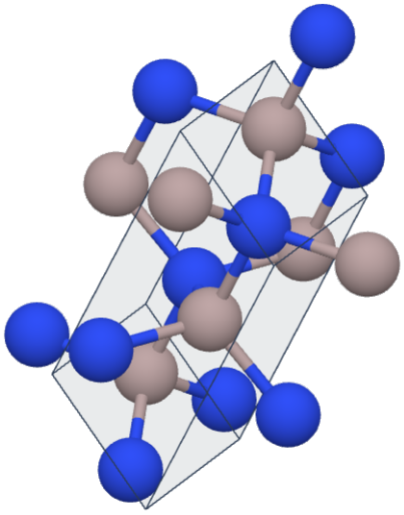

FIGURE 3.14: AlN wurtzite structure. Extracted from (*AlN mp-661* n.d.)

For any wurtzite structured material and its alloys the induced piezoelectric polarization field can be written as

$$P^{PE} = (d_{15}\epsilon_{31})\mathbf{x} + (d_{15}\epsilon_{23})\mathbf{y} + (d_{31}\epsilon_{11} + d_{31}\epsilon_{22} + d_{33}\epsilon_{33})\mathbf{z} \tag{3.2}$$

where z is taken along the c-axis and ϵ_{11}, ϵ_{22} and ϵ_{33} are the strain along the x, y and z axis, respectively, and ϵ_{23} and ϵ_{31} are shear strains. d_{31}, d_{33} and d_{15}, illustrated in Fig. 3.15, are the piezoelectric coefficients for the wurtzite crystal structure.

The relation between strain-electric field for this kind of piezoelectric material with 6mm point group symmetry ($\epsilon_{ij} = d_{ijk}E_k$) is expressed as $\epsilon_{11} = \epsilon_{22} = d_{31} \cdot E_3$, $\epsilon_{33} = d_{33} \cdot E_3$, $2\epsilon_{23} = d_{15} \cdot E_2$, $2\epsilon_{13} = d_{15} \cdot E_1$ and $\epsilon_{12} = 0$.

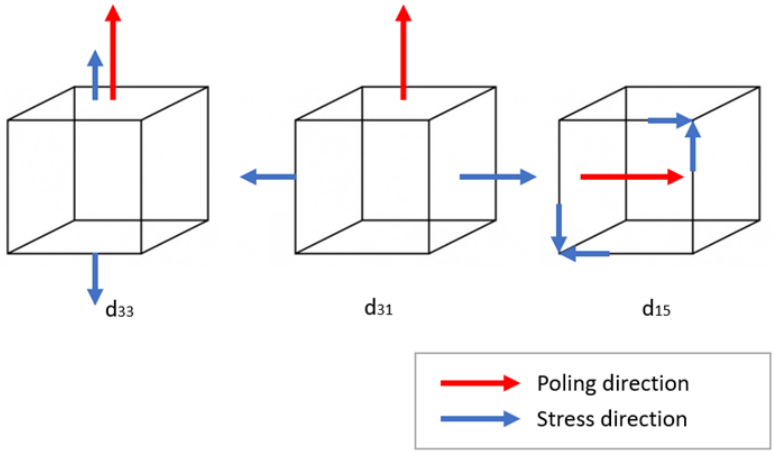

FIGURE 3.15: Three independent piezoelectric coefficients $d_{31}(= d_{32})$, $d_{15}(= d_{24})$, $_{d33}$ for AlN

The coefficient d_{33} is commonly used to characterize the piezoelectric property based on its feasibility and simplicity. It can be evaluated by Piezoresponse Force Microscopy (PFM) measurements which are based on the converse piezoelectric effect as a direct and effective measurement method, i. e., an excitation voltage is applied onto the surface of the film by the conducting probe of the PFM; the deformation of the film induced by the electric field when an AC modulation signal is applied can be detected by the a photodetector and the lock-in amplifier. Then, the piezoelectric coefficient can be obtained.

The intrinsic value d_{33} is, nevertheless, larger than the effective measurement once the clamping effect of the substrate is present as well as a non-ideal electric field distribution applied by PFM cantilever during characterization of the piezoelectric properties (Zhang et al., 2015). Although, the inhomogeneity of the applied electric field by the PFM probe doesn't affect greatly measurements for the range of thickness we aim on using, 60nm - 240nm, as the electric field in AlN film increases very slowly with $z < 1\mu m$ allowing electrostriction to be neglected for such weak

electric fields according to (Bi et al., 2014a). Additionally, for structures with top electrode larger deformation is verified in the electric region under the same excitation voltage, i. e., the deformation of the top surface increases as the size of the top electrode is increased because the increase in size of top electrode leads to contribution of more dipoles involved to the deformation of the top surface in the piezoelectric films.

The displacements also increase with the increase in thickness under the same external voltage due to the increasing self-heating effect which caused lower defects in films (Hernando et al., 2008), (Dubois and Muralt, 2001), (Martin et al., 2004), (Ababneh et al., 2010). (Zhang et al., 2015) showed that the impacts of substrate constraints to the displacements become smaller as the thickness increases, achieving piezoelectric coefficient d_{33} close to the value for the bulk material when the AlN was deposited as thick as 2.4 μm.

All parameters such as electric field, thickness and substrate constraints influence the final displacements and piezoelectric coefficient estimation since the substrate confines the motion of AlN thin films whereas the electric field distribution may confine its deformation range.

In comparison with PZT, the lower piezoelectric coefficient verified in AlN films can be mitigated by a significantly reduced dielectric constant that leads to lower parallel plate capacitance of AlN and an improvement in the signal-to-noise ratio (Reza Ali and Prasad, 2019). However, the interest in using AlN lies not only on the high piezoelectric coefficients achieved, the largest among the nitrides (Ambacher, 1998) in the range 3.4-6.4 pC/N (Reza Ali and Prasad, 2019), but also due to its full compatibility with the complementary metal oxide semiconductor (CMOS) processing due to characteristics such as high melting point (3273K), high Curie Temperature of over 2000°C and the maintainance of its piezoelectric properties up to 1150°C in Ar, in addition to an excellent physical and chemical stability in atmosphere at temperatures exceeding 700°C with anti-corrosive properties, which makes it a suitable candidate for MEMS technology.

AlN exhibits several other useful properties such as high electrical resistivity (in the order of $10^4 \Omega \cdot m$), low leakage current hence low dielectric loss, high acoustic velocity ($\approx 5500 m/s$ for transversal bulk waves, $\approx 11354 m/s$ for longitudinal ones and $\approx 5607 m/s$ for surface waves, high thermal conductivity ($2.85 W \cdot cm^{-1} K^{-1}$ at room temperature), high knoop hardness ($1300 kg/mm^2$), transparency and high degree of clarity in the visual (transmission is about 80% between 300-550nm Jacquot et al., 2002) and infrared regions and low thermal expansion coefficient ($5.3 \times 10^{-6} K^{-1}$ perpendicular to c-axis), some of utmost importance for reducing signal degradation and cross talk effects in high frequency integrated circuits (Pawar et al., 2018).

Such excellent properties present potential applications in active and passive device fields, thermal management, high-speed circuitry and protective wear resistant hard coatings. As thin film, AlN can be used in metal-insulator-semiconductor (MIS) devices, heat sink in electronic packaging, component for high frequency electro-acoustic devices on Si (surface acoustic wave, SAW, devices) (Lin et al., 2013), (Benetti et al., 2006), (Bénédic et al., 2004), thin film bulk acoustic resonators (FBAR) (Weber et al., 2006), Lamb wave devices (Yantchev and Katardjiev, 2013), optical coatings for spacecraft components due to transparency in visible spectrum and electroluminescence device in the range of 215-490 nm (Jacquot et al., 2002). Also, the engineering of AlN band gap allows for applications in the semiconducting industry for various optoelectronic properties such as photovoltaic, hydrogen storage, light and field emission (Sivadasan et al., 2016) as for ultraviolet light-emitting diodes and photo detectors (Chen et al., 2009).

AlN growth has been shown by metal-organic chemical vapour deposition (MOCVD) (Tsubouchi and Mikoshiba, 1985), (Chubachi, Sato, and Kojima, 1984), (Shuskus, Reeder, and Paradis, 1974), laser chemical vapour deposition (LCVD) (Radhakrishnan, 1995), electron cyclotron resonance plasma assisted chemical vapour deposition (ECR-PACVD) (Zhang et al., 1993) an molecular beam epitaxy (Karmann et al., 1997), Auner and Jin, 1999, (Wu, Jia, and Zhang, 2012). However disadvantages of some of these techniques are the high substrate temperature in the range 600-1200°C, and the use of expensive and corrosive gas mixtures. (Song, Fu, and He, 2009) have shown improved dielectric properties for AlN thin films deposited by sputtering technique in comparison with Metal-Organic Chemical Vapour Deposition and Plasma-Enhanced Chemical Vapour Deposition. In addition, reactive sputter deposition (Okano et al., 1994), (Wang and Lakin, 1982), (Benetti et al., 2006), (Xu et al., 2001), and PLD (Wang et al., 2011), (He et al., 2013), (Jacquot et al., 2002) though, can produce highly textured c-axis-oriented AlN thin films achievable at a relatively low temperature compatible with the integration in CMOS or other technologies sensitive to heat for the micro-electromechanical systems technology (Tonisch et al., 2006b) even if epitaxial growth of AlN only occurs at high temperatures.

The lower degree of texture, however, does not impact the inverse piezoelectric effect since it is mainly affected by the dipole orientation but hardly by grain boundaries. This is verified by the piezoelectric coefficient d_{33}, in comparison with high temperature deposition processes, as shown by (Tonisch et al., 2006a) to slightly reduce from 5.5 pm/V down to 5.1 pm/V if the FWHM of the rocking curve – a parameter that quantifies the degree of film texture and for a (002)-oriented AlN film is generally taken as less than 4° as precondition of good piezoelectric property (Zhang et al., 2015) – reached 10° or higher. This evaluated highly textured polycrystalline AlN thin films with a (002) preferential orientation deposited at low temperature by reactive sputtering (350 - 500°C), exhibiting grain size of 20 - 30 nm, RMS roughness

of 2 - 5 nm and FWHM ranging from 0.3 - 10.7°. The crystal quality may, nevertheless, affect with higher intensity the coupling factor k^2 because structural defects which may cause scattering in case of surface or bulk acoustic devices, for example.

Both piezoelectric coefficient and dielectric constant in AlN films are reported to be strongly dependant on its crystal structure, preferential orientation of c-axis, defects and polar distributions of the grains (Kamohara et al., 2007) and, consequently, on the texture and smoothness of the substrate material as reported by (Pawar et al., 2018), who have also remarked that the roughness of the bottom electrode is directly proportional to the leakage current in the AlN thin film, since its spike-like surface would act injecting charge carries more efficiently.

Hence, to improve the performance of the AlN in final devices as both actuator and detector, high quality (002) oriented AlN thin films are required for their strong piezoelectricity in the (002) orientation, along the c-axis direction (Bi et al., 2014b).

Such crystal quality is also envisaged for optimization of a room-temperature fabrication process since AlN provides excellent chemical stability, which, actuate as a protection layer for the bottom layers during SiO_2 etching by HF acid. Only KOH or NaOH containing solutions or $Ar/Cl_2/BCl_3$ plasmas (where the addition of F to the discharges considerably reduces the rate of discharge etching) (Pearton et al., 1993) can etch epitaxial and single crystal AlN at the temperature below 80°C (Chen et al., 2009), and allow lift-off process even if AZ400K photoresist developer must be used (Mileham et al., 1995) as it was reported to etch polycrystalline AlN with contrasting etch rates for different planes, due to strong anisotropy of the AlN wurtzite structure, in such a way that (100) planes are etched preferentially compared to the (002) plane, reducing the etch rate significantly for wet processes. (Saravanan et al., 2004) evidenced AlN etch by HF solution with a very low etching rate of the order of $< 0.3nm/min$ allowing the possibility of successfully release of AlN structures on sacrificial layers of SiO_2, by BHF / HF solutions.

Its electrochemical properties are also influenced by the stoichiometry of deposited AlN as tested by (Vacandio et al., 1997): they showed that for tests performed with H_2SO_4 and HCl the AlN stoichiometric presented the lowest anodic corrosion currents, whereas the films with mixed phases were subjected to localized attacks and then dissolved. However, if AlN is lightly under stoichiometry it is already considered good enough for the aimed chemical stability, since not only this coating do not dissolve completely, but the corrosion current is 1000 times lower than before. For the stoichiometric sample the currents were so low that they reached the detection limit of the apparatus showing that stoichiometry is an important parameter to improve corrosion resistance.

The aforementioned decrease of substrate temperature during deposition

is a desirable requirement for applications compatible with silicon technology and, in our case, to allow the full room temperature process proposed in chapter 2 on the LSMO / STO / Si-based substrates.

The integration of semiconductor with perovskite oxides opens the possibility for development of new types of devices combining the properties of dielectrics, ferroelectrics, superconductors and semiconductors, justifying the interest in analysing AlN films on such materials, as it shows promising science and technology significances (Zhu et al., 2008). Nevertheless, deposition of AlN onto oxides was performed by very few groups so far, where epitaxial AlN films were evidenced when deposited onto $SrTiO_3$ substrates without the existence of an oxide phase in AlN films (Fujioka et al., 2001) (Wang et al., 2002a) (Zhu et al., 2008).

3.3 Methods

The growth of different layers in our samples has led to the need of several deposition techniques: Molecular Beam Epitaxy (MBE) for the oxide buffer on Si, Pulsed Laser Deposition (PLD) for the conductive oxide layer, namely, LSMO, and piezoelectric film when AlN was used, and finally either sol-gel or sputtering for PZT integration, as described in Table 3.1. Each of these growth techniques are briefly discussed below.

Material	**Deposition Technique**	**Where**	**By whom**
LSMO/STO /Si STO /Si STO /SOS STO /SOI	MBE	Cornell University DG Schlom group	C. A. Adamo Z. Wang
STO	PLD (770°C)	GREYC	V. Pierron
LSMO	PLD (750°C)	GREYC	V. Pierron
AlN	PLD (RT)	GREYC	V. Pierron
Au	PLD (RT)	GREYC	V. Pierron
Au	GATAN PECS (RT)	GREYC	V. Pierron / L. Araújo
PZT	Sputtering (600°C)	CRISMAT Caen 600°C	G. Poullain C. Cibert J. Manguele
PZT	Sputtering RT + RTA (650°C)	INL Lyon	B. Vilquin
PZT	Sol-gel RT + RTA (650°C)	INL Lyon	B. Vilquin

TABLE 3.1: Deposition techniques for the used materials

3.3.1 Molecular Beam Epitaxy (MBE)

Molecular Beam Epitaxy is a precisely controlled deposition process at monolayer scale, ensured by a very low deposition rate of typically a few angstrons per seconds that induces a layer-by-layer growth, carried on a Ultra-High Vacuum (UHV) environment widely used for high-quality epitaxial film growth of several materials, amongst which, functional oxides and III-V semiconductors. It uses the sublimation of extremely pure solid elements heated in separate effusion cells so the source material is transformed in its gaseous state. These particles then expand and condensate onto the substrate, reacting with it until the epitaxial arrangement occurs.

The vacuum in the range of $10^{-10} - 10^{-9}$ Torr delivers an environment free of contamination in such a way that the atoms and/or elements sublimated from target materials may impinge the sample surface without colliding with residual atoms in the deposition chamber, generating the so-called *molecular beam* between the cell aperture and the substrate, resulting in a high-quality epitaxial growth.

The switch of mechanical shutters placed in front of evaporators sources on the molecular beams path allows for simple controlling of the process allowing development of structures with abrupt and sharp interfaces. Furthermore, the chemical composition of the film can be cautiously controlled and tuned by changing the temperature of each effusion cell and impurities can be evaporated onto the growing film through separated sources resulting in a doping profile with a spacial resolution not easily achieved by more conventional methods, all this enabling provision of a precise reproducibility of all parameters involved in the deposition (Morresi, 2013) (Yin, 2013b).

A molecular beam epitaxy system consists of a stainless-steel growth chamber, as shown in figure 3.16, connected to other chambers by gate valves that avoid contamination when transferring the sample and maintain pressure inside the growth chamber as low as possible. Besides the main ion pump, the pumping system includes a combination of a titanium sublimation pump that can reduce the residual gas pressure down to minimum values and liquid nitrogen cryopanels, since cryogenic temperatures act as an entangled for impurities.

Three effusion cells are displayed in figure 3.16 where the crucible is easily identified as the container for the final compounds to be deposited, their components or yet different elements to serve as doping impurities. During deposition, there is a direct exposition of the atomic beams to the sample surface, and both temperatures (of substrate and effusion cell) are stabilized by a Proportional-Integral-Derivative (PID) controller. Moreover, for the deposition of oxide or nitrite films, the desired atmosphere can be introduced using an external gas source.

Thanks to the UHV environment the in-situ growth can be monitored through

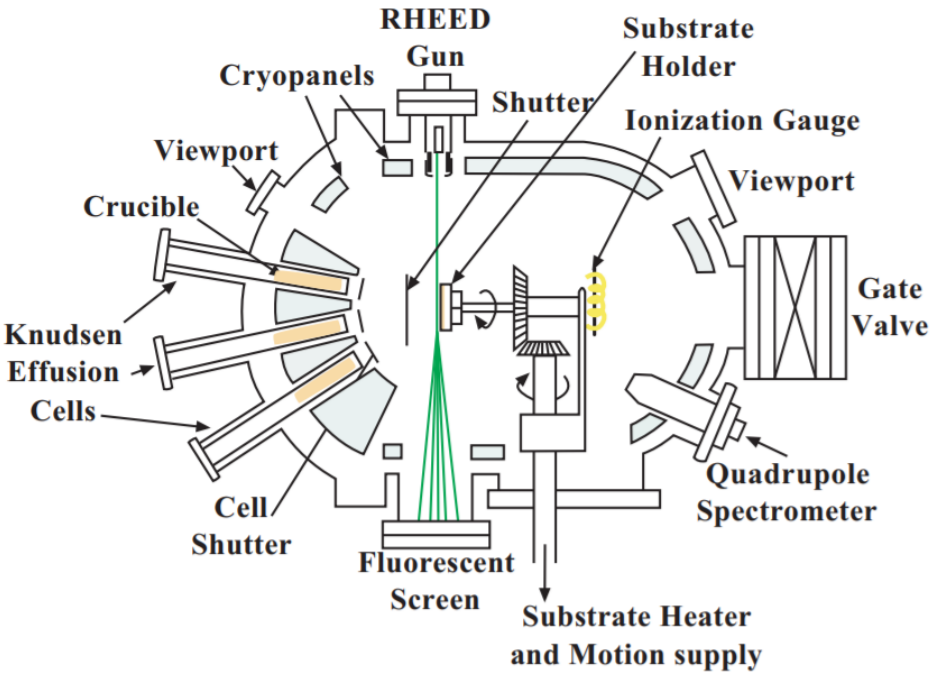

FIGURE 3.16: Schematic of a typical MBE system Morresi, 2013

a scanning high-energy electron diffraction apparatus, namely the Reflective High-Energy Electron Diffraction (RHEED) that employs a small glancing angle reflection mode of operation enabling sensitivity to the uppermost layers, as indicated in figure A.1. This feature reveals without interference the real time changes in the growing surface as is better explained in Appendix A.

3.3.2 Pulsed Laser Deposition (PLD)

Pulsed Laser Deposition (PLD) is a versatile deposition technology with relatively simple configuration as shown in figure 3.17 used for a variety of materials such as functional oxides, nitrides, carbides, metals, high-temperature superconductors and even polymers (Yin, 2013b). Its ability to stoichiometrically transfer material from a multicomponent target to a growing film is based on evaporation of the target material through ionization by means of heating due to a succession of laser pulses forming a transient plasma plume that expands reaching the substrate surface, within the duration of a a laser pulse, where the atomic species ablated from the target material finally nucleate with a very high density to form the thin film.

The stoichiometry of the film deposited by PLD, favored by the high-power laser pulses, is very close to the target material's one and the deposition is performed in UHV in the order of 10^{-9} mbar. A KrF excimer laser with wavelength of 248 nm and pulse duration of 30 seconds is generated by an external laser system and focused onto the target material's surface through a series of optical lens. The optical index of the target material is the mainly determinant of the ablation depth of the

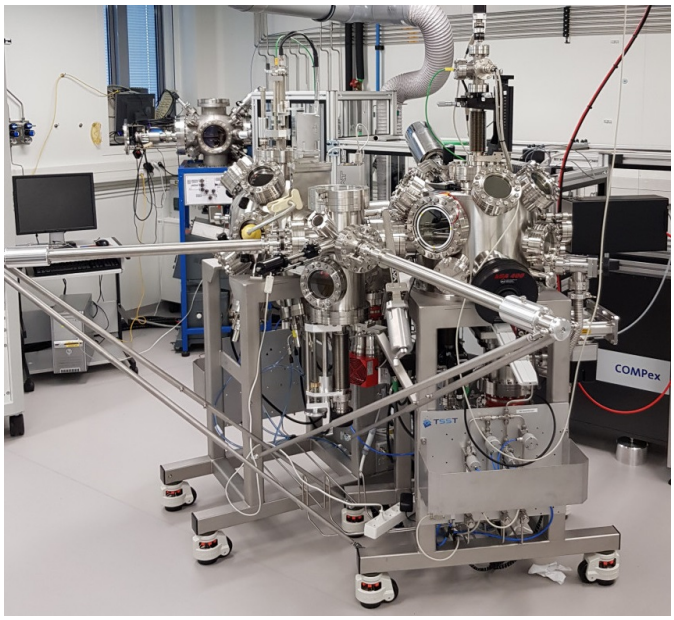

FIGURE 3.17: PLD system at GREYC laboratory

laser beam.

The generated plasma plume is influenced by a variety of user-controlled parameters such as laser energy, pulse duration, background pressure and target-substrate distance. The substrate temperature must be cautiously increased in order to ensure thermal diffusion of the ablated species decreasing nucleation density for more homogeneous thin films and enhancing the crystallization process (Ferguson et al., 2009) but without menacing an overheat that would lead to a deviation in stoichiometry from the target material's one and hence undesired phases in the deposited layers (Yin, 2013b). The target-substrate distance also plays an essential role as it determines the activation energy and flux of deposited atoms arriving at substrate surface, it typically varies from 2 to 10 cm (Yin, 2013b) since a smaller distance could cause a re-sputtering process and a bigger one would lack kinetic energy of the deposited atoms.

During deposition of certain materials, such as oxides and nitrites, a reactive gas in the growth chamber may be necessary to compensate for losses during ablation process, avoiding, for example, oxygen vacancies that would result in degradation of electrical properties.

The configuration of the used PLD system from TSST company used in this thesis for the deposition of STO, LSMO, AlN and Au is represented in Figure 3.18.

The samples of $10 \times 5mm^2$ are cleaned and inserted in PLD chamber equipped with in-situ reflection high-energy electron diffraction (RHEED) at the GREYC laboratory located in Caen, France. A KrF excimer laser of $\lambda = 248$ nm and laser repetition rate of 1 Hz - 5 Hz is used.

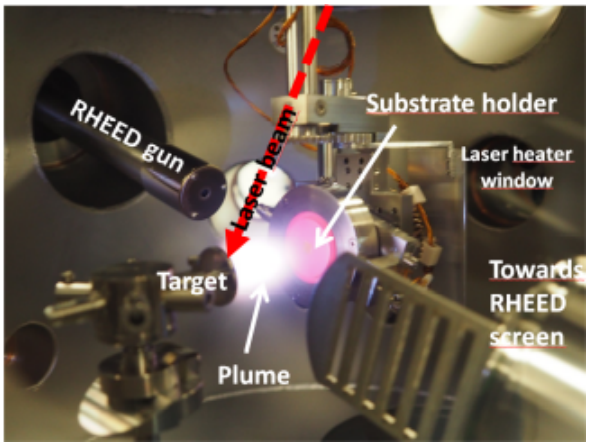

FIGURE 3.18: Configuration of our PLD system at GREYC

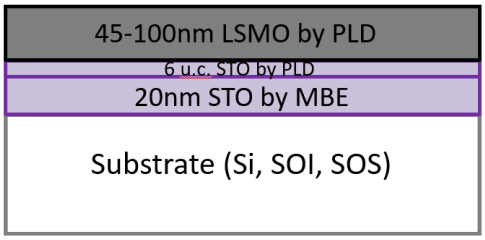

FIGURE 3.19: Schematic representation of the LSMO thin film deposited on STO/Si-based substrates

Before deposition, the substrates were heated to the desired temperature in vacuum environment. STO and LSMO films are deposited at 0.1 mbar and 0.17 mbar O_2 partial pressure respectively, to compensate for oxygen loss in the process, with the substrate temperature maintained at 750°C or 770°C. After deposition, the films are cooled down to room temperature at 10°C per minute rate in 700 mbar O_2 pressure. The schematic representation of the LSMO/STO/Si-based heterostructures is shown in Figure 3.19 with the respective thicknesses of each layer and the techniques used for their growth.

The parameters used in deposition by PLD are shown in Table 3.2. The results in terms of crystallography and surface roughness will be evaluated and discussed in section **Results** in the end of this chapter.

Material	Thickness	Rate	Temperature	Pression (O_2)
STO	2 nm	1 Hz	770°C	0.2 mbar
LSMO	45 nm	3 Hz	750°C	0.2 mbar
AlN	120 nm (20k shots)	5 Hz	RT	Vacuum
Au	8 nm	5 Hz	RT	Vacuum

TABLE 3.2: Deposition parameters by pulsed layer deposition

3.3.3 Sputtering

Both sol-gel and sputtering have been widely used methods for developing c-axis oriented PZT layers due to its simplicity, good reproducibility and compatibility with standard Si-fabrication technology. Although sputtering at room-temperature is preferred due to the advantage of low temperature operation possibility, high temperature depositions are also considered for comparison of process parameters influence on the growth, texture and orientation of the films. In general, as-deposited films at room temperature are amorphous and post-deposition annealing is essential to transform the amorphous structure of the film into the envisaged ferroelectric-perovskite phase, for our films this is achieved through a rapid thermal annealing (RTA) at $650^{o}C$ as it marks the temperature at which the pyrochlore to perovskite phase transformation is completed (Kwok and Desu, 1992).

Sputtering consists of a physical vapour deposition method for producing coatings in a vacuum environment and it involves the striking of high-energy ions onto a solid which knocks off atoms from the surface. Ionic sputtering techniques include diode sputtering, ion-beam sputtering and magnetron sputtering. The latter is a high-rate vacuum coating technique commonly used for depositing metals, alloys and compounds onto a wide range of materials with thicknesses up to about 5 μm with high purity and high adhesion (Swann, 1988).

The process principle is based on the ejection of atoms or molecules of a material from a target by the bombardment of high-energy particles to directly coat substrates. When the bombardment is done by positive ions derived from an electrical discharge in a gas, it is called cathodic sputtering.

Fabrication of highly sensitive infrared detector devices require the deposition of epitaxial PZT thin films on a suitable bottom electrode as LSMO. For such PZT with tetragonal perovskite structure, the epitaxy must be guaranteed along the c-axis since it is the polarization axis. The growth of epitaxial PZT thin films was achieved by other groups on oxide substrates such as MgO (Takayama and Tomita, 1989) or SrTiO (Triscone et al., 1996), and on epitaxial oxide electrodes such as SrRuO and $SrRuO_3$ on Si(100) (Shimizu et al., 2000) and with a yttria stabilized zirconia buffer layer (Eom et al., 1993), however, all these processes required high temperatures and attempts to prepare PZT on bare Pt/MgO for substrate temperature below 550-600 °C have given rise to nonferroelectric pyrochlore phases or a mixture of ferroelectric perovskite and nonferroelectric pyrochlore phases (Bouregba et al., 2001).

We have successfully deposited, then, epitaxial c-axis oriented 400 and 500 nm PZT thin films with a tetragonal perovskite structure by magnetron sputtering technique while heating the substrate at only 600°C. Such samples were used as

our reference for performing and characterizing PZT sputtering deposition at room-temperature followed by a rapid thermal annealing at 650°C during 30 seconds under oxygen.

The PZT deposition at 600°C was performed using a multi-target RF magnetron sputtering, at CRISMAT by G. Poullain and C. Cibert, from 3 metallic targets with an Ar/O_2 mixture with ratio 90%/10% and in-situ deposition at 600°C. The exact conditions for the samples are total pressure during sputtering of 0.7 Pa, substrate temperature of 600°C with a ramp up of 15°/min and a ramp down of 30°/min; Power for each target equal to Pb = 0.7 W/cm^2, Zr= 2.7 W/cm^2 and Ti= 3.3 W/cm^2, and the deposition speed was estimated at about 100 nm/h.

3.3.4 Sol-gel

The wet chemical deposition by sol-gel method concerns the two chemical states after which the technique is named and is fully illustrated in figure 3.20. The *sol* consists of a colloidal solution of several starting materials in sub-micron solid particles form that are dispersed in the solvent as the precursor (Davies and Rideal, 1961). Such particles are usually from organometallic compounds for most ferroelectric oxides deposition, later submitted to hydrolysis and poly-condensation near room-temperature to prepare the precursor solution.

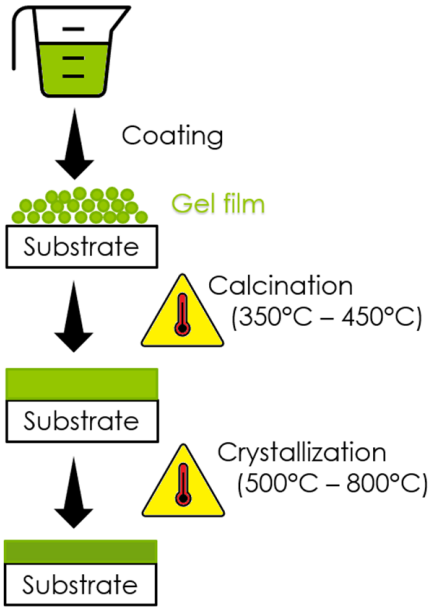

FIGURE 3.20: Sol-gel deposition process

The sol is spread onto the substrate by either spin-coating, spraying or dip-coating and it is solidified by a series of thermal treatments to form a crystalline oxide film, during which it is first dried in order to remove the solvent and the discrete colloidal particles precipitate to form *gel*, in general an irreversible process

due to its covalent nature interaction; The gel is a cross-linked polymeter network with abundance of pores that shrink during a calcination at elevated temperatures, in the range of $350^oC - 400^oC$ forcing the gel network to collapse and leading to smaller contact angle of the grains and higher density (Yin, 2013b).

The organometallic compounds are decomposed by removing -OH and other functional groups so that only oxide material remains in the film after calcination, resulting an amorphous layer of the desired film that is subjected to a final post-thermal treatment at higher temperatures ($500^oC - 800^oC$) to crystallize and enhance the crystalline phase of the deposited layer.

The thermodynamically stable perovskite phase of PZT crystallizes, via a lead-deficient transient non-ferroelectric pyrochlore-type phase (stable between 450°C and 550°C), between 500°C - 700°C (Carim et al., 1991). A Rapid Thermal Annealing is then necessary over the temperature region of the pyrochlore phase stability, to enhance the perovskite one (Griswold et al., 2011). The perovskite crystallization temperature can be reduced by extra lead organic compound in the sol-gel solution (which can also compensate the lead loss during the thermal treatments) or increased by using a Zr-rich PZT.

3.4 Characterization techniques

As described in table 3.3, several characterization techniques have been used to evaluate the deposited materials.

Characterization Technique	Model	Where	By whom
XRD	PANalytical	LCS	L. Araujo
XRD	RIGAKU (Smartlab)	INL	B. Vilquin
AFM	NanoObserver CSI	GREYC	L. Araujo
PFM	NanoObserver CSI	GREYC	L. Araujo
R(T)	Homemade	GREYC	V. Pierron L. Araujo
P(E)	Homemade	CRISMAT	G. Poullain C. Cibert J. Manguele
P(E)	Homemade	INL	B. Vilquin P. Romeo

TABLE 3.3: Characterization techniques of our deposited materials

3.4.1 X-Ray Diffraction (XRD)

X-ray diffraction measurements allow the full analysis of the crystalline structure of epitaxial thin films based on the dual wave/particle nature of X-rays. The diffraction

pattern of each material is a signature that enables the identification and characterization of the compounds even for chemically identical materials, such as quartz and cristobalite, for example, two different arrangements of SiO_2, or still Anatase, Brookite and Rutile exhibiting drastically different diffraction patterns for TiO_2 materials. Besides crystal structure and phase composition of a sample, XRD allows the determination of several parameters such as lattice parameters, alloying, doping, solid solutions, macrostrain such as residual strain, epitaxy, texture and orientation, crystallite size and microstrain. One may also have in-situ capabilities as evaluation of all these properties as a function of time, temperature, and gas environment.

A monochromatic beam of x-rays interacting with a target material suffers an elastic scattering of the x-ray photons, i. e., the wavelength is kept constant while the wave vector is changed. The x-ray beams diffracted by the atoms in a periodic crystalline structure interfere with each other, producing a structure-dependent intensity that is a composition of constructive and destructive interferences, such that the kind and arrangement of the atoms in the crystal structure determines the intensities of the diffracted waves and the size and shape of unit cells define the possible diffractions' directions. For certain angles between the incident and the diffracted beams, 2θ, the electrons in each atom - arranged in a periodic array with long-range order able to produce diffraction - coherently scatter light, i. e., the diffraction of x-rays by crystals occurs producing constructive interference and it is described by Bragg's Law (equation 3.3), illustrated in Fig. 3.21:

$$2dsin\theta = n\lambda \tag{3.3}$$

where d is the space between the parallel diffracting planes, λ symbolizes the wavelength of the x-ray and n stands for the diffraction order. The wavelength of X-rays are similar to the distance between atoms in a crystal, which is why X-ray scattering is used to study atomic structures.

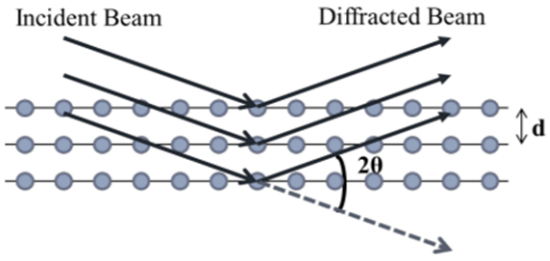

FIGURE 3.21: Bragg's law illustration for diffraction in crystalline structure

Such measurements are performed with an x-ray diffractometer, a system composed of a microfocus rotating anode x-ray tube, a twin-crystal monochromator, a series of aperture slits, an X-ray detector and a mechanical rotation system as

illustrated in Fig. 3.22.

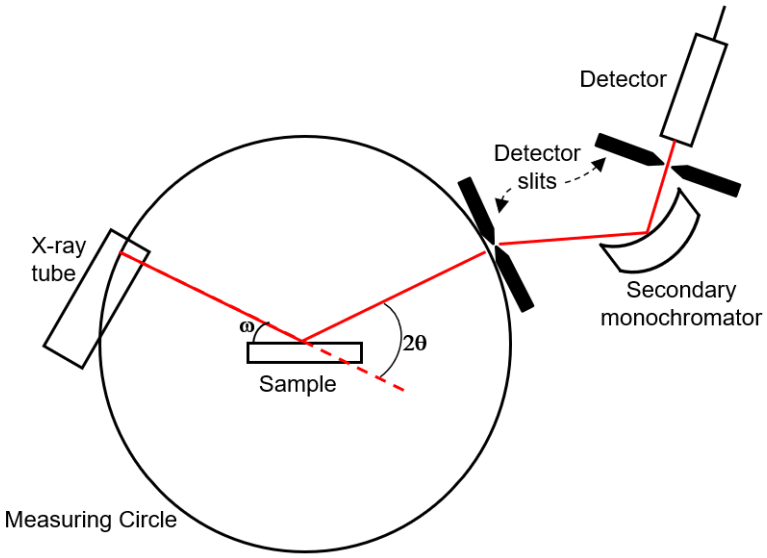

FIGURE 3.22: Configuration of an x-ray diffractometer

Inside the x-ray tube, the collision of high-velocity electron beam onto a cathode target material, typically cooper, leads to a conversion of about 1% of the kinetic energy of the electron beam into X-ray radiation whereas the remaining is dissipated as heat (Yin, 2013a). The material's choice determines the wavelength produced, reasonably long, 1.54056 Å, for Cu conducting to good resolution in registration of the pattern.

Once the splitting of the 2p orbitals in cooper (energy levels LII and LIII) is very small (0.020 keV), the two wavelengths $K_{\alpha_1} = 1.54056$Å and $K_{\alpha_2} = 1.54439$Å are very similar, although the peaks are distinctly asymmetric: K_{α_1} peak exhibits almost twice the intensity of the K_{α_2} peak.

Since K_β has much lower intensity than K_α (approximately five times smaller), its use as main line is not considered since it would lead to very poor signal to noise ratio, the reason why a monochromator is required to optimize instrumental setups by removing this component, commonly a Ni filter, keeping the desired emission line, k_{α_1}, as incident x-ray beam.

Finally, the angular resolution is determined by a series of aperture slits on the path of diffracted x-ray beams that serve to define the divergence angle and width of the incident beam. An x-ray detector is responsible for measuring the intensity of the diffracted beams while changing the angles in the rotational system.

Diffraction patterns are collected as absolute intensity vs 2θ, however this peak position depends on instrumental characteristics such as wavelength, so to make the measurements instrument-independent they are best reported as relative

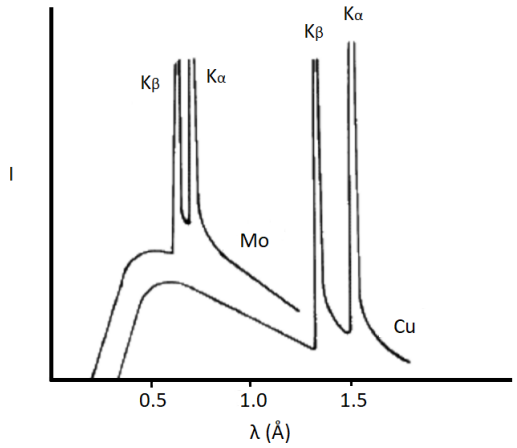

FIGURE 3.23: Typical X-ray spectrum generated by Mo and Cu targets.

intensity (the absolute intensity of every peak by the absolute intensity of the most intense peak, as percentage) vs d_{hkl} which is an intrinsic material property.

Through the change of several crystallographic angles in the rotational system, structural characterization can be realized in diverse XRD modes: $\theta - 2\theta$ scan, ω scan, ϕ scan, pole figure, X-ray reflectivity and reciprocal space mapping, as displayed in figure 3.24.

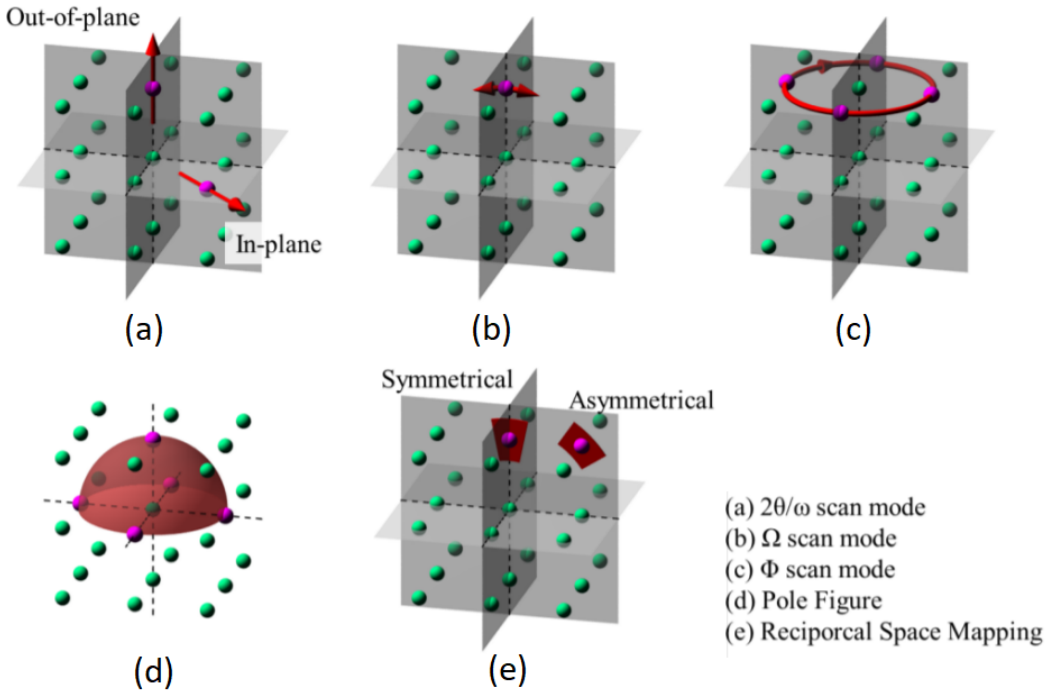

FIGURE 3.24: XRD modes of analysis in the reciprocal space for a cubic crystalline structure. Extracted from (Yin, 2013a)

$\theta - 2\theta$ **scan:** For the scans realised in this mode, both angles 2θ and ω are

rotated simultaneously while keeping This mode simultaneously rotates 2 and angles while keeping $\theta = \omega$ to keep the scattering vector δk always along the normal direction of the film surface during the complete scan resulting in the analysis of the reciprocal vector and the lattice constant in the out-of-plane direction.

ω **scan:** This mode is also known as rocking curve and it differentiates from the previous one due to the maintenance of the 2θ angle constant while changing ω (simultaneous rotation in the same direction of the incident and diffracted beams). This mode enables the analysis of the crystalline quality of the film in terms of mosaicity, curvature, misorientation and inhomogeneity.

ϕ **scan:** The scan in this mode is performed fixing the corresponding χ angle of the detected crystalline plane while φ angle rotates from 0° to 360°. It allows the analysis of the orientation of the film crystalline structure and the symmetry of the crystalline plane around the normal to the surface being studied.

Pole figure: Pole figures are obtained by the change in χ angle for a series of ϕ scans, covering a semi-spherical surface analysed region in the reciprocal space, with a fixed 2θ angle (fixed length of scattering vector). It provides more detailed information than the ϕ scan about the symmetry of the analysed crystalline structure.

Reciprocal Space Mapping: This mode consists in a series of ϕ scans with varying 2θ angle for each scan to provide a more complete amount of information about the texture, the crystalline quality, the internal strain, and the fine structure of the film crystal.

X-ray reflectivity (XRR): This mode provides information on films density, thickness, roughness and interface quality of the different layers of a heterostructure through the evaluation of the many characteristics of the resultant pattern such as the plateau that provides information on sample size, roughness, absorption and the instrument used for measurement itself (confirmed by the background). The critical angle provides information on the film's density and the distance between peaks, on the layer thickness. From the amplitude, one may obtain the roughness, interface quality, density variations and resolution. The rotational system in XRR measurement has a very small incident angle usually less than 10 when rotating $\theta\varphi$ and φ angles simultaneously. This results in the X-ray beam being partially reflected at the surface and different interfaces of a heterostructure. The outcoming X-Ray beam in then the interference of all the reflected X-ray beams and the reflectivity of the heterostructure is determined by the thickness, the electron density, and the roughness of each layer. The related parameters of each layer can be derived by using Fourier transform or a transfer-matrix method. The calculation of individual layers of films in a multilayer structure requires Parratt method to extract the parameters for each film.

3.4.2 Resistivity versus temperature

The electrical characteristics of the LSMO thin films on each substrate were evaluated by a four point resistance measurement for a temperature range between 300 K and 400 K. The resistivity of the samples were obtained straightforwardly by a measurement set-up with 4-probes with finite tip radius placed collinear and equidistant, supported by a spring that helps minimizing the damage on the samples when contact is established.

A current source supplies current to flow between the external probes while a voltmeter measures the voltage across both probes of inside (such probes do not draw any current since they are connected to the voltmeter with high impedance). The advantage of such method in comparison with two probes technique is that it eliminates the contact resistance between film and probes, improving accuracy of the results. The resistivity is directly calculated as

$$\rho = \frac{V}{I} \cdot \frac{\pi}{ln2} d \tag{3.4}$$

where ρ stands for the resistivity calculated in $\Omega \cdot m$ and d for the distance between two probes. I is the applied current by the current source and V the measured voltage by the voltmeter.

3.4.3 Polarization versus electric field

The polarization of ferroelectric films is normally performed through the use of a Sawyer-Tower circuit, where the ferroelectric film is connected in series with a reference capacitor driven by an AC signal generator and measured by an oscilloscope. The channel X of the oscilloscope displays the voltage of the applied AC signal and the channel Y, the voltage drop across the reference capacitor. The later is proportional to the accumulated charge on the film's surface and we can derive both the polarization and applied electric field by (Yin, 2013a):

$$P = \frac{Q}{S} = \frac{C_{ref} V_y}{S} \tag{3.5}$$

$$E = \frac{V_x - V_y}{d} \tag{3.6}$$

where S is the area and d is the thickness of the ferroelectric capacitor.

The macroscopic polarization hysteresis loops, P(E), of the PZT films were performed on samples with $250 \times 250 \mu m^2$ top Pt electrodes patterned by lift-off process. The Sawyer-Tower (ST) circuit was driven by a sine wave of amplitude 20 V and frequency 500 Hz. The capacitors were contacted on a Suss MicroTec PM5 probe

station. A standard capacitor Cst of 22 pF serving as a charge holder, was used during the hysteresis measurements.

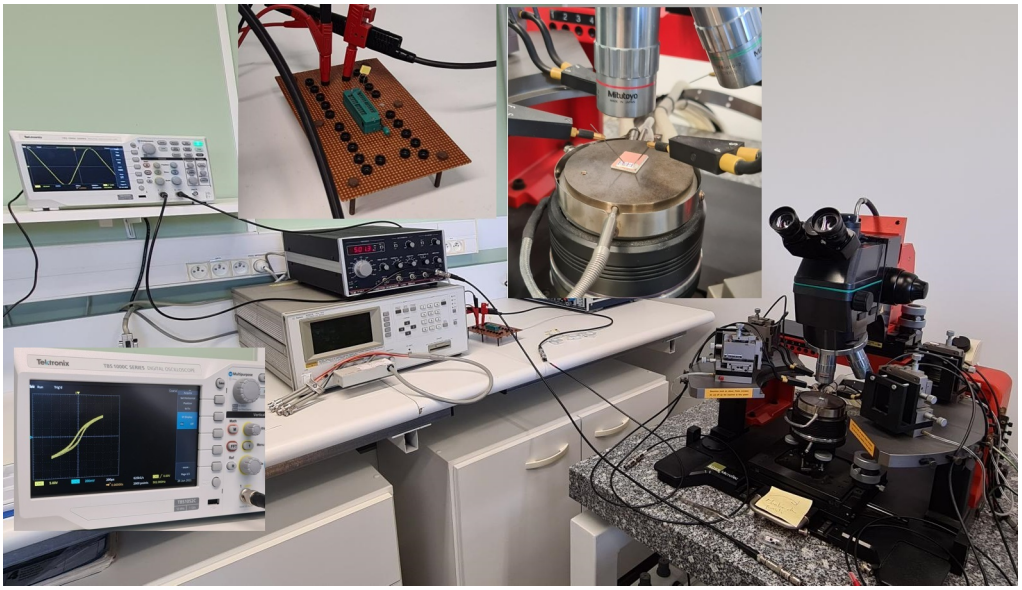

FIGURE 3.25: Measurement setup for P-E measurement at CRISMAT

The polarization and the electric field were calculated using the following equations:

$$P = \frac{C_m V_0}{A_{PZT}} \tag{3.7}$$

$$E_f = \frac{V_i}{t_{PZT}} \tag{3.8}$$

where P represents the polarization in $\mu C/cm^2$, the measuring capacitor has its capacitance defined by C_m in μF, V_0 is the measured voltage in V, A_{PZT} is the area of the PZT film given in cm^2, E_f stands for the electric field in kV/cm, V_i the applied voltage in kV, and t_{PZT} is the PZT film thickness in cm (Deshpande and Saggere, 2007).

3.4.4 Atomic Force Microscopy

Atomic Force Microscopy (AFM) is used to investigate the morphology and growth structure of the thin films, through the operating principle illustrated in figure 3.26. The instrument consists of a cantilever with a sharp tip mounted on its one end that is usually formed from silicon, silicon oxide or silicon nitride and is typically 100 μm long, 20 μm wide, and 0.1 μm thick. The cantilever motion causes the reflected light to impinge on different segments of the photodiode.

The three common modes of operation of AFM scans are (Shah, 2010):

1. **Contact mode:** the probe tip is dragged across the surface and the resulting image is a topographical map of the sample surface. The dragging motion of

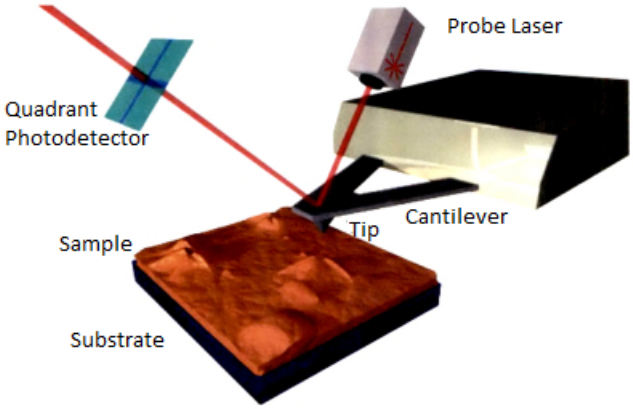

FIGURE 3.26: Schematic representation of atomic force microscope. Extracted from (Shah, 2010).

the probe tip, combined with adhesive forces between the tip and the surface can distort measurement data and damage the sample.

2. **Non-contact mode:** the instrument senses Van-der-Waal attractive forces between the surface and the probe tip held above the sample surface. Unfortunately, these forces are substantially weaker than the contact mode forces, so weak in fact that the tip must be given a small oscillation and ac detection methods are used to detect the small forces between tip and sample.

3. **Tapping mode:** it overcomes the limitations of the conventional scanning modes by alternately placing the tip in contact with the surface to provide high resolution and then lifting the tip off the surface to avoid dragging the tip across the surface. During scanning, the vertically oscillating tip alternately contacts the surface and lifts off, generally at a frequency of 50 to 500 kHz. Tapping mode imaging works well for soft, adhesive, or fragile samples, allowing high resolution topographic imaging of sample surfaces that are easily damaged or otherwise difficult to image by other AFM techniques.

3.4.5 Piezoresponse Force Microscopy

Piezoresponse Force Microscopy (PFM) is a versatile characterization technique that has been extensively used for exploring nanoscale ferroelectric and piezoelectric phenomena in thin films due to its remarkably high resolution and ease of use (Li et al., 2015), (Peter et al., 2006). Its use has been also intensively demonstrated with ferroelectric oxide systems (Kalinin, Shao, and Bonnell, 2005), but its use extends over a large range of materials such as biological (Kholkin et al., 2010) (Halperin et al., 2004), polymeric (Gysel et al., 2008), (Park et al., 2014), hybrid organic-inorganic (Coll et al., 2015), (Kutes et al., 2014) and two-dimensional materials (Cunha Rodrigues et al., 2015), (Kim et al., 2016).

It is based upon a modification on the AFM setup where a conductive cantilever is used in addition to a contact mode, to allow the local direct application of an electric field at the film surface. The imaging mechanism is then based on the detection of the electromechanical response induced by the film's displacement resulted by the inverse piezoelectric effect and detected by the conductive tip dynamics and a four quadrant photodiode setup.

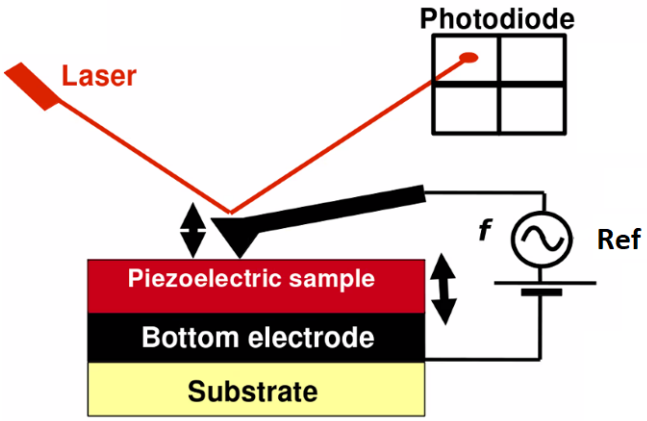

FIGURE 3.27: Principle of a typical PFM setup

A sinusoidal ac voltage with amplitude smaller than the coercive voltage of the electric film is applied in this setup to avoid the destruction of ferroelectric domains structures and to overcome the difficulty in detecting a static displacement induced by electric field that is generally too weak to be easily detected because of the relatively large surface roughness (Yin, 2013a). The local surface of the ferroelectric/piezoelectric film vibrates at the same frequency as the one applied and a lock-in amplifier uses the applied ac voltage as reference to extract the electrical signal associated with vibration from a highly noisy background. While scanning the surface line by line, the PFM image displays for each pixel the amplitude and phase of vibration.

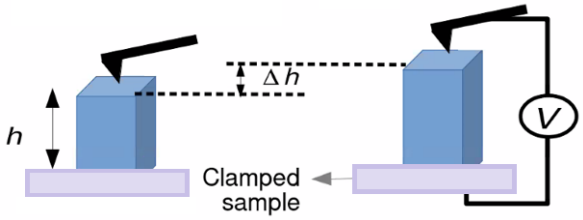

FIGURE 3.28: Principle of displacement measurement of a piezoelectric material by PFM

The orientation and strength of the permanent polarization under the PFM tip determines the mechanical vibration provided by the ac voltage application, such that, if it is along the normal of the film, z axis, the local surface will extend or contract, as exhibited in figure 3.28, which characterizes also the measurements we performed in this thesis. The amplitude of the longitudinal vibration is related to d_{33}

value. The other case would be when the permanent polarization is parallel to the film surface which under aplication of the ac voltage, responds to it with a surface film shear and an amplitude of transverse vibration related to d_{14} and d_{25} values. However, to quantify the piezoelectric coefficient, a reference material with a known piezoelectric coefficient, like quartz film for example, is commonly used to perform the calibration between the output amplitude in voltage and the piezoelectric constant.

PFM Imaging

The ferroelectric properties of our studied PZT films were characterized by PFM measurements through the creation of artificial domains by poling normally a 5×5 μm^2 surface through a scanning with +10V dc voltage applied on the cantilever tip (domain down), followed by -10V dc voltage to reverse the piezoelectric dipoles in a 2×2 μm^2 surface central area (domain up). The out-of-plane piezoelectric response was then collected with a 4 V ac drive voltage at about 330 kHz in a 15×15 μm^2 scan to verify that the poling was uniformly and completely achieved without leaving traces in the topography. The two stable states of polarization were maintained and re-read after several hours to evaluate the ferroelectric properties of the deposited PZT films.

3.5 Results

3.5.1 LSMO/STO PLD growth on Si-based substrates

The electrical characteristics of the LSMO thin films on Si, SOS and SOI substrates were evaluated by a four point resistance measurement for a temperature range between 300 K and 400 K, from which the resistivity of the samples were calculated. The results are exhibited in figure 3.29 for the samples described in table 3.4.

Nomenclature	Substrate	LSMO thichness
BA164	Si ZW890	45 nm
BA166	Si ZW890	45 nm
BA162	SOI2 ZW600	45 nm
BA165	SOI2 ZW600	45 nm
BA102	SOS ZW602	45 nm
BA081	SOS ZW602	45 nm

TABLE 3.4: Nomenclature and details on samples presented for the evaluation of LSMO deposited by PLD onto Si-based substrates

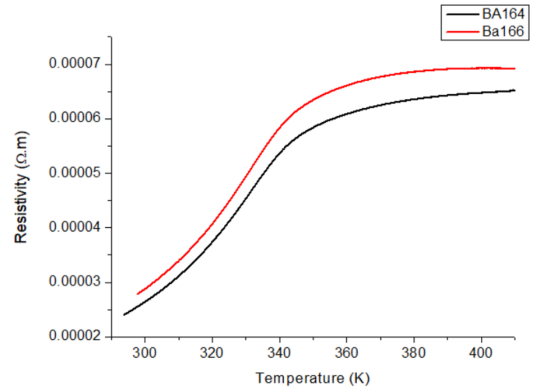

(a)

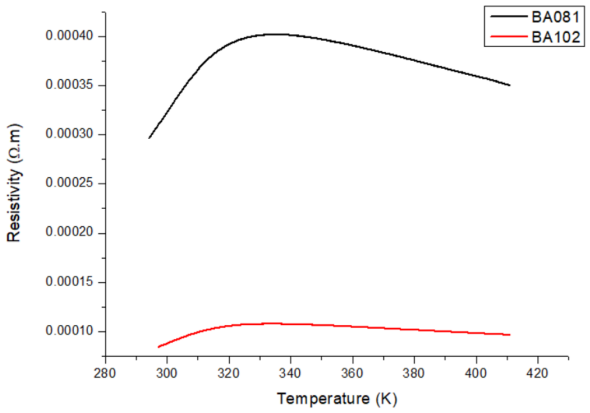

(b)

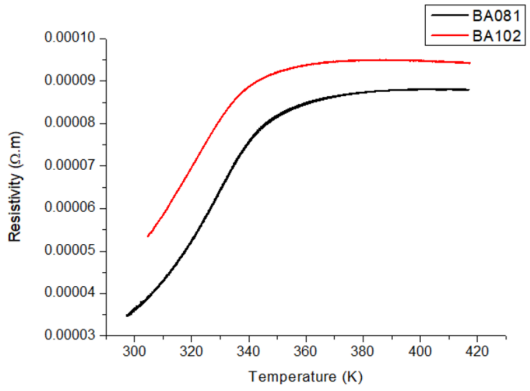

(c)

FIGURE 3.29: Resistivity vs temperature measured for 45-nm thick LSMO thin films deposited onto STO buffered (a) Si, (b) SOI and (c) SOI substrates by PLD at GREYC

The films grown on STO buffered Si and SOS exhibit excellent electrical characteristics with the resistivity in the order of $10^{-5}\Omega \cdot m$ validating the PLD parameters deposition of LSMO/STO thin films. The ones grown on SOI substrates, however, show an important drop on resistivity values with further increase of temperature which may be due to a poor quality STO. The parameters and deposition conditions used for the deposition onto SOI substrates were the same as for the other two cases. Extra 2 nm of fresh STO were grown by PLD before LSMO deposition however, as seen in the measurements, the resistivity is still degraded in comparison with the Si and SOS substrates.

The crystalline quality and epitaxial relationship between film and substrate grown by PLD were evaluated by X-ray Diffractometer (XRD). A long-range (20°-80°) $\theta - 2\theta$ scan was performed for each sample, with a step size of 0.0084° and 50 seconds per step, revealing exclusively (00l) orientation, which indicates the c-axis epitaxial growth of LSMO and STO layers. Such diffraction patterns can be seen in figure 3.30 for Si substrate.

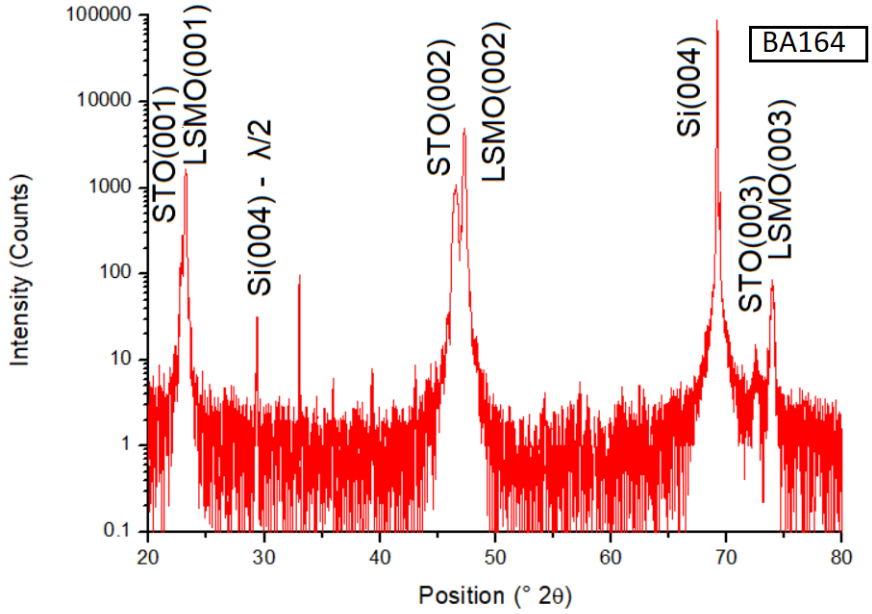

FIGURE 3.30: Full range $\theta - 2\theta$ scan from 20°-80° on epitaxial LSMO/STO PLD deposited on Si substrate

Figure 3.31 exhibit the full scan XRD for LSMO/STO grown on SOI substrate between 20°-80° with a step size of 0.0084° and 30 seconds per step. For this kind of samples, the angle correction was performed using the topmost silicon of reference by an omega scan around 34.5°, once it defines the orientation that the epitaxial growth of subsequent layers will follow (diffraction peak at about $2\theta = 35.1°$). The peak of the topmost silicon, with width equal to 440 nm, on the SOI wafer is found very close to the diffraction peak of the bottom Si, as observed in Figure 3.32,

along with the omega scan was also performed at the LSMO(002) peak to evaluate its quality which shows satisfactory full-width half maximum (FWHM) value of 0.495. These measurements were made by using a step size of 0.02 and two seconds per step.

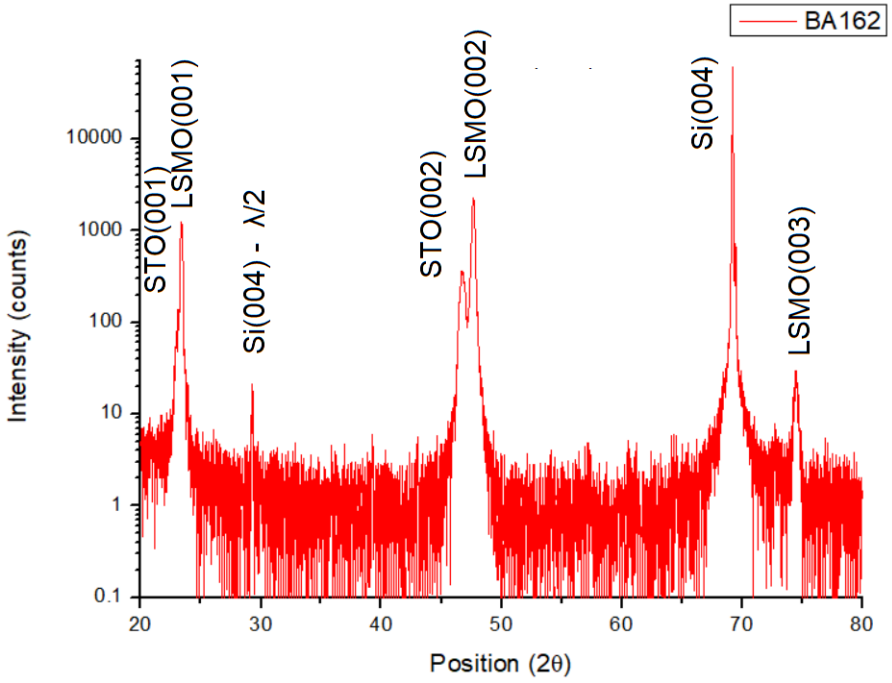

FIGURE 3.31: Full range $\theta - 2\theta$ scan on epitaxial LSMO/STO PLD deposited on SOI substrate with 440 nm of top silicon

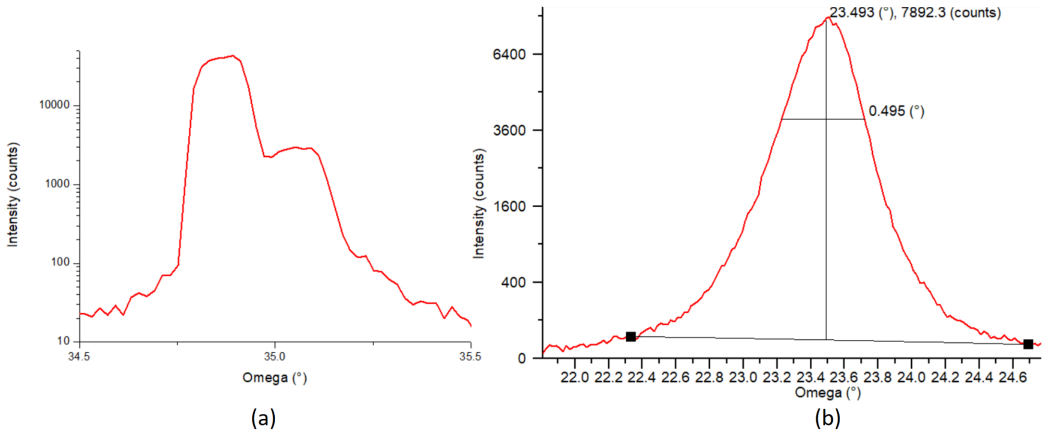

FIGURE 3.32: (a) Omega scan around 34.5° for definition of both Si surfaces diffraction peaks in SOI substrate and (b) omega scan at LSMO(002) peak

XRD measurements of the last substrate case, Silicon-on-Sapphire (SOS), is shown in figure 3.33 and they are presented in paper under revision at the time of writing in Applied Surface Science. Figure 3.33(a) shows the full range $\theta - 2\theta$

XRD scan revealing only (00l) orientation. The LSMO/STO have preferential c-axis epitaxial growth onto SOS substrate. The silicon (004) peak is seen at about $2\theta \approx 69^o$ and the series of (10-12) diffraction peaks from the sapphire substrate indicate that the sapphire crystal is cut along r-plane.

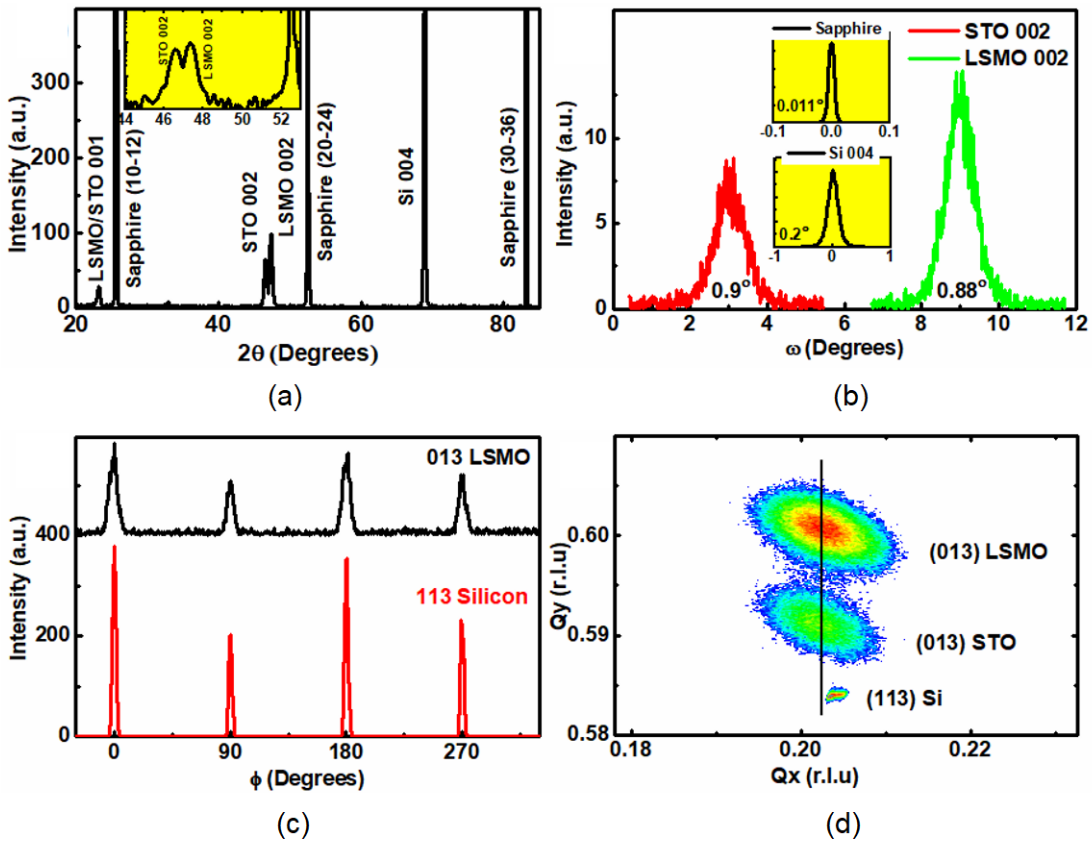

FIGURE 3.33: XRD measurements for 30 nm of epitaxial LSMO/STO PLD deposited on SOS substrate: (a) Full range $\theta - 2\theta$ scan with inset in log scale intensity showing the data zoomed around (002) peaks of STO and LSMO layers, (b) omega scan rocking curves around (20-24) sapphire, (004) silicon, (002) STO and (002) LSMO with FWHM about 0.011^o, 0.2^o, 0.9^o and 0.88^o respectively. (c) Asymmetric phi-scans around (013) plane of LSMO and (113) of Si, and (d) reciprocal space maps around (013) reflections of LSMO film and STO buffer layer and (113) reflection of Silicon.

The rocking curves (omega scan) around the (002) peaks of LSMO and STO, (004) peak of silicon and (20-24) of Sapphire are exhibited in figure 3.33(b), from which the full-width half maximum (FWHM) values were calculated for LSMO and STO layers resulting in approximately 0.88 and 0.9 respectively. This value is slightly higher than the values reported by our group for LSMO/STO/Si films fully deposited by MBE (Méchin et al., 2012) and comparable to other values reported in literature on Si substrate (Vila-Fungueiriño et al., 2018).

To understand how the in-plane epitaxial relationship between film and

substrate is established, asymmetric -scans around the (013) and (113) peaks of LSMO and Silicon were performed as shows figure 3.33(c). A four-fold symmetry with 90° peak separation confirms that the LSMO/STO layers grow in diagonal-on-cube geometry with 45° in-plane rotation on Silicon substrate, to bypass the large lattice mismatch between STO (0.3905 nm) and Si (0.534 nm) unit cell parameters. Therefore, the in-plane hetero-epitaxial relationship between film and substrate can be viewed as LSMO[100]//STO[100]//Si[110]// Sapphire whereas the out-of-plane is LSMO(001)//STO(001)//Si(001)// Sapphire(10-12).

Reciprocal space maps around (013) reflections of LSMO film and STO buffer layer and (113) reflection of Silicon in figure 3.33(c) show that the peaks of LSMO and STO are aligned vertically.

The SOS substrate, despite the slight difference in FWHM values in comparison with the aforementioned references, still reports a strong crystalline quality of our thin films. This has led us to investigate its use in our suspended structures in order to obtain flatter beams since the smaller epitaxial strain in the structure release causes less deformation.

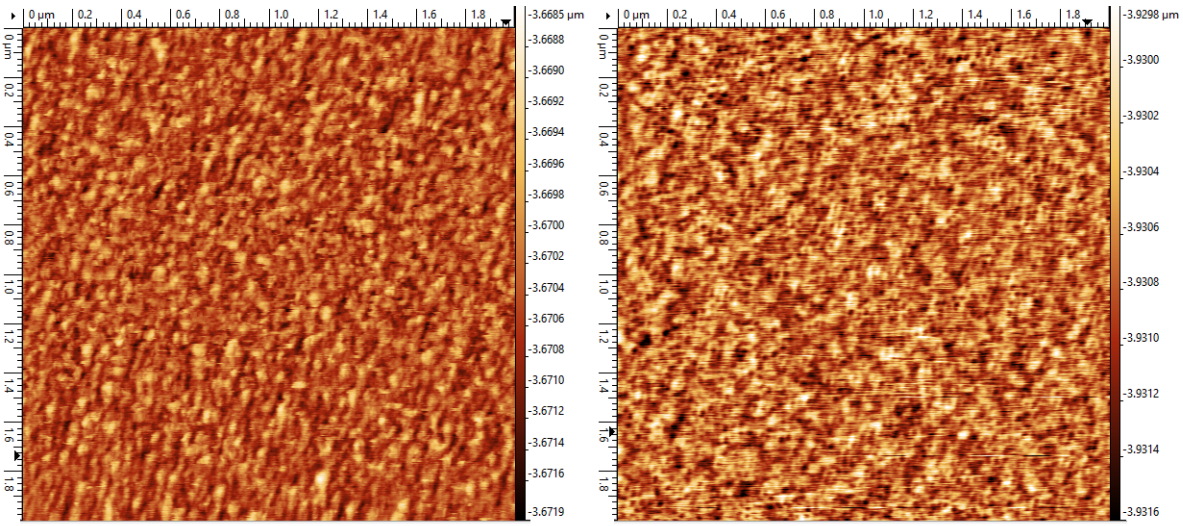

FIGURE 3.34: AFM images of 2×2 μm^2 scan of the 45 nm thick LSMO layer on STO/Si for samples (a) BA166 (Z scale 3.4 nm) and (b) BA164 (Z scale 1.8 nm)

Atomic Force Microscopy (AFM) measurements using a Nano-Observer system from Concept Scientific Instruments were performed to characterize the surface morphology of the films in resonant mode with standard Al-coated Si probes showing nominal resonant frequency of 300 kHz. The 2×2 μm^2 AFM images of LSMO layers are presented in figure 3.34 for two different samples, both exhibiting smooth surfaces with the rms roughness evaluated with Gwyddion software and found to be equal to 0.3±0.04 nm and 0.38±0.03 nm, in accordance with good

LSMO found in literature (Pellegrino et al., 2009).

The detailed structural and electrical characterizations of the LSMO/STO/SOS and LSMO/STO/Si heterostructures show that the LSMO film properties are competitive with those directly grown on oxide substrates. Specially for the SOS case, since so far no attempts have been made on the integration of manganite films on SOS substrate, providing the possibility to use industrially compatible SOS substrates for the development of applicative MEMS devices.

3.5.2 PZT growth by sputtering and sol-gel

The PZT/LSMO/STO/Si heterostructures were obtained thanks to the successive use of 3 different deposition methods, namely sputtering at 600°C, sputtering at room temperature and sol-gel technique. We selected the chemical composition Zr:Ti=52:48 of PZT, since it exhibits the material's largest piezoelectric coefficient, near the so called morphotropic phase boundary.

High temperature process: Sputtering at 600°C

A first series of PZT was deposited, in a colaboration with CRISMAT, in a muti-target RF magnetron sputtering system from 3 metallic targets using power during deposition of Pb: 0.7 $W.cm^{-2}$ / Zr : 2.7 $W.cm^{-2}$ / Ti : 3.3 $W.cm^{-2}$), in a pressure of 0.7 Pa of 90% Ar / 10% O_2 atmosphere at 600°C (ramp up of 15°/min and down of 30°/min). PZT was deposited on top of LSMO/Si and LSMO/STO both with orientation (100) and 400 nm thick, the former at 1,800 shots while the later at 1,600 shots exhibiting deposition rate of about 100 nm/h.

The crystallinity of the samples was characterized by performing X-ray diffraction (XRD) measurements in $\theta - 2\theta$ configuration as well as rocking curves around the 002 peak of PZT, where the full-width at half-maximum (FWHM) of the peak could be estimated. The data was collected using a PANalytical X'Pert PRO diffractometer with Cu-Kα radiation.

Such PZT films with thickness 400 nm have shown orientation preferential (001) orientation, however with some visible (110) patterns.

A fast fatigue problem due to a plumb deficiency was observed and corrected for the next deposition of 500 nm PZT films on LSMO/STO/Si.

The second series of high temperature sputtered PZT was deposited on LSMO/STO/Si substrates with a thickness of 500 nm, showing exclusively (00l) oriented PZT peaks.

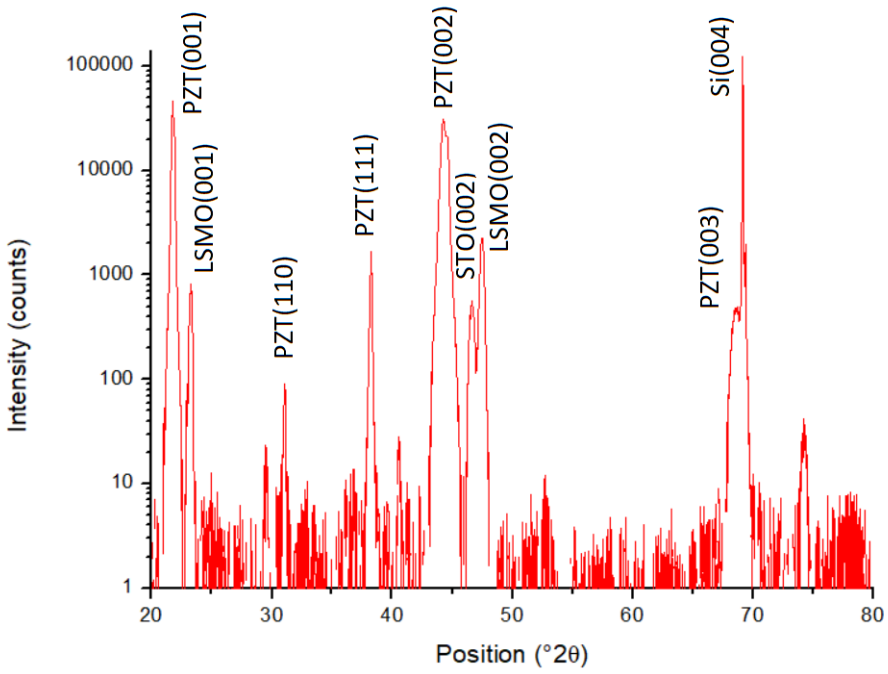

FIGURE 3.35: $\theta - 2\theta$ scan for 400 nm of PZT (series MPZT1191) deposited by sputtering at 600C on Si substrate

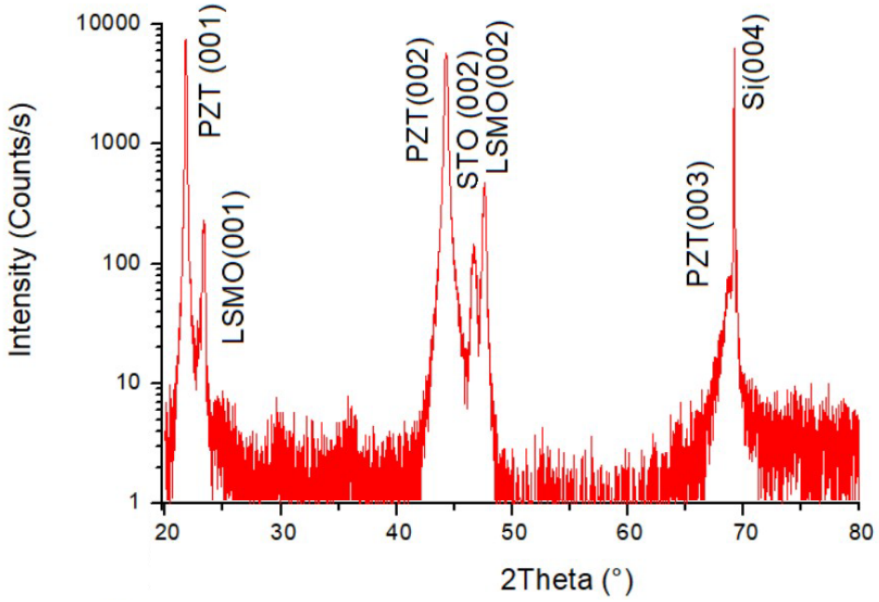

FIGURE 3.36: $\theta - 2\theta$ scan for 500nm of PZT (series MPZT1201) deposited by sputtering at 600°C on Si substrate

The FWHM of the rocking curve around the 002 peak of PZT presented in Fig. 3.37 was equal to 0.35°, confirming the high structural quality of the deposited layers. Good crystalinity was evidenced also for STO and LSMO with FWHM obtained from rocking curves equal to 0.30° and 0.24°.

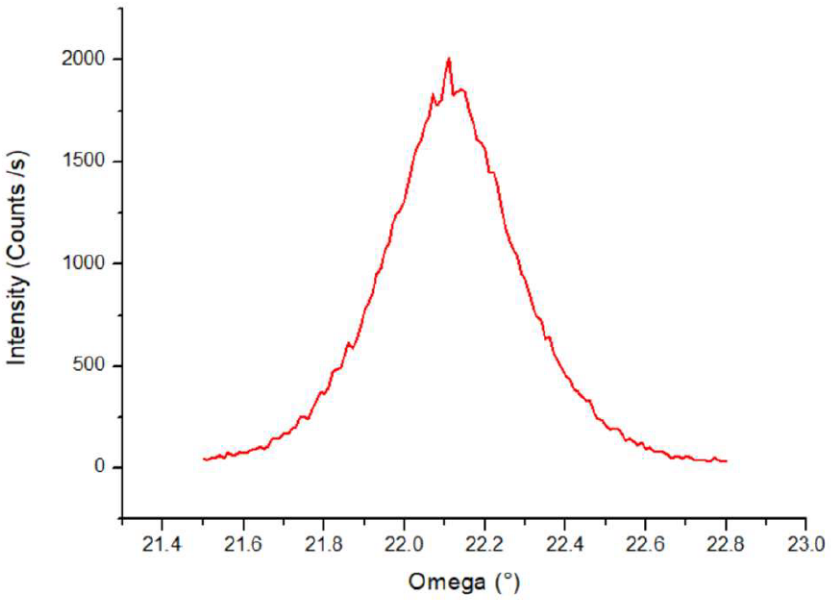

FIGURE 3.37: Omega scan for 500 nm of PZT(002) deposited by sputtering at 600°C used as reference

Test samples have been prepared, where Pt layers were deposited on the PZT films by sputtering at room temperature and patterned using a lift-off process in order to design top electrodes of $250 \times 250 \mu m^2$ size and to perform polarization hysteresis (P – E) loop measurements using a Sawyer-Tower (ST) circuit, driven by a sine wave of amplitude 15 V and frequency 200 Hz. The capacitors were contacted on a Suss MicroTec PM5 probe station. A standard capacitor C_{st} of 22 pF serving as a charge holder, was used during the hysteresis measurements. Even though the 400 nm PZT had shown fairly square ferroelectric cycles, this second series of PZT have displayed good remnant polarization around 25 $\mu C/cm^2$ with a high coercive field of 100 kV/cm at 200 Hz, as shown in figure 3.38.

Atomic Force Microscopy (AFM) measurements using a Nano-Observer system from Concept Scientific Instruments were performed to characterize the surface morphology of the films in resonant mode with standard Al-coated Si probes showing nominal resonant frequency of 300 kHz. The roughness of each sample was evaluated as 0.9 nm, 0.65 nm, 1.4 nm and 1 nm, for the surfaces shown in figure 3.39 (a), (b), (c) and (d), respectively.

Scans in a larger surface of $20 \times 20 \mu m^2$ were also performed to verify the homogeneity of the films, as shown in figure 3.40. The film smoothness is seen in the whole surface, where the rms roughness was kept in low range of values, as for this sample it was 0.91 nm for the larger evaluated surface.

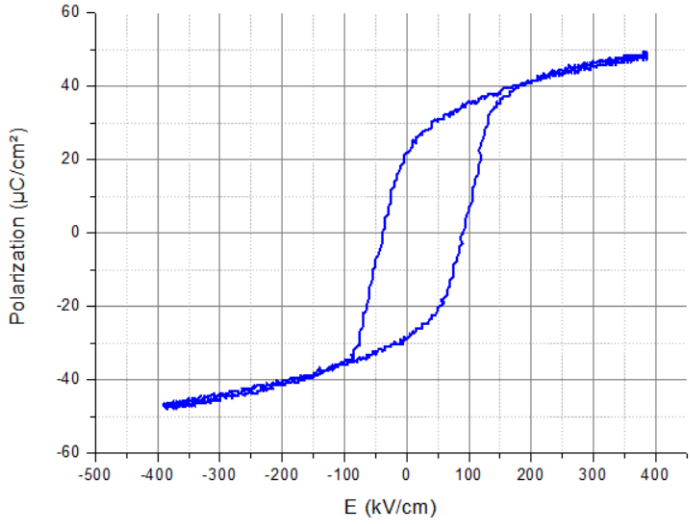

FIGURE 3.38: $P(E)$ measurement for 500 nm of PZT deposited by sputtering at 600°C

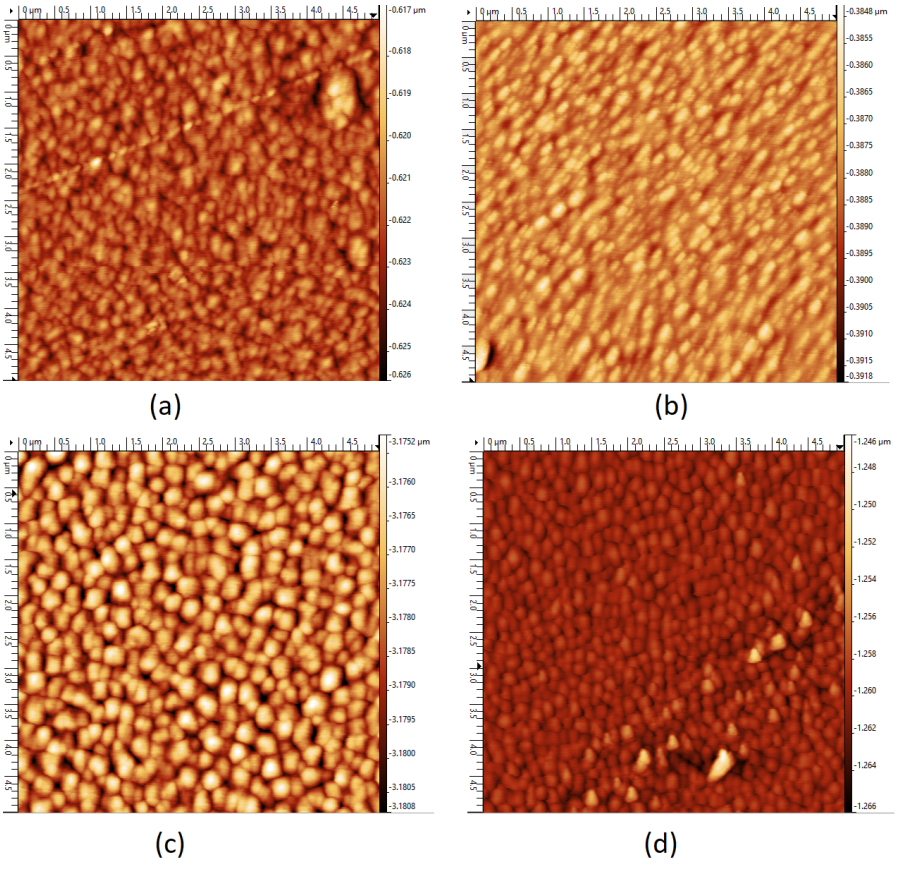

FIGURE 3.39: AFM $5 \times 5 \mu m^2$ scan of (a,b) 400 nm PZT on LSMO/STO/Si (z scale 9 nm and 7 nm respectively) and (c,d) 500 nm PZT LSMO/STO/Si (z scale 5.6 nm and 0.02 μm)

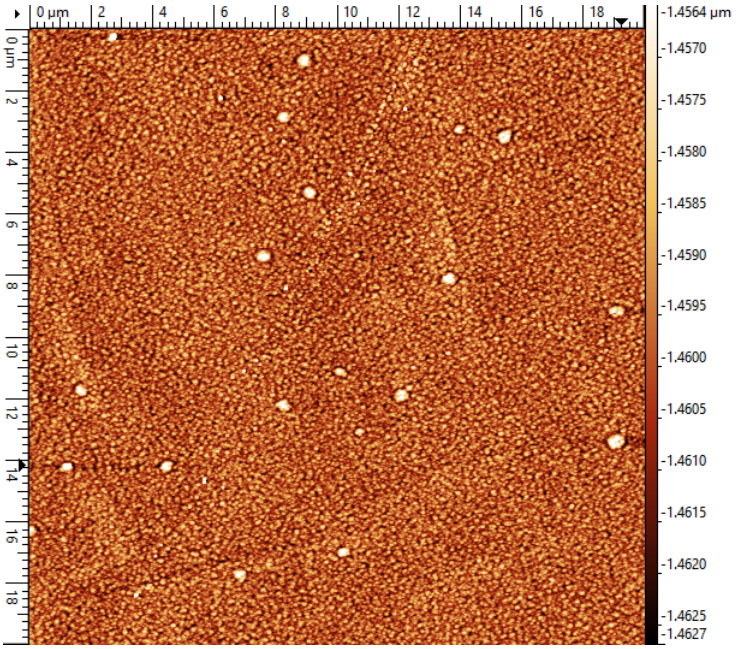

FIGURE 3.40: AFM $20 \times 20 \mu m^2$ scan of 400 nm PZT on LSMO/STO/Si

Since the 500 nm PZT with stoichiometric correction has been successfully integrated epitaxially with our LSMO/STO/Si heterostructures as confirmed by the (00l) peaks of the PZT layer as well as those of LSMO and STO with FWHM of the rocking curve around the 002 peak of PZT equal to 0.35°, and it has also exhibited good fatigue properties along with a smooth surface, it has been taken as reference for comparison with the room temperature PZT depositions towards a room temperature integration process.

Room temperature process: Sputtering at RT and sol-gel

As for the previous case, PZT was deposited on LSMO/STO/Si samples in a sputtering system, however, kept in room temperature with only a rapid thermal annealing (RTA) carried out at 650°C during 1 minute under oxygen. Although high temperatures are still required during this step, the utilization of the technique keeps inside the proposed scope of our integration process since the RTA can be performed after PZT is patterned by lift-off, excluding the need for etching it.

For the sol-gel deposition, however, a step of calcination at 350°C under air is needed once the spin coated layers are deposited, until achievement of the desired thickness. It renders the lift-off of PZT impossible and an etching must then be performed to pattern this material. Either 100 nm or 240 nm PZT thin films were deposited by these techniques.

The crystallinity of the samples was characterized again by performing XRD measurements in $\theta - 2\theta$ configuration, collected using a PANalytical X'Pert

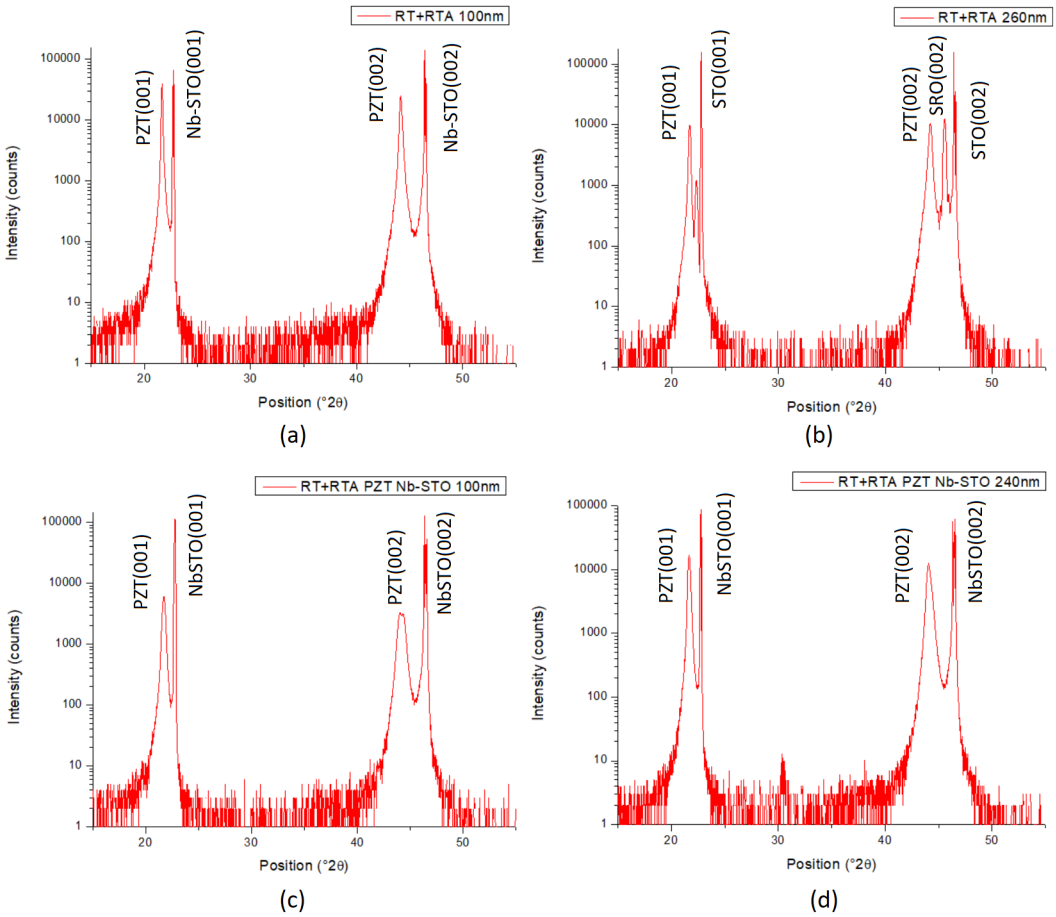

FIGURE 3.41: $\theta - 2\theta$ XRD scan of (a) 100 nm of PZT deposited by RT sputtering on NbSTO with RTA of 650°C, (b) 260 nm of PZT deposited by sputtering followed by 650°C RTA on SRO-STO substrate and (c, d) 100 nm and 240 nm thick respectively of PZT deposited by RT sputtering on NbSTO conductive substrate

PRO diffractometer with Cu-Kα radiation. Figure 3.41 shows the respective XRD $\theta - 2\theta$ scans for the two deposition methods realized at INL by Bertrand Vilquin for different thickness, namely, 100 and 260 or 240 nm; These methods had the epitaxial growth of PZT onto LSMO/STO/Si confirmed where the 00l peaks of the aforementioned layers were observed. No parasitic phases of the PZT were observed.

Atomic Force Microscopy (AFM) measurements, shown in figure 3.43, were performed using the same equipment (Nano-Observer system from Concept Scientific Instruments) with standard Al-coated Si probes in resonant mode (300 kHz) to evaluate the surface roughness of 100 nm room temperature deposited PZT thin films. The PZT deposited by RT sputtering method has exhibited rms roughness of 1.02 nm and the sol-gel one of 0.53 nm.

Other test samples, deposited on Nb-STO substrates, have been prepared to compare the evolution of the properties as the thickness is increased. Aiming a low PZT thickness however, to integrate the bridge structure, we have limited this

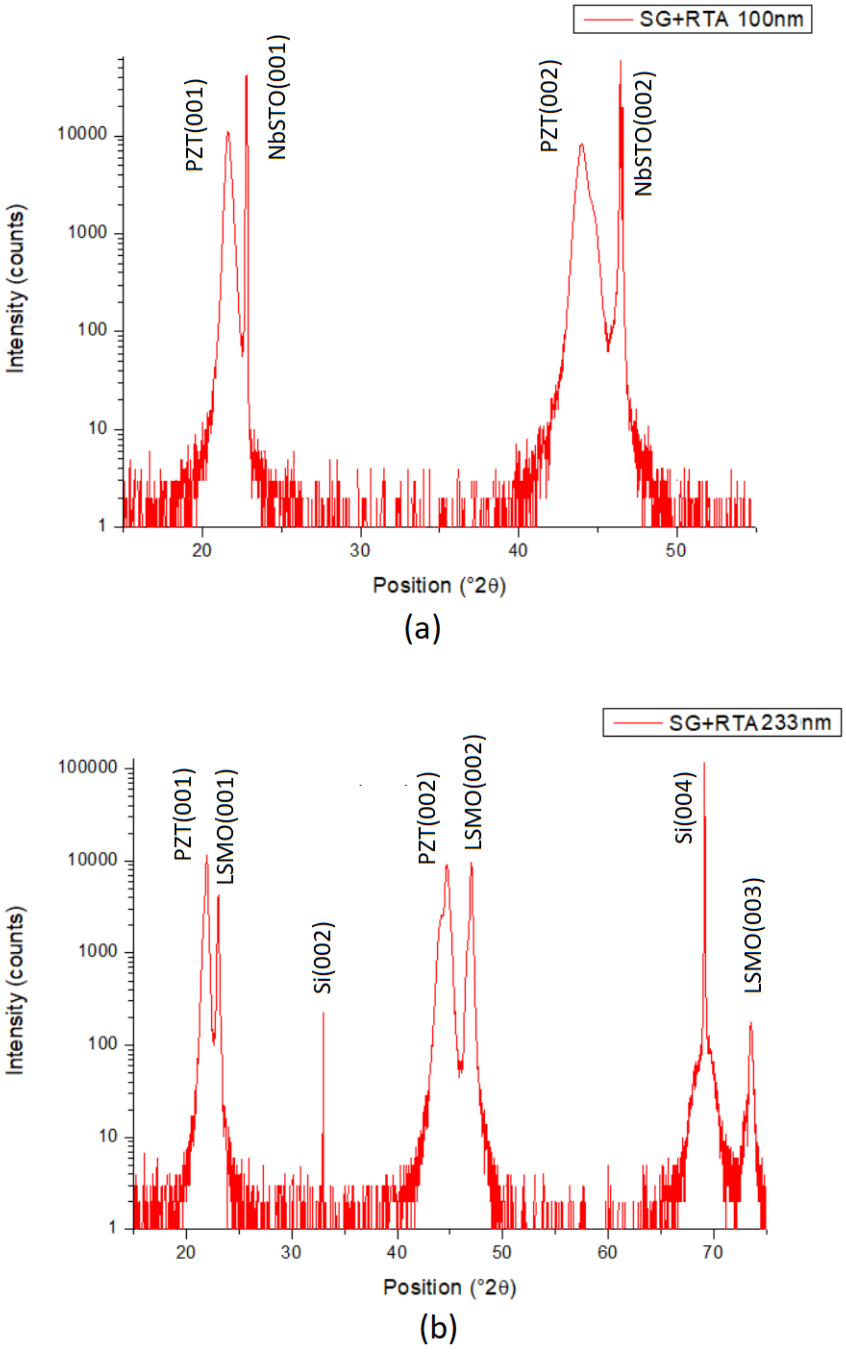

FIGURE 3.42: $\theta - 2\theta$ XRD scan of (a) 100 nm of PZT on NbSTO and (b) 233 nm of PZT deposited by deposited on LSMO/STO/Si by sol-gel method sputtering followed by 650°C RTA with RTA of 650°C

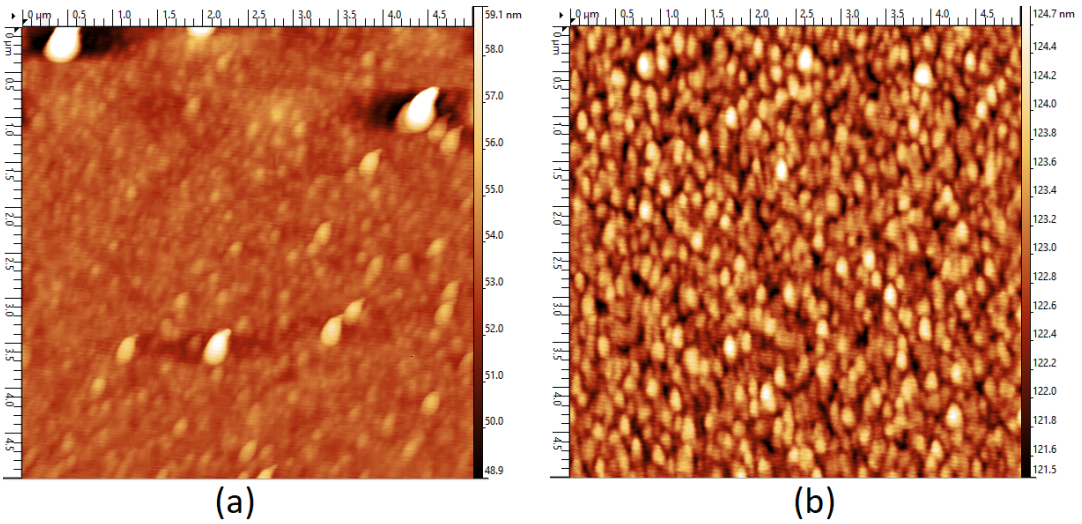

FIGURE 3.43: AFM $5 \times 5\mu m^2$ scan of 100nm (a) RT sputtered PZT (z scale 10.2 nm shown in lateral bar) and (b) sol-gel deposited (z scale 3.2 nm)

comparison for 100 nm and 240 nm (233 nm for sol-gel). The AFM results are shown in figure 3.44 for the RT sputtered PZT and in figure 3.45 for the sol-gel. The (a) of both figures exhibits the surface scan for the 100 nm thick PZTs with rms surface of 0.74 nm and 0.33 nm, for RT sputtering and sol-gel, respectively. Whereas the (b) of each figure stands for the 240 nm RT sputtered PZT with rms roughness 0.38 nm and sol-gel with 0.81 nm.

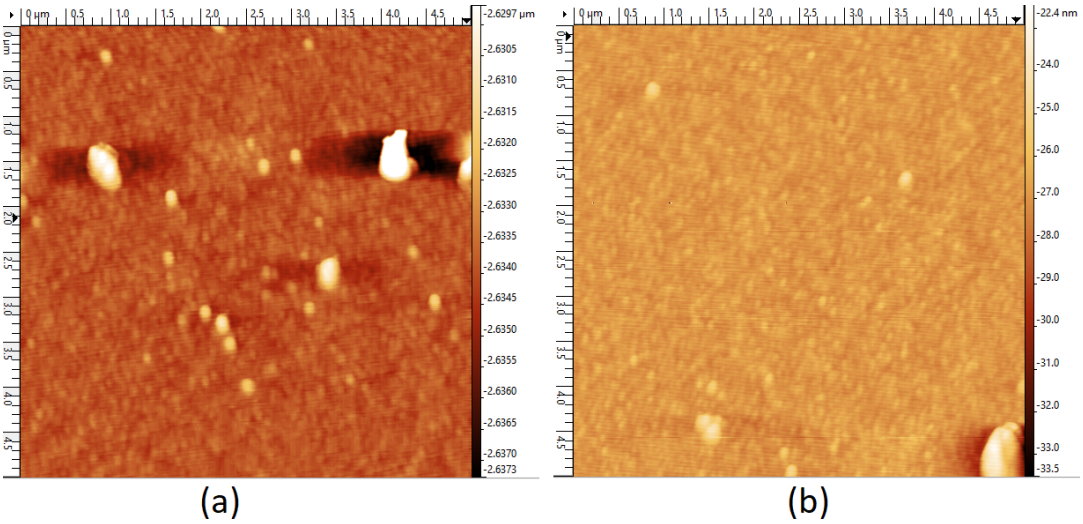

FIGURE 3.44: AFM $5 \times 5\mu m^2$ scan of RT sputtered (z scale 7.6 nm) (a) 100 nm and (b) 240 nm PZT (z scale 11.1 nm)

The outstandingly low roughness of the SG PZT has lead an investigation through a wider area, verifying that it is homogeneous all over the deposited surface, leading to a rms roughness evaluated as 0.24 nm for a $20 \times 20\mu m^2$ AFM scan for PZT grown on Nb-STO, as displayed in figure 3.46.

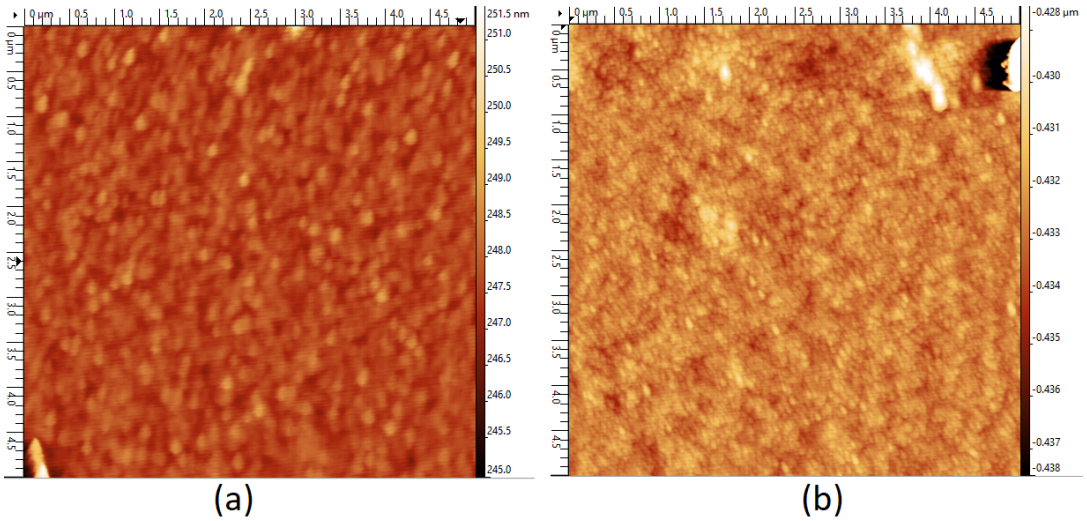

FIGURE 3.45: AFM $5 \times 5 \mu m^2$ scan of sol-gel (SG) (z scale 2.5 mum) (a) 100 nm and (b) 233 nm PZT (z scale 0.01 mum)

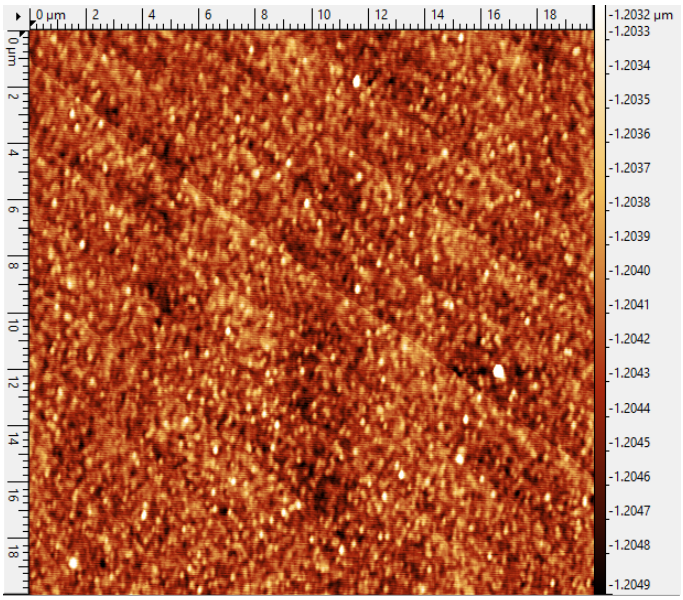

FIGURE 3.46: AFM $20 \times 20\ \mu m^2$ scan of 233 nm PZT deposited by sol-gel technique (z scale 1.6 nm)

In addition Piezoresponse Force Microscopy (PFM) employing doped diamond probes with an elastic constant of about 2.8 $N.m^{-1}$ was used to investigated the piezoelectric properties of the as-grown PZT films on LSMO/STO/Si (001). The ferroelectricity of the materials was tested by PFM technique through the creation of artificial domains by the application of an electric field. As shown in figure 3.47 the writing process with either 10V or -10V between a diamond probe and the LSMO bottom contact has led to two stable states of polarization on PZT films. The writing did not degrade the topography and has lasted for hours. The butterfly-like amplitude hysteresis loop curves evidences the asymmetry on electrodes by a shift around the zero bias voltage axis.

The artificial domains are created by applying +10 V (dc) to a 6x6 μm^2 area, -10 V (dc) to a smaller, typically 2x2 μm^2 area and scanning the larger 15x15 μm^2 surface with 4V ac voltage.

The same conditions of PZT growth by SG method and RT sputtering were used on conducting Nb-STO substrates for thickness effect evaluation. The PFM images are shown in figure 3.48. All the samples exhibit high contrast of stable artificially poled ferroelectric surfaces and excellent ferroelectricity.

PZT by sol-gel had normally exhibited better results with higher achievable amplitudes vs bias voltages values and better contrasts in the PFM images, this was expected since PZT by sputtering can present some distortion in crystallography due to energetic bombardment which does not take place with sol-gel deposited films. However, PZT by RT sputtering had shown very close performance that could be enhanced by choosing to work with a 240 nm PZT thickness for our devices.

Pt layers were finally deposited on the PZT films by sputtering at room temperature and patterned using a lift-off process in order to design top electrodes of $250 \times 250 \mu m^2$ size and to perform polarization hysteresis (P – E) loop measurements, shown in figure 3.49, using a Sawyer-Tower (ST) circuit, driven by a sine wave of amplitude 20 V and frequency 500 Hz. The capacitors were contacted on a Suss MicroTec PM5 probe station. A standard capacitor C_{st} of 22 pF serving as a charge holder, was used during the hysteresis measurements.

The PZT deposited by sputtering at high temperature exhibits a great hysteresis loop, as seen in blue, with low coercive field, Ec, $Pr = 22 \mu C/cm^2$ comparable to a good 180 nm PZT by sputtering 500°C found in literature on Pt/Ti/SiO2/Si as shown in the insert (Bouregba et al., 2003). The room temperature processes have shown smaller but similar remnant polarization and inflated loops indicating a slightly lower quality of the dielectric, where the PZT deposited by sol-gel has exhibited a more important value of E_c.

For the CA656 samples (SG 100 nm and RT 100 nm) the bottom electrode was verified to be somewhat of lesser quality, leading to artificially inflated cycles, this was also a result of the very low thickness of the films resulting in a minor conductance, that required a higher frequency for measurement of the cycles to limit the cycle swelling. For the SG, measured at 5 kHz, it led to $Pr = 21 \mu C/cm^2$ and Ec = 100 kV/cm, and $Pr = 10 \mu C/cm^2$ and Ec =100 kV/cm for the RT sputtering, although the 100 nm thick PZT film has led to a very distorted cycle almost unexploitable. It is better to extract such values from the thicker 200 nm PZT films.

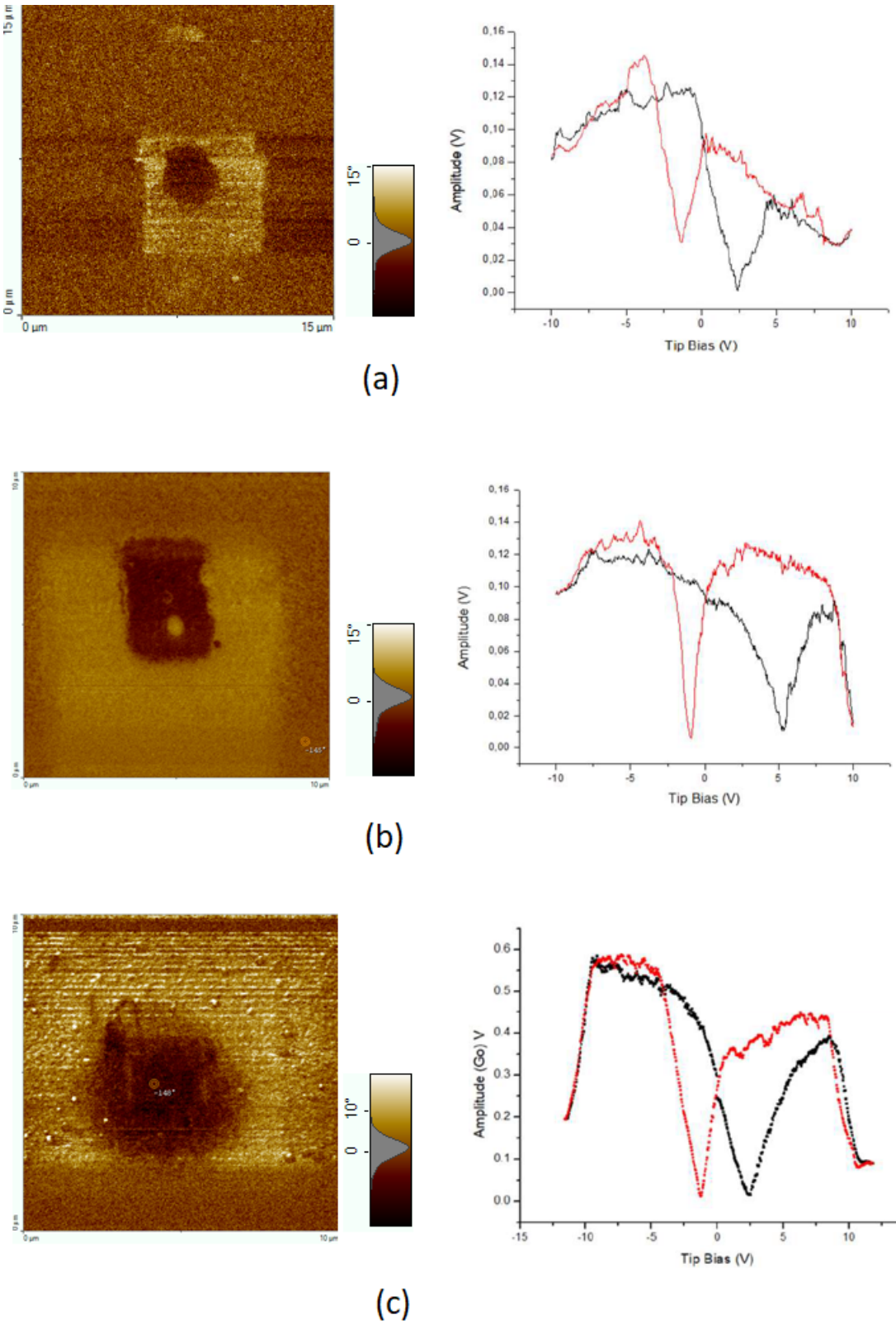

FIGURE 3.47: PFM phase images and amplitude vs. tip bias spectroscopy of (a) 500nm of PZT deposited by sputtering at 600°C, (b) 100 nm of PZT deposited by sol-gel process and (c) 100nm of PZT deposited by RT sputtering on 45 nm-thick LSMO bottom electrode

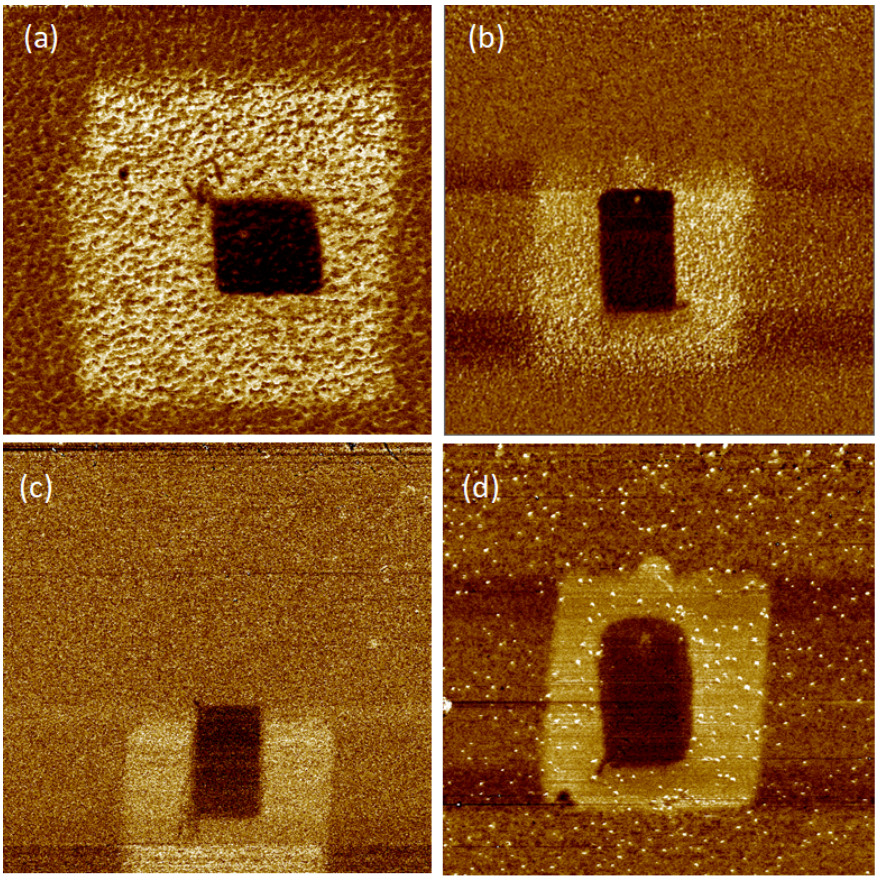

FIGURE 3.48: PFM images for (a) 100 nm SG, (b) 233 nm SG, (c) 100 nm RT sputtering and (d) 240 nm sputtering depositions of PZT on Nb-STO substrates

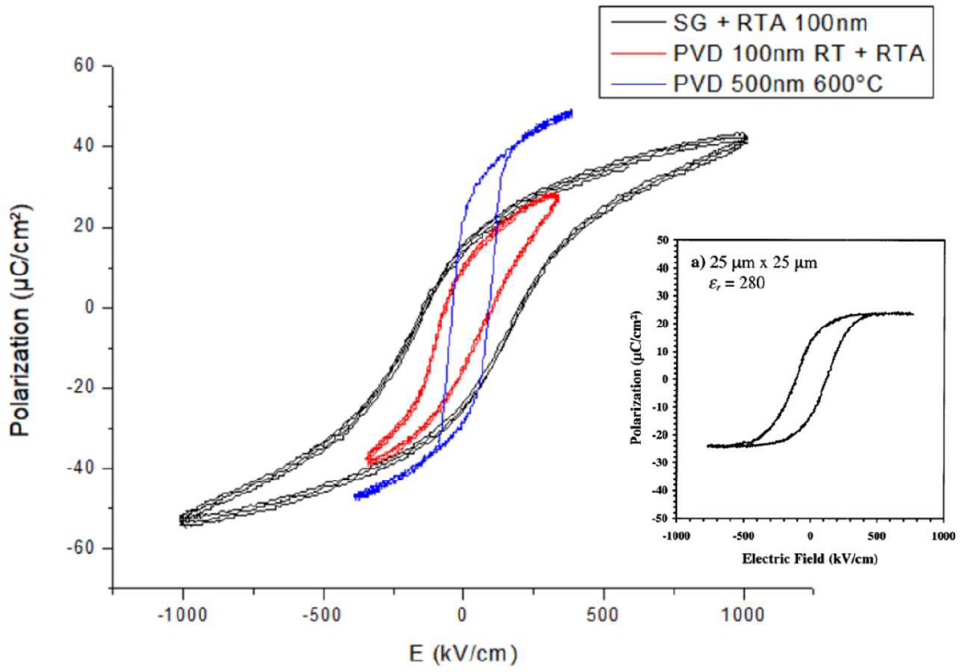

FIGURE 3.49: Polarization hysteresis loop comparison for PZT deposited by sputtering at high temperature, room temperature + RTA and sol-gel + RTA

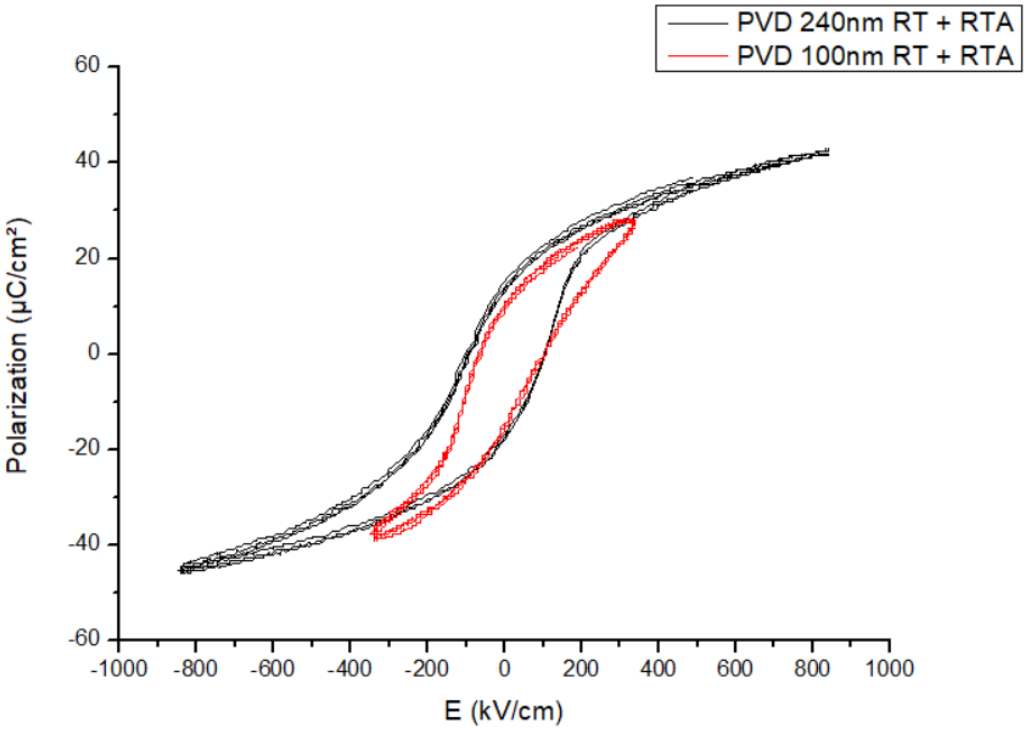

FIGURE 3.50: Polarization hysteresis loop comparison for different thickness of PZT by sputtering RT

For this reason, given the good results for the 230 nm - 240 nm PZT, 233 nm

thick PZT was deposited onto LSMO/STO thin films to explore such heterostructure to be integrated in our devices. Depositions by RT sputtering and SG were again performed in two samples respectively named CA508 and CA660.

The in-plane epitaxial relationship between films and substrate is determined by φ-scans around the (202) peaks of PZT, LSMO and Silicon, shown in Figure 3.51 for sample CA508. A clear four-fold symmetry with 90° peak separation confirms that the PZT/LSMO layers grow in diagonal-on-cube geometry with 45° in-plane rotation on Silicon substrate as do the buffer STO in such substrates, owing to its large lattice mismatch with Si (a_{STO} =0.3905 nm and a_{Si} =0.534 nm) unit cell parameters. The in-plane and out-of-plane hetero-epitaxial relationship between film and substrate can be viewed as PZT[100]//LSMO[100]//STO[100]//Si[110] with the 45° rotation and PZT (001)//LSMO(001)//STO(001)//Si(001) as all epitaxy layers are c-oriented.

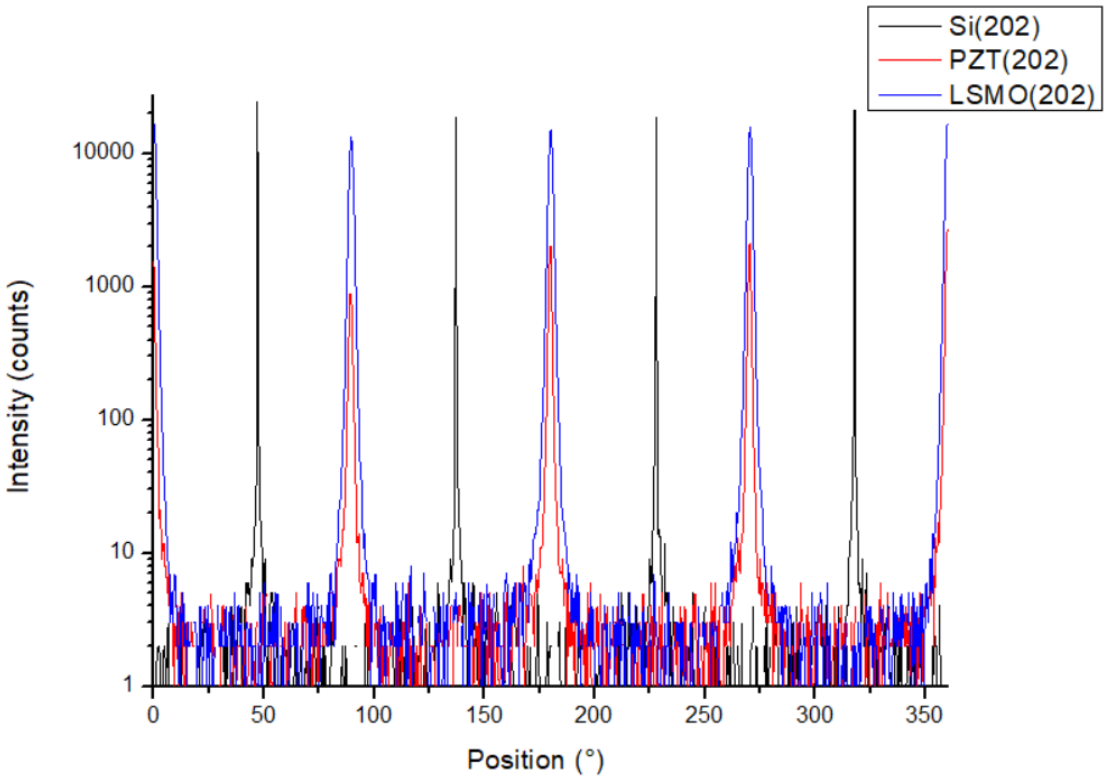

FIGURE 3.51: XRD φ-scan of 240 nm thick PZT deposited by RT sputtering onto NbSTO and (b) 233 nm of PZT deposited by deposited on LSMO/STO/Si by sol-gel method sputtering followed by 650°C RTA with RTA of 650°C

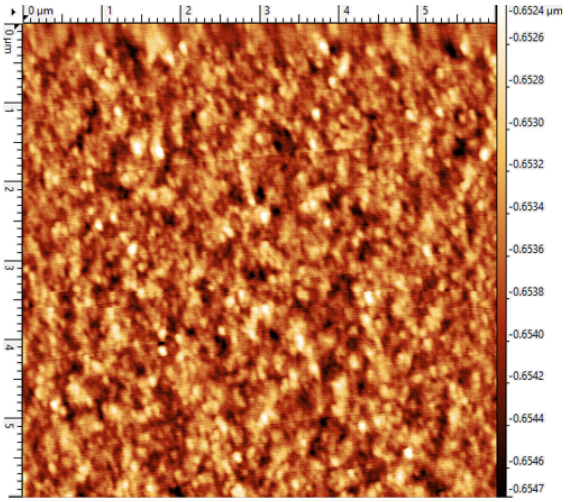

FIGURE 3.52: AFM scan of 6x6 μm^2 area of sample CA660 exhibiting a rms roughness of only 0.37 nm

PFM measurements were performed for both samples and are exhibited in figures 3.54 and 3.53.

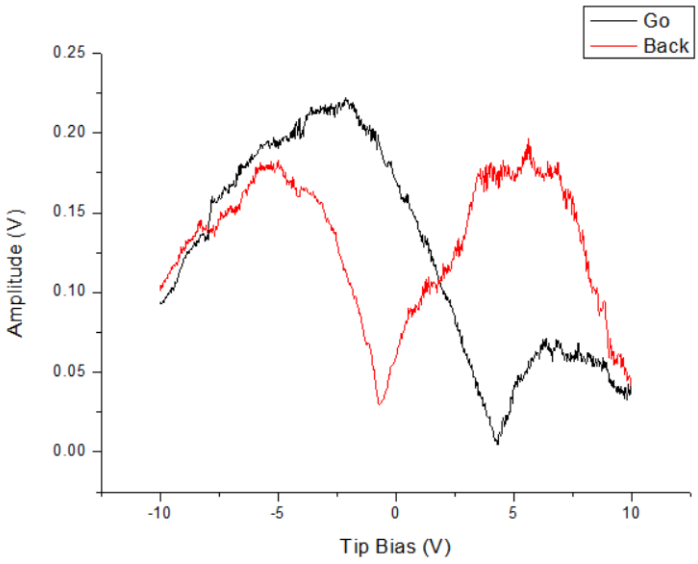

FIGURE 3.53: PFM spectroscopy for sample CA508 exhibiting a typical hysteresis amplitude vs voltage bias loop

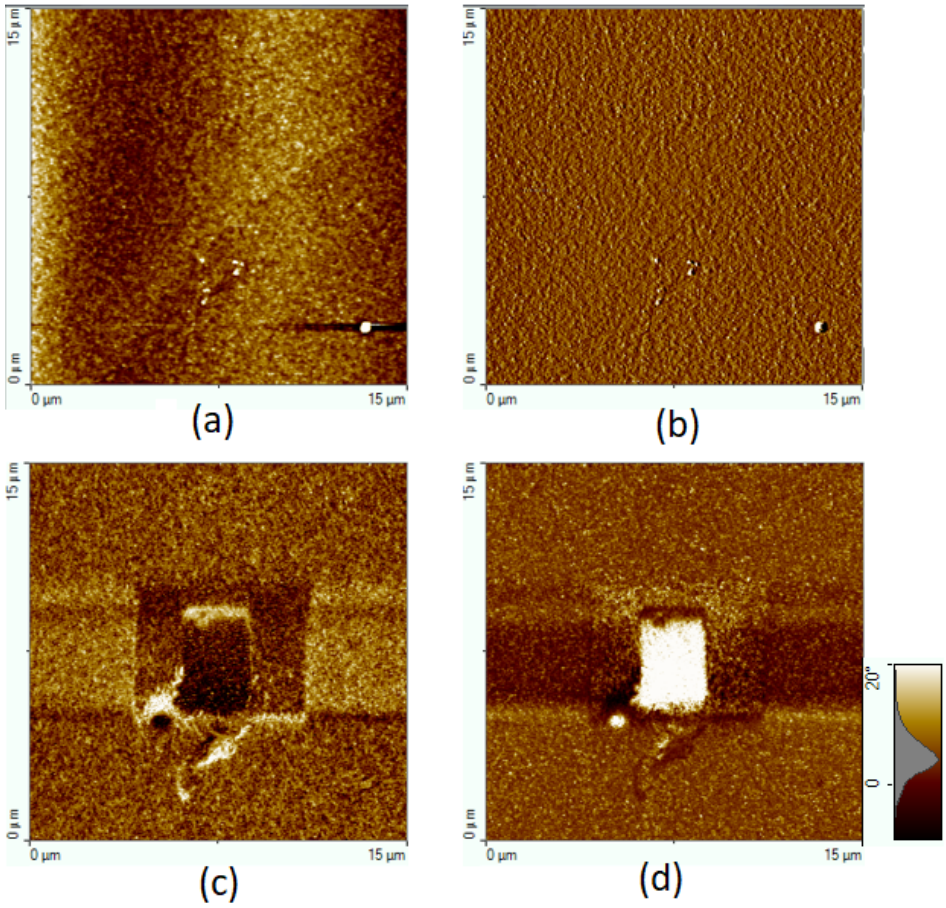

FIGURE 3.54: PFM $15 \times 15 \mu m^2$ imaging of sample CA508 after artificial domains creation with +10V dc applied to a $2 \times 2 \mu m^2$ area and -10V dc applied to a $6 \times 6 \mu m^2$ area exhibiting great contrast for all the defined regions

Both samples were then measured using a ST circuit with a sinusoidal signal at 500 Hz and $E_{max} = 860 kV/cm$ (20V). For the sample CA660 values of Pr = 10 $\mu C/cm^2$ and Ec = 66 kV/cm were obtained with little fatigue up to 10^9 cycles (Pr = 8.9 $\mu C/cm^2$ and Ec = 87 kV/cm). For the CA508, Pr = 16.4 $\mu C/cm^2$ et Ec = 87 kV/cm also with little fatigue at 10^8 cycles Pr = 16.1 $\mu C/cm^2$ Ec = 106 kV/cm and Pr = 15.9 $\mu C/cm^2$, Ec = 103 kV/cm for 10^9 cycles.

The fatigue was performed with a sinusoidal signal of 10 V (430 kV/cm) at 100 kHz, which is considered fast but necessary to be able to measure up to 10^9 cycles.

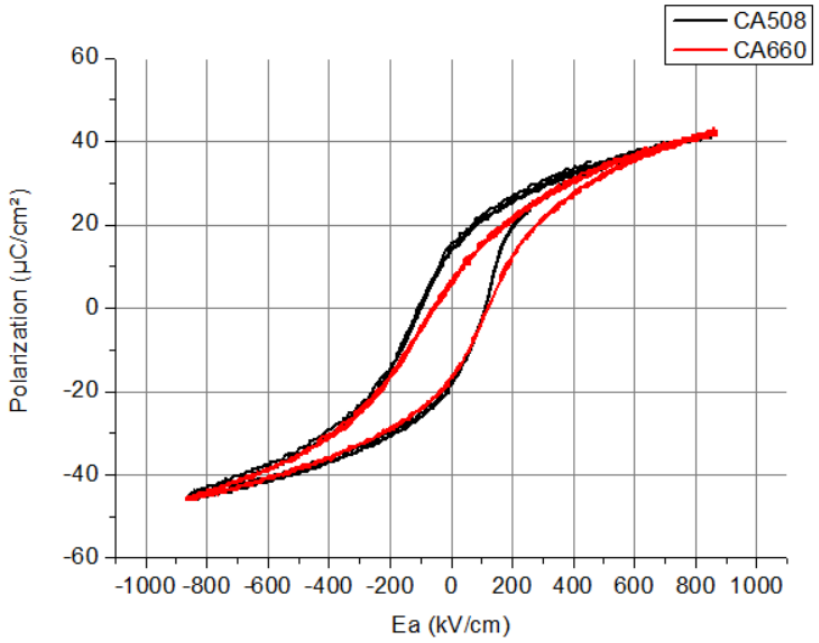

FIGURE 3.55: Polarization hysteresis loop comparison for samples CA508 and CA660

All the PZT films had their dielectric properties compared by patterning Pt circular contacts on top of the films with 100 μm diameter, leading to a $7.85398 \cdot 10^{-9} m^2$ surface, using a ST-circuit with 1 kHz frequency and 50 mV applied between two electrodes. The voltage value was fixed and the respective values for capacitance, loss tangent, real applied voltage and current passing through the capacitor are read at a capacitance meter. From the values of voltage and current, we have calculated the impedance Z, whereas the resistance (and subsequently the resistivity) is evaluated from the loss tangent, as shown in figure 3.56. They have all exhibited good values for ϵ and resistivity. However, as confirmed by the AFM and PFM characterizations, the thicker films with either 233 or 240 nm show better performances than the thinner ones resulting in higher resistivity of the PZT films with equally low tangent losses (reduced dielectric losses within the capacitor).

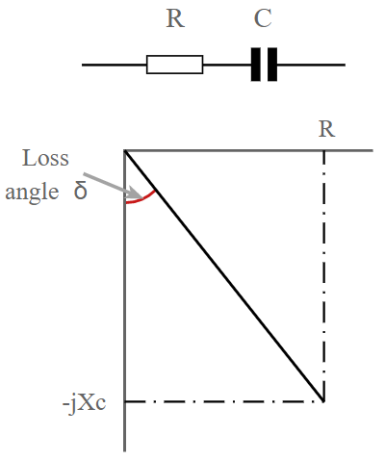

FIGURE 3.56: Schematics of basic equivalent series resistance for PZT capacitor measurements and the definition of a capacitor loss tangent, where Xc represents the reactance of the capacitor in ohms and R its resistance. Extracted from (©, n.d.).

Sample	Thickness PZT (nm)	Cp (pF)	$\epsilon(F/m)$	ϵ_r	$tan\delta$	Z (Ω)	Resistivity ($\Omega \cdot cm$)
CA656_ SG	100	193	$4.91 \cdot 10^{-9}$	555	0.04	$.13 \cdot 10^{5}$	$7.73 \cdot 10^{7}$
CA656_RT	100	283	$7.21 \cdot 10^{-9}$	814	0.01	$2.80 \cdot 10^{5}$	$2.11 \cdot 10^{8}$
NbSTO_SG_1	100	77	$1.96 \cdot 10^{-9}$	222	0.01	$1.01 \cdot 10^{6}$	$7.75 \cdot 10^{8}$
NbSTO_SG_2	233	38	$2.25 \cdot 10^{-9}$	255	0.01	$2.10 \cdot 10^{6}$	$1.57 \cdot 10^{9}$
NbSTO_RT_1	100	91	$2.32 \cdot 10^{-9}$	262	0.01	$8.69 \cdot 10^{6}$	$6.56 \cdot 10^{8}$
NbSTO_RT_2	240	50	$3.06 \cdot 10^{-9}$	345	0.01	$1.58 \cdot 10^{6}$	$1.19 \cdot 10^{9}$
CA660_SG	233	96	$5.70 \cdot 10^{-9}$	644	0.02	$8.41 \cdot 10^{5}$	$3.11 \cdot 10^{8}$
CA508_RT	240	99	$6.05 \cdot 10^{-9}$	684	0.01	$8.13 \cdot 10^{5}$	$6.03 \cdot 10^{8}$

TABLE 3.5: Dielectric properties comparison for the thin films of PZT deposited by sputtering in room temperature and sol-gel techniques

3.5.3 Growth of AlN by PLD

60 nm of AlN thin films were deposited by pulsed laser deposition at the conditions described in table 3.2 on either gold or LSMO bottom electrode. XRD measurements were performed showing highly textured AlN with c-axis preferential orientation when deposited on LSMO/STO films, as shown in figure 3.57. However, the AlN under same conditions deposited on top of a gold surface has shown a diffraction pattern exhibiting many phases, displayed in figure 3.58.

Atomic force microscopy scans were realized as shown in figures 3.59 - 3.60 for surface evaluation.

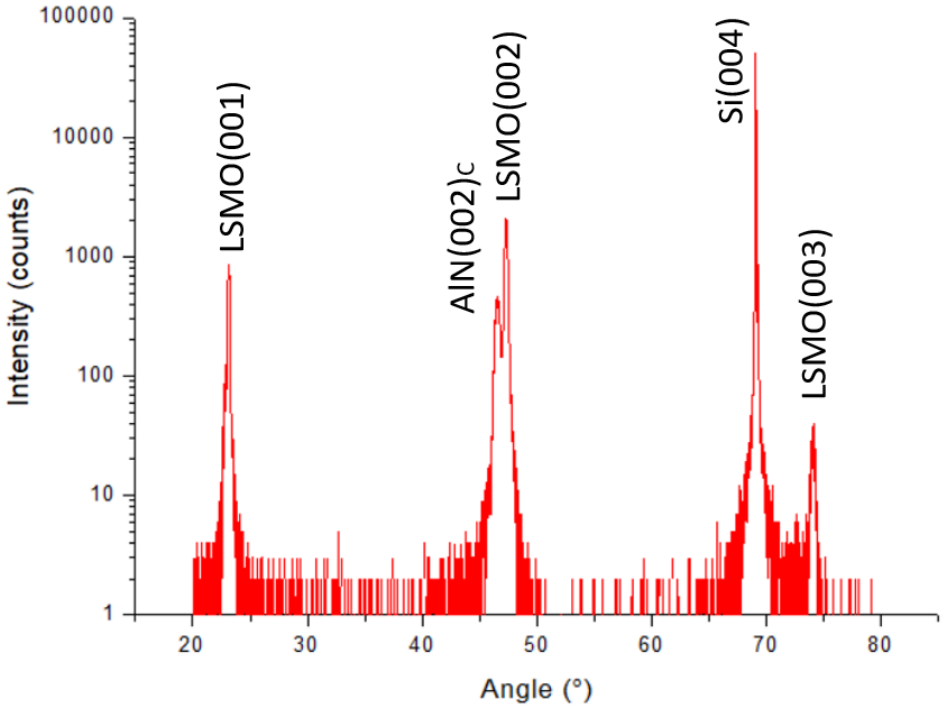

FIGURE 3.57: XRD of 60nm of AlN deposited by PLD at room temperature on 45 nm-thick LSMO bottom electrode

The root-mean-square (RMS) surface roughness of the 60 nm thick AlN thin film grown on top of a gold electrode was $R_q \approx 10.44 \pm 2.6nm$, and $R_q \approx 0.4 \pm 0.07nm$ for the same thickness of AlN grown onto LSMO/STO, as low as the ones found in literature Zhu et al., 2008, both parameters were calculated in Gwyddion under a scanning range of 5x5 μm^2 determined by atomic force microscopy (AFM) in tapping mode.

The atomically flat LSMO/STO surfaces onto which AlN was deposited in the latter case and the high kinectic energies of the ablated growth precursors in the PLD plume have favoured a highly textured c-axis preferential oriented AlN growth with a rather smooth surface even if the presence of oxygen in the bottom electrode may have cause some disorders at the interface level Fujioka et al., 2001. Whereas for the AlN deposited on top of a gold electrode, hexagonal microrods in the wurtzite phase showing planar and morphologically smooth surfaces were identified with an average size of about $5\mu m$, indicating that the base layer of AlN grows as very thin AlN islands, as reported by Sivadasan et al., 2016, that accommodates Al and N atoms in the form of hexagonal microrod structures along $< 0001 >$ direction due to slow growth velocity at low temperatures that leads such atoms to have enough time to move to the lower energy sites (Hua-Jie et al., 2017). The polycrystalline nature observed in XRD pattern indicates the presence of all possible orientation in ensemble of such microrods.

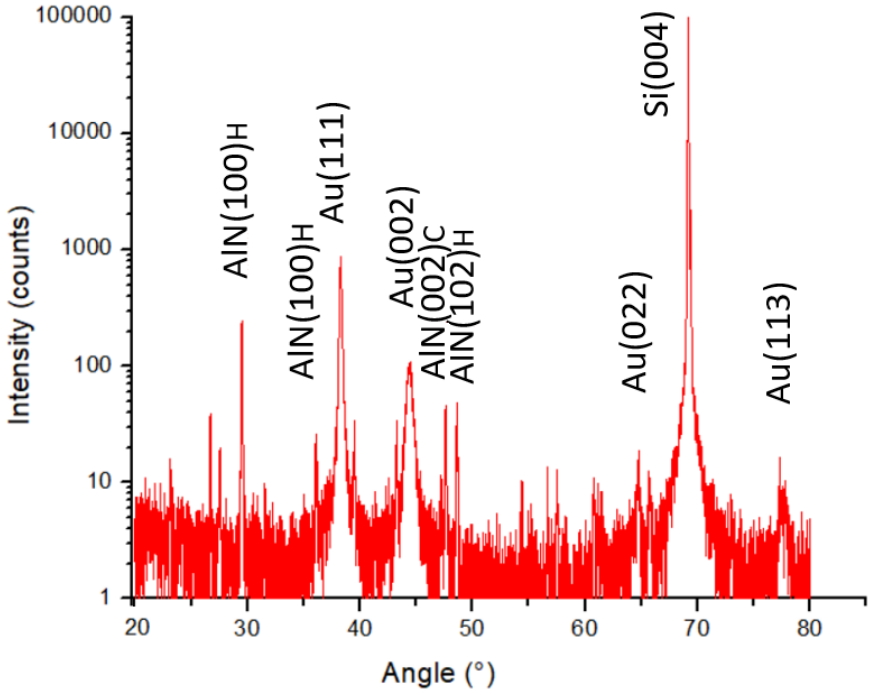

FIGURE 3.58: XRD of 60nm of AlN deposited by PLD at room temperature on 100 nm-thick gold bottom electrode

A crystallographic structural study showing (hkl) planes of (200) and (220) at 2θ values of 45.76 and 67.08 degree, respectively, correspond to the cubic phase of AlN base layers on intrinsic gold.

PFM measurements were performed for both samples either on gold or on LSMO and are exhibited in figure 3.61.

Both loops exhibit similar amplitude values, which allows us to validate the use of LSMO as a bottom electrode for AlN growth, since no such heterostructures were performed by other groups.

3.6 Conclusion

The films deposited by PLD at GREYC laboratory LSMO / STO / Si and mainly LSMO / STO / SOS object of study in this thesis for the further use in devices fabrication were carefully studied structurally and electrically. They exhibit very good quality and the results for SOS substrate are gathered in an article under revision at Applied Surface Science (Chaluvadi et al., 2022).

The integration of the selected piezoelectric materials, namely PZT and AlN, have also led to thin films of great characteristics. The (00l) orientation of the

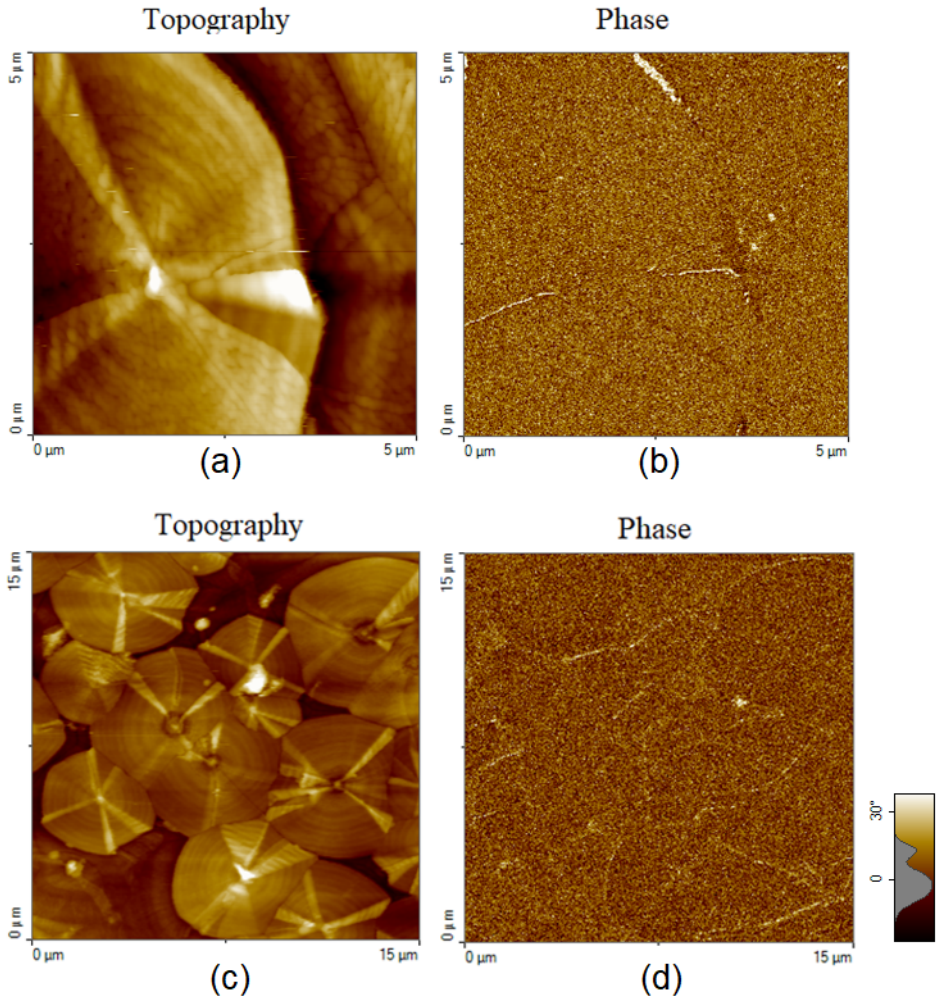

FIGURE 3.59: AFM scan over (a), (b) 5x5 μm^2 and (c), (d) 15x15 μm^2 of 60nm of AlN deposited by PLD at room temperature on gold bottom electrode

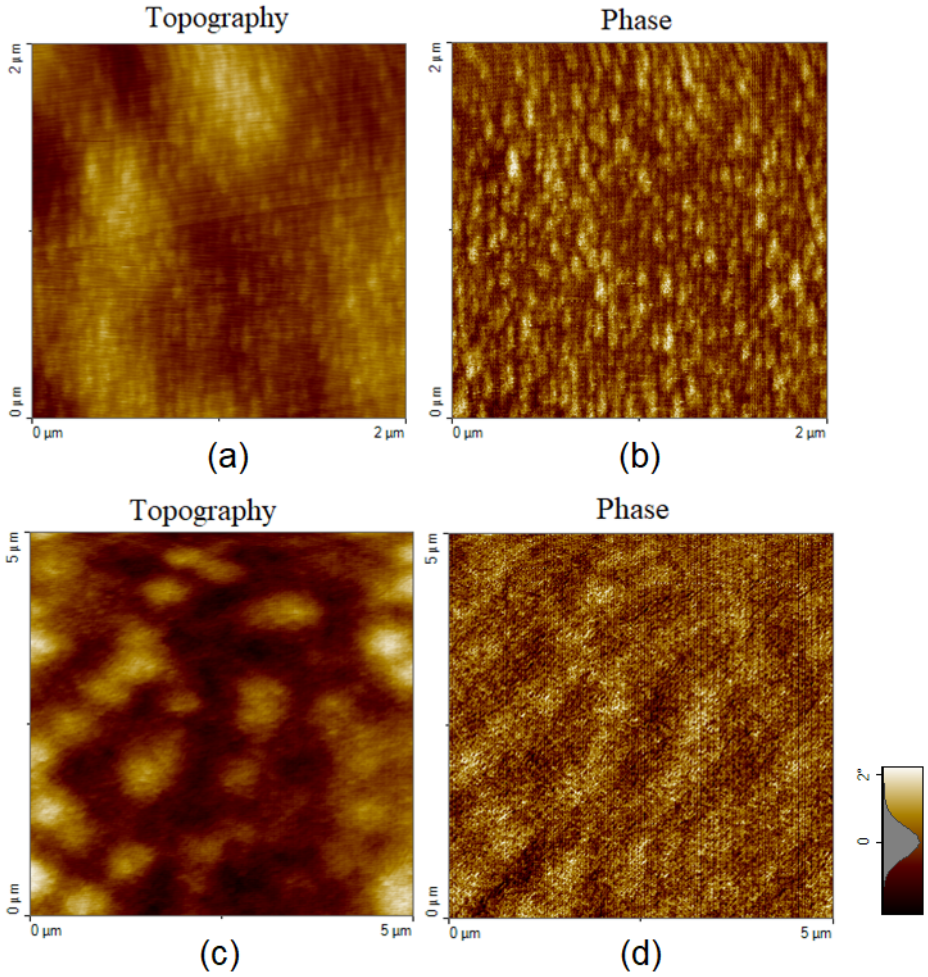

FIGURE 3.60: AFM scan over (a), (b) 2x2 μm^2 and (c), (d) 5x5 μm^2 of 60nm of AlN deposited by PLD at room temperature on 45 nm-thick LSMO bottom electrode

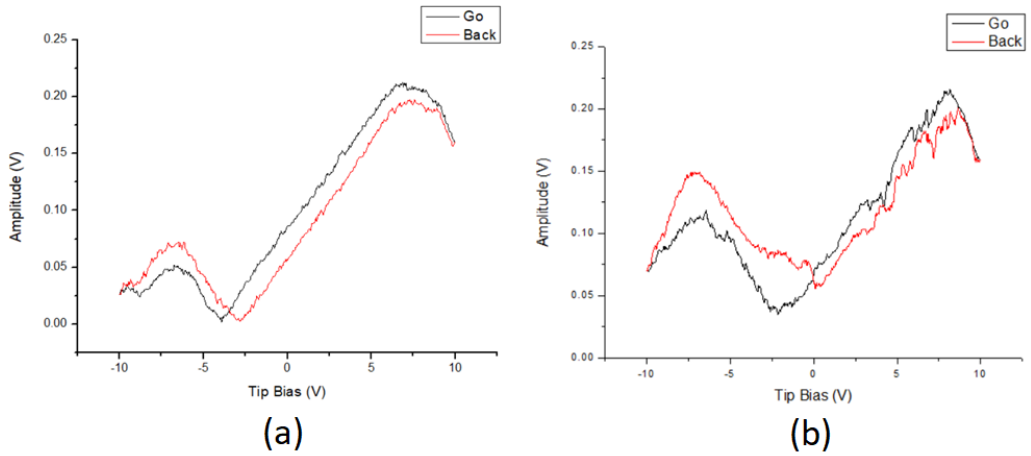

FIGURE 3.61: Spectroscopy amplitude vs bias voltage measurement in PFM for PLD RT deposited AlN on Au and on LSMO

PZT and AlN layers were evaluated by X-ray diffraction showing that we obtained epitaxial films even at room temperature depositions for PZT with RTA for 1 minute in 650°C, which still allows the PZT to be patterned by lift-off process as desired. The films have shown excellent fatigue properties as expected and we were able to measure up to 10^9 cycles. AlN have also shown highly oriented c-axis peaks diffraction patterns and an analysis in AFM have shown that it grows completely different from the microrod formation found when deposited onto gold, which is probably due to a growth in the cubic phase, to match with the LSMO pseudo-cubic structure. In terms of actuation, by using PFM the amplitude vs bias voltage measurements have shown comparable signals either with gold or LSMO bottom electrode, however, smoother surfaces were obtained when grown onto LSMO which may reduce the leakage current due to smaller verified granularities.

I presented the results for both integrations of piezoelectric materials PZT and AlN onto LSMO/STO/Si heterostructure on three virtual conferences as oral presentations in 2021: European Materials Research Society (E-MRS) - 20th to 23rd September, Journées de la Matière Condensée (JMC 2021) - 24th to 27th August- and Symposium on Design, Test, Integration and Packaging of MEMS/MOEMS (DTIP 2021) - 25th - 27th August. For the latter, one article was published at IEEE Explore containing the results for PZT deposited at 600°C (De Araújo et al., 2021). The remaining results are in use for preparation of a second article on room temperature deposition of epitaxial PZT onto LSMO to be submitted in a peer reviewed journal.

Chapter 4

Suspended double clamped LSMO bridges

The advancements in fabrication of high-quality epitaxial oxide thin films by MBE, PLD and sputtering techniques, as described in the previous chapter, allows not only the growth of stoichiometric epitaxial oxide thin films with precise composition but also of artificial heterostructures.

The continuous trend towards low-thermal-budget and low-temperature processing has boosted our interest in developing a full room-temperature integration process of piezoelectric materials into simple bridge suspended structures, apart from the necessary annealing treatments, as described in the next sections.

Three different kind of fabrication are detailed and the corresponding results exhibited in the form of electrical and thermal characterizations as well as static Digital Holographic Microscopy measurements. The influence of processing conditions on the control of the resulting materials and etching rates are discussed.

4.1 Fabrication Process

The fabrication of successful clamped-clamped suspended beams requires at the start point the definition of the very basic parameters such as the substrate choice and the width of the structures to be fabricated. Both parameter of great importance when evaluating the strain effects of epitaxial strain in the LSMO/STO and the Si-based substrates.

In (Liu, 2019) and (Guillet et al., 2019), simple LSMO/STO beam structures were fabricated on Si substrate. Such fabrication requires at first the deposition and definition of gold contacts by lithography to enable the future contacts for the LSMO layer. To enhance the fabrication yield, a protection film may be deposited on top of the LSMO beam, to increase its hardness, this is generally done by a layer of amorphous STO deposited by PLD at room temperature in order not to degrade the

LSMO electrode - which has been verified when a layer of Al_2O_3 is directly deposited by ion beam deposition (a high energetic deposition method). The bridges' patterns on LSMO/STO are then defined and etched vertically using an ion beam etching process followed by their release from the silicon substrate, using the same mask, in SF_6 plasma using reactive ion etching technique. The parameters are set to favour the lateral etching of silicon in comparison with the depth.

The length of the bridges are typically defined as 50, 100, 150 and 200 μm in order to have a more global understanding of our results also as a function of bridge length.

Simple 4 μm-large 45 nm-thick LSMO on STO simple bridges were fabricated by (Liu, 2019) using a silicon substrate as shown in the schematics in figure 4.1. However, the release of the epitaxial strain has led to an observed curvature on the bridge's transverse profile, observed in Figure 4.2, that highly increases its resonant frequency detection.

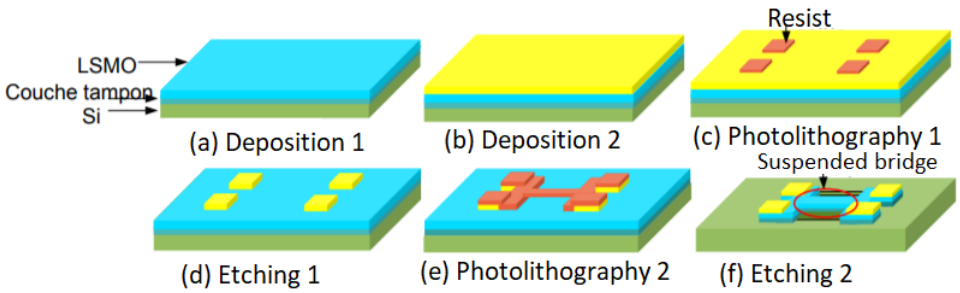

FIGURE 4.1: Complete fabrication process for simple bridge structures on LSMO / STO / Si. Extracted from (Liu, 2013a)

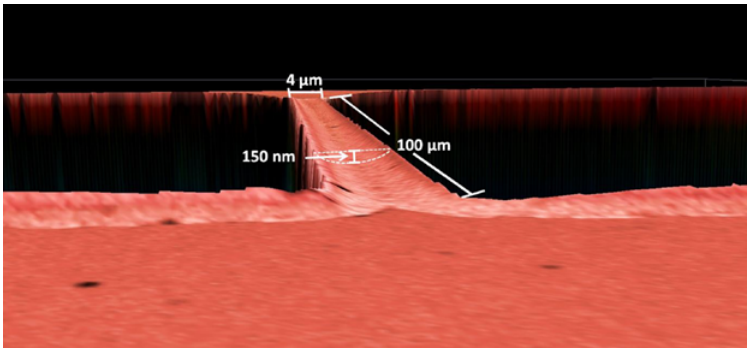

FIGURE 4.2: Confocal image of simple LSMO/STO suspended bridge. Extracted from (Liu, 2019)

The difficulty linked to work with suspended structures of such materials subjected to high residual strains is, first of all, related to the intrinsic difficulty of fabrication itself: the release of the materials from substrate can lead to the breakage of the bridges if the residual strain is too high. However, even in the case where

fabrication is successful, a second problem may take place: if any cracks are present in stress concentrated points, they may propagate along crystal directions since the materials are epitaxially grown and the device can break during operation. Hence, to ensure a better performance of the device as well as to guarantee that its resonant frequency detectability lays in typical vibration meter equipment, it is of high interest the flatness of the suspended beam. Since it's a resultant effect of the epitaxial strain release, the use of Silicon On Insulator (SOI) substrates was seen as a promising idea due to the possibility of keeping, as a part of the suspended structure, a thin layer of Si as well, retaining the epitaxial strain of the top films and rendering the structure flat with a lower resonant frequency. The other approach is to use Silicon-on-Sapphire (SOS) substrates to keep the residual strain in slightly lower levels.

The choice of substrates, as described in chapter 3, thus gives rise to three techniques adapted to each of them for the manufacturing process. First of all, a 20 nm epitaxial buffer layer of $SrTiO_3$ (STO) is deposited by MBE (Molecular Beam Epitaxy) at Cornell University (USA) in all Si-based commercially available substrates, as discussed in the previous chapter.

The wafers were then diced into several 10×10 mm^2 substrates for the subsequent deposition of an extra 6 u.c. STO layer to obtain a clean surface and 30 or 45 nm thick $La_{2/3}Sr_{1/3}MnO_3$ (LSMO) films by PLD equipped with in-situ reflection high-energy electron diffraction (RHEED) at the GREYC laboratory located in Caen, France. A KrF excimer laser of $\lambda = 248$ nm and laser repetition rate of 1 Hz was used.

Such heterostructures are the depart point for the three different fabrication technology branches we developed. Each one will be further explained separately in the following sections.

4.2 Methods and calibration

4.2.1 Gold contacts

GATAN model 682 PECS (precision etching and coating system), shown in figure 4.3, is a sample preparation technique for SEM and TEM specimens that provides the possibilities of uniform coating of films, etching and cleaning contaminated surfaces of the samples. In this thesis, I used GATAN exclusively for the Au contact depositions for the top pads on the devices for electrical measurements.

Target	Voltage (keV)	Current (μA)	Pressure (Pa)	rpm	Time (s)
Au	10	614	4×10^{-3}	40	600

TABLE 4.1: GATAN PECS gold deposition parameters. The same parameters are also used for Cr and Al_2O3, resting only a function of the time to achieve the desired thickness

FIGURE 4.3: Front view of the precision etching and coating system used at the clean room at GREYC laboratory

After sample insertion into the chamber and vacuum achieved in the order of 10^{-6} Torr, the ion canons, pointed towards the target with a 45° angle, are fed with a high voltage and currents and the pressure inside the chamber is adjusted to 5×10^{-3} Pa. Once the current is stable in both the right and left canons, Argon (Ar) is introduced into the chamber to be ionized in Ar^+ due to the presence of high currents. The Ar^+ ions are then directed towards the target for bombardment, a physical action that removes the material and deposes it onto the substrate located at 45° below.

Both the deposition rate and the thickness of the film are controllable by adjusting the power of the ion canons which can vary from 1 keV to 10 keV and the current that passes into canon guns focused onto the target, since this determines the strength of the physical action between the target and the Ar^+ ions. The parameters used in deposition is displayed at Table 4.1. The deposition rate for the gold coating under such conditions is about 8 nm/min.

4.2.2 UV photolithography

The patterning of structures in microfabrication context consists of the transfer of a motif to a photosensitive material, typically photoresist, by selective exposure to a

radiation source to change its physical properties at the exposed areas, namely, its chemical resistance to developer solution.

The photoresist we use for our lithography processes is the Shipley S 1813 a positive resist, i.e., the exposed material is etched away by the developer whereas the unexposed area is resilient. Its use goes far beyond a temporary mask for etching an underlying layer as we often also employ the photoresist as a template for patterning deposited materials after photolithography, as is the case for our piezoelectric actuators/detectors, to subsequently etch the resist away in a process called *lift-off*.

The first lithographies were performed using the MJB3 Suss Microtech Mask aligner for UV photolithography with a physical mask, as shown in Figure 4.4. This equipment allows the alignment between mask (constituted by a glass plaque with the patterns on chromium) that is hold under vacuum and the sample cautiously placed as aligned as possible to require in a second moment just the fine offsets and rotations alignment with the screw axis. The resolution is defined by the kind of contact selected. Once mask and sample are on contact, they are exposed using a UV lamp (400 nm) of high intensity (350 W) for around 6 seconds for the LSMO patterns.

Aiming better resolution and process simplicity, the same patterns for the complete structure were then realized by laser photolitography MicroWriter ML®3 Pro from DMO acquired in july 2020 at GREYC, as shown in Figure 4.5, which offers the possibility to modify the mask (designed in either KLayout or CleWin) accordingly to the adaptations for each fabrication process, since it is hold in software: instead of illuminating the sample through a physical mask, such direct-write lithography project the exposure pattern directly onto the photoresist by computer-controlled optics. This provides to the process greater flexibility as it can be rapidly modified at no cost and better reliability of performance.

Layers of resins up to several hundreds of microns can be written with a single laser sweep, thanks to several optical treatments that guarantee a very large depth of focus. The track surface slope and a focus lock is performed by automatic system selection of a number of locations across the exposed area to locally measure the surface height interpolating all other exposure locations from these previous measures to which small corrections may be added in real-time during the exposure to prevent distortions by loss of focus in varying topography (one of the limiting factors of MEMS lithography, due to presence of high aspect features).

The alignment structures consist of $20 \times 20\ \mu m^2$ squares distributed around the $10 \times 5\ \mu m^2$ sample transferred to the sample along with the first pattern to be used as reference for positioning and correcting fine offsets in rotation for the subsequent layers design. A Virtual Mask Aligner mode is at disposal and it displays the pattern to be exposed on top of the real-time microscope image, as a traditional

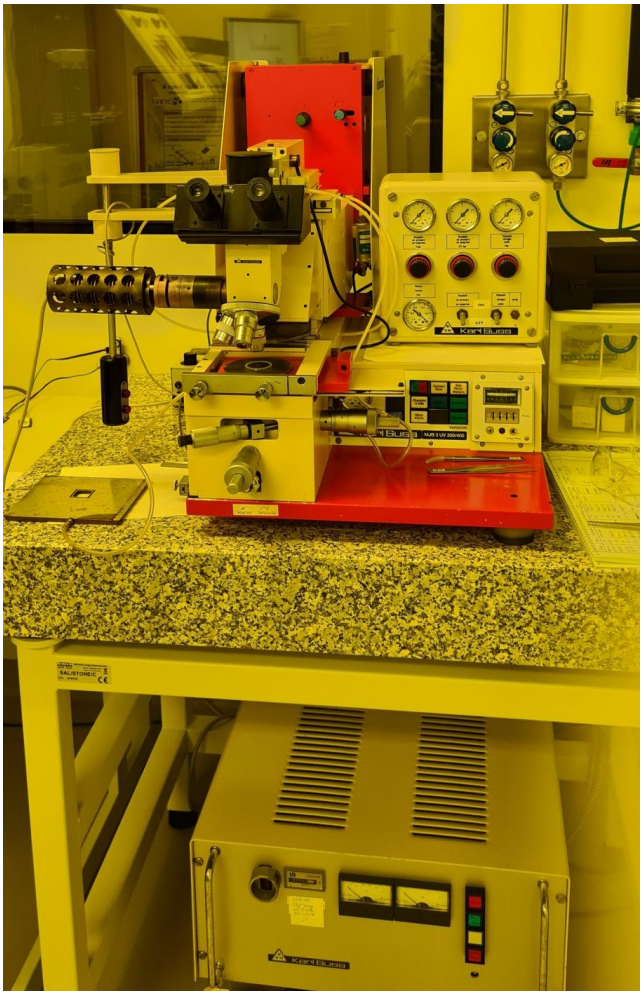

FIGURE 4.4: MJB3 Suss Microtech Mask aligner for UV photolithography system

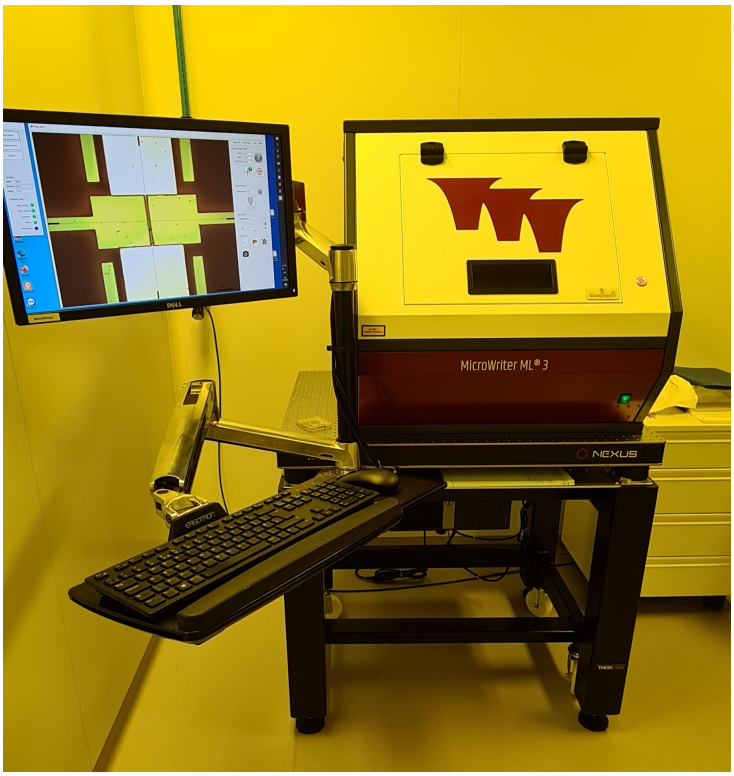

FIGURE 4.5: MicroWriter ML®3 Pro

Material	Dose	Exposition (mJ/cm^2)
LSMO	0.7	150
Au/LSMO	1.2	100
Au/AlN/LSMO	0.9	100
PZT	0.8	150

TABLE 4.2: Tested doses for each material lithography illumination

mask aligner.

The accuracy of the pattern transfer from the mask to the resist, however, depends on the wavelength of the radiation source and the dose required to achieve the desired change of properties in the photoresist. Once the physics of the exposure process plays a major role in affecting the dose actually received (a highly reflective bottom layer may result in the photosensitive material experiencing a more important dose from the addition of incident and reflected radiations in comparison to an absorbing underlying film, resumed to one path) prior to lithography we have performed test doses for all the used materials in this thesis as exhibited in Table 4.2.

The complete lithography is characterized, nevertheless, as a sequence of process steps as listed below:

1. **Dehydration bake:** to improve adhesion by achieving complete evaporation of solvents through annealing process for 5 minutes at 90°C;

2. **Resist spin coating:** the sample is centralized and safely positioned for rotation held under vacuum, for droplet application of a positive photosensitive resin (S1813), such that the UV-exposed parts are soluble in a soda-based solution. The rotation is carried out with a spinner with predefined speed of 4000 rpm during 40s to evenly spread the PR by centrifugal force.

3. **Soft bake:** the sample is again put in the hotplate at 90°C for 5 minutes in order to drive off some of the resist's solvent to make it more viscous, resulting in its significant loss of mass and consequently thickness.

4. **Alignment and exposure:** patterns on mask are aligned to specific features on samples, proceeding to the exposure to cause selective chemical property change in the resist.

5. **Develop:** after the pattern transfer through exposure, the sample is immersed in developer solution during 40 seconds while stirring to make sure all the edges are well defined. This process removes the exposed resist keeping only the designed structures that will be ready for the subsequent steps, namely, material deposition or etching. The sample is then rinsed in deionized water for at least one minute to stop the development process.

4.2.3 Etching techniques

Etching, defined as the removal of unwanted material from substrates, is an essential step in fabrication of any micro-(nano-)devices and can be classified in two types: dry and wet etching. The former, as suggested by its name, is performed in a dry environment and the etching process can vary as one can use plasma etching, reactive gaseous species, physical bombardment, etc. For my fabrication process, I used mainly Ion Beam Etching (IBE) and Reactive Ion Etching (RIE), further described in the next topics, but also chemical etching with KI and HF.

The etching process can be isotropic or anisotropic. It is said to be anisotropic when a preferential direction is observed, such as by IBE. The isotropic etching is obtained when all crystallographic directions are attacked with equal speed. We used a change in parameters in RIE to obtain both types for Si substrates.

As for the wet chemical etching, it is a process done in a bath of liquid phase etchant. The basic principle lies in the dissolution of the material to be removed by immersion into appropriate chemical bath, however, the process simplicity compared to dry etching is generally accompanied by a lost in precision and control. Hence, this process was kept exclusively for the gold pads etching for the LSMO contacts.

KI solution

The bigger contact pads on gold necessary to connect the bottom electrode, LSMO, to a PCB for electrical characterization don't require an exceptional resolution and can be etched by a wet method. Gold etchants are solutions based on potassium iodide and iodine (KI/I_2) chemistry and compatible with both positive and negative photoresist materials.

A KI solution was prepared using 1.2 g of iodine (I_2), 4 g of potassium iodide (KI) and 20 ml de water mixed with magnetic rotation for about 10 minutes. The gold and iodine form gold iodine which solubility can be improved by adding KI to the solution and, if necessary, the etch rate can be reduced approximately 50% by adding 1 part deionized water to 2 parts etchant. Other halogenides can substitute the iodine/iodide with exception of fluorine which does not form soluble gold compounds, but we kept the same recipe for all the fabricated structures. The chemical reaction that takes place is the following:

$$2Au + I_2 \rightarrow 2AuI \tag{4.1}$$

The sample with the patterned contact pads was then put into the KI solution for 30 seconds. It is important to move the sample for the whole time because if the etchant at the surface becomes saturated while a fresh etchant cannot reach the sample surface the etching will slow down. Therefore, stirring the sample will cause the etchant to be brought to the surface promoting the maintenance of etching.

The etchant with our selected mixture ratio etchs gold in room temperature with an etch rate greater than 200 nm/min.

Once the etching is completed, the sample was carefully transferred to deionised water to rinse the etchant away for about 1 minute. The sample was again transferred to another beaker with DI water for another 1 minute rinse. Once this was done, the sample was placed on a flat surface and dried by blowing with nitrogen gun.

A microscopy inspection with red filter was performed to make sure that it doesn't show any traces of unetched gold and the sample was then ready for the next lithography step.

Buffered Hydrofluoric Acid (HF) wet etching

Hydrofluoric Acid (HF) solution is a well-known etching mechanism for silicon dioxide, SiO_2, either as a pre-treatment for native oxide cleaning or for its common use as sacrificial layer in surface micro-machining.

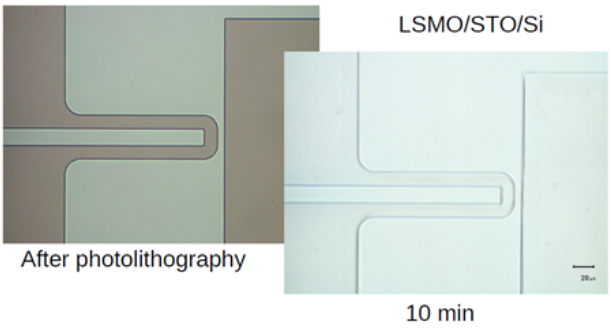

FIGURE 4.6: $6\mu m$ LSMO/STO/Si cantilevers before and after a 10 minute bath in buffered HF solution

The chemical reactions that occur are

$$SiO_2(s) + 6HF(l) \rightarrow 2H_2O(l) + H_2SiF_6(aq) \tag{4.2}$$

$$SiO_2(s) + 4HF(l) \rightarrow 2H_2O(l) + SiF_4(aq) \tag{4.3}$$

Etch rate, however, is known to increase with HF concentration and the reactivity of SiO_2 is reduced with annealing or densification of the grown oxide, as is the case of quartz that is soluble in HF while coesite (the densest form of SiO_2 at 3.01 g ml^{-1}) is insoluble in the same solution (Monk, Soane, and Howe, 1993). It has been shown that increasing boron dopant concentration in HF acid can increase the etch rate, in such a way that, it has been used as a calibration factor to measure the boron concentration in an oxide film (Schwettmann, Dexter, and Cole, 1973), (Pliskin, 1968).

Since the plasma etching of SiO_2 in RIE is extremely time consuming, we decided to proceed with the silicon dioxide removal by buffered HF bath. Nevertheless, for our HF solution, we estimated an approximated etch rate of 0.3 nm/min for the buffer STO that was completely etched away after a 10 min HF immersion as exhibited in Figure 4.6, whereas the it took about 30 min for the 2 μm SiO_2, an etch rate greater than in RIE with CHF_3 plasma with a roughly estimated ratio of 4.

To protect the bottom STO from being etched causing the release of the top LSMO layer, Aluminum Nitride (AlN) was chosen as protection layer due to its excellent chemical stability and possibility to actuate as both protection layer during HF bath in fabrication process and as actuator/detector of final device. After the wet etching, the samples were placed in ethanol to facilitate the liquid evaporation after the process. However, due to strong Van der Waal forces, *stiction* was generally verified by the pull down of the center of the freestanding beams by capillary forces during drying and characterizes the main problem in such process, risking

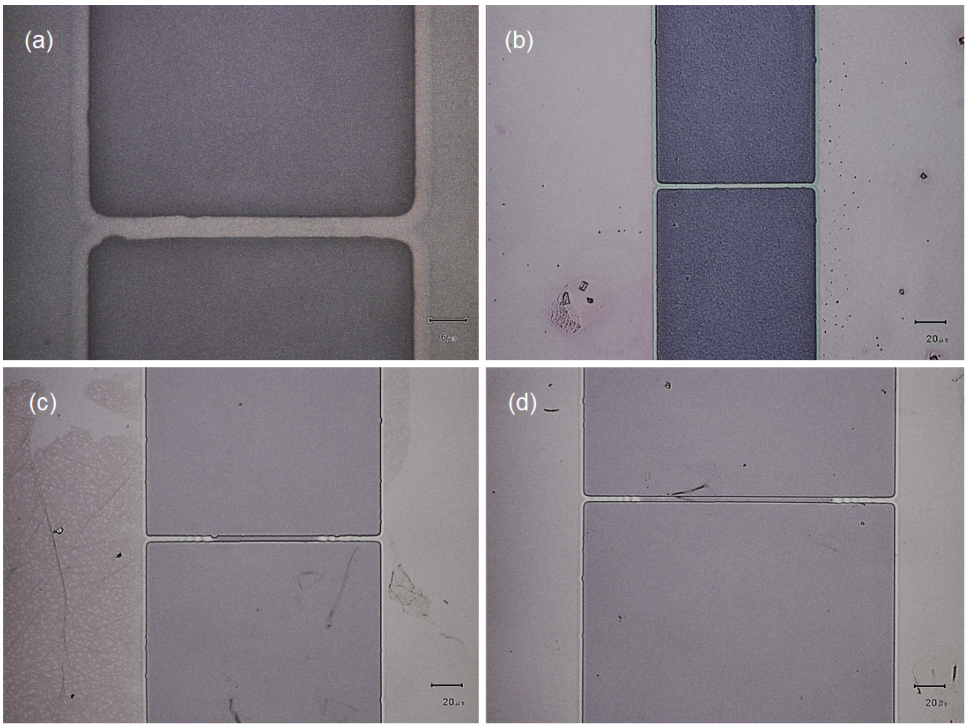

FIGURE 4.7: 4 μm bridges suspended by HF wet etching of the sacrificial layer SiO_2 showing successful release for 50 and 100 μm long bridges and stiction for 150 and 200 μm long ones

the collapse of the suspended structures.

This is shown in Figure 4.7 for 4 μm bridges suspended by the removal of the sacrificial layer SiO_2 and characterizes one of the main problems in MEMS fabrication when wet etching is used to release the structure from substrate.

Stiction in surface micromachining takes place when adhesion forces between fabricated structures and substrate are stronger than the restoring elastic forces. It is observed when contacting surfaces roughness approach the nanometer scale and whereas sometimes desired in semiconductor industry for bonding purposes, it is a notorious source of MEMS malfunctioning.

When the internal pressure of the liquid is lower than outside then the solids are pushed together by pressure forces, bridged by the liquid.

The silicon treatment with HF leaves the silicon surfaces hydrophobic with either H or F termination, which favours the hydrogen bonding (dipole-dipole attraction in which the hydrogen atom in a polar molecule interacts with an electronegative atom of an adjacent molecule) and the dispersion van der Waals attraction forces between two hydrophobic surfaces.

When silicon passes through an HF treatment without a subsequent DI water rinse, its surface dangling bonds are mainly terminated by hydrogen, however,

a significant amount of fluorine (about 0.12 of a monolayer) can be detected in the surface as reported in (Tong et al., 1993). The DI water rise allows a drastically decrease in the number of Si-F bonds degrading the bondability of the hydrophobic Si surfaces due to the smoothness of an buffered HF silicon substrate: Si-F bonds are located mainly at chemical reactive sites such as atomic steps and surface defects in such a way that a small roughness surface leads to depletion of Si-F bonds and smaller probability of bonds.

Such stiction problems could also be avoided by using HF vapours to isotropically remove the unwanted portions of SiO_2. However this approach results in low etching rate (even lower than the one achieved by RIE if the same concentration of HF is used) as exhibited in Table 4.3 and the best results are only achieved in a very narrow temperature window.

HF	Material	Etching rate	Temperature
10%	SiO_2 lateral	≈100 nm/min	20°C
10%	SiO_2 depth	≈50 nm/min	20°C
10%	STO lateral	≈300 nm/min	20°C

TABLE 4.3: Etch rates for buffered HF etching of SiO_2

At last, the release of structures could be guaranteed if a critical point dryer were used. A process that not only releases, but also cleans and dries flexible structures based on avoidance of tangencial forces caused by surface tension during evaporation by working, as the name says itself, in the critical point where physical characteristics of liquid and gases are indistinguishable and the compounds can be converted in either one without ever crossing the interfaces between liquid and gas.

An important point to keep in mind is that HF acid nevertheless extremely dangerous if ever in contact with the skin and a formation was necessary before any manipulations and all the personal protective equipment were used in maximum security as listed in Figure D.1 in appendix D. The workstation handling, waste disposal and actions in the event of an accident were some of the topics covered. The handling of vapour HF would require additional safety precautions, another reason why it wasn't a desired option.

If needed, HF can be neutralized with potassium hydroxide (a base) and water. A reaction that produces potassium fluoride salt and water.

For the etching performed at room-temperature, a difference between lateral and thickness etch rate was evidenced being normally of 2:1. Lateral etching was measured by successive etching steps of 8 μm large bridges, where the unetched part

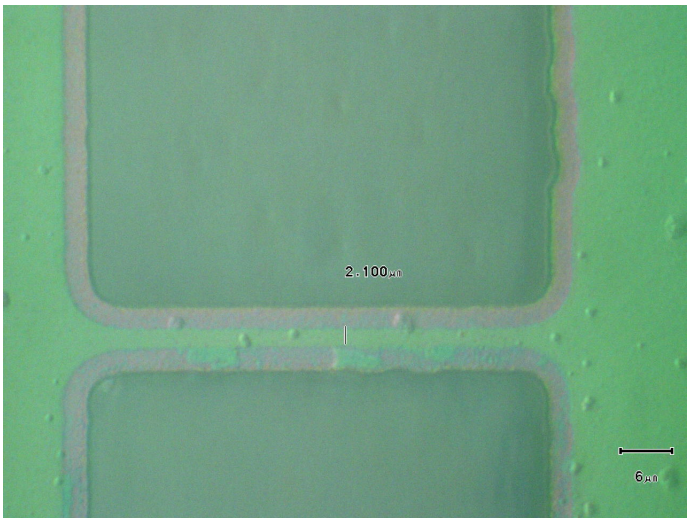

FIGURE 4.8: SiO_2 lateral etching evaluation after 30 minutes in HF bath at 20°C

was measured as shown in figure 4.8 by optical microscopy.

The thickness etching was measured by mechanical profilometer, but also by DHM as shown in figure 4.9 to have a better understanding on the different etch rates by evaluation of the patterns on surface of partially etched SiO_2, as seen in figure 4.10.

Such difference in preferential etching planes is seen in figure 4.10 where the reaction by-products exhibit low diffusivity in the native oxide, resulting in mainly lateral diffusion leading to the observed patterns on the SiO_2 surface. The evaluated thickness etch rate was of about 50 nm/min while of 100 nm/min for lateral etching.

Material	Etch Technique	Etch Rate
SiO_2	RIE	17 nm/min
SiO_2	HF	50 nm/min

TABLE 4.4: Comparison for SiO_2 etching in HF acid bath and RIE dry etching technique, shown to be almost 3 times faster.

Ion Beam Etching

Ion Beam Etching (IBE) is a widely used technique capable of etching a large range of materials during fabrication process. The reason due to its purely physical sputtering principle of operation that allows the removal of any material not protected by the resist by collision of a mono-energetic beam of Argon accelerated and directed ions from an ion source. This technique enables excellent profile control thanks to a variable etch beam angle relative to sample surface features. It is used for my process to etch LSMO and STO when fabricating simple bridges. This has shown an

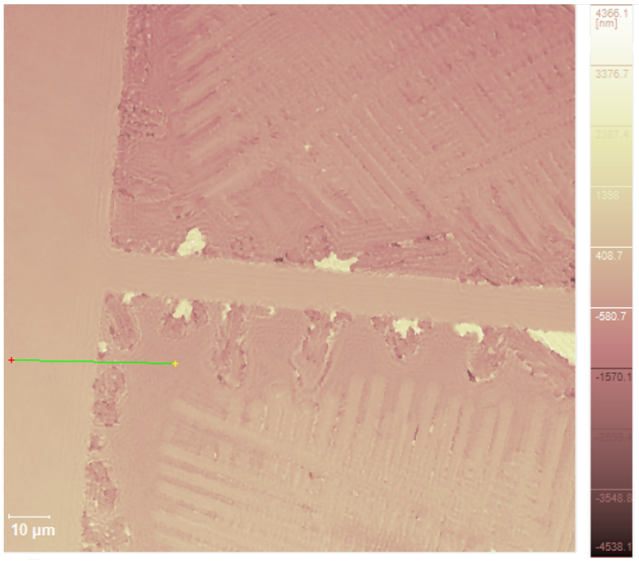

FIGURE 4.9: SiO_2 etching rate (depth) after 10 minutes in HF bath at 20°C

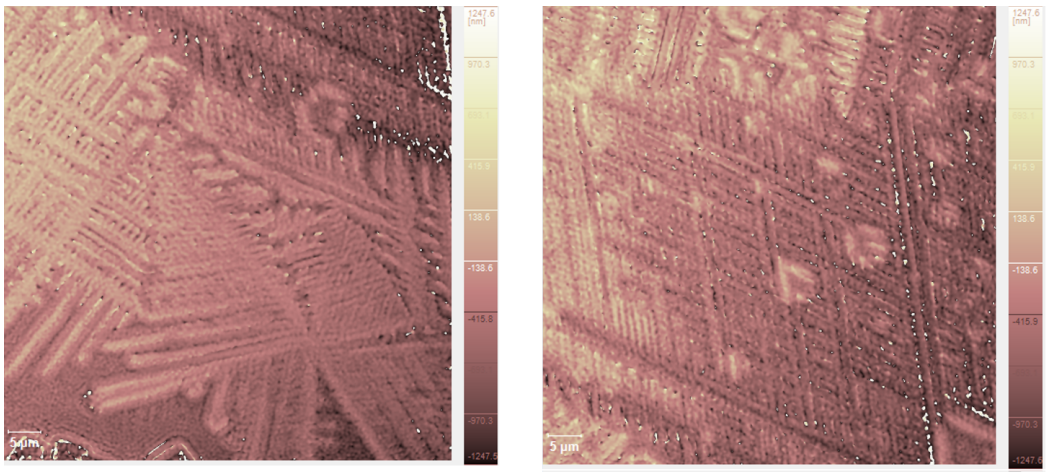

FIGURE 4.10: SiO_2 surface etching patterns after 10 minutes in HF bath at 20°C

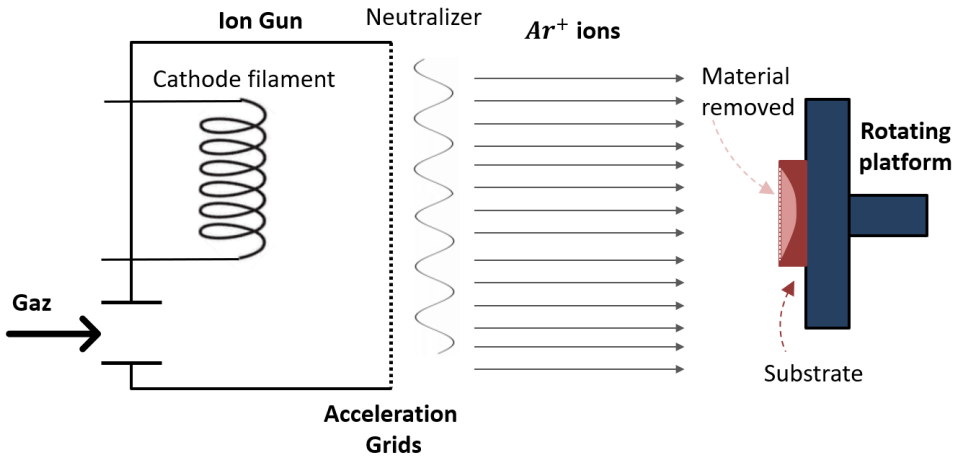

FIGURE 4.11: Schematics principle of ionic beam etching

important option and sometimes even gold due to its better lateral definition not achievable with KI solution.

The principle of IBE is presented in Figure 4.11. The introduced gas into the discharge room is ionized by collision with the electrons emitted by a tungsten filament that constitutes the cathode. The ion beam is channelled by a grid that also prevent the electrons from entering the etching zone. The ions are accelerated by a series of three grids and they are then neutralised by a tungsten filament before arriving at the sample in the low pressure chamber.

The etching conditions used for our IBE system are shown in Table 4.5 whereas the etching rates are displayed in Table 4.6.

Discharge current (A)	Beam voltage (V)	Neutralization current (A)	Current/Voltage cathode
0.4	600	1.6	6-9V/4.75-6V [1]

TABLE 4.5: Etching parameters for IBE etching technique

	LSMO	Au	Si	PZT	Photoresist
Etching rate (nm/min)	5	35	8	10	30

TABLE 4.6: Etching rates for the different materials using IBE etching technique

To test the effect of a sample which undergoes 30 minutes of etching time in IBE chamber, R(T) for LSMO was measured before and after an etching with usual conditions, completely covered with resin. Figure 4.12 shows that the two measurements are identical which proves that LSMO is not degraded by this fabrication step.

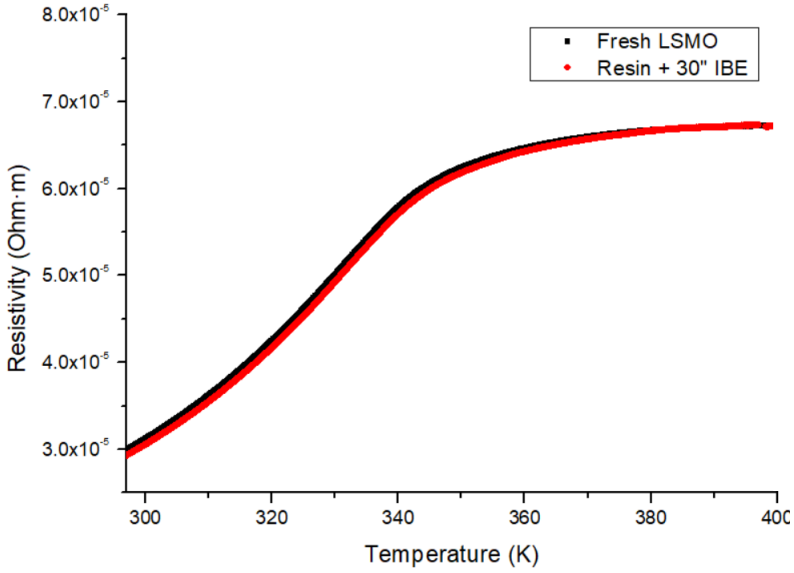

FIGURE 4.12: LSMO thin film resistivity comparison before and after 30 minutes in IBE etching, covered in photoresist

Reactive Ion Etching

Reactive Ion Etching (RIE) is a well-known technique for highly anisotropic etching, ideal for producing vertical profiles, in which chemically reactive gases and ion bombardment are used for removal of material achieving very high aspect ratio structures. It has been a key development that allows devices to reduced in size enabling faster electronics to be placed on the same chip. It is a directional etching technique that uses a combination of both physical action and chemical reaction. I will use it at low power and high pressure when aiming to favour isotropic etching to release the LSMO/STO bridges from the Si substrate, or with higher power and lower pressure to etch Si in depth and keep it as a part of the structure to be released from the SiO_2 in an HF bath.

The sample is placed on a table in the etching chamber and vacuum is established. The gases introduced in the chamber are wisely chosen depending on the material to be removed, as reported in Table 4.7, as well as the gas flux and power applied to the system. Our RIE system disposes of four gases arrival: SF_6, CHF_3, O_2 and Ar. The etching rates are also reported in Table 4.7.

The application of RF power at 13.56 MHz to the powered electrode (cathode) by keeping the other electrode (anode) grounded causes plasma to be initiated, as represented in Figure 4.13, as a result of gas molecules ionized by the electric field.

Etching material	Etchant	Gas flux (sccm)	Power (W)	Pressure (Torr)	Etching rate (μm/min)
Si (depth)	SF_6	30	40	0.03	0.47
Si (lateral)	SF_6	30	30	0.05	0.2
Si on Sapphire (depth)	SF_6	30	40	0.03	0.4
Si on Sapphire (lateral)	SF_6	30	30	0.05	0.1
SiO_2	CHF_3 +2% O_2	30+0.6	75	0.04	17
Photoresist	O_2	20	15	0.03	70
Cleaning	Ar + O_2	20+20	30	0.03	–

TABLE 4.7: RIE plasma generation parameters and etching rates

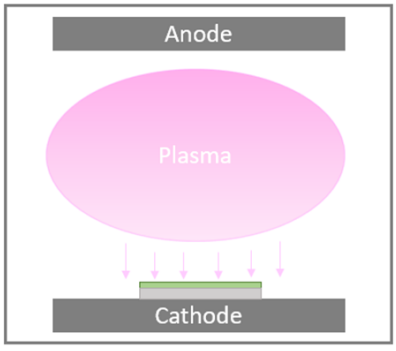

FIGURE 4.13: Schematic representation of Reactive Ion Etching vacuum chamber with plasma formation

The RF applied power plays an important role in both generation of reactive gaseous species in the bulk plasma, such as excited molecules and radicals, and at the density of the charged species, i. e., electrons and ions. The extraction of these ions from the plasma and subsequent energization towards the sample is performed due to an additional DC bias voltage that contributes to the directionality of etching and desorption of reaction by-products from the surface of the sample.

The parameters of etching for silicon depending on the step of fabrication are due to the interest in either a anisotropic or isotropic process, as to achieve the removal of Si preferentially in depth to arrive at the SiO_2 layer or laterally to release the suspended structures.

The effect of prolonged exposition of the sample to the plasma in the LSMO's quality was tested by measurement of it's resistance in the range 300 - 420 K of temperature, R(T), before and after exposition to the SF_6 plasma.

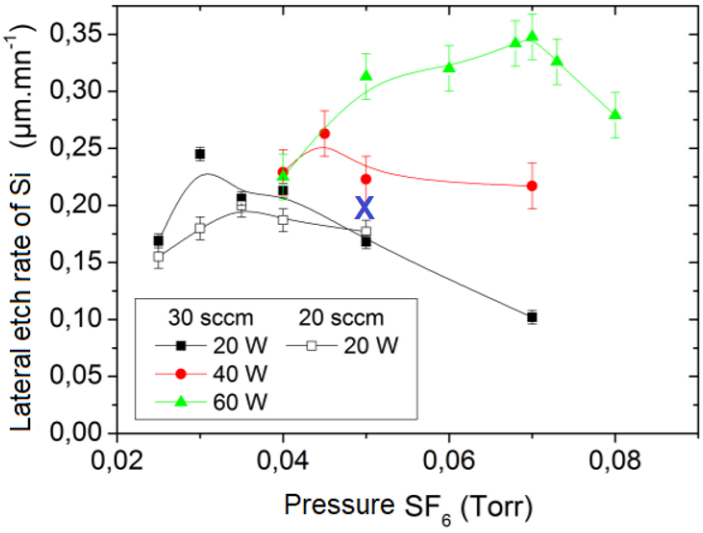

(a)

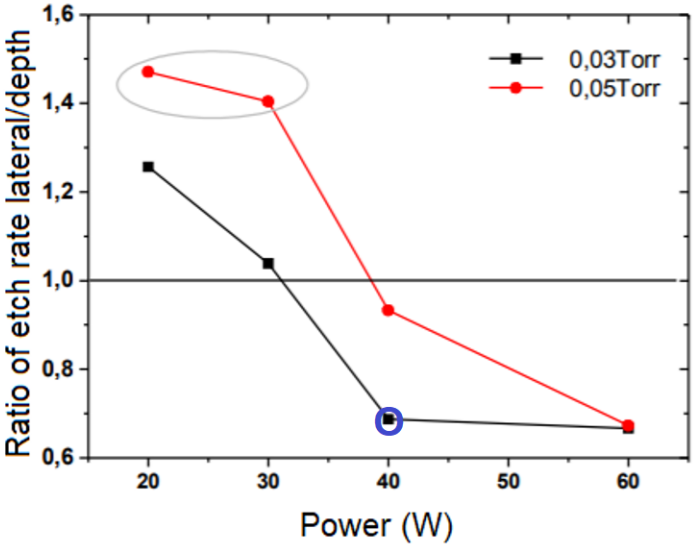

(b)

FIGURE 4.14: Etch rate of Si for (a) lateral etching in Reactive Ion Etching in SF_6 as a function of pressure for different gas fluxes and the (b) ratio of etching between lateral and depth etching for two different pressures. Extracted from (Liu, 2013a)

FIGURE 4.15: Reactive Ion Etching controller and its vacuum chamber (model PLASSYS MG 200) at the clean room at GREYC laboratory

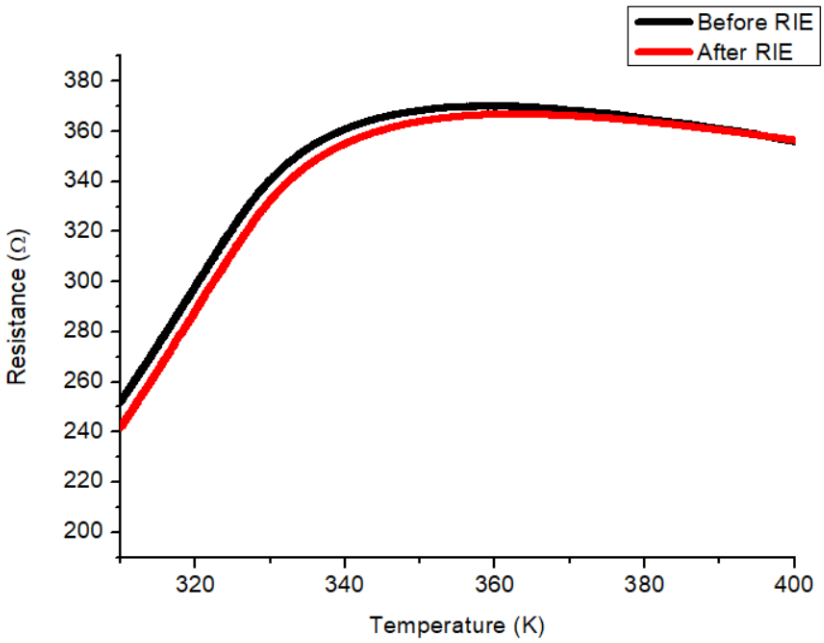

FIGURE 4.17: LSMO R(T) before and after 20 min exposure to SF_6 plasma in Reactive Ion Etching vacuum chamber

The sample had its curve R(T) measured before starting the tests, and then was coated with photoresist in spin coating with a rotation of 4000 rpm for 40 seconds and centrally placed in RIE under a SF_6 plasma with a gas flow rate of 30 sccm for 20 minutes with a pressure of 0.05 Torr and power of 30 W. The photoresist was withdrawal in acetone and ethanol bath, and the curve R(T) were once again measured.

For the release of the bridges, as in figure 4.16, we have used reactive etching of silicon as to achieve an isotropic etching to completely remove the bottom silicon under the beam with the shown parameters for the Si lateral etching.

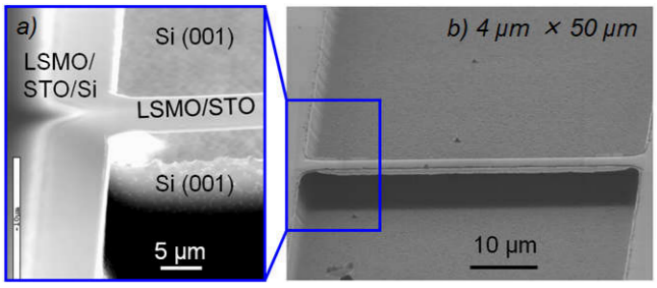

FIGURE 4.16: Scanning electron microscope (SEM) photographs of free standing 50 nm thick LSMO/CTO suspended micro-bridges extracted from (Liu et al., 2019)

The Figure 4.17 showns that RIE did not degrade the LSMO thin film when protected by photoresist.

Material	SF_6 plasma	CHF_3 plasma	HF acid	HCl acid	KI solution
LSMO	X	X	X	✓	X
STO	X	X	✓	X	X
PZT	X	X	✓	✓	X
AlN	X	X	X	✓	X
Si	✓	X	X	X	X
SiO2	X	✓	✓	X	X
Au	X	X	X	X	✓

TABLE 4.8: Compatibility table between etchants and etched materials present in the heterostructures of interest for resonant MEMS fabrication. X represents that the material isn't etched by the associated etchant, whereas ✓signs that etching takes place.

4.3 Static Characterization

The static characterization can be realized by several microscopy techniques. Here, I had used three different kinds namely Confocal Microscopy, Digital Holographic Microscopy (DHM) and the Keyence Digital Microscope. Each one has its advantages as shown in the next subsections for evaluation of the same sample of simple $4\mu m$ large LSMO/STO bridges fabricated onto Si substrate.

4.3.1 Confocal Microscopy

Confocal technology allows the measurement of surfaces height trough the conversion of conventional images into optical sections by preserving the signal for the areas within the depth of focus of the objective, improving the image contrast, the lateral resolution and system noise. The imaging technique utilizes an aperture at the confocal plane of the chosen objective and this way out-of-focus light is prevented from entering the imaging system resulting in exclusively in-focus plane on the sample captured (Keyence, n.d.[b]).

Its performance is improved by the use of a LED over a laser, since it avoids interference patterns and scattering typical of laser light sources and they offer great versatility once it enables different wavelengths to be used depending on sample characteristics.

Vertical resolution is limited by the instrument noise and it is dependent of the numerical aperture (NA), a measure of the microscope's ability to gather light and resolve fine specimen detail at a fixed object distance, for confocal microscopy measurements. We used a Sensofar S-neox confocal laser microscope equipped with a blue light-emitting diode (LED, λ =405 nm) to inspect the surface of our samples. Sensofar deliver nanometer level system noise for any measurements technique at the highest possible lateral resolution for an optical instrument (Keyence, n.d.[b]).

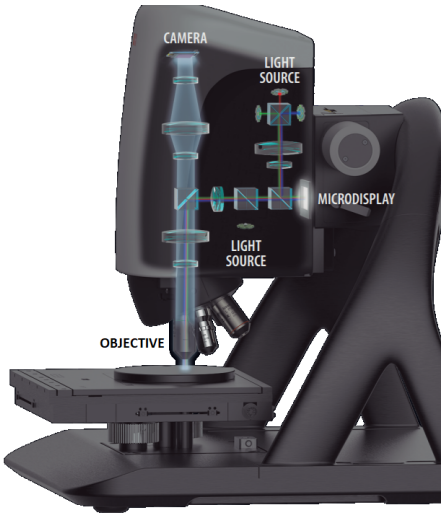

FIGURE 4.18: S-neox confocal microscope schematics. Extracted from (Keyence, n.d.[b])

LEDs with shorter wavelengths, as the used one, are used on those applications where the highest lateral resolution is required. Rayleigh criterion can be used to determine the smallest resolvable dimension by an optical system and shows its relation with the chosen wavelength:

$$r = \frac{1.22\lambda}{2NA} \tag{4.4}$$

Confocal profiling provides the highest lateral resolution, up to 0.15 μm line & space. The spatial sampling, using such microscopy, can be reduced to 0.01 μm, ideal for critical dimension measurements. Such great resolution have allowed us to investigate the transversal curvature of the suspended bridges due to the release of residual strain as several points were measurable over a profile crossing the bridges.

2D images were acquired with 1220$\times$ 1024 pixels for the aforementioned 4μm large LSMO/STO bridges as exhibited in figure 4.19. The etched area is clearly seen with a brighter contrast, displaying the fact that the structure is indeed completely suspended. The different lengths of the bridges are shown in Figure 4.20. From the 2D images and the acquired z-axis information, a 3D reconstruction of the whole structure is possible as shown in figure 4.21. However, since this is simply a 3D reconstruction no actual data is available for the region under the bridge and one can only verify the etching depth from such image (around 7.6 μm).

4.3.2 VHX Series Digital Microscope

The VHX series digital microscope from Keyence, as exhibited in figure 4.22 provides a large depth of field and high resolution, which is ideal for observation of 3D structures together with its possibility of observation at a free angle for 360° control.

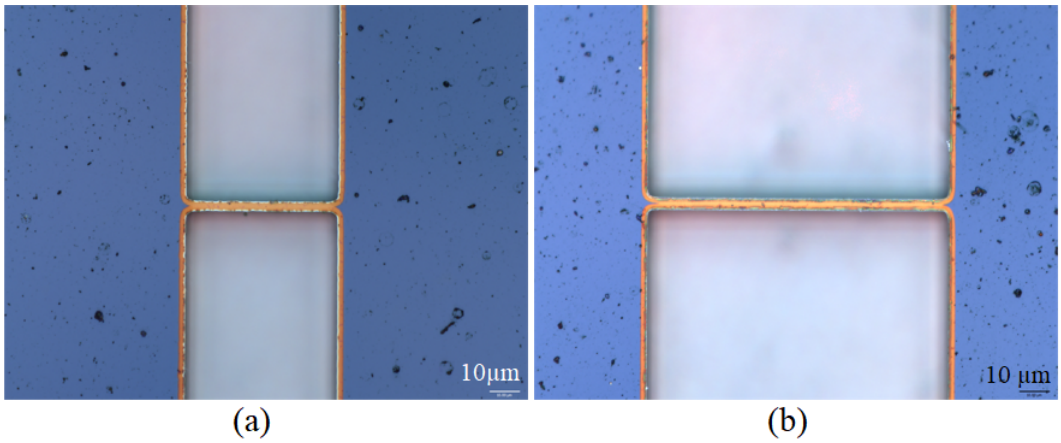

FIGURE 4.19: 2D confocal image for 4μm large 100 nm-thick LSMO on STO suspended suspended bridge fabricated on Si substrate evidencing the release of the beams from substrate by a contrasted area for (a) 50 μm and (b) 100 μm long structures.

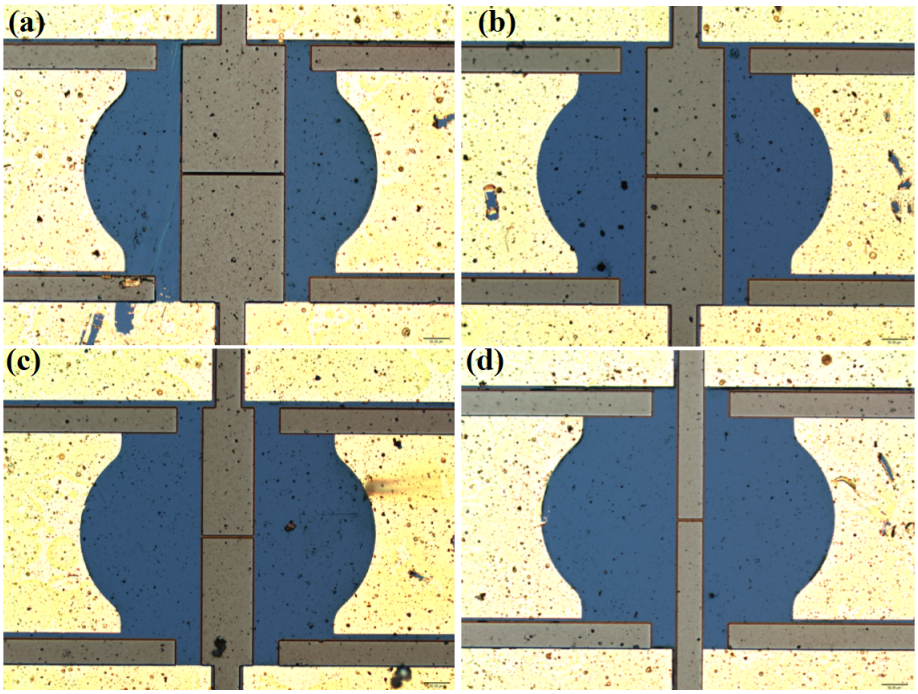

FIGURE 4.20: 2D confocal image for four 4μm large 100 nm-thick LSMO on STO suspended suspended bridge fabricated on Si substratefor (a) 50 μm and (b) 100 μm, (c) 150 μm and (d) 200 μmlong structures.

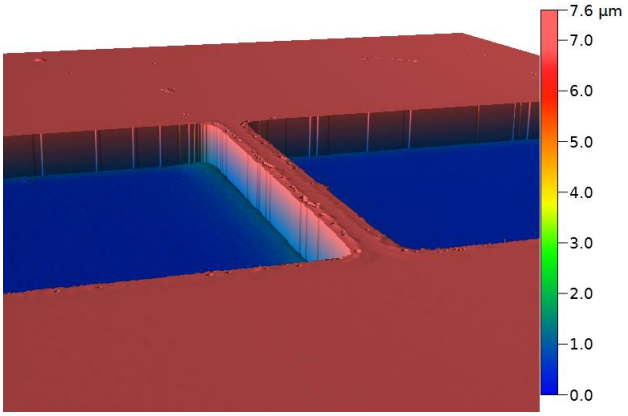

FIGURE 4.21: 3D reconstruction of confocal image for 4μm large 100 nm-thick LSMO on STO suspended suspended bridge fabricated on Si substrate.

Our interest in using such microscopy for the fabricated suspended bridges was the possibility of an angular visualization of the samples, enabling the investigation of the etch under the bridges, as it was impossible by the 3D observation with confocal microscopy since no moving parts compose the microscope structure.

Here, the deep composition helps capture a perfectly focused image, even at high magnification (in a range that goes from 0.1× to 6000×) and with the lens tilted. The VHX scans the different focal points of a sample, then combines them into a single image, dramatically reducing analysis time. In addition, it enables some extra features for better detail analysis of highly reflective or low contrast samples such as bright and dark field, transmission illumination and polarized illumination.

FIGURE 4.22: Features of the VHX Series Digital Microscope, Keyence, (a) microscope view and free-angle variation for controlled observation, (b) multi-light function, (c) optical shadow effect and (d) in-depth composition to capture a perfectly focused image. Extracted from (Keyence, n.d.[a]).

The functionalities provided by the equipment are numerically treated to provide better visualization of the samples under study, the multi-light function, for

example, uses omnidirectional light data captured automatically to adjust the lighting settings to get a clear picture, as well as the optical shadow effect mode, which captures multiple images of a view under different lighting angles. This allows one to observe surface details that are normally too difficult to be seen by the enhancement of the recorded accurate shadow differences.

In this sense, Differential Interference Contrast Illumination (DIC) allows users to observe even minimal differences in height on samples, enabling the visualisation of patterns without any preprocessing.

Observation of highly reflective surfaces is equipped with a diffuse lighting adapter to allow the sample to be seen from all directions under uniform reflections since the problem of such samples when observed with conventional microscopes is the a reflection of the unidirectional light that makes inspection difficult.

Such microscope was used for the characterization of the same sample as exhibited on figure 4.23. A magnification of $\times 2000$ was used to observe the sample in good details as well as a composition of focus for the bottom substrate and the suspended single bridge, which is the reason why the whole image is net.

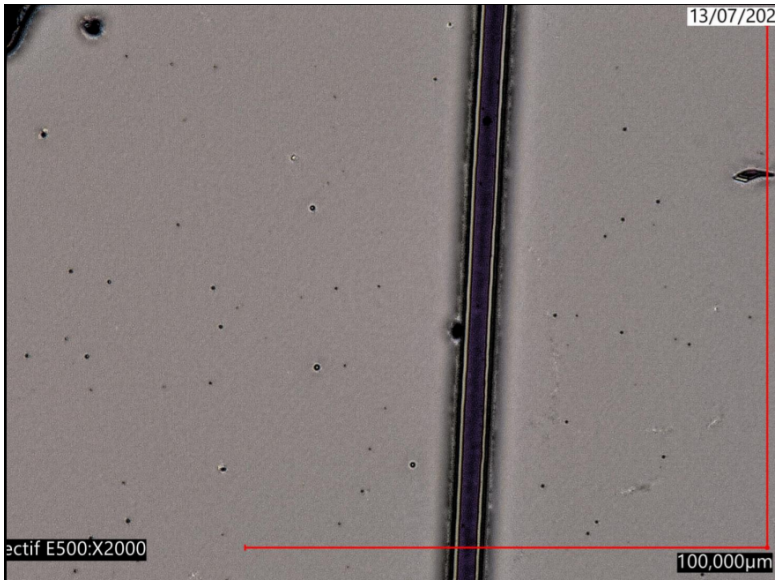

FIGURE 4.23: Imaging of LSMO/STO/Si 4μm bridges using Keyence Microscopy

Figure 4.24 shows the depth measurements along a line for the captured image, exhibiting around 7.5 μm of etched silicon, which is coherent with Si etch rate in RIE given 15 minutes under SF_6 leads to an expected depth of 7050 nm for the sample.

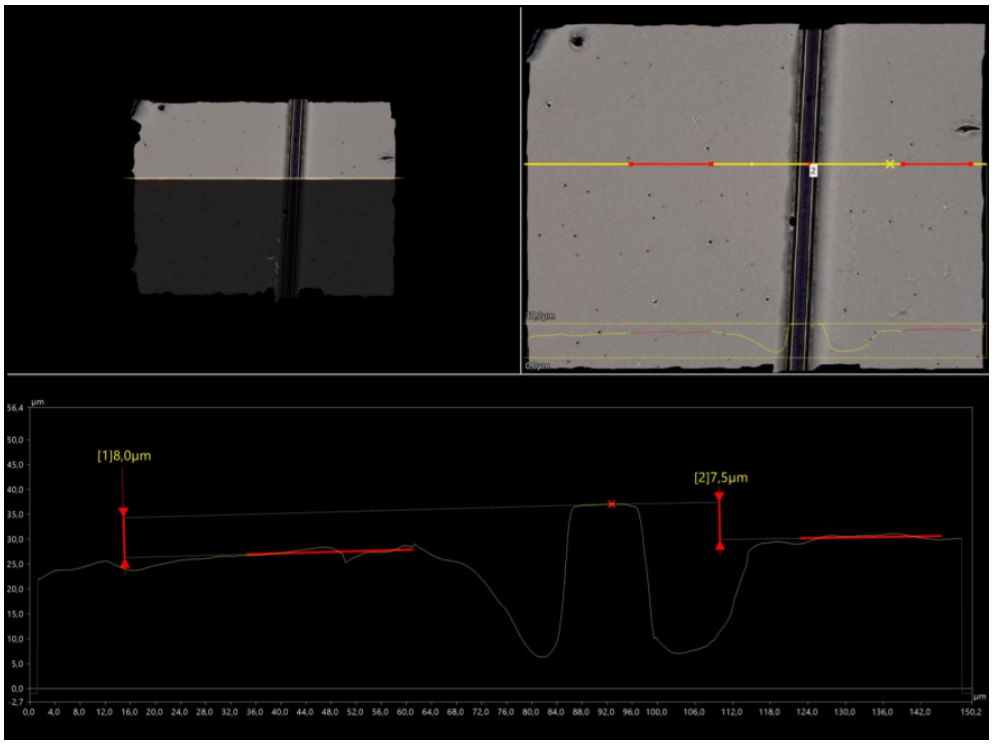

FIGURE 4.24: Imaging of LSMO/STO/Si 4μm bridges using Keyence Microscopy with the profilometer measurement

However, we could not take advantage of the tilt of the objectives to acquire information on the 3D structure of the sample, since the high magnification greatly limits the possible angles being impossible to see under the bridge and I could only use it within an intervention from the society at our laboratory. Finally, the advantage that this microscope would have in comparison with the confocal one, previously used, has shown to be incompatible with our sample dimensions therefore adding no extra analysis features. To better judge the features in common, another uses of the equipment would be necessary to test for different samples and conditions.

4.3.3 Digital Holographic Microscopy (DHM)

The Digital Holographic Microscopy (DHM) is a microscope objective (MO) that produces a magnified image of the sample used as an object for the hologram[2] creation, enabling the measurement of precise quantitative information about 3D structures with a single hologram acquisition, with high acquisition rate, i. e., in the video frequency. Both amplitude and phase-contrast images can be numerically reconstructed from hologram as well with a high reconstruction rate (around 1 Hz) from the calculation of scalar diffraction in the Fresnel approximation and the phase aberration associated with the use of a MO is corrected by a digital method. The

[2]Optical element presenting information about an optical wave.

obtained phase contrast is quantitative and can be used directly for applications in optical metrology.

The detectors capable of receiving an image function by a sensitivity to the intensity of light, losing phase information in this process. Dennis Garbor was able to encode phase modifications as variations in intensity for the first time enabling the possibility to represent the observed objects as phase images and obtain quantitative 3D information, which entitled him as inventor of holography.

The DHM captures the holograms formed by two coherent beams with slightly different propagation directions interfering, namely the reference beam and the object beam. This is done in such a short acquisition time (from 1 - 100 μs depending on the object and configuration of the microscope) that the measurements are insensitive to environmental vibrations and ambient light. It's use limitation would be for materials that diffuse to strongly by their nature due to the impossibility of forming holograms through a fog phase information, the typical local slopes of the surface structure must be smaller than the maximum acceptance angle of the objective used for measurement. Samples showing surface roughness smaller than 200 nm in reflection configuration are normally in the acceptable range.

Simplified optical principle: The beam source, consisting of a laser diode, is separated into two different beams: an object beam, O, and a reference one, R. The objective collects the retro diffused wavefront which is then recombined with the reference beam to form a hologram in the camera.

Two beams recombined are coherent and form a hologram if the difference between their optical paths is less than the source coherence distance (0.5 mm), hence, the length of R must be adjusted to be the same as that of the object beam. This is performed by the DHM R2200 by electronically modulating the source to ensure a coherence length of 0.5 mm in air.

The wavelengths for each laser as well as their combinations is shown in the Table 4.9.

	λ_3	λ_1	λ_2	Λ_{1-2}	Λ_{1-3}
Wavelength	668 nm	684.8 nm	793.8 nm	5.0 μm	27.25 μm
δh	334nm	342.4nm	396.9nm	2.5μm	13.6μm

TABLE 4.9: Wavelength characteristics for DHM measurements and the measurable heights

The use of each set of lasers must be chosen accordingly with the sample's requirements as shown in table 4.9.

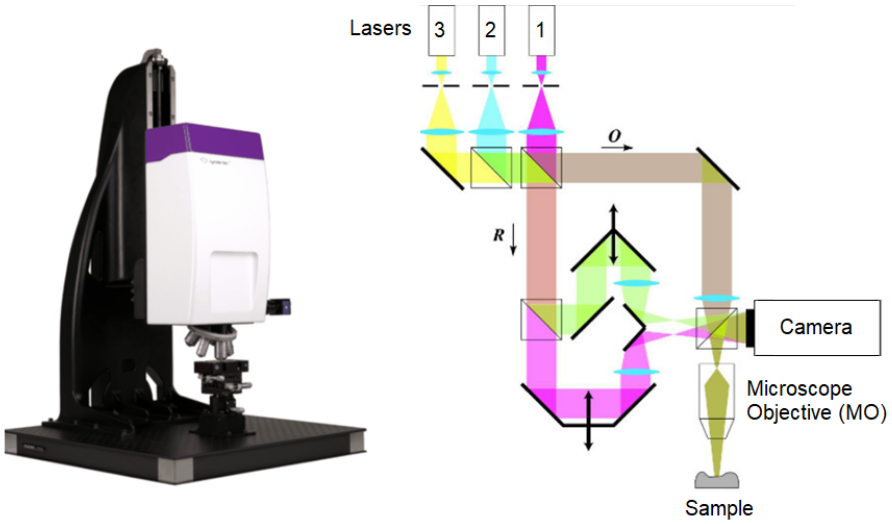

FIGURE 4.25: DHM R2200 from Lyncée Tec and its optical principle

In my first tests with such microscope, the z-axis measurements wouldn't match the ones previously measured by confocal microscope or even mechanical profilometer. By performing tests with each laser at its saturation values by changing the shutter parameter, it was observed that a minor dislocation of lasers 2 and 3 had taken place when the microscope was delivered at the GREYC laboratory site. Whereas the main laser exhibited is focus in the middle of the screen during measurements, the other two were mainly located in the bottom right, in such a way that the compositions of lasers allowing the vertical measurements in the micrometer region were not possible.

I could then participate in the intervention for the laser alignment and from this point all the measurements for our different samples were enabled.

As shown in table 4.10 the lateral resolution of the DHM is comparable with confocal microscope if we chose an objective of 50× magnification or higher. For vertical measurements however, we achieved comparable measurements.

Objective/Properties	**NA**	α(°)	**WD (mm)**	**FOV max (μm)**	**Resolution in x-y (μm)**
× 10	0.3	17.4	11	475	0.732
× 20	0.4	23.6	1.15	234	0.361
× 50	0.75	48.6	0.37	94.2	0.145
× 100	0.85	58.2	0.33	47.1	0.073

TABLE 4.10: DHM properties for correspondent objectives used for sample analysis. *WD* stands for Working Distance and *FOV* for Field of View.

DHM presents a less user friendly interface and some inherent difficulties for measurements, such as optimization for acquiring a high quality hologram. This

is done by the optimization of the fringes in holograms.

The hologram fringe contrast is given by the ratio $(Max - Min)/(Max + Min)$ with an ideal value equal to 1 where the minima is an acquisition image value as dark as possible and the maxima, as bright as possible. The contrast is quantified reliably by the standard deviation of the histogram of the hologram. If a single wavelength is used the fringes are in a single diagonal direction, however, if a mode with simultaneous wavelengths is chosen then the fringes in holograms are observed in two perpendicular diagonal directions.

One must work in video mode for rapid refresh rate adjustment of settings. The camera settings must be adjusted through the use of an histogram tool for fine adjustment of camera shutter (exposure time) and gain (this must not be high to avoid electronic noise) in such a way as to ensure that the measured intensities lie between 0 and 255. If blue pixels are seen, the image is exhibiting underexposed pixels, if red, overexposed ones. One must take care to word in absence of saturation for reliable measurements.

The optimization of coherence is the optimal position of focus and determines the position of the sample at an optimal distance from the objective. The adjustment of height for working distance until interferences fringes on hologram plus contrast maximization by standard deviation of the hologram histogram window must be obtained as high as possible.

The interest in using DHM, despite the more complex measurements, lies mainly in the possibility to measure the vertical displacement of samples in a dynamic mode: the stroboscopic one. In this mode, periodic (or any reproducible movements) can be tracked. Special electronics allow the synchronization between the movement of the sample and the image acquisition and illumination leading to a high performance stroboscopic measurement. The measurement time can be made short enough to ensure that the sample does not move vertically more than a few nanometer, this was particularly important in my measurements when working in a hundred of kilo Hertz range. Enough light must be collected for the sample to ensure a low noise high quality measurement, hence, the pulsed stroboscopic mode works with a pulsed laser down to 7.5 ns where the shutter of the camera is set to integrate the intensity of several pulses to add enough signal for producing a good quality hologram. The video stroboscopic mode must be on so that the laser is continuously on and the camera is trigged to cover all the sample positions during its cycle.

Figure 4.26 shows the DHM images for static characterization of the same sample studied with the two previously presented microscope, exhibiting an etched height of 7.3 μm in accordance with previously measured values.

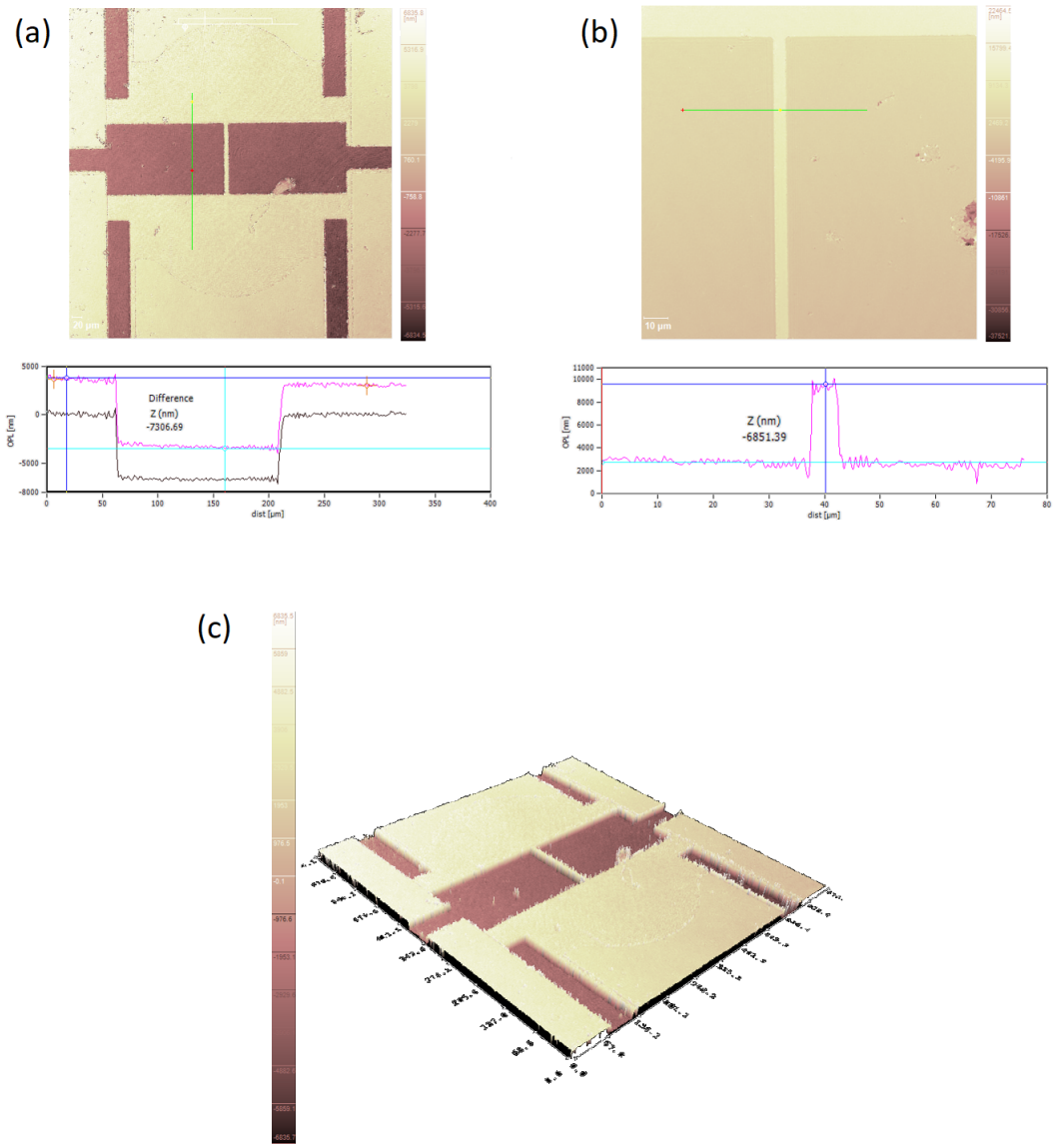

FIGURE 4.26: DHM measurements of 4 μm large LSMO/STO bridges using 10 $\times$ magnification for 100 nm long beams visualization and (a) etched profile for non-suspended parts, (b) z measurement for a transverse profile over the suspended structure showing the structure is slightly bended downwards and (c) a 3D numerical reconstruction of the beam.

4.4 Simple LSMO / STO / SOS or Si suspended bridges

Once in possession of the complete LSMO/STO/SOS stack of materials, the first step was to deposit gold on top of the LSMO to guarantee its contact plots to be used in the final suspended devices for the electrical and thermal characterization.

This was performed first by a thin film coating by PLD with 9000 shots and 5 Hz rate at room temperature in order not to degrade LSMO, but due to the low deposition rate, about 80 nm deposited bu GATAN complemented the whole gold layer, in a total of approximately 100 nm.

The fabrication of LSMO/STO/Si and LSMO/STO/SOS suspended bridges is done in two *lithographies* stages: a first mask that defines the LSMO contacts and another for the LSMO patterns themselves.

For that purpose, a mask, designed in CleWin for a $10 \times 5mm^2$ sample, composed of two overlapped layers, was developed. The alignment patterns consisting of $20 \times 20\mu m^2$ squares were disposed in 8 different points defined as (-4,0), (-2,2), (0,2), (2,2), (4,0), (2,-2), (0,-2) and (-2,-2) relative to the center (0,0), together with the first layer of the mask for the definition of the LSMO contacts. The superposition of both masks is displayed in Figure 4.27.

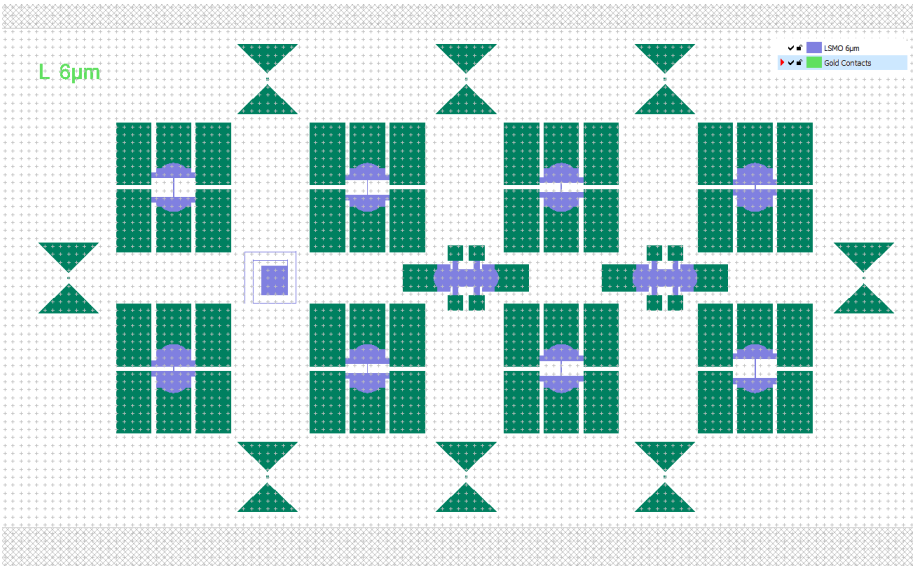

FIGURE 4.27: Mask design for simple bridges on SOS and Si substrates showing the patterns for defining LSMO layer in purple superposed by green ones representing the gold contact pads

After the gold was patterned with the specific dose and exposure, it was developed for 40 seconds and etched in a KI solution for 30 seconds. The photoresist was kept for the PLD deposition at ambient temperature of a protection layer of about 30 nm thick amorphous STO (a-STO) layer. The resist was then rinsed away in acetone for lift-off and and a new photoresist layer deposition was performed in the

complete sample that was again placed in the MicroWriter ML3 Pro for the LSMO patterning. The resolution for exposure was set to 1 μm, since the smaller patterns are the bridges' width within a range of 3-10 μm. This process was followed by the subsequent develop bath for 40 seconds and the sample was placed in Ion Beam Etching for the removal of unwanted LSMO outside the delimited patterns. The bridges were then released in a SF_6 plasma using Reactive Ion Etching.

With the whole structure suspended, I perform the electrical characterization in order to have a comparison with the depart values to validate that the whole process, despite its many etching steps, do not degrade the LSMO layer by the results in Table 4.11 for the structures on SOS substrate.

Bridge reference	**R (Ω)**	**L(m)**	**W(m)**	**t(m)**	**ρ (Ω.m)**
P50	10429	5E-5	2.6E-6	4.5E-8	1.9E-5
P100_1	17598.7	1E-4	2.5E-6	4.5E-8	2.0E-5
P100_2	17145.4	1E-4	2.9E-6	4.5E-8	2.2E-5
P150_1	27550.3	1.5E-4	2.5E-6	4.5E-8	2.1E-5
P150_2	14432.5	1.5E-4	5.5E-6	4.5E-8	2.4E-5
P200_1	34696.9	2E-4	2.5E-6	4.5E-8	1.9E-5
P200_2	35590.9	2E-4	2.7E-6	4.5E-8	2.1E-5

TABLE 4.11: Measured resistivity values for the suspended bridges on sample BA081

Static measurements for structural study of the prepared LSMO/STO/SOS sample shown in figures 4.28 - 4.30 were performed using confocal microscopy, at CIMAP laboratory.

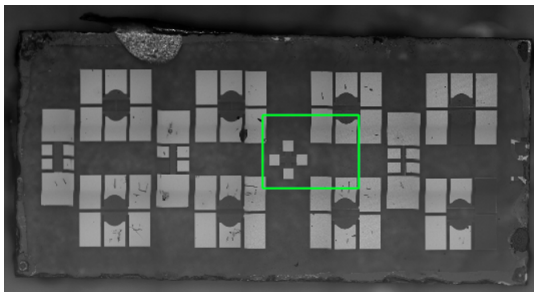

FIGURE 4.28: Confocal overview image for LSMO/STO/SOS sample

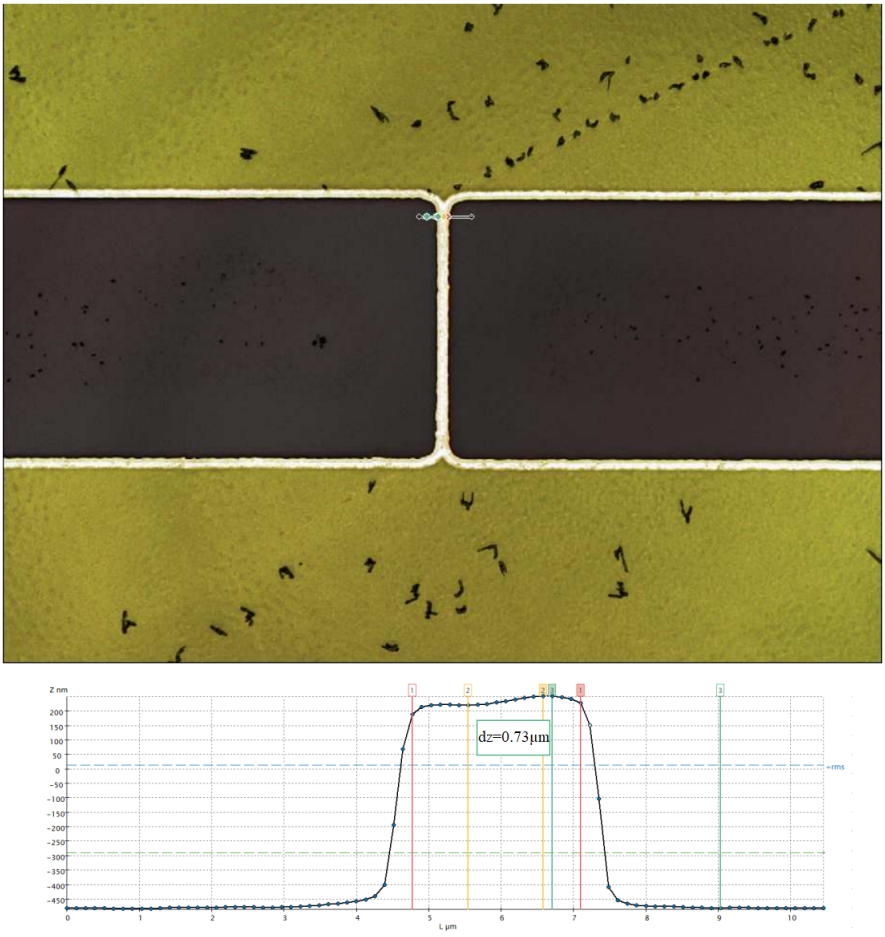

FIGURE 4.29: Confocal image for 50μm long 4μm thick LSMO/STO/SOS sample

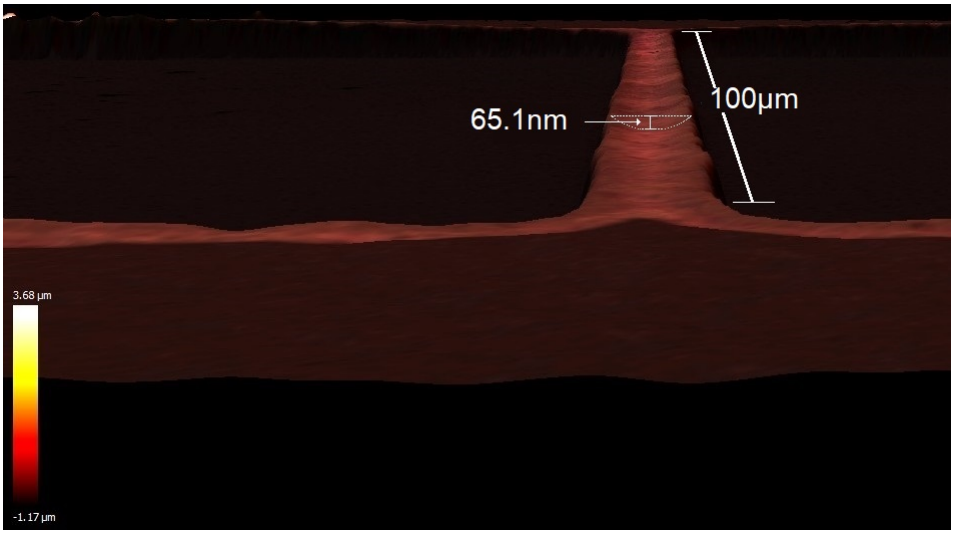

FIGURE 4.30: Topography of a 100 μm long bridges fabricated on SOS substrate exhibiting a much smaller distortion than the one obtained on Si substrates due to smaller epitaxial strain

Further structural studies of such sample were performed using digital holographic microscopy (DHM-R2200). Figure 4.31(a) shows a 3D-reconstruction image of a 3 μm large $\times$ 100 μm long suspended beam. The thickness shown in the phase image and optical microscopy (seen as a white color corresponding to lateral etching underneath the a-STO/LSMO/STO/Si) of figure 4.31(b) confirmed by the thickness profile in figure 4.31(c), verifies that the full a-STO/LSMO/STO/Si stack was etched since the measured step was 800 nm and the typical width of Si on the SOS substrates is of 700 nm.

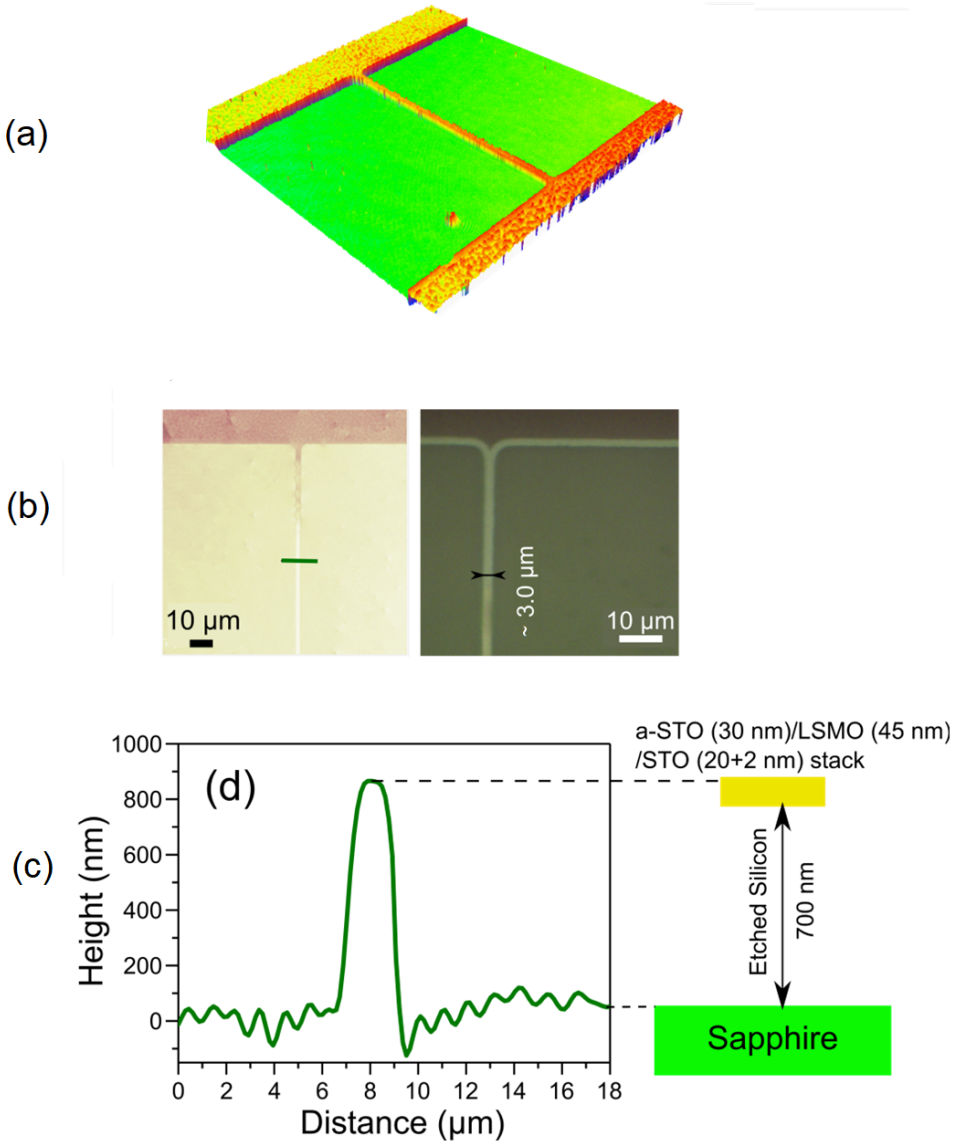

FIGURE 4.31: (a) 3D-reconstruction image in DHM R2200, (b) phase numerical reconstructions image in DHM with topographic information on the sample and optical microscope image of a 3 μm wide 100 μm long suspended bridge and the (c) thickness profile at the center position obtained from phase information

The silicon etching rate was about 0.4 $\mu m/min$ in depth and $\mu m/min$ in lateral direction, which is lower than the verified for the same structures on bare Si substrates due to the limited gap for the reactions to occur. Several LSMO suspended bridges with different bridge length dimensions (50 μm – 200 μm) were fabricated and the bridges' profiles were precisely determined for later resistivity calculation.

Figures C.1 to C.4 in appendix C show the exact measurement of each bridge's final width, after Gwyddion treatment of the phase data, in 10 different selected cross-section positions. The measured widths were calculated as 2.6±0.13, 2.9±0.1, 2.5 or 5.5 (due to contact problem in lithography) and 2.7±0.13 (in μm)for the 50, 100, 150 and 200 μm bridges, respectively. These values were used in the determination of the resistivity for each bridge, as shown in table 4.11. The electrical measurements were performed under vacuum by a four-point measurement technique. Such low electrical resistivity values in the range of 1.9 - 2.4 m$\Omega \cdot cm$ obtained for the freestanding micro-bridge structures further stress that the quality of LSMO thin layer is not degraded even after several lithographic process steps.

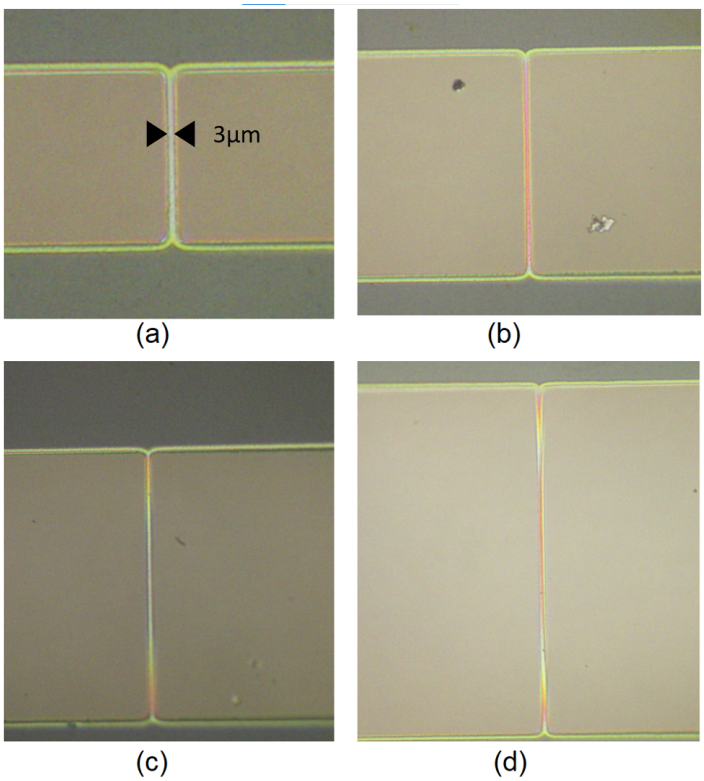

FIGURE 4.32: Optical microscope images for 50, 100, 150 and 200 μm long Al_2O_3 / LSMO / STO bridges on SOS substrate

Another protection layer was used during this process, Al_2O_3, integrated to the structure by ion beam deposition (GATAN) on the sample's surface instead of a-STO also leading to a successful fabrication (Figure 4.32), despite a slight increase in the resistivity of the LSMO film as shown in figure 4.33.

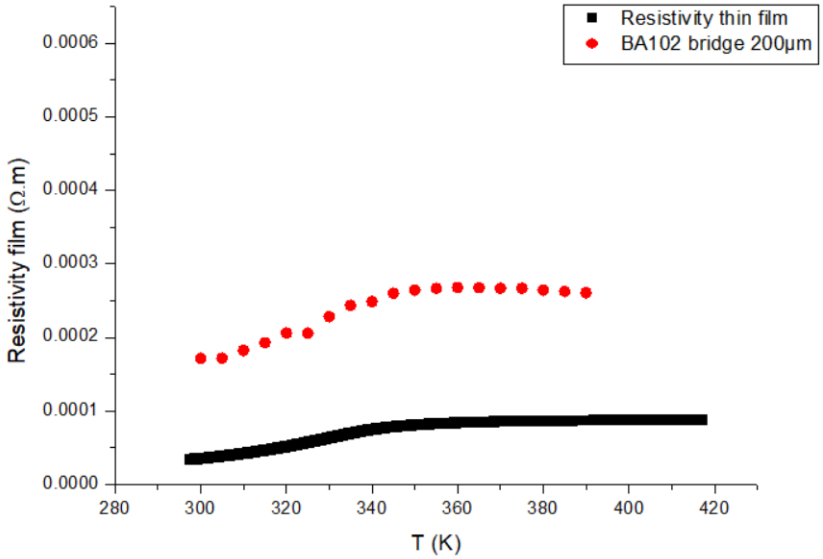

FIGURE 4.33: Al_2O_3/LSMO/STO bridges on SOS substrate resistivity measurements

Similar process is done for the samples on Si substrate, leading to equally good results, as seen in figure 4.34, for 6 μm bridges in the same length range with 100 nm of LSMO measured under vacuum.

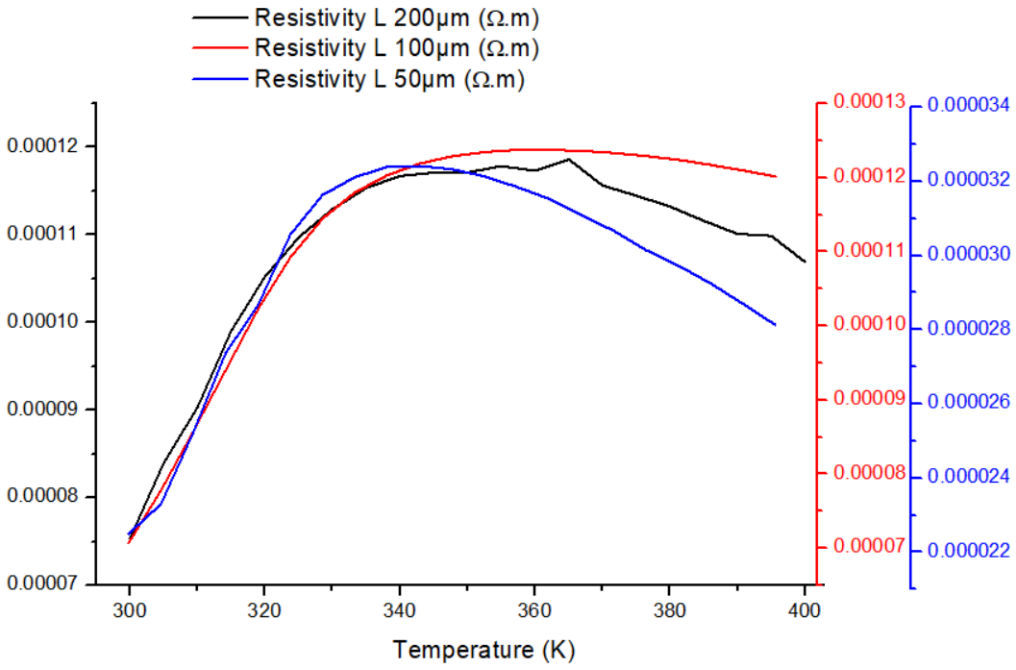

FIGURE 4.34: Suspended 6μm large 100 μm long suspended LSMO resistivity on Si substrate

4.5 Towards integrated piezo-LSMO MEMS

4.5.1 PZT actuated suspended LSMO/STO beams on Si substrates

The epitaxial LSMO/STO/Si heterostructures were used for the room temperature growth of epitaxial PZT by sputtering technique. PZT is the piezoelectric material responsible for the actuation and detection of the resonant structure, hence, kept in both extremities of the beam as well as all over the bridge itself. It is the first pattern transferred to the sample in this kind of process fabrication.

Figures 4.35, 4.36 and 4.37 detail the complete fabrication process for this kind of structure. Starting with the STO and LSMO depositions by MBE and PLD (steps 1-3), the photolithography for the PZT is performed in step 4 exhibiting the areas where PZT will be patterned by lift-off after develop in step 5.

Due to the need of superposition of bridges given the presence of a piezoelectric material covering the beam, the alignment using the MJB3 Suss Microtech mask aligner equipment has showed to be problematic since the smallest sample derivation during contact would lead to misplaced structures leaving the LSMO/STO bridge uncovered in some point. Therefore, all the lithographies for this kind of fabrication were performed by direct-write using the MicroWriter ML3 Pro.

The piezoelectric material was deposited by room temperature sputtering in collaboration with INL at step 6 and lift off was performed by simple acetone bath during 5 minutes, displaying the pattern of PZT that covers the whole bridge and both extremities where contacts will be patterned, as shown in step 7.

In the sequence, gold is deposited all over the sample, contacting both LSMO bottom electrode and PZT at step 8. Onto this structure, resist is deposited by spin coating (step 9) and a second lithography is performed to pattern the LSMO bridge as well as the regions where the contacts will be defined. Step 10 shows this lithography process where the bridge being patterned must be finely aligned with the existing PZT structure in the sample. The bath on develop solution defines the structure to be achieved after etching (step 11).

The sample is put in the IBE chamber and etched for 15 minutes (step 12), to achieve the LSMO/STO profiles shown in step 13. Once again, the sample is covered in photoresist in step 14 before the third lithography, as specified in step 15. This lithography redefines the contact pads since the gold was still contacting all the surface of PZT and LSMO as seen in step 13. The definition of the contacts then patterns big pads on top of the LSMO (shown in the extremities of the structures) as well as two big rectangles on top of the PZT. This design for the mask to determine the PZT top contacts is due the fact that the gold is already well defined on top of the bridge by the ion beam etching, needing only to be separated from both sides to allow both actuation and detection, one in each extremity. The mask that separates

the contacts for PZT is made larger than the bridge to avoid KI lateral etching of the well defined contacts on top of the 6 μm bridges.

Once the sample is patterned by the lithography exposure and developed, it is immersed in KI solution for 30 seconds for etching the unwanted gold (step 16). The sample is almost complete (step 17), the only remaining process being the release of the bridge from substrate, which is achieved in two steps: lithography of the bridge pattern (the same one used for patterning the LSMO structure), seen in step 18, and finally the reactive ion etching in SF_6 plasma that will etch the bottom silicon laterally under the bridge, releasing it from the substrate (step 19). The final structure is exhibited in step 20, consisting of the LSMO/STO suspended bridge with the PZT structure patterned from one clamped edge to another of the beam and its respective top gold contacts, as well as the gold contacts for the bottom LSMO, all this supported by the Si substrate.

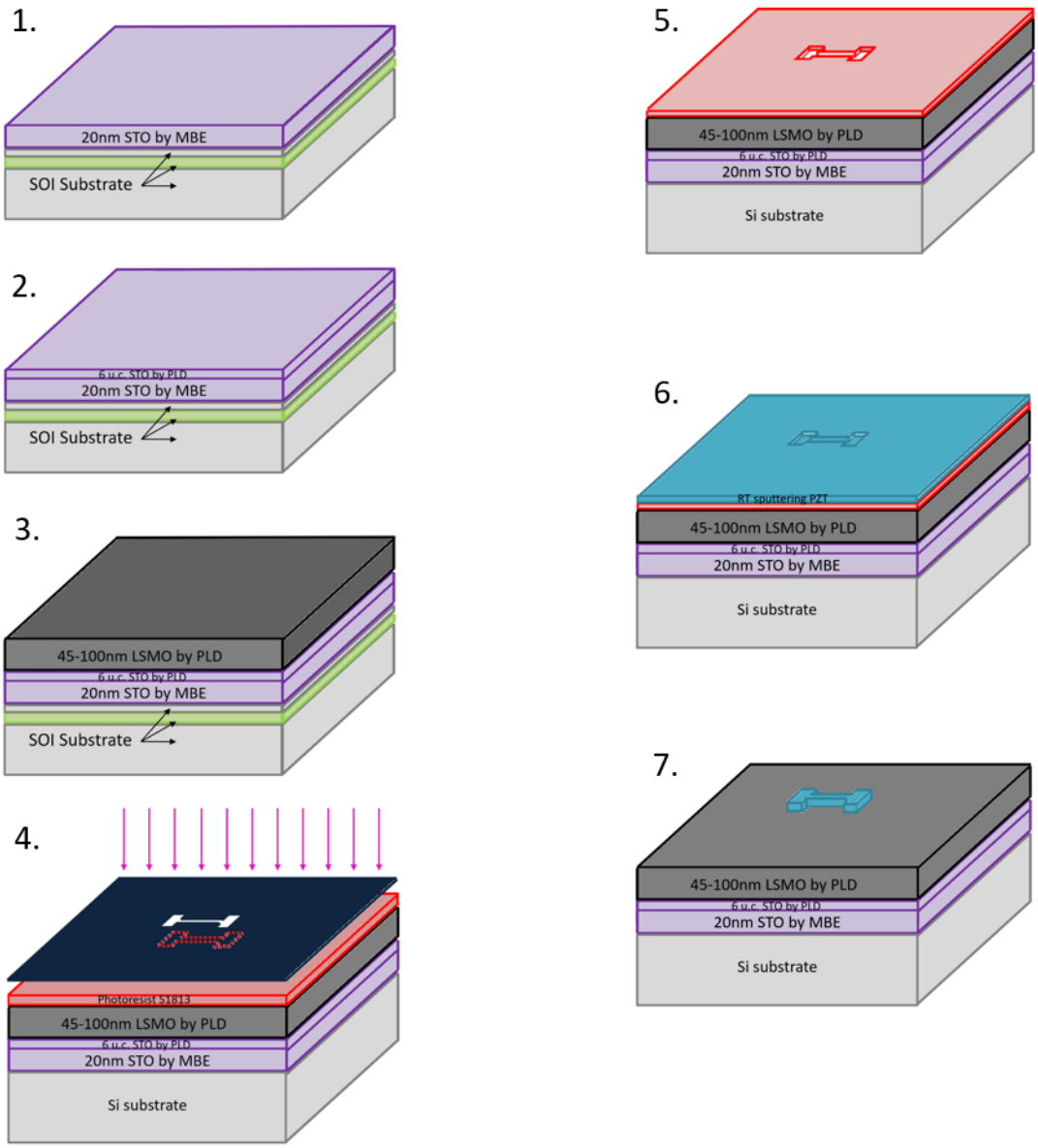

FIGURE 4.35: Schematics of fabrication steps 1-7

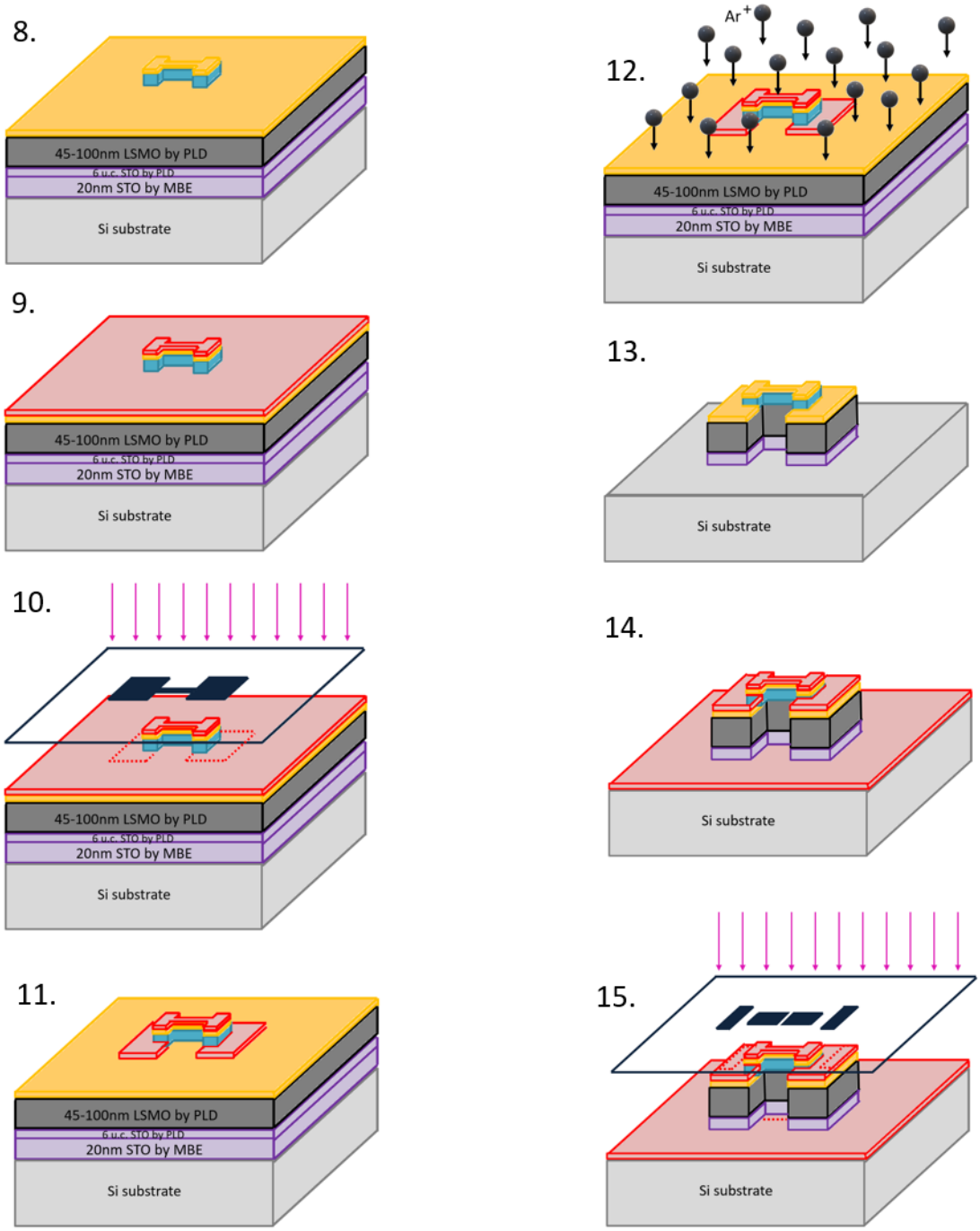

FIGURE 4.36: Schematics of fabrication steps 8-15

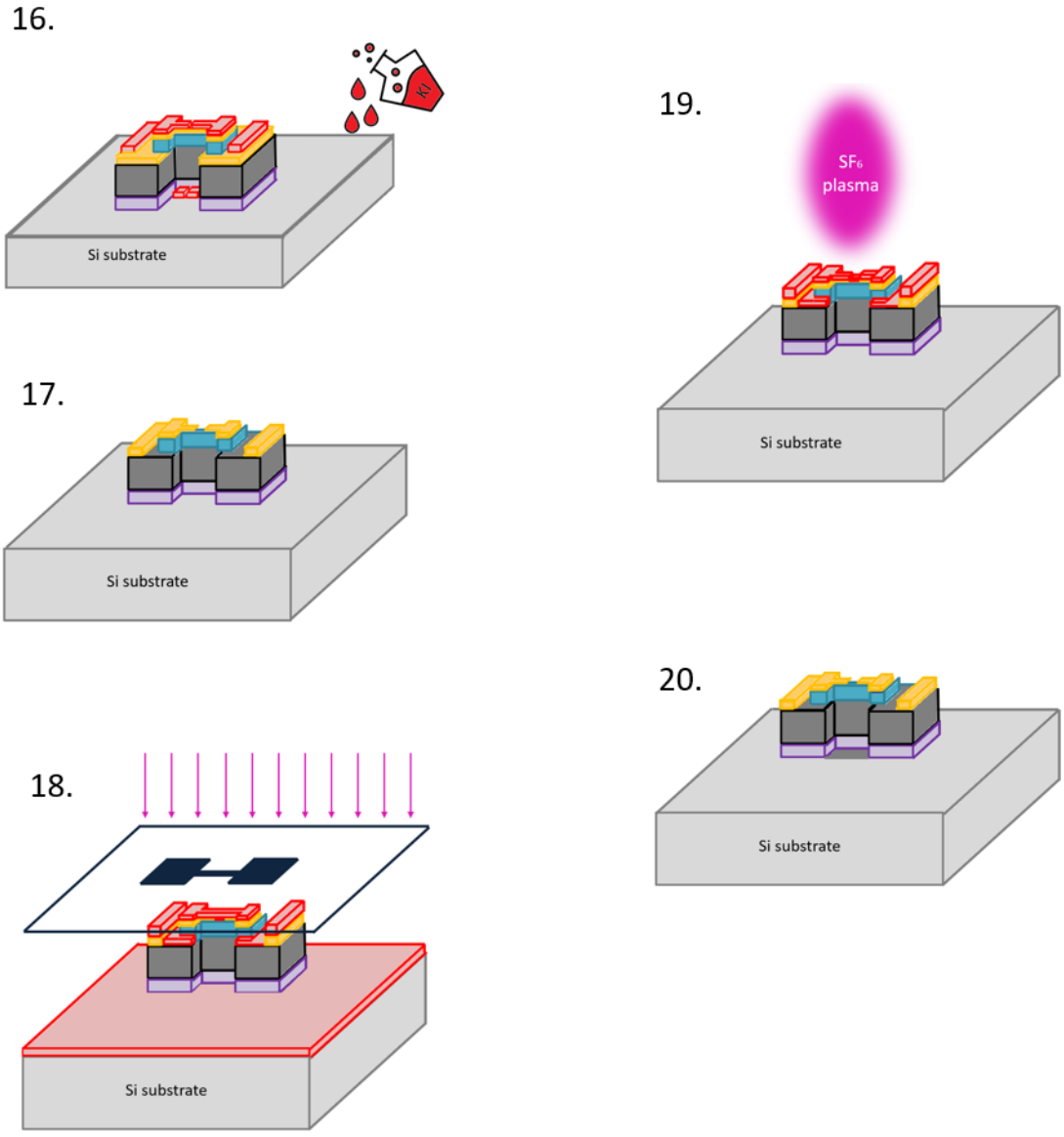

FIGURE 4.37: Schematics of fabrication steps 16-20

Top electrodes for PZT

Three different electrode deposition methods were tested to find the best fit for use as PZT top contact. A Pt film was deposited on 1/3 of the PZT layer by sputtering at room temperature, whereas the other 2/3 was divided for two kinds of Au deposition, either by PLD followed by GATAN, or exclusively direct GATAN deposition, all the contact pads were patterned using a lift-off process in order to design top electrodes of 250 $\times$ 250 μm^2 size.

The polarization hysteresis (P - E) loop measurements, shown in figure 4.38, performed via a Sawyer-Tower (ST) circuit with the PZT capacitors contacted on a Suss MicroTec PM5 probe station in series with a standard capacitor $C_{st}$of 22 pF serving as a charge holder, are displayed in figure 4.38.

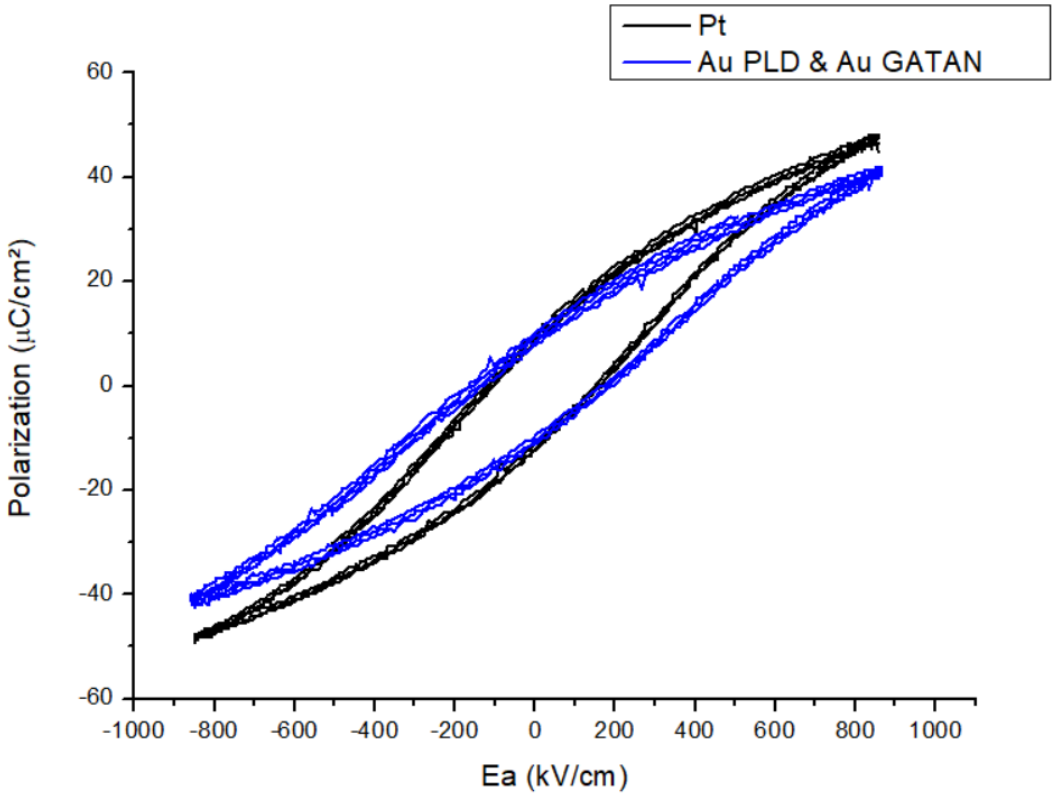

FIGURE 4.38: Hysteresis loop for sputtered PZT at 600°C with top electrodes test: sputtered Pt, Au by PLD followed by GATAN and Au by Gatan directly

Both metals have shown similar curves for the P(E) study, Pt on PZT exhibiting about 160 kV/cm coercive field and a slightly higher value for gold electrodes, around 170 kV/cm. However, a difference was seen in terms of the film's capacitance as shown in table 4.12.

The interest in having a lower capacitance in the piezoelectric film is the

	Platinum	Gold GATAN	Gold PLD + GATAN
Capacitance	490 pF	460 pF	420 pF
Loss tangent	0.02	0.02	0.02

TABLE 4.12: Capacitance and loss tangent measurements for determination of top electrode for PZT

possibility of a better signal-to-noise ratio. Since the deposition of gold by PLD followed by GATAN to increase the deposition rate showed the best capacitance results on PZT and it allows in the fabrication process a single mask for patterning both the LSMO and PZT contacts, this has been the choice for the piezoelectric top electrodes.

Etching of PZT

An alternative to the PZT pattern by lift-off, excluding the IBE option which has shown an etching rate smaller than 15 nm/min, is the wet etching in buffered HF and HCl solution. Since PZT is etched by HF and the HCl helps removing the metal-fluoride residues in the reaction. This solution leads to high etching and high selectivity with respect to photoresist, and was tested on test samples deposited on Nb-STO.

Our SG epitaxial PZT, patterned with 10 μm large briges has shown an etch rate of about 100 nm/min with great selectivity. Tests were performed to check on the resist usage under such chemical attacks as well as to evaluate the lateral etching of PZT under such conditions. The PZT was patterned and then etched in a solution of buffered HF and HCl at 55°C. Leaving the sample up to 15 min under the etchant bath, the PZT undercutting was mainly evidenced in the corners by a round effect and measurable by the white borders in optical microscopy as demonstrated in figure 4.39. It has resulted in an etching rate of around 215 nm/min in accordance with values found in literature (Wang et al., 2002a). The lost of lateral resolution is due the use of PR for such prolonged time, a mask of silicon nitride or gold is better suited if PZT is to be etched longer than 30 seconds. Since there must be a gold contact for the PZT actuation, the mask gold may be kept for this objective, in the end. However, a lateral protection for the bottom LSMO should be envisaged since the etchant HCl would also etch LSMO as well as further studies on the effects of such process on LSMO's electrical characteristics.

The main difficulties in arriving to the end of the fabrication for such heterostructures, however, was in defining the gold contacts. First attempts were performed by KI etch of the patterned contacts, but the resolution of the patterns onto

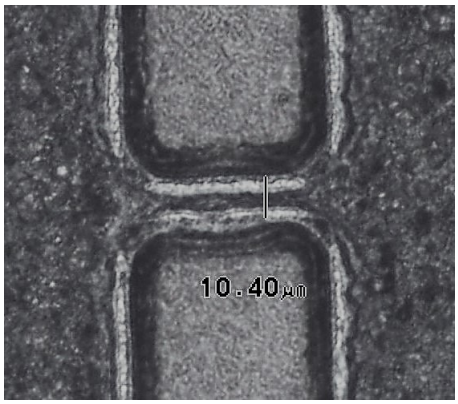

FIGURE 4.39: 100 nm SG PZT wet eching in buffered HF+HCl solution at 55°C

the beam was easily lost with a wet etching process. A few tests were also done by trying to pattern gold by lift-off, however, even after several hours in acetone bath, the lift-off wouldn't take place. Hot acetone and SVC14, a photoresist stripper, were also tested. Finally, in ultrasound, we managed to release the gold remaining to the ajacent borders of PZT patterns, however, again, the gold patterned structure lost resolution once ultrasound had to be performed several times to achieve the complete removal of unwanted areas of gold. The proposed solution hence lies in using IBE a directional etching technique that will well define these structures, avoiding lost of resolution or short-contact between LSMO and PZT contacts.

4.5.2 AlN actuated suspended LSMO beams on SOI substrates

The epitaxial LSMO/STO/SOI stack enables the possibility of highly textured c-axis AlN room-temperature deposition by PLD as shown in the previous chapter. Since AlN is to be used initially as a protection layer during the fabrication process against chemical etching of STO by HF acid during bridges release, the LSMO/STO must be first patterned and etched in order to ensure the covering of the complete bridge structure with AlN. AlN deposited by PLD under the same conditions to be deposited onto LSMO, was grown onto a Au/Cr/Si heterostructure and it was tested into HF acid at 20°C during 20 minutes resulting in no measurable etching.

A mask, designed in CleWin for a $10 \times 5mm^2$ sample, composed of four overlapped layers, was developed for this process. The alignment patterns consisting of $20 \times 20\mu m^2$ squares were disposed in 8 different points as defined previously, together with the first layer of the mask for the definition of the LSMO patterns as displayed in Figure B.1 in Appendix A.

Figures 4.40 - 4.42 show all the steps for this proposed process.

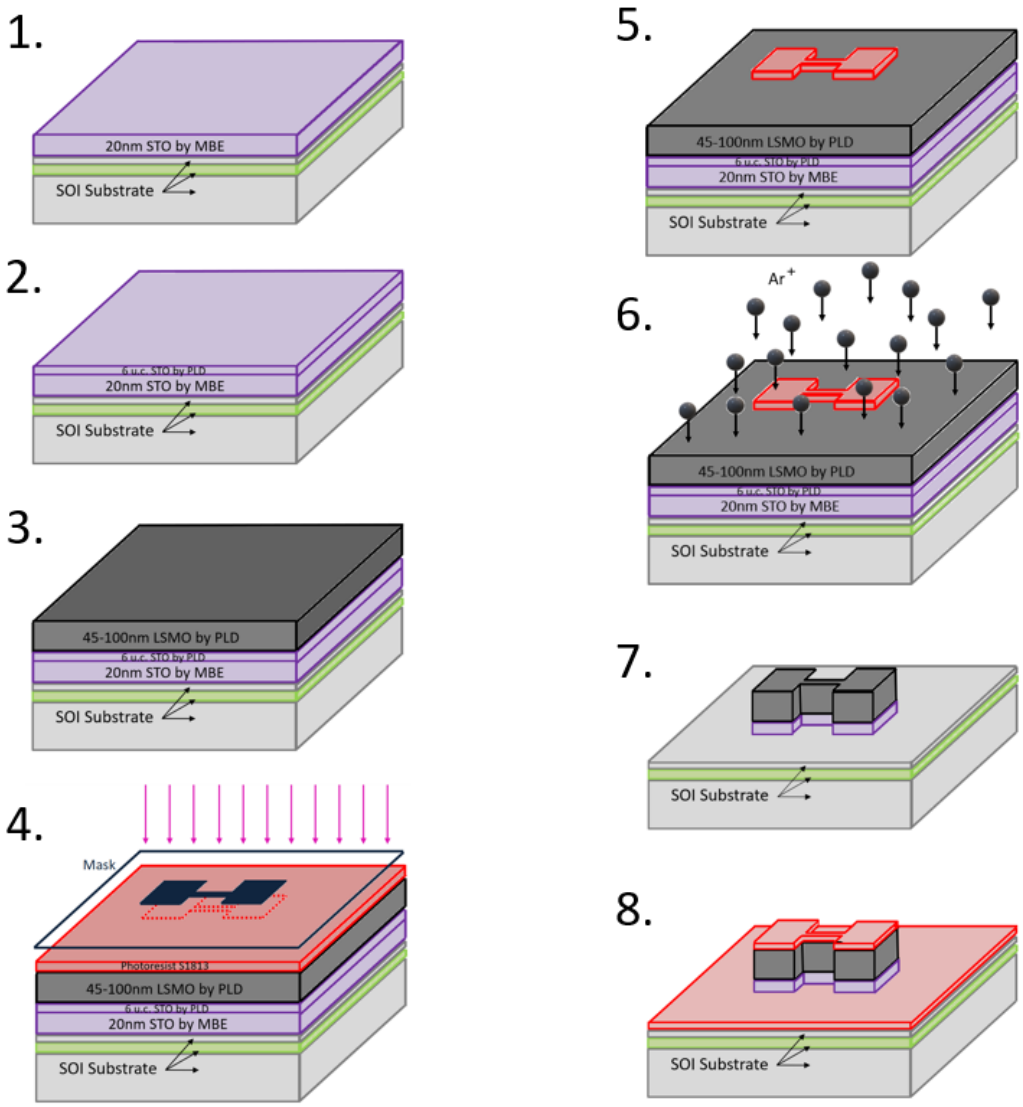

FIGURE 4.40: Schematics of fabrication steps 1-8

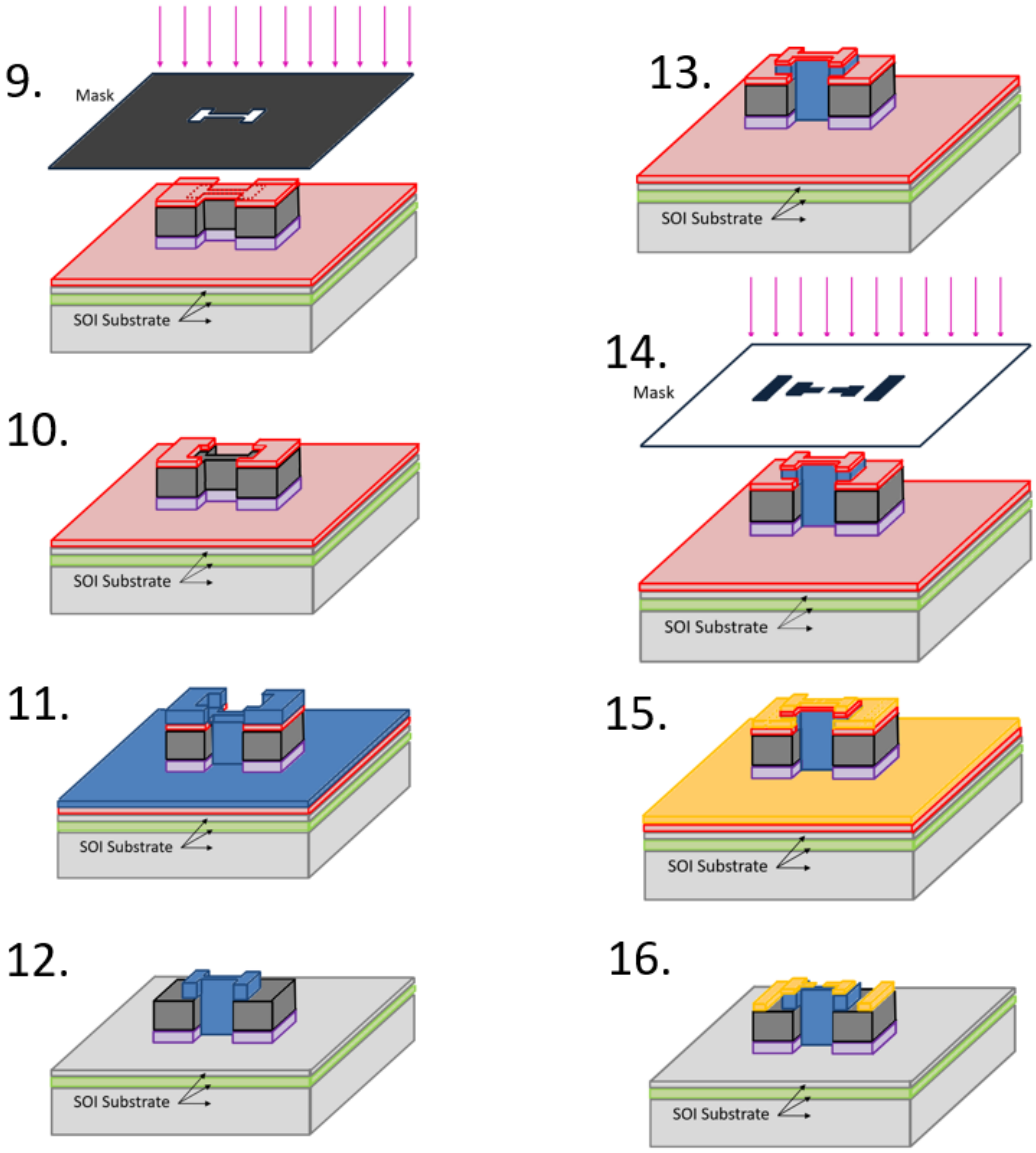

FIGURE 4.41: Schematics of fabrication steps 9-16

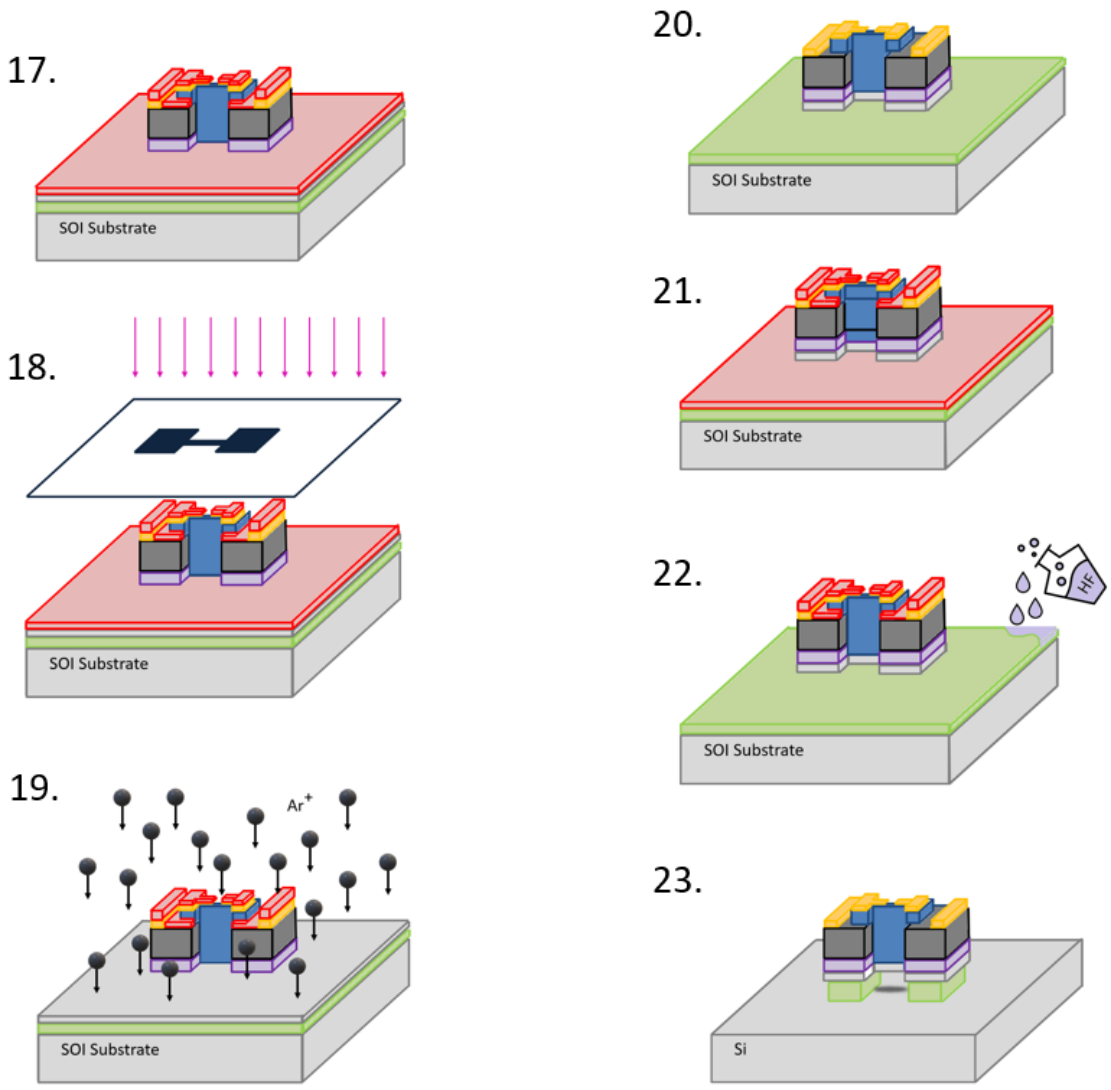

FIGURE 4.42: Schematics of fabrication steps 17-23

The laser photolithography in MicroWriter ML3 Pro was performed with the positive photosensitive resin (S1813). The sample was cleaned in acetone and ethanol baths and then annealed for 5 minutes in 90°C for evaporation of water. The deposition was carried out with a spinner for 40s with 4000 rpm which resulted in approximately 1700 nm of photoresist thickness which was then annealed for another period of five minutes again at 90°C. Testing doses were previously performed for each material to determine the necessary illumination dose and can be found in Table 4.2 and the resolution for exposure was set to 1 μm, since the smaller patterns are the bridges' width of 6 μm. The direct-write photolithography of the desired patterns requires the inversion of the mask to uniquely expose the exterior of the designed structures, a configuration that can be easily set by software, but shown inverted in Figure B.2 directly in the mask design itself for a more graphical understanding. This is represented by step 4 in the Figure 4.40 describing the whole

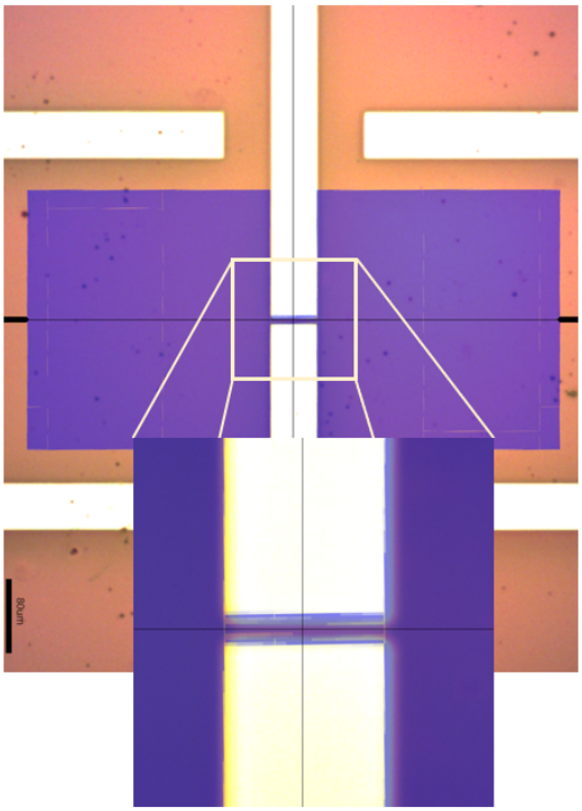

FIGURE 4.43: Lithography alignment between LSMO patterns of 6 μm large bridges and 10μm large AlN superposed ones to protect laterally the full beams

fabrication process. Steps 1-3 are the respective deposition of 20 nm of STO by MBE, 6 u.c. of STO by PLD and 45 nm of LSMO by PLD.

The patterned LSMO/STO in step 5 is etched by IBE in the sequence (step 6). Steps 7 and 8 show the etched bridge patterns with the LSMO contact pads for later gold deposition and the resist deposition in the sample, which is then submitted to new photolithography with the mask B.3 in step 9 and the development freeing the bridge area and its extremities in step 10 for larger AlN coverage of the whole beam and at the points of greater strain in final structure for actuation and detection (clamped edges). This coverage is better understood with the zoomed visualisation of LSMO and AlN masks superposition, Figure 4.43.

To avoid the time consuming ionic beam etching of aluminium nitride (see Table 4.4), AlN is then deposited by room temperature PLD technique with 9000 shots at a 5 Hz rate (step 11) followed by a lift-off process (step 12). At this point, both the LSMO and mainly the STO are protected by Aluminum Nitride (AlN) against future HF attack. A new layer of resist is deposited and patterned as the gold contacts for LSMO and for the piezoelectric actuation and detection (steps 13 and 14).

The next step was victim of several attempts of lift-off patterning and KI

etching techniques, being the main drawback in the complete fabrication tests to not arrive upon the final integrated device:

1. After defining the gold contacts by direct-write lithography for both AlN actuation/detection and LSMO electrical contacts with an inverted mask in order to keep resist in such regions, a lift off in acetone bath at room temperature was attempted. The sample was stirred for about 5 minutes intercalated with baths into hot acetone at 60°C for 10 minutes. This cycle was performed 3 times but no relevant patterning was verified. Gold was seen not only on the whole patterns regions but also all around it, being removed mainly just in the samples borders inhomogeneously. Finally, the sample was put into ultrasound to force the attached gold to be removed from the sample, but AlN deposited at room temperature onto LSMO has shown to have a very low adhesion and it was easily removed by this method.

2. The same procedure was attempted with SVC14, a high performance positive photoresist stripper formulation expected to remove resist easier than acetone for lift-off purposes. However, even leaving the sample for hours into SVC14 bath has not resulted in the desired patterns. Instead of using ultrasound again, a more mechanical method was tried by using a soft paper to help gold to be peel off the sample. This again have removed some parts of the deposited AlN.

3. The gold has been deposited onto AlN immediately after PLD deposition of AlN, in such a way that the AlN lift-off pattern has also defined the gold top contacts. This is shown in figure 4.44. From this point the gold was protected by both sides with larger squares of resist leaving just the region in the middle of the bridge at disposal for KI attack. This has separated the actuation and detection contacts, each side corresponding of 1/3 of the bridge length. However, the LSMO contacts were still needed, and by trying to use the lift-off technique for this part of the process, we had again problems in the small gap between the AlN and LSMO contacts, leading to short circuits in some parts of the samples. The order here must be inverted if this combination of lift-off and KI is envisaged to be used: first one must deposit gold onto LSMO and pattern its contacts followed by KI etching; From this step, the same process performed here for AlN plus gold deposition and further pattern by lift-off may be performed. At the end, the gold on top of AlN must be etched in the middle of the bridge as to form the actuation and detection contacts for AlN, one of each side of the beam.

If the test number 3 for contacts definition is believed to take too many steps and since the contacts on top of AlN must continue on top of the bridge, a highly directional etching will necessary, so, after gold deposition by PLD and gatan, in step

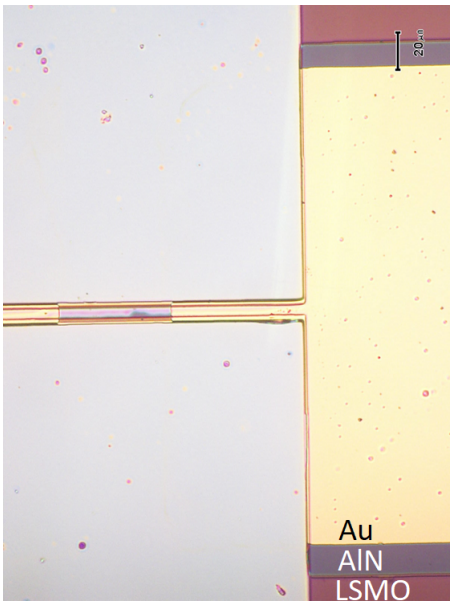

FIGURE 4.44: Clamped edge microscope image showing gold onto AlN onto LSMO perfectly aligned forming the full integrated actuation for the patterned bridges

15, it is proposed that the next process will be the IBE etching for about 3 minutes (step 16). This will require however an extra step into oxygen plasma using RIE for the removal of residual resist before continuing the determined process. From this point, the process shall continue with resist deposition, lithography of the complete pattern with the bridges now presenting the same width as the AlN's one (larger than LSMO bridge for lateral protection) in steps 17 and 18 shown in Figure 4.42. Such steps have been done without the piezoelectric integrated and are feasible with no great difficulties if the alignment patterns have been well designed. IBE is again performed to etch away the Si not belonging to the designed pattern, in step 19, and step 20 shows already the whole bridge structure that is to be released.

The complete fabrication process is finished in step 21 by the release of the clamped-clamped beam in HF bath that etchs SiO_2 underneath the bridge in a rate close to 100 nm/min. And the step 23 exhibits simply the final device, fully suspended. A better understanding on HF wet etching is given in the following topic.

4.6 Actuation using an external piezoelectric disk

4.6.1 Resonators clamped-clamped beam MEMS

Resonators based on MEMS, with different geometry layouts, fabrication techniques and packaging, find a wide range of typical applications such as chemical substances detection (Goeders, Colton, and Bottomley, 2008), (Fanget et al., 2011), biological substances detection (Hunt and Armani, 2010), (Eom et al., 2011), (Braun et al., 2005),

(Johnson and Mutharasan, 2011) and energy harvesting (Anton and Sodano, 2007), but also more complex ones such as resonant high-electron-mobility transistor (R-HEMT) (Faucher et al., 2009), resonant bolometers, among others.

They are all based, nevertheless, on the resonance phenomenon. A change in the resonant behaviour is detectable due to interactions with the environment (either light, magnetic field or chemical molecules, to name a few).

Our interest lies, however, into the harmonically forced vibration study of resonant MEMS, i. e., a system in which the oscillations are driven by an applied harmonic actuation force of amplitude F_0 and frequency ω characterized by the following force balance equation (Brand et al., 2015):

$$m\frac{d^2}{dt^2}u(t) + c\frac{d}{dt}u(t) + ku(t) = F_0 sin\omega t \tag{4.5}$$

which has a steady-state solution of the type

$$u(t) = \frac{F_0}{k}D(r,\zeta)sin[\omega t - \theta(r,\zeta)] \tag{4.6}$$

where

$$D(r,\zeta) \equiv \frac{1}{\sqrt{(1-r^2)^2 + (2\zeta r)^2}} \tag{4.7}$$

$$\theta(r,\zeta) \equiv arctan(\frac{2\zeta r}{1-r^2}), \in [0,\pi] \tag{4.8}$$

$$r \equiv \frac{\omega}{\omega_0} \tag{4.9}$$

where the coefficient F_0/k represents the quasi-static displacement amplitude achievable by the system if very low frequencies are verified, whereas the variable D is defined as the ratio of the dynamic displacement amplitude (u_{max}) to the quasi-static amplitude (F_0/k) and is therefore referred to as *dynamic magnification factor*. As for the other parameters, θ represents the lag angle of the displacement with respect to the applied force, r is the frequency ratio as defined in equation 4.9 and ζ is the damping ratio.

The exact value of D_{max} and the corresponding displacement amplitude at resonance is given by

$$D_{max} = \frac{1}{2\zeta\sqrt{1-\zeta^2}} \tag{4.10}$$

This leads to a theoretically infinite value for r=1 when the driving frequency coincides with the undamped natural frequency. If damping effects are considered, however, D_{max} occurs at $r < 1$ but still very close to $r = 1$ if $\zeta \leq 0.2$, such

that

$$D_{max} = D(r = 1) = \frac{1}{2\zeta} = Q \tag{4.11}$$

The quality factor, Q, can be experimentally evaluated in MEMS resonators through the bandwidth method (half-power method, for -3dB). Most well-designed MEMS resonators have quality factors well in excess of 5 (Brand et al., 2015). Once the shape of the resonant peak is known, the value of Q may be estimated by the formula

$$Q \approx \frac{\omega}{\delta\omega} = \frac{f_{res}}{\delta f} \tag{4.12}$$

where ω_{res} is the resonant frequency, $\delta\omega \equiv \omega_2 - \omega_1$ is the frequency bandwidth determined by ω_1 and ω_2 that are calculated for the response value of maximum amplitude divided by $\sqrt{2}$. The equivalent values in Hz take into account the relation $f = \omega/2\pi$.

All of the formulas listed are based on the assumptions that the material is linear elastic and isotropic with Young's modulus E, shear modulus G, and Poisson's ratio ν.

Therefore, when applying the results to an anisotropic material, such as silicon, care should be taken in specifying the equivalent isotropic elastic constants corresponding to the appropriate direction(s).

Also, each device is assumed to have a uniform mass density ρ (per unit volume), all support conditions are considered *ideal* (perfectly clamped, perfectly free, etc), effects of any surrounding fluid are neglected, and, unless indicated otherwise, all devices are assumed to have a uniform thickness h.

The simple deformations for beams structures can be described for three kinds of mechanical vibration, namely, axial, torsional and flexural.

The axial vibrations are the ones occurring along the x-axis for 1D structure beams and have its resonant frequencies calculated by

$$\omega_n = \lambda_n \sqrt{\frac{E}{\rho L^2}} \tag{4.13}$$

where $\lambda_n = n\pi$ for the doubly clamped beam, n being the mode number.

The torsional vibrations are the ones leading to twists about the x-axis and are given by equation 4.14:

$$\omega_n = \lambda_n \sqrt{\frac{4Gh^2}{\rho b^2 L^2}} \tag{4.14}$$

where b is the "width" dimension for such transverse case vibration.

Finally, the flexural (bending) vibrations out-of-plane (along z-axis) have the resonant frequencies at

$$\omega_n = \lambda_n \sqrt{\frac{Eh^2}{12\rho L^4}} \tag{4.15}$$

Table 4.13 shows the coefficients for doubly-clamped case. If the beam's width dimension (b for the transverse case and h for the lateral case) is not small relative to length L, this wide-beam effect may be taken into account in an approximate manner by replacing E with an *effective Young's modulus* of $E_{eff} = E/(1-\nu^2)$.

	Bridge
λ_1	4.730
λ_2	7.853
λ_3	10.996
$\lambda_n, n > 3$	$(2n+1)\pi/2$

TABLE 4.13: Dimensionless coefficients values for the calculation of the resonant frequencies for the flexural modes of a clamped-clamped beam structure

4.6.2 Dynamic Measurements

Attachment to external piezoelectric tests

The dynamic measurements of our samples in the DHM were performed using a commercial external piezoelectric with resonant frequency at 1.2 kHz or 4.2 kHz (reference KPSG-100 from KINGSTATE and ABT-441-RC from MULTICOMP PRO fabricants, respectively) to which the samples were glued for their evaluation under vibration. To guarantee the energy transfer from the external piezo to the fabricated structures, some tests were primarily done using an AFM cantilever with known resonant frequency.

I used a typical AFM Si cantilever double side coated on Pt (SPM probe model ANSCM-PT) of length 225 μm, width 30 μm and thickness $3\mu m$ with a radius tip smaller than 30 nm and k between $1-5N/m$. First the resonant frequency was measured using the Nano-Observer Scanner for the atomic force microscope from Concept Scientific Instruments (CSI) as demonstrated in figure 4.45.

From this information, I attached the cantilever from its extremity in the

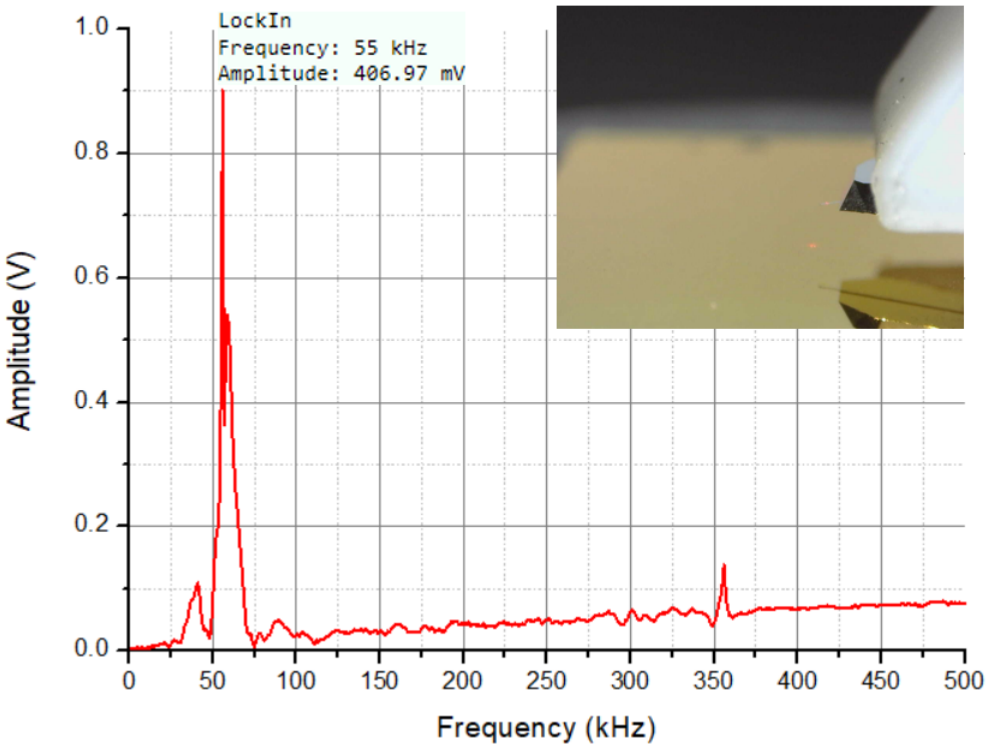

FIGURE 4.45: Resonance frequency of AFM cantilever measured by Nano-observer Scanner using CSI AFM

external piezoelectric by using a droplet of silver paste, to test the damping level this material would add to the system and verify is the vibrations on the cantilever would be measurable using the Digital Holographic Microscope, as in figure 4.46.

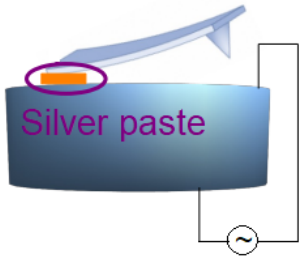

FIGURE 4.46: Setup for dynamic measurements on DHM using external piezoelectric disk

In Koala software, using a 50× objective, and taking 100 samples per period with a sinusoidal wave of 4 Vpp, I set a frequency range from 50 kHz to 60 kHz to be scanned and measured the displacement of the cantilever tip from the phase information numerically reconstructed from the holograms in three different points as shown in figure 4.47 using a synchronized phase monitor. Between 50-55 kHz a great change in amplitude had already been verified and the measurements could be stop in this range, which is shown as the axis x, as only half of the defined frequency

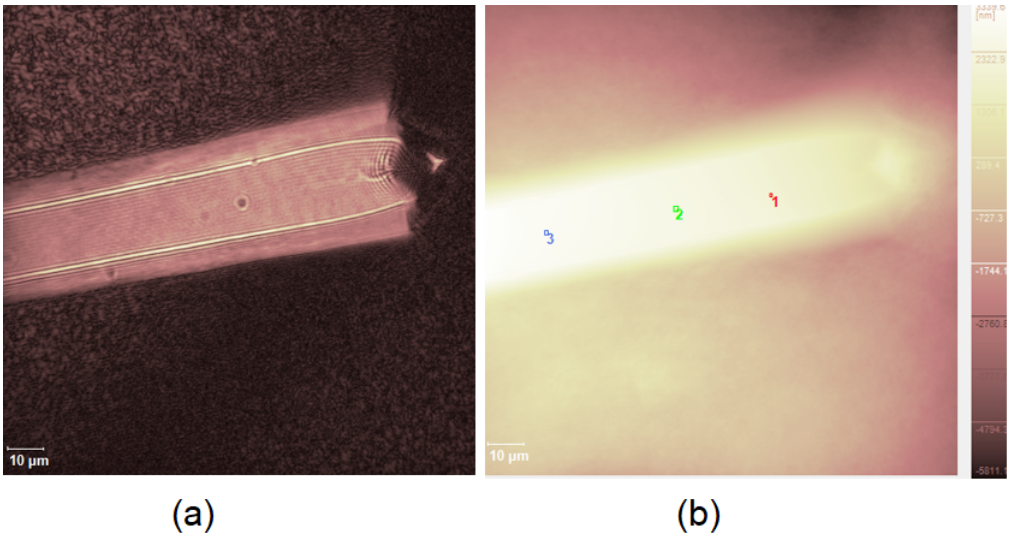

FIGURE 4.47: Measured points location on cantilever

scan range was displayed. The result is exhibited in figure 4.48 in the time domain where the resonant frequency was seen around 52.6 kHz in accordance with the previously measured value.

Bridges dynamic evaluation with external piezo forced vibration

Once the use of silver paste was validated as a reliable way to attach the samples to the external vibration source, simple bridges fabricated consisting of Al_2O_3/LSMO/ STO/SOS heterostructures were put under vibration through the coupling to an external piezoelectric buzzer using the same silver paste for transmission of the mechanical vibrations by using the set-up shown in figure 4.49.

The sample, consisting of 20 nm Al_2O_3, 45 nm of LSMO and 20 nm of STO suspended $3\mu m$ large clamped-clamped beams had its flexural theoretic first mode resonance frequencies calculated as

Length (μm)	f_R (kHz)
50	311.4
100	77.9
150	34.6
200	19.5

TABLE 4.14: Resonant frequency determination of Al_2O_3 / LSMO / STO suspended beams by equation (4.15)

Such values are extracted from the theoretical curve for such heterostructe with parameters shown in table 4.15 and graph plotted in figure 4.50.

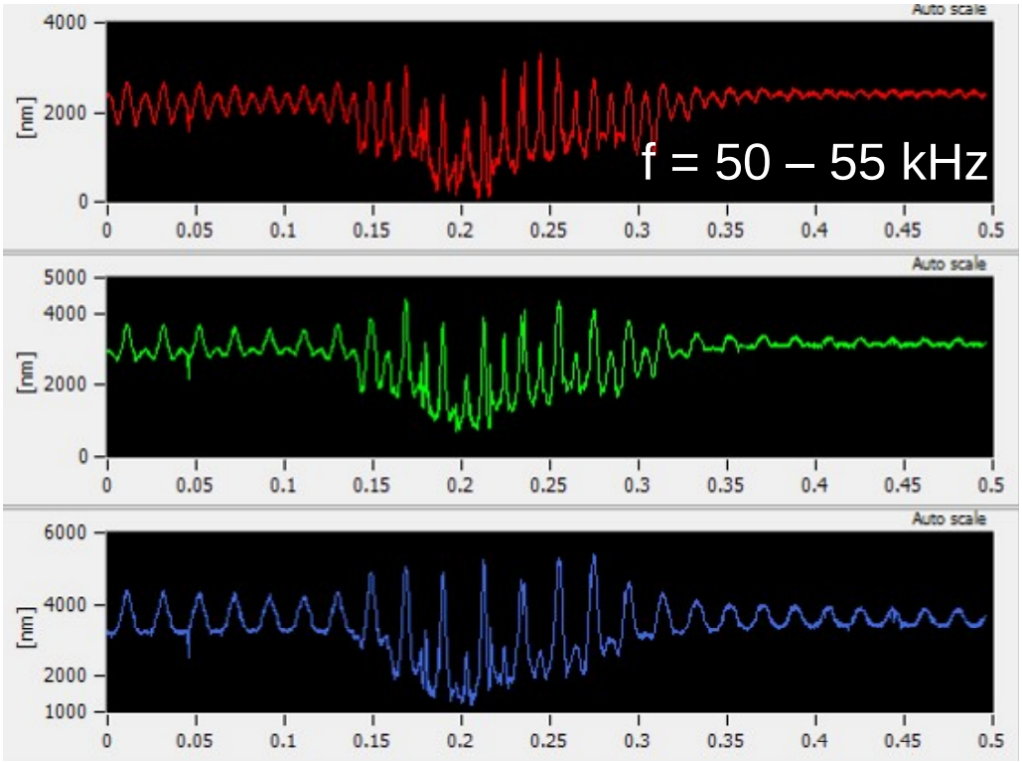

FIGURE 4.48: DHM measurements for AFM cantilever resonant frequency. The y axis represents the displacement exhibited in nanometers whereas the x axis defines the percentage of measurements range preset to be scanned.

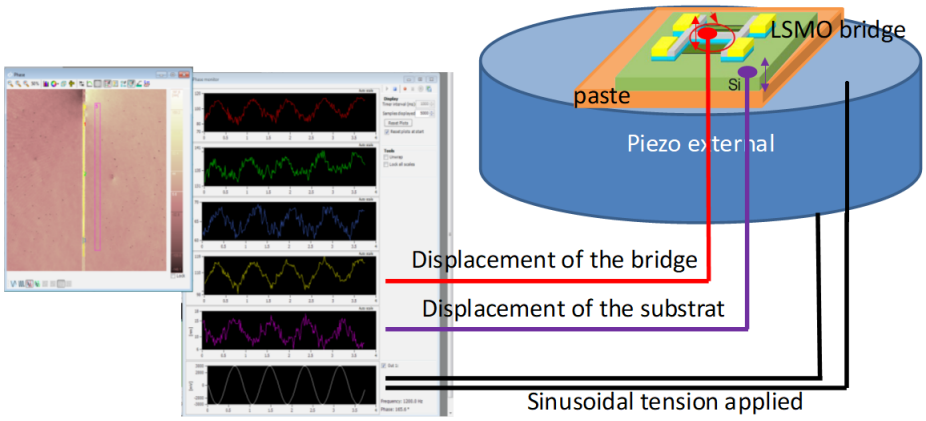

FIGURE 4.49: Setup for attachement of structures onto an external piezoelectric actuation source fed by the stroboscopic unit of the DHM

Material	Thickness (nm)	Young's Modulus (GPa)	Poisson ratio	Density (kg/cm^3)
Al_2O_3	20	215	0.21	3750
LSMO	45	562	0.43	6280
STO	20	238	0.22	5120

TABLE 4.15: Mechanical properties of materials for resonant frequency determination. (Auerkari, 1996) (Le Bourdais, 2015) (Huang et al., 2006)

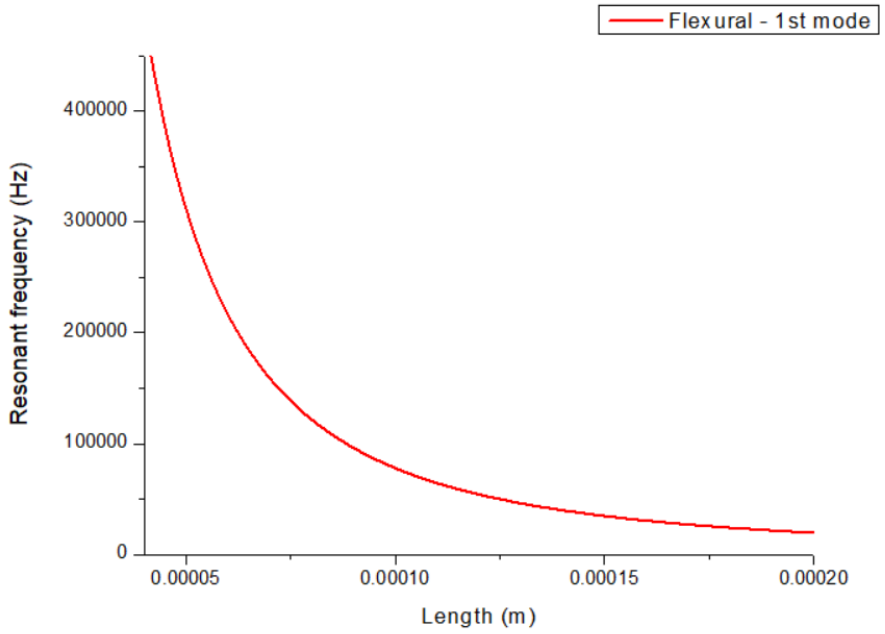

FIGURE 4.50: Theoretical curve for resonant frequencies for first flexural mode of clamped-clamped beams with parameters shown in table 4.15

The measurements were performed at the frequency ranges close to the corresponding theoretical values to evaluation of the first flexural resonant mode.

Since the displacements are no bigger than the maximum Δh for single laser measurements in the DHM, only the main one was used in order to have more precise measurements. The structures were put under vibration by feeding the external piezoelectric buzzer with 10V ac voltage (sinus wave). A duty cycle as small as 0.3% was used to acquire the phase measurements as to reduce divergences due to time average measurements at the chosen point since small deflections are expected. 50 samples per period were taken using steps of 200 Hz, 500 Hz and 200 Hz for the 100 μm, 150 μm and 200 μm bridges. The time domain measurements can be visualised in figures 4.51 - 4.53.

A relevant change in amplitude vibration was evidenced for the 100 μm, 150 μm and 200 μm bridges around 89 kHz, 46 kHz and 32 kHz as shown in Figure 4.54.

The bar error for each resonant frequency estimation was calculated from the gaussian fit of the increase in amplitude around such frequencies and is shown in Figure 4.55. The value 2σ was taken to achieve a precision of nearly 95%.

From the same parameters, a higher mode was evaluated to test the structure under vibration at frequencies in the order of hundreds of kHz. The resonant frequencies were calculated and are shown in figure 4.56, respective to the sixth

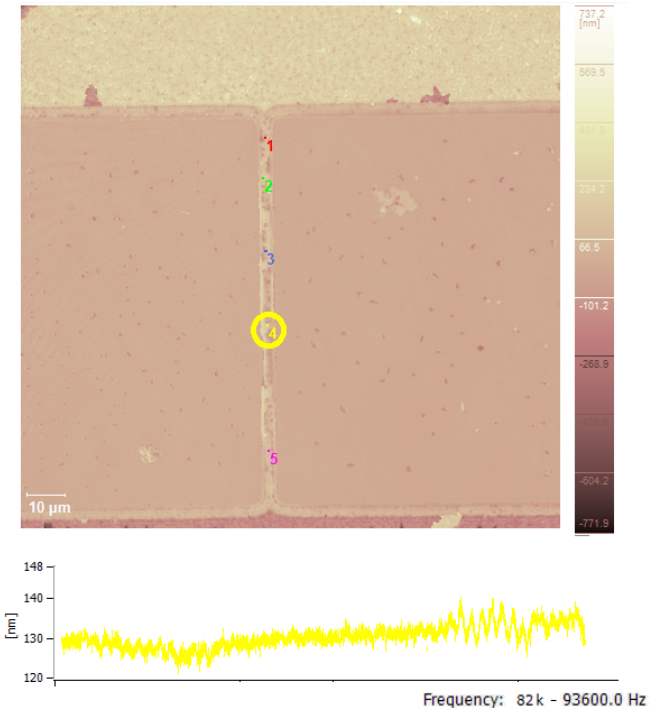

FIGURE 4.51: DHM measurement for 100 μm long Al_2O_3 / LSMO / STO 3 μm large bridges on SOS substrate glued to external piezoelectric material excited with a 10 V_{pp} sinus wave

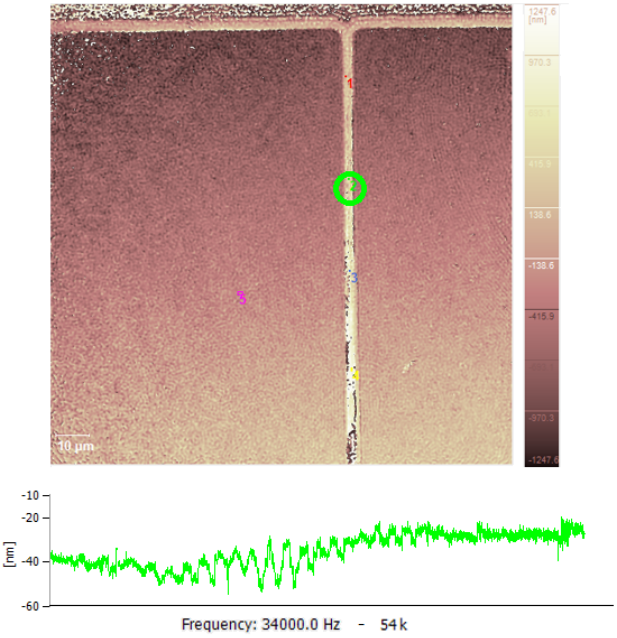

FIGURE 4.52: DHM measurement for 150 μm long Al_2O_3 / LSMO / STO 3 μm large bridges on SOS substrate glued to external piezoelectric material excited with a 10 V_{pp} sinus wave

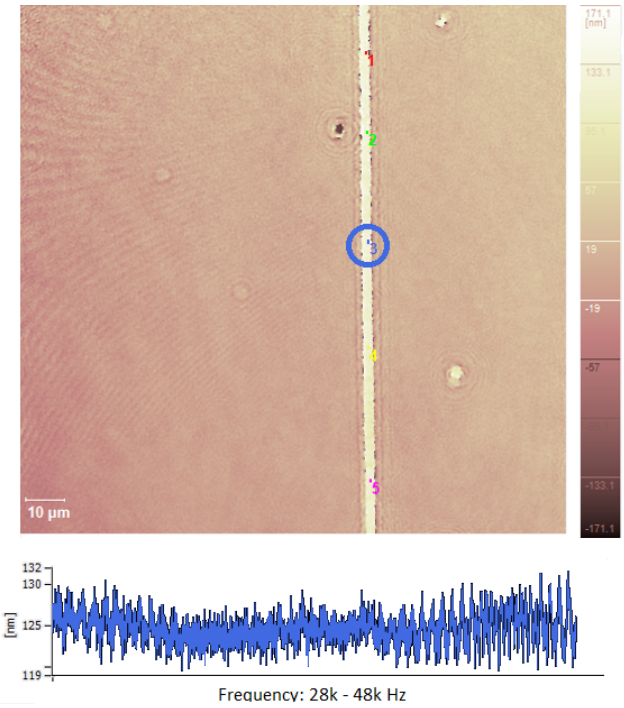

FIGURE 4.53: DHM measurement for 200 μm long Al_2O_3 / LSMO / STO 3 μm large bridges on SOS substrate glued to external piezoelectric material excited with a 10 V_{pp} sinus wave

mode of flexural vibration. Once the range of frequencies is known, measurements are performed in DHM through a frequency scan within the expected range with 50 samples by period and a duty cycle even smaller, of only 0.1%. The peak displacement values were evaluated and recorded for each measured frequency, to compose the frequency evaluations and such information was used to plot the displacement vs frequency curves for the 100, 150 and 200 μm long bridges.

From the differences between the measured values and the theoretical ones, a difference of tens of kHz is observed, the Young's modulus of the whole structure was re-evaluated as an *apparent* value by performing a fit for the measured values using the same law for resonant frequency calculation, using simply the $E_{volumetric}$ as variable, i. e., considering that all the incertitudes are reduced to the value of the elastic module of the whole bridge volume, seen together. Such value, previously evaluated as $E_{theory} = 404$ GPa was fitted as $E_{fit} = 587$ GPa and matches with the fit for the first mode resonance previously shown. It is also in accordance with the fact that the residual strain (ϵ) in the suspended beams would increase its elastic modulus, as shown by the more general equation:

$$f_0 = 1.028\sqrt{\frac{E_d}{\rho_d}} \cdot \frac{d}{L^2} \cdot \sqrt{1 + 0.295\frac{L^2}{d^2}\epsilon} \tag{4.16}$$

From the sigma values, one can still observe that as expected Q in inversely

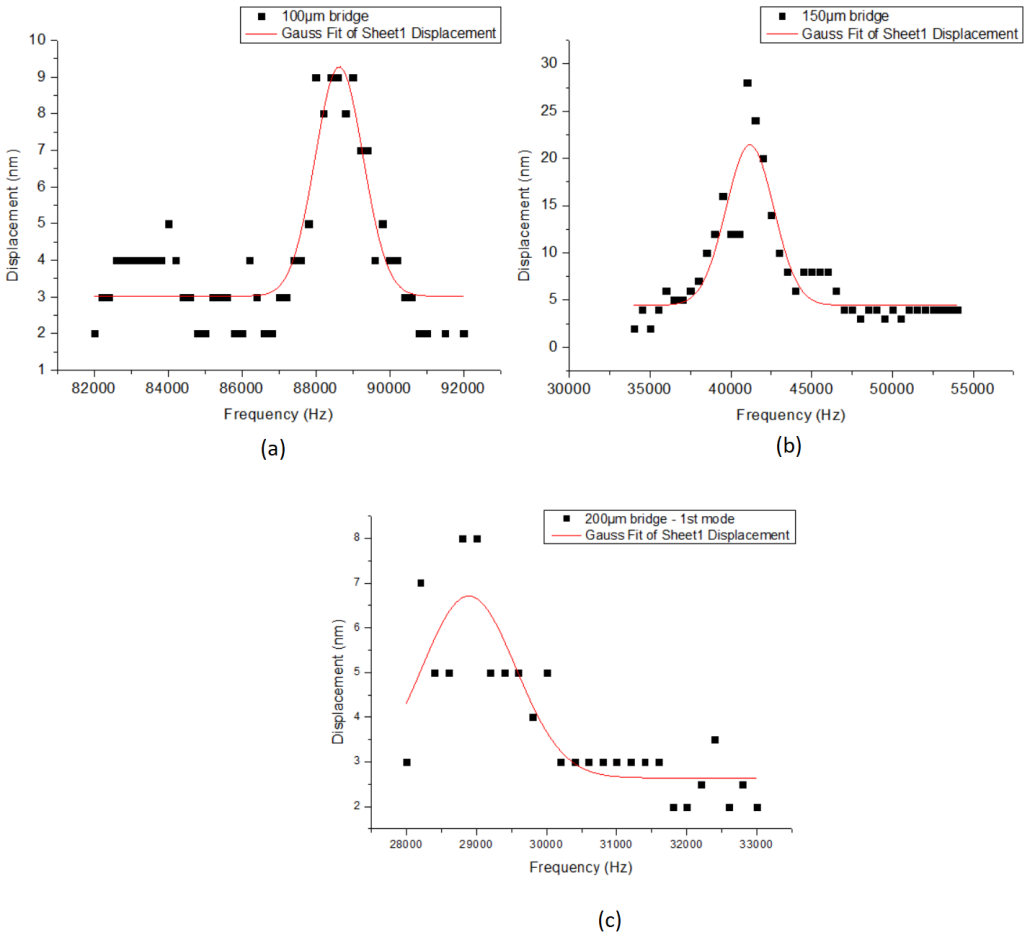

FIGURE 4.54: Measured points *vs* frequency and gaussian fit of the experimental values around the resonant frequency for 100, 150 and 200 μm long Al_2O_3 / LSMO / STO on SOS substrate: (a) $f_R = 88.6$ kHz, $\sigma = 648.6$, (b) $f_R = 41.2$ kHz, $\sigma = 1470.9$ and (c) $f_R = 28.9$ kHz, $\sigma = 669.1$

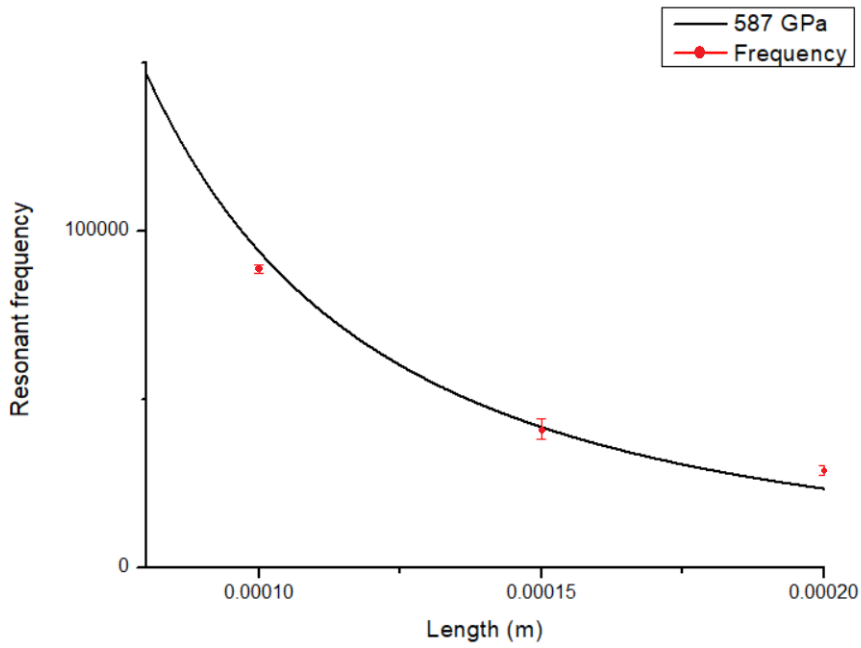

FIGURE 4.55: Fit for the measured points for a volumetric Young's modulus of the whole suspended structure as 587 GPa instead of the 404 GPa calculated one in theoretic calculations for Al_2O_3 / LSMO / STO suspended beams

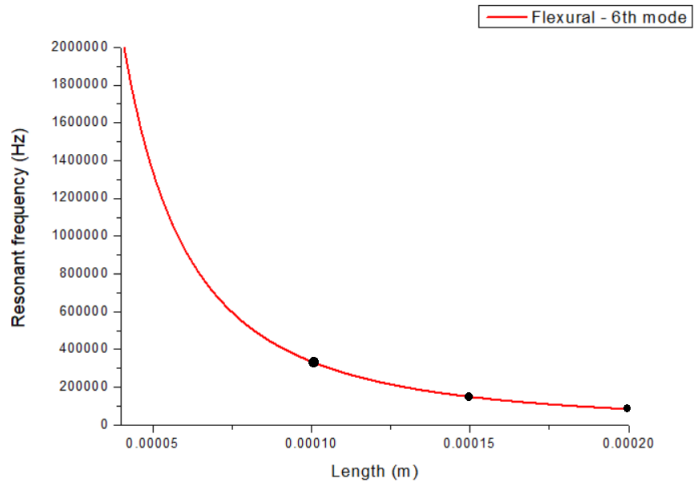

FIGURE 4.56: Theoretical curve for resonant frequencies for sixth flexural mode of clamped-clamped beams with parameters shown in table 4.15 for Al_2O_3 / LSMO / STO / SOS suspended bridges

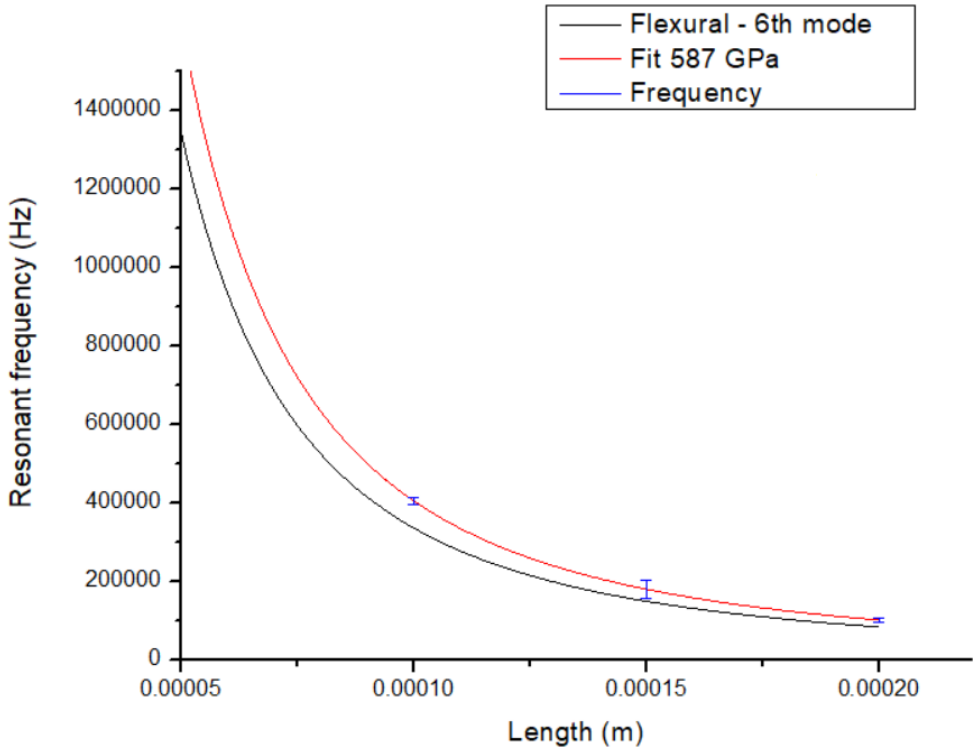

FIGURE 4.57: Measured frequencies shown upon comparison with the theoretical curve and best fitting curve for the volumetric average Young modulus, $E = 587GPa$.

proportional to the resonant frequency, and the fact that we manage to fabricate structures with lower resonance frequencies enhance our quality factor. The measurements here were all performed in air, which greatly reduced the quality factor for the structure, however some measurements under vacuum are already envisaged in order to estimate the performance of future application of these devices as resonant MEMS bolometers.

4.7 Conclusion

Successful fabrication of suspended bridges onto different substrates was achieved by following the fabrication process proposed by (Liu, 2019). The parameters for SOS, however, had to be better evaluated since the limited thickness of silicon sandwiched between LSMO/STO and sapphire substrate, typically 700 nm, considerably reduces the lateral etching rate of silicon.

Suspended simple bridges were fabricated onto both Si and SOS and it was verified in confocal microscopy that LSMO grown on STO buffered SOS substrates indeed exhibited smaller strain. From this information, we have subsequently tested such structures in dynamic mode, put on oscillation by being attached to an external piezoelectric disk, driven and measured by DHM in stroboscopic mode. The resonant frequencies were a few kHz higher than theoretical values and the bridges were

proved to have enough mechanical resistance upon resonant vibration as no beams were broken.

Masks based on the same design were drawn using CleWin software, first optimizing the alignment structures size after a few initial tests and then dynamically adding to this base structure pattern all the subsequent layers proposed in the definition of the new process for the integrated devices, that were continuously changed and optimized considering the order the steps that should be taken or even resolution problems. Test doses were performed for all the materials used as well as etching rate evaluations. AlN's stability was tested in advance against HF acid and it has showed no etching, proving the ideal material for our proposed fabrication on SOI substrates, however, its inadvertently etching in developer solution has led the fabrication process to be done in such a way as to avoid its contact with the developer.

One of the main problems encountered during fabrication was the definition of the gold contacts on either PZT or AlN. For AlN, a solution based in inverting the order of contacts definition (first LSMO pads definition through lithography followed by KI etching, then AlN ones by lift-off procedure at the same time of AlN itself) is believed to be sufficient for solving the problem since I could manage to achieve up to this point in fabrication with great alignment of all the structures and feasibility of pattern by lift-off. This must be soon enough achieved, since due to technical problems (machine failure) the fabrication had to be put on hold as I finish this thesis, and could be an issue for an upcoming article. For PZT, the contacts must be etched by IBE technique, since no lift-off was ever successfully achieved neither on top of the PZT neither in the adjacent areas. This has happened for 3 different PZT samples and we were lead to believe that probably the PZT roughness was playing a major role into sticking gold to its neighbourhood. However, since we arrived to pattern Pt electrodes onto the same PZT samples where gold showed difficulties, it is believed that our ion beam deposition gatan system deposits gold somehow conformal around the tridimensional borders of the already patterned structures in our samples.

Chapter 5

Conclusion and future perspectives

A proof of concept for a new approach in integration of high-quality epitaxial $La_{2/3}Sr_{1/3}MnO_3$ (LSMO) thin films onto $SrTiO_3$ buffered silicon (Si) and Silicon-on-Sapphire (SOS) substrates was performed, with detailed structural and electrical characterizations of the LSMO/STO/SOS heterostructures where the LSMO film properties were competitive with those directly grown on oxide substrates. The fabrication of simple suspended bridges onto industrially compatible SOS substrates was shown as a manner of achieving suspended structures with smaller residual strain which was verified by confocal measurements, hence, less rigid for dynamics evaluation for the development of applicative MEMS devices. So far no attempts have been made on the integration of manganite films on SOS substrate.

The proposal of the completely integrated structure disposing of self-actuation and detection was done by the study of several heterostructures compatible with the full developed clean-room fabricated process. For this, we have successfully demonstrated epitaxial integration of PZT onto LSMO/ STO thin films on Si substrates by three different deposition methods, where the rocking curves are comparable with habitual values on SRO-STO substrates and also comparable with good values reported in literature (Nguyen et al., 2017). Such epitaxial PZT films, even if deposited with considerably low temperatures when compared to typical PZT deposition found in literature, exhibit sufficient piezoelectric effect for MEMS applications actuated with low driving voltages (10V). Room temperature sputtering deposition allowing PZT pattern by lift-off process have shown comparable performance with the higher temperature processes, either sputtering at 600°C or sol-gel followed by RTA technique, when deposited with about 240 nm thickness to avoid leakage currents.

High contrast of stable artificially poled ferroelectric surfaces was evidenced, proving the good ferroelectricity of the films and P(E) was also found to be comparable with good PZT found in literature (Deshpande and Saggere, 2007).

The use of room temperature deposited PZT, besides the shown excellent

results, has the advantage of allowing a full room-temperature process. The RTA process largely reduces the duration time at high temperature decreasing grain size for the PZT films and also the possibility of any chemical reactions/elements diffusion between films and substrate. However, the lift-off of gold contacts onto PZT was hardly accomplished for several samples, requiring its contacts to be etched by IBE technique. The latter option has not been demonstrated during this thesis due to lack of time.

AlN, a lead-free material, has also shown good piezoelectric properties and excellent chemical stability upon HF acid attack. Due to the low adhesion verified between as-grown AlN by RT PLD deposition and LSMO/STO thin films, the order of lift-off and contacts definition has shown to be crucial to the success of device fabrication. This means that, the big contact pads for LSMO contact can be primarily fabricated by simple lithography and KI etching since no greater definition is necessary. However, the contacts for AlN actuation and detection region in the clamped edges of the bridge structure need to be done separately for two reasons: the first, the need for micrometer resolution on top of the bridge pattern on both sides, and the second being the small gap in our design between the LSMO and AlN contacts that have shown to make lift-off of both contacts at the same time with simple acetone bath prohibitive (in such cases where ultrasound was used the lift off was verified, however the AlN patterns mainly on the bridge patterns would also be partially removed). Other attempts have been tried to define all the device contacts, but they had all led to dead ends in the fabrication process. The order inversion proposed however is very promising since the most difficult part which is defining the contacts for AlN due to the need of a very good alignment and the micrometer resolution on top of the bridge have already been successfully achieved.

Due to the higher amplitude and higher stability of the output signal, the first resonant mode of vibration of the beam was chosen in order to investigate its electromechanical properties. The structures were put under vibration in air environment through an external excitation and had their resonant frequency measured via a synchronized phase monitor of a Digital Holographic Microscope using the composition of two different wavelengths allowing to set a reference on the substrate without the appearance of phase jumps during measurements.

From such measurements, it was possible to evaluate the effect of the strain as an increase in the Young's modulus of the complete heterostructure - the mechanical parameter that measures the stiffness of the solid stack of materials - for bridges composed of Al_2O_3/LSMO/STO on SOS commercially available substrate. A higher resonance mode was also measured for verification, but at hundreds of kHz range the measurements become noisier, the duty cycle must be again reduced to attempt to capture the smallest time fraction for each sample per period for the phase evaluation to follow the bridge vibration at such high frequencies. Although DHM allows

the dynamics measurements up to 25 MHz, it was found that in the MHz range, the number of possible defined number of samples/period is greatly reduced, which makes it impossible an assertive evaluation in time domain with only 9 samples acquired per analysed period. The microscope disposes of a MEMS toolkit specialized for such measurements that must enable the frequency sweep over a larger range of frequencies than we can now, in much less time. For further evaluations of devices, and to use the proposed fabrication described in this thesis in future applications, the acquisition of such toolkit should be considered.

To go further into the devices characterization, measurements under vacuum are expected to be made to increase the quality factor and to allow the performance evaluation into realistic resonant bolometers.

Finally, this thesis proposes solutions for the possible choice of the substrate, electrode and piezoelectric materials, for the process flow to be followed and for the measurement of the resonant properties. Even if the final piezo-LSMO integrated MEMS device has not be successfully fabricated I am confident that we are close to success and that this innovative devices can show improved performance in the field of resonant bolometers or magneto-electric sensors in the future.

Appendix A

RHEED

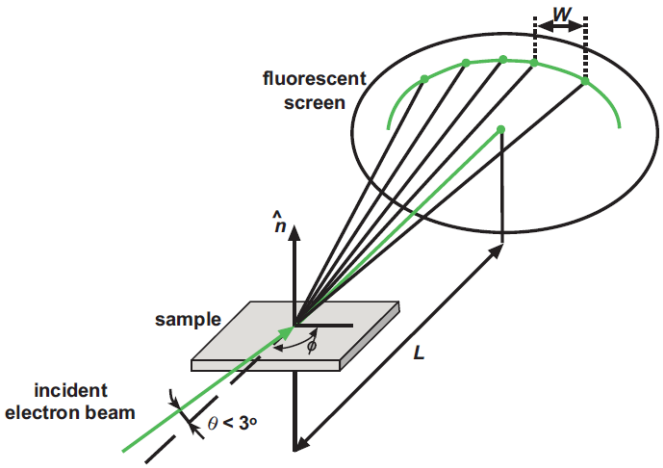

FIGURE A.1: Schematic diagram of RHEED geometry with incident electron beam at an angle θ to the sample's surface plane and the respective RHEED pattern (Morresi, 2013)

The incident electron beam generated by thermionic emission strikes the sample's surface at near-grazing incidence (an angle θ of incidence normally in the range 1^o - 3^o) so the penetration depth of the electron beam into the sample surface is limited to a few nanometers before it is reflected onto a phosphorescent screen.

Based on Laue method, a crystal generates a set of diffracted beams that show the internal symmetry of the crystal thus enabling to generate stereographic projections of such crystals trough the so called Laue diagrams, that take into account Bragg's Law:

$$n\lambda = 2d_{hkl}sin\theta_{nh,nk,nl} \tag{A.1}$$

where n is the integer number referring to the order of diffraction, λ is the wavelength and d is the interplanar spacing; for a given d, the diffraction pattern contain the diffracted beams corresponding to the first order of diffraction, n=1, of a certain wavelenght, the second order, n=2, of half the wavelength $\lambda/2$ and so on.

The maximum intensity of the diffracted beams is seen when the difference between the wavevectors of the incident and diffracted beams, k and k' respectively, intercepts the reciprocal lattice rods shown in figure A.2a for a two dimentional periodic lattice with unit cell vectors denoted as a and b. An Ewald sphere of radius k (equal to the magnitude of the wavevector of the diffracting electrons) is then defined such that the end of the incident wavevector intersects the origin of reciprocal space as in figure A.2b (Diehl et al., 2003). The intersection of the Ewald sphere with the reciprocal lattice rods provides the positions of all possible diffraction peaks from the surface structure that generates this set of rods, i. e., it selects the electrons with wavevectors k', forming spots on the screen (Morresi, 2013) that give the signature of the deposited layer, the Fourier transform of the sample crystalline structure in reciprocal space (Yin, 2013b). An ideal surface presenting perfect-ordered atoms exhibits a series of streaky lines on RHEED pattern whereas diffused lines with lower contrast will be seen in case of real crystalline surfaces, however, if the surface is not flat, this will result in many scattered electrons transmitted through surface asperities to all directions leading to a RHEED pattern constituted by many spotty features indicating a 3D growth mode.

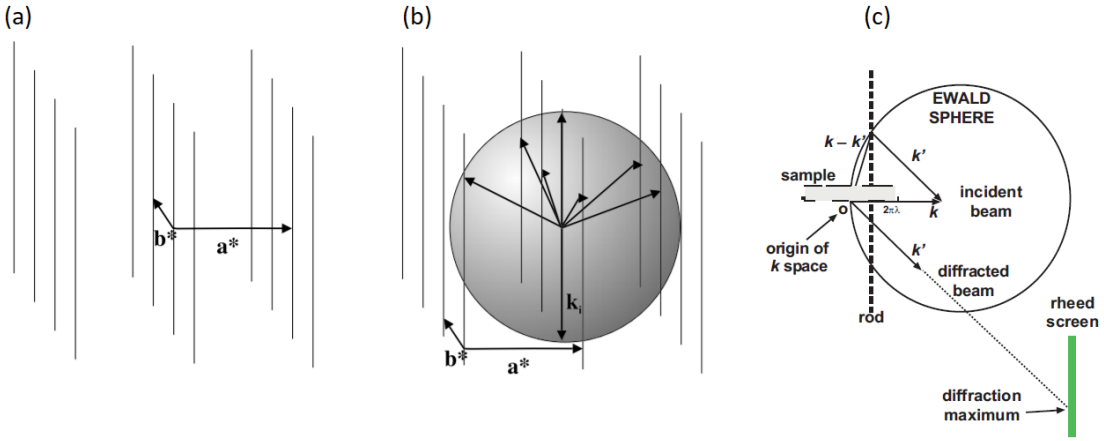

FIGURE A.2: Schematic diagram of (a) reciprocal lattice rods, (b) Ewald's sphere construction Diehl et al., 2003 and the intersection between the Ewald sphere and a particular reciprocal lattice rod (Morresi, 2013)

RHEED intensity oscillation can still be used for thickness evaluation of the deposition, since for a 2D growth, one oscillation period of a specular electron beam corresponds exactly to a monolayer of the film grown during this period and together with RHEED patterns this feature can help fully monitor all the important parameters for optimal growth, such as crystalline structure, lattice constants, surface roughness, growth mode and number of monolayers. The oscillation period depends on the material flux to the surface, the substrate temperature and the growth mechanisms (Morresi, 2013).

Appendix B

Masks for AlN/LSMO/STO/SOI

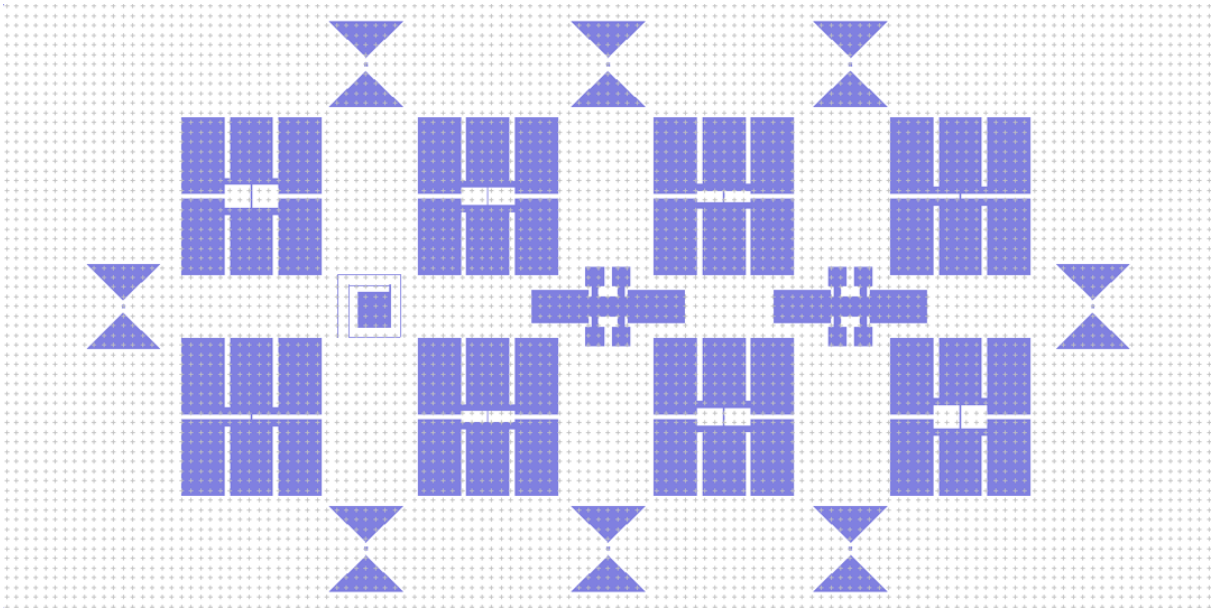

FIGURE B.1: Layout of the LSMO patterns

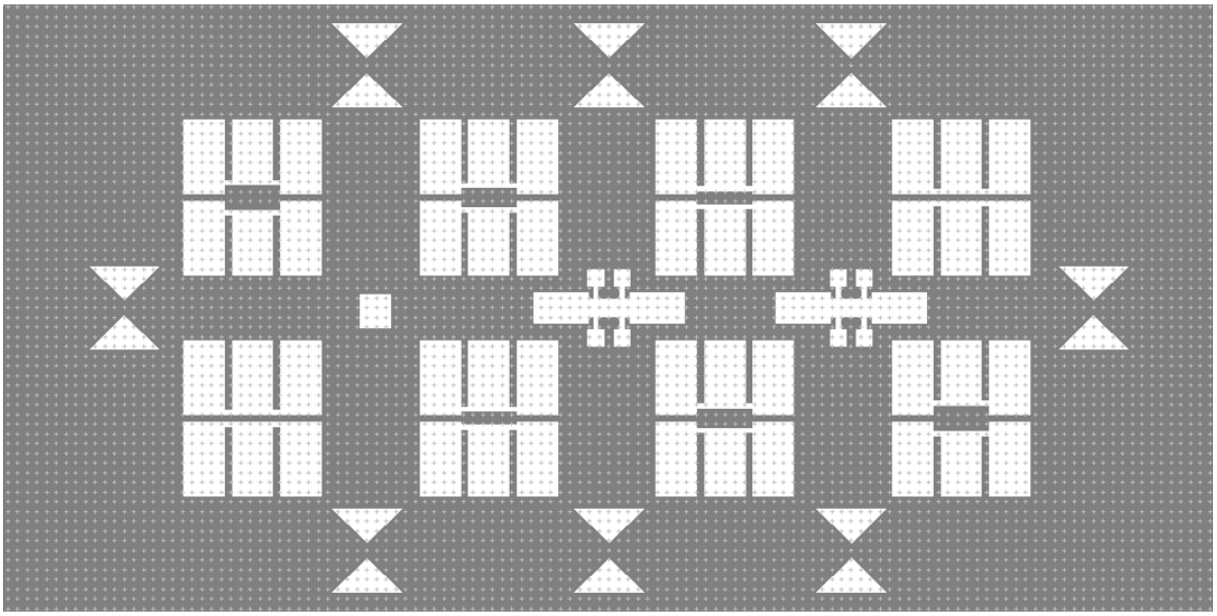

FIGURE B.2: Layout of the LSMO inverted patterns

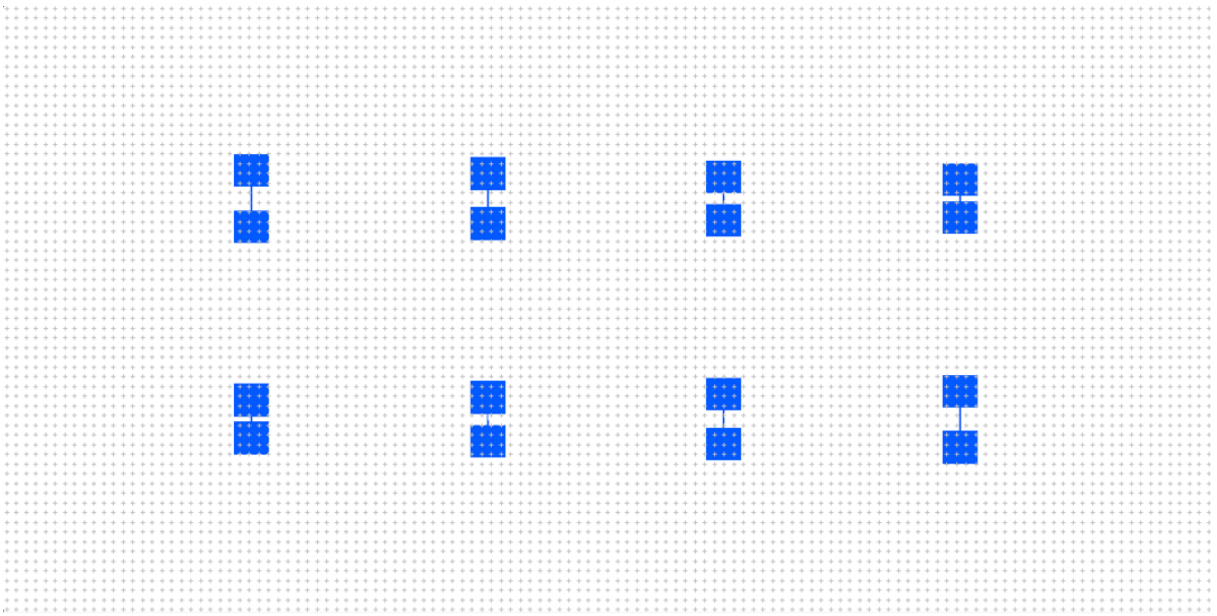

FIGURE B.3: Layout of the AlN patterns

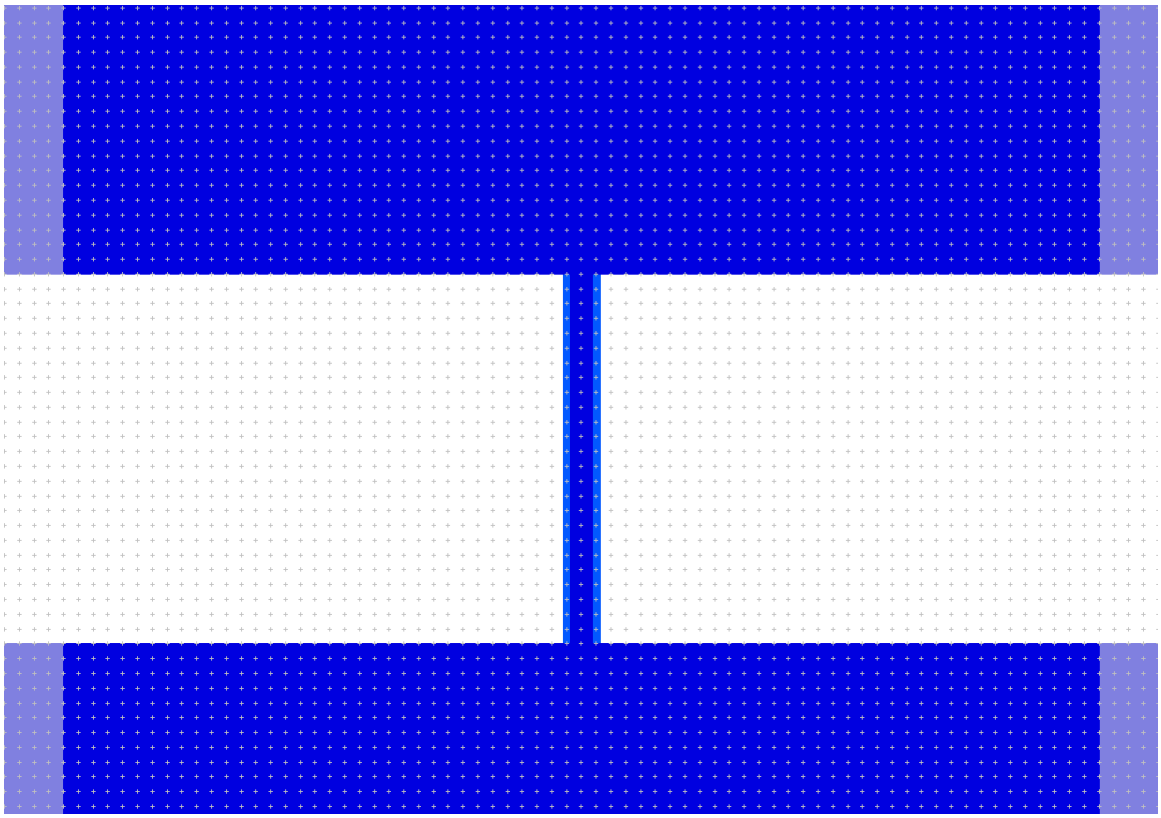

FIGURE B.4: Layout of the AlN superposed on LSMO patterns

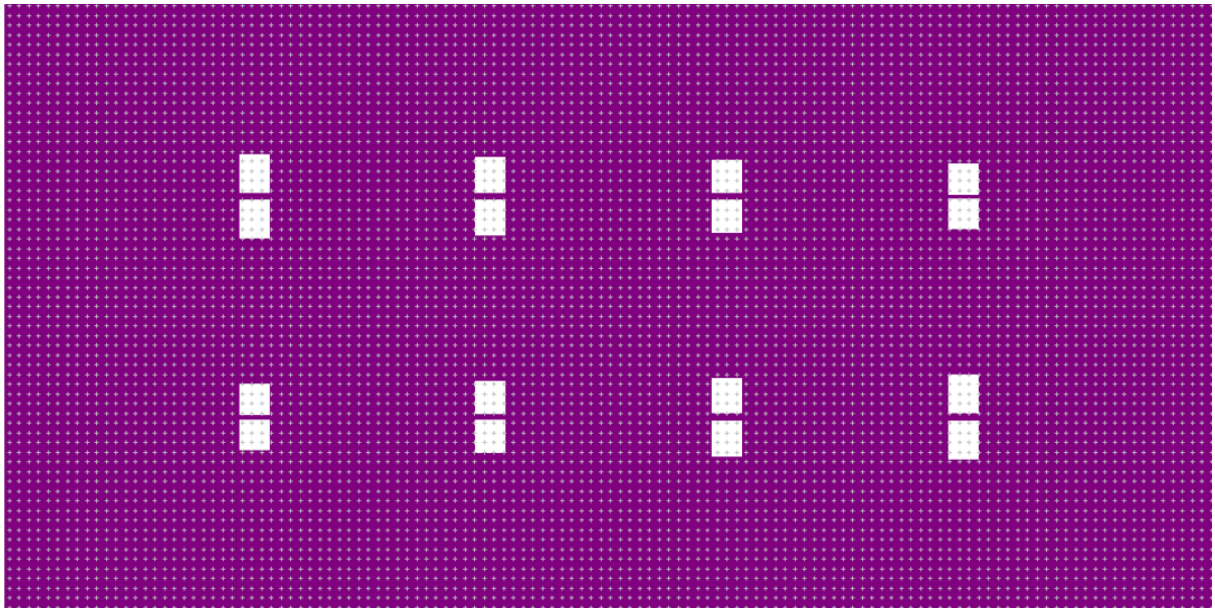

FIGURE B.5: Layout of the lithography pattern for definition of top contact for the AlN patterns

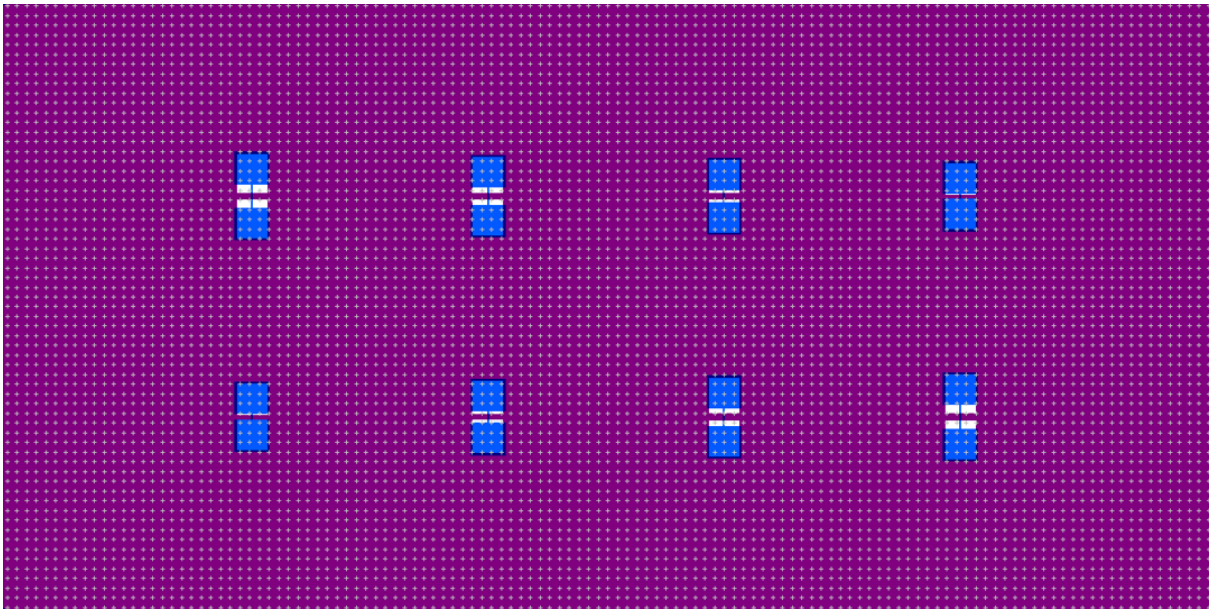

FIGURE B.6: Layout of the lithography pattern for definition of top actuation contact superposed on the AlN patterns

Appendix C

Width measurement for resistivity calculation

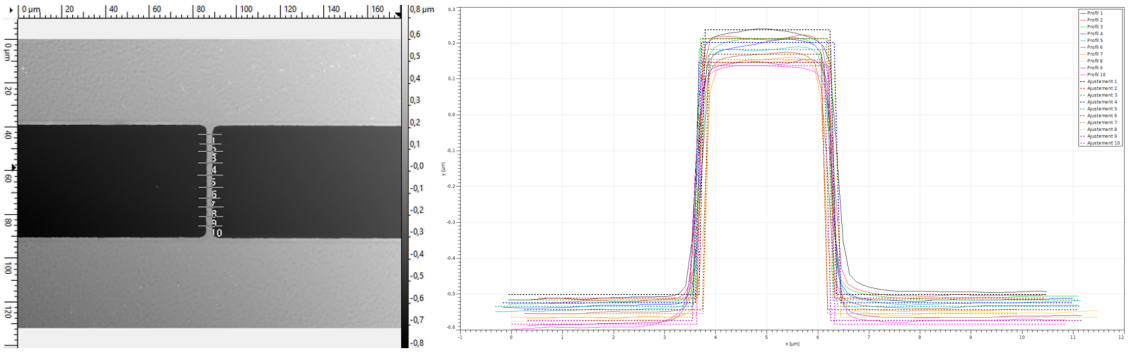

FIGURE C.1: Points measured in transversal profile of 50 μm bridge for width evaluation

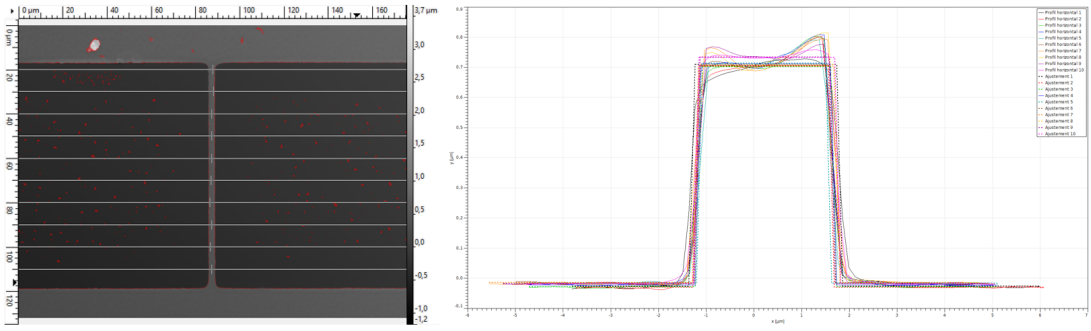

FIGURE C.2: Points measured in transversal profile of 100 μm bridge for width evaluation

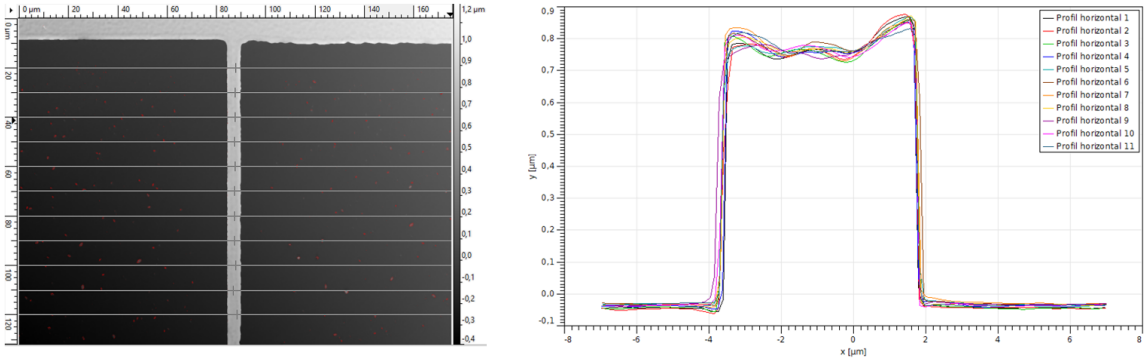

FIGURE C.3: Points measured in transversal profile of 150 μm bridge for width evaluation

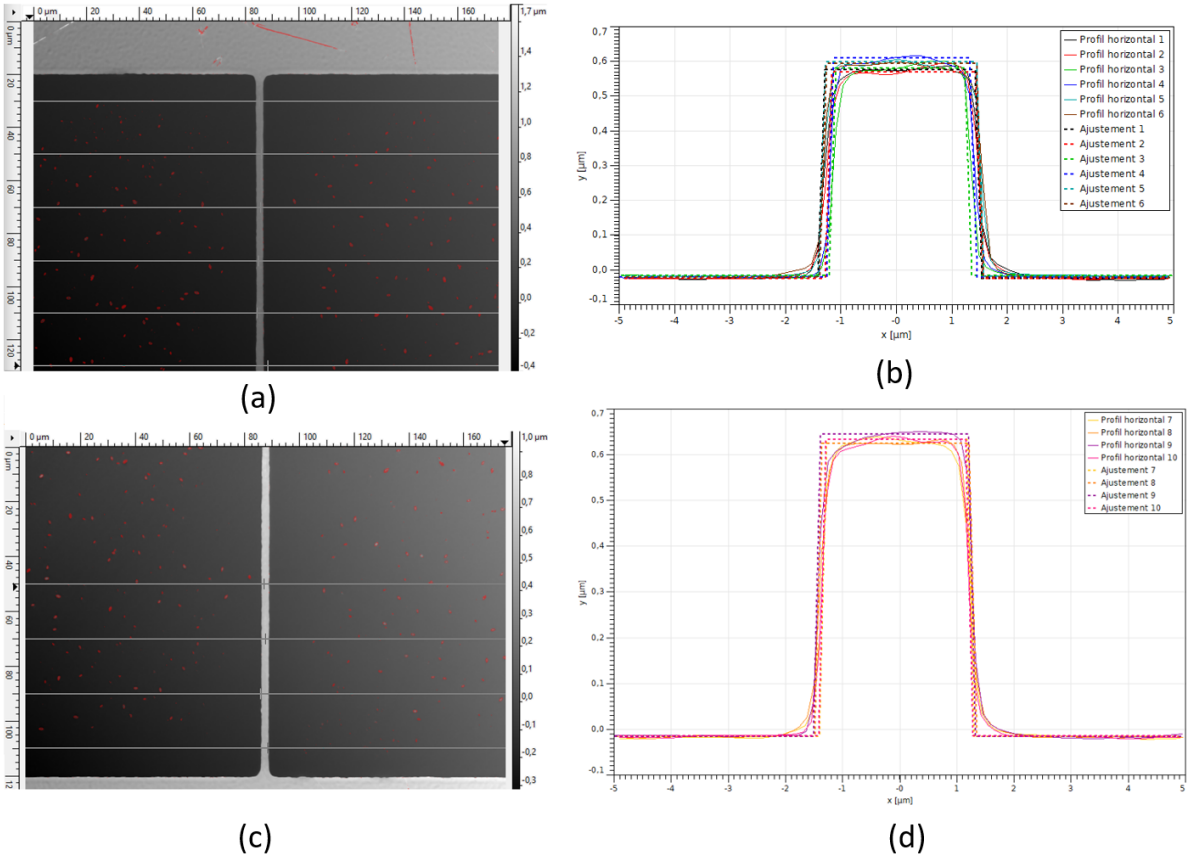

FIGURE C.4: Points measured in transversal profile of 200 μm bridge for width evaluation

Appendix D

HF safety rules manipulation

FIGURE D.1: Personal protective equipment for prevention measures when manipulating HF

Appendix E

SOI substrates fabrication

SOI wafers basis formation is the silicon direct bonding to an oxidized silicon wafer, which results in strong silicon-oxygen bonds and visualized in Figure E.1. The result is a silicon top layer electrically insulated from the bottom wafer enabling, in the semiconductor industry for example, the optimization of device properties in the device layer. This technique is known as BESOI (bond etchback SOI), and is only one of the large variety of achieving SOI substrates.

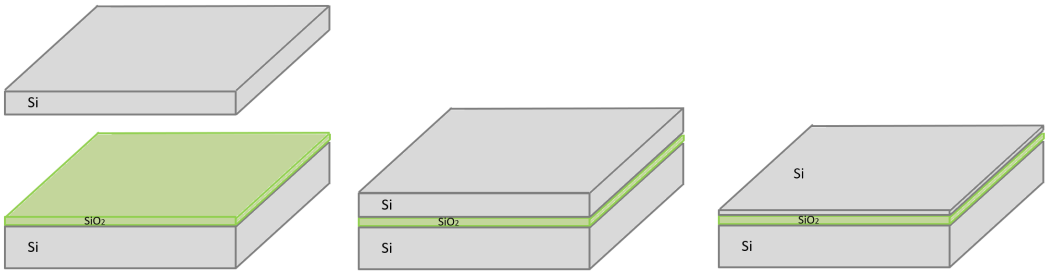

FIGURE E.1: Silicon-on-insulator (SOI) wafer fabrication by bonding an oxidized wafer to a silicon wafer: surface preparation, room temperature joining and annealing (bond improvement) and subsequent top wafer thinning

A standard RCA-1 cleaning process is applied to the bare silicon wafer to remove organic residue and films from the wafer by the decontamination work based on sequential oxidative desorption and complexing with hydrogen peroxide, ammonium hydroxide and water (H2O2-NH4OH-H2O). A further cleaning RCA-2 may be needed to complete the surface cleaning with H2O2-HCl-H2O. This step leaves the surface smooth with a rugosity smaller than 0.5nm and in a hydrophilic condition with silanol groups (with the connectivity Si-O-H). If the oxide is, however, grown by a chemical vapour deposition (CVD) method, a chemical mechanical polishing (CMP) may be necessary in order to guarantee enough smoothness for successful bonding, since already neither is the surface perfectly flat nor have the hydrogen bonds long range.

An oxide layer can be grown in the second Si wafer by thermal oxidation, a process exhibiting negligible incubation period in the 800°C-1000°C temperature

range, but not in low temperature processes (Massoud, 1995), where other techniques such as PECVD would be preferable.

The bonding of hydrophilic silicon surfaces is done via intermediate water molecules. A mild thermal treatment is needed to achieve satisfactory surface energies (1300 mJ/m^2) and results in an almost constant value from 150 to 800°C. The reaction that takes place during annealing leads to siloxane bond formation which is much stronger than hydrogen ones:

$$Si - OH + HO - Si \rightarrow Si - O - Si + H_2O \tag{E.1}$$

If low temperatures are needed, a low temperature direct bonding (from room temperature to 400°C) can be performed by the assistance of an oxygen plasma activation, where the UV from plasma discharge breaks the Si-O and Si-H bonds and the surface is oxidized, the oxide being porous allows the diffusion through it which is beneficial for water removal.

The top Si is thinned until desired thickness, I have used 440 nm-thick topmost silicon SOI substrates.

Bibliography

Ababneh, A. et al. (Sept. 2010). "The influence of sputter deposition parameters on piezoelectric and mechanical properties of AlN thin films". In: *Materials Science and Engineering B* 172, pp. 253–258. DOI: 10.1016/j.mseb.2010.05.026.

Adamo, C. et al. (2009). "Effect of biaxial strain on the electrical and magnetic properties of (001) $La_{0.7}Sr_{0.3}MnO_3$ thin films". In: *Applied Physics Letters* 95, p. 112504. DOI: 10.1063/1.3213346.

Akai, D. et al. (Apr. 2005). "Ferroelectric properties of sol-gel delivered epitaxial $Pb(Zr_x,Ti_{1-x})O_3$ thin films on Si using epitaxial $\gamma - Al_2O_3$ Layers". In: *Applied Physics Letters* 86, p. 202906. DOI: 10.1063/1.1929083.

AlN mp-661 (n.d.). https://materialsproject.org/materials/mp-661/. Accessed: 2010-10-26.

Ambacher, O. (1998). "Growth and applications of Group III-nitrides". In: *Journal of Physics D: Applied Physics* 31.20, pp. 2653–2710. DOI: 10.1088/0022-3727/31/20/001. URL: https://doi.org/10.1088/0022-3727/31/20/001.

Anton, Steven R. and Henry A. Sodano (2007). "TOPICAL REVIEW: A review of power harvesting using piezoelectric materials (2003-2006)". In: *Smart Materials and Structures*.

Atanasov, Victor and Avadh Saxena (May 2011). "Electronic properties of corrugated graphene: The Heisenberg principle and wormhole geometry in the solid state". In: *Journal of physics. Condensed matter : an Institute of Physics journal* 23, p. 175301. DOI: 10.1088/0953-8984/23/17/175301.

Auciello, O. and Rainer Waser (1995). *Science and Technology of Electroceramic Thin Films*. Kluwer Academic, Dordrecht, The Netherlands: Springer Netherlands.

Auerkari, Pertti (1996). *Mechanical and physical properties of engineering alumina ceramics*.

Auner, G. W. and F. Jin (Feb. 1999). "Microstructure of low temperature grown AlN thin films on Si(111)". In: *Journal of Applied Physics* 85.7879. DOI: 10.1063/1.370600.

Baek, S. H. et al. (2011). "Giant Piezoelectricity on Si for Hyperactive MEMS". In: *Science* 334.6058, pp. 958–961. DOI: 10.1126/science.1207186.

Banerjee, N. et al. (2014). "Fabrication of piezodriven, free-standing, all-oxide heteroepitaxial cantilevers on silicon". In: *APL Materials* 2, p. 096103. DOI: 10.1063/1.4893355.

Banerjee, Sanjay K. (1997). "Applications of silicon-germanium-carbon in MOS and bipolar transistors". In: *Microelectronic Device Technology*. Ed. by Mark Rodder et al. Vol. 3212. International Society for Optics and Photonics. SPIE, pp. 118 –128. DOI: 10.1117/12.284583. URL: https://doi.org/10.1117/12.284583.

Benetti, Massimiliano et al. (Feb. 2006). "Growth and characterization of piezoelectric AlN thin films for diamond-based surface acoustic wave devices". In: *Thin Solid Films* 497, pp. 304–308. DOI: 10.1016/j.tsf.2005.10.073.

Bennett, S. P. et al. (2017). "Magnetic field response of doubly clamped magnetoelectric microelectromechanical AlN-FeCo resonators". In: *Applied Physics Letters* 111 (25), p. 252903. DOI: 10.1063/1.5011728.

Bhaskar, U.K. et al. (Nov. 2016). "A flexoelectric microelectromechanical system on silicon". English. In: *Nature nanotechnology* 11. Advance online publication, pp. 263–266. ISSN: 1748-3387. DOI: 10.1038/NNANO.2015.260.

Bi, Xiaomeng et al. (Apr. 2014a). "A model for longitudinal piezoelectric coefficient measurement of the aluminum nitride thin films". In: *Journal of Materials Science Materials in Electronics* 25. DOI: 10.1007/s10854-014-1885-3.

– (Apr. 2014b). "A model for longitudinal piezoelectric coefficient measurement of the aluminum nitride thin films". In: *Journal of Materials Science Materials in Electronics* 25. DOI: 10.1007/s10854-014-1885-3.

Biasotti, Michele et al. (Feb. 2013). "Fabrication and electromechanical actuation of epitaxial $SrTiO_3$ (001) microcantilevers". In: *Journal of Micromechanics and Microengineering* 23, p. 035031. DOI: 10.1088/0960-1317/23/3/035031.

Bilani-Zeneli, O. et al. (2008). *$SrTiO_3$ on piezoelectric PMN-PT(001) for application of variable strain*. DOI: 10.1063/1.2975167.

Bénédic, F. et al. (Feb. 2004). "Surface acoustic wave devices based on nanocrystalline diamond and aluminium nitride". In: *Diamond and Related Materials* 13, 347–353. DOI: 10.1016/j.diamond.2003.10.020.

Borowiak, A.S. et al. (2012). "Pulsed laser deposition of epitaxial ferroelectric Pb(Zr,Ti)O_3 films on silicon substrates". In: *Thin Solid Films* 520.14. Proceedings of the EMRS 2011 Spring Meeting Symposium D: Synthesis, Processing and Characterization of Nanoscale Multi Functional Oxide Films III, pp. 4604–4607. ISSN: 0040-6090. DOI: https://doi.org/10.1016/j.tsf.2011.10.139. URL: https://www.sciencedirect.com/science/article/pii/S0040609011018797.

Bourdais, D. et al. (Sept. 2015). "Epitaxial manganite freestanding bridges for low power pressure sensors". In: *Journal of Applied Physics* 118, p. 124509. DOI: 10.1063/1.4931885.

Bouregba, R. et al. (Jan. 2001). "Epitaxial PZT thin films on TiO_x covered Pt/MgO substrate by RF magnetron sputtering". In: *Ferroelectrics* 256, pp. 47–68. DOI: 10.1080/00150190108015973.

Bouregba, R. et al. (Oct. 2003). "Sawyer–Tower hysteresis measurements on micron sized Pb(Zr,Ti)O_3 capacitors". In: *Review of Scientific Instruments* 74, pp. 4429–4435. DOI: 10.1063/1.1606533.

Brand, Oliver et al. (2015). *Resonant MEMS: Fundamentals, Implementation, and Application*. Vol. 11. Advanced Micro and Nanosystems. Wiley-VCH, 512 pages. URL: https://hal.archives-ouvertes.fr/hal-00934452.

Braun, Thomas et al. (2005). "Micromechanical mass sensors for biomolecular detection in a physiological environment". In: *Phys. Rev. E* 72 (3), p. 031907. DOI: 10.1103/PhysRevE.72.031907. URL: https://link.aps.org/doi/10.1103/PhysRevE.72.031907.

Bukharaev, A. A. et al. (2018). "Straintronics: a new trend in micro- and nanoelectronics and materials science". In: 61.12, pp. 1175–1212. DOI: 10.3367/ufne.2018.01.038279. URL: https://doi.org/10.3367/ufne.2018.01.038279.

Cao, Wenwu and L. Eric Cross (1993). "Theoretical model for the morphotropic phase boundary in lead zirconate - lead titanate solid solution". In: *Phys. Rev. B* 47 (9), pp. 4825 –4830. DOI: 10.1103/PhysRevB.47.4825.

Carim, A. H. et al. (1991). "Microstructure of SolutionProcessed Lead Zirconate Titanate (PZT) Thin Films". In: *Journal of the American Ceramic Society* 74 (6), 1455–1458.

Chaluvadi, Sandeep Kumar (2017a). "Influence of the epitaxial strain on magnetic anisotropy in LSMO thin films for spintronics applications". Thèse de doctorat dirigée par Méchin, Laurence Electronique, microelectronique, optique et lasers, optoelectronique microondes Normandie 2017. PhD thesis. URL: http://www.theses.fr/2017NORMC248.

– (Dec. 2017b). "Influence of the epitaxial strain on magnetic anisotropy in LSMO thin films for spintronics applications". Theses. Normandie Université. URL: https://tel.archives-ouvertes.fr/tel-01717569.

Chaluvadi, Sandeep Kumar et al. (2020). "Epitaxial strain and thickness dependent structural, electrical and magnetic properties of $La_{0.67}Sr_{0.33}MnO_3$ films". In: *Journal of Physics D: Applied Physics* 53.37, p. 375005.

Chaluvadi, Sandeep Kumar et al. (Mar. 2022). "Integration of epitaxial $La_{2/3}Sr_{1/3}MnO_3$ thin films on silicon-on-sapphire substrate for MEMS applications". In: *Applied Surface Science* 579, p. 152095. DOI: 10.1016/j.apsusc.2021.152095.

Chen, Da et al. (2009). "The influence of the AlN film texture on the wet chemical etching". In: *Microelectron. J.* 40, pp. 15–19.

Chen, F. et al. (Apr. 2007). "Polarization switching and fatigue in $Pb(Zr_{0.52}Ti_{0.48})O_3$ films sandwiched by oxide electrodes with different carrier types". In: *Applied Physics Letters* 90.192907. DOI: 10.1063/1.2737912.

Chen, M.-S., T.-B. Wu, and J.-M. Wu (Jan. 1996). "Effect of textured LaNiO3 electrode on the fatigue improvement of $Pb(Zr_{0.53}Ti_{0.47})O_3$ thin films". In: *Applied Physics Letters* 68.1430. DOI: 10.1063/1.116103.

Chubachi, Yoshiki, Kiyotaka Sato, and Kojima (1984). "Reflection high energy electron diffraction and X-ray studies of AlN films grown on Si(111) and Si(001) by organometallic chemical vapour deposition". In: *Thin Solid Films* 122.3, pp. 259–270. ISSN: 0040-6090. DOI: https://doi.org/10.1016/0040-6090(84)90052-X.

Coey, J. M. D., M. Viret, and S. von Molnár (1999). "Mixed-valence manganites". In: *Advances in Physics* 48.2, pp. 167–293. DOI: 10.1080/000187399243455. eprint: https://doi.org/10.1080/000187399243455. URL: https://doi.org/10.1080/000187399243455.

Coll, Mariona et al. (Apr. 2015). "Polarization Switching and Light-Enhanced Piezoelectricity in Lead Halide Perovskites". In: *The Journal of Physical Chemistry Letters* 6, pp. 1408–1413. DOI: 10.1021/acs.jpclett.5b00502.

Collins, M. and W. M. Saslow (1996). "Temperature-dependent pitch and phase diagram for incommensurate XY spins in a slab geometry". In: *Phys. Rev. B* 53 (13), pp. 8533–8538. DOI: 10.1103/PhysRevB.53.8533. URL: https://link.aps.org/doi/10.1103/PhysRevB.53.8533.

Cross, Eric (2004). "Materials Science: Lead-Free at Last". In: *Nature* 432.7013, p. 24.

Cunha Rodrigues, Gonçalo da et al. (2015). "Strong piezoelectricity in single-layer graphene deposited on SiO_2 grating substrates". In: *Nature Communications* 6, p. 7572. DOI: 10.1038/ncomms8572.

Davies, J.T. and E.K. Rideal (1961). *Interfacial Phenomena*. Academic Press. ISBN: 978-0-12-206056-4.

De Araújo, Laryssa Mirelly Carvalho et al. (2021). "Use of epitaxial PZT thin films for La2/3Sr1/3MnO3based MEMs devices on SrTiO3/Si". In: *2021 Symposium on Design, Test, Integration Packaging of MEMS and MOEMS (DTIP)*, pp. 01–05. DOI: 10.1109/DTIP54218.2021.9568662.

Deshpande, Mandar and Laxman Saggere (2007). "PZT thin films for low voltage actuation: Fabrication and characterization of the transverse piezoelectric coefficient". In: *Sensors and Actuators A: Physical* 135.2, pp. 690–699. ISSN: 0924-4247. DOI: https://doi.org/10.1016/j.sna.2006.07.022. URL: https://www.sciencedirect.com/science/article/pii/S0924424706005152.

Desu, Seshu B. and In K. Yoo (1993). "Time-Dependent Dielectric Breakdown in $BaTiO_3$ Thin Films". In: *Journal of The Electrochemical Society* 140.9, pp. L133–L135. DOI: 10.1149/1.2220893. URL: https://doi.org/10.1149/1.2220893.

Diehl, R. et al. (Jan. 2003). "Low-energy electron diffraction from quasicrystal surfaces". In: *Journal of Physics: Condensed Matter* 15, R63. DOI: 10.1088/0953-8984/15/3/201.

Dörr, K. et al. (2009). "A model system for strain effects: epitaxial magnetic films on a piezoelectric substrate". In: *Eur. Phys. J. B* 71.3, 361–366.

Du, Xiao-Hong et al. (1998). "Crystal orientation dependence of piezoelectric properties of lead titanate near the morphotropic phase boundary". In: *Applied Physics Letters* 72.19, p. 2421. DOI: 10.1063/1.121373.

Dubois, Marc-Alexandre and Paul Muralt (June 2001). "Stress and Piezoelectric Properties of AlN Thin Films Deposited onto Metal Electrodes by Pulsed Direct Current Reactive Sputtering". In: *Journal of Applied Physics* 89. DOI: 10.1063/1.1359162.

Eom, C. B. et al. (May 1993). "Fabrication and properties of epitaxial ferroelectric heterostructures with ($SrRuO_3$) isotropic metallic oxide electrodes". In: *Applied Physics Letters* 63.2570, American Institute of Physics. DOI: 10.1063/1.110436.

Eom, Kilho et al. (June 2011). "Nanomechanical resonators and their applications in biological/chemical detection: Nanomechanics principles". English. In: *Physics Reports* 503.4-5, pp. 115–163. ISSN: 0370-1573. DOI: 10.1016/j.physrep.2011.03.002.

Fanget, S. et al. (2011). "Gas sensors based on gravimetric detection - A review". In: *Sensors and Actuators B: Chemical* 160.1, pp. 804–821. ISSN: 0925-4005. DOI: https://doi.org/10.1016/j.snb.2011.08.066. URL: https://www.sciencedirect.com/science/article/pii/S0925400511007891.

Faucher, Marc et al. (2009). "Amplified piezoelectric transduction of nanoscale motion in gallium nitride electromechanical resonators". In: *Appl. Phys. Lett.* 94, p. 233506. DOI: 10.1063/1.3153504.

Ferguson, J. D. et al. (2009). "Measurements of Surface Diffusivity and Coarsening during Pulsed Laser Deposition". In: *Phys. Rev. Lett.* 103 (25), p. 256103. DOI: 10.1103/PhysRevLett.103.256103. URL: https://link.aps.org/doi/10.1103/PhysRevLett.103.256103.

Fujioka, H. et al. (2001). "Epitaxial growth of semiconductors on $SrTiO_3$ substrates". In: *Journal of Crystal Growth* 229, pp. 137–141.

Funakubo, Hiroshi et al. (2012). "Epitaxial PZT films for MEMS printing applications". In: *MRS Bulletin* 37.11, 1030–1038. DOI: 10.1557/mrs.2012.271.

Giang, D.T. Huong et al. (2016). "Fabrication and characterization of PZT string based MEMS devices". In: *Journal of Science: Advanced Materials and Devices* 1.2. Special Issue in Memory of Dr. P.E. BROMMER, pp. 214–219. ISSN: 2468-2179. DOI: https://doi.org/10.1016/j.jsamd.2016.05.004. URL: https://www.sciencedirect.com/science/article/pii/S2468217916300466.

Goeders, Karen M., Jonathan S. Colton, and Lawrence A. Bottomley (Feb. 2008). "Microcantilevers: Sensing Chemical Interactions via Mechanical Motion". In: *Chemical Reviews* 108.2. DOI: 10.1021/cr0681041.

Griswold, E. M. et al. (2011). "Phase transformations in rapid thermal processed lead zirconate titanate". In: *Journal of Materials Research* 10 (12), 3149–3159. DOI: 10.1557/JMR.1995.3149.

Gueye, M. et al. (2014). "Bending strain-tunable magnetic anisotropy in Co_2FeAl Heusler thin film on Kapton". In: *Appl. Phys. Lett.* 105, p. 062409. DOI: 10.1063/1.4893157.

Guillet, Bruno et al. (2019). "Low-frequency noise considerations for sensors based on manganites". In: *HAL Id: hal-02336146*. DOI: 10.5075/epfl-ICLAB-ICNF-269309.

Guirardel, M. et al. (2004). "PZT polarization voltage effects on off-centered PZT patch actuating silicon membrane". In: *Sensors and Actuators A: Physical* 110.1. Selected Papers from Eurosensors XVI Prague, Czech Republic, pp. 385–389. ISSN:

0924-4247. DOI: https://doi.org/10.1016/j.sna.2003.08.016. URL: https://www.sciencedirect.com/science/article/pii/S092442470300548X.

Gysel, Roman et al. (Apr. 2008). "Restricted Domain Growth and Polarization Reversal Kinetics in Ferroelectric Polymer Thin Films". In: *Journal of Applied Physics* 103, p. 084120. DOI: 10.1063/1.2907990.

Haeni, J et al. (Sept. 2004). "Room-Temperature Ferroelectricity in Strained $SrTiO_3$". In: *Nature* 430, pp. 758–61. DOI: 10.1038/nature02773.

Halperin, C. et al. (June 2004). "Piezoelectric Effect in Human Bones Studied in Nanometer Scale". In: *Nano Letters - NANO LETT* 4. DOI: 10.1021/nl049453i.

He, Huan et al. (Nov. 2013). "Effect of AlN buffer layer on the microstructure and bandgap of AlN films deposited on sapphire substrates by pulsed laser deposition". In: *Journal of Materials Science: Materials in Electronics* 24. DOI: 10.1007/s10854-013-1431-8.

Heine, Thomas (Jan. 2015). "Transition Metal Chalcogenides: Ultrathin Inorganic Materials with Tunable Electronic Properties". In: 48.063108, pp. 65–72. DOI: 10.1021/ar500277z. URL: https://doi.org/10.1021/ar500277z.

Hemberger, J. et al. (2002). "Structural, magnetic, and electrical properties of single-crystalline $La_{1-x}Sr_xMnO_3$ $(0.4lt;xlt;0.85)$". In: *Phys. Rev. B* 66 (9), p. 094410. DOI: 10.1103/PhysRevB.66.094410. URL: https://link.aps.org/doi/10.1103/PhysRevB.66.094410.

Herman, Marian A., W. Richter, and Helmut Sitter (2004a). *Epitaxy: Physical Principles and Technical Implementation*. Chap. 1. ISBN: 978-3-662-07064-2.

– (2004b). *Epitaxy: Physical Principles and Technical Implementation, Homo- and Heteroepitaxial Crystallization Phenomena*. Chap. 2. ISBN: 978-3-662-07064-2.

Hernando, J. et al. (Oct. 2008). "Simulation and laser vibrometry characterization of piezoelectric AIN thin films". In: *Journal of Applied Physics* 104, pp. 053502 –053502. DOI: 10.1063/1.2957081.

Herrera-May, Agustín L. et al. (Sept. 2009). "Resonant Magnetic Field Sensors Based On MEMS Technology". In: *Sensors* 9, pp. 7785–7813. DOI: 10.3390/s91007785.

Hua-Jie, WANG et al. (Feb. 2017). "Growth of Hexagonal AlN Crystalline Microrod by Physical Vapor Transport Method". In: *Journal of Inorganic Materials* 32, p. 215. DOI: 10.15541/jim20160250.

Huang, Q.J. et al. (2006). "Study of the elastic constants in a $La_{0.6}Sr_{0.4}MnO_3$ film by means of laser-generated ultrasonic wave method". In: *Ultrasonics* 44. Proceedings of Ultrasonics International (UI'05) and World Congress on Ultrasonics (WCU), e1223–e1227. ISSN: 0041-624X. DOI: https://doi.org/10.1016/j.ultras.2006.05.193. URL: https://www.sciencedirect.com/science/article/pii/S0041624X0600237X.

Hunt, Heather K. and Andrea M. Armani (2010). "Label-free biological and chemical sensors". In: *Nanoscale* 2 (9), pp. 1544–1559. DOI: 10.1039/C0NR00201A. URL: http://dx.doi.org/10.1039/C0NR00201A.

Isarakorn, Don (Jan. 2011). "Epitaxial Piezoelectric MEMS on Silicon". In: DOI: 10.5075/epfl-thesis-4939.

Jacquot, Alexandre et al. (Jan. 2002). "Optical and Thermal Characterization of AlN Thin Films Deposited by Pulsed Laser Deposition". In: *Applied Surface Science* 186, pp. 507–512. DOI: 10.1016/S0169-4332(01)00767-X.

Jaffe, B, R. S. Roth, and S. Marzullo (1954). "Piezoelectric properties of lead zirconate-lead titanate solid solution ceramics". In: *Journal of Applied Physics* 25, pp. 809–810. DOI: 10.1063/1.1721741.

Johnson, Blake N. and Raj Mutharasan (2011). "Biosensing using dynamic-mode cantilever sensors: a review". In: *Biosens Bioelectron.* 32 (1), pp. 1–18. DOI: 10.1016/j.bios.2011.10.054.

Kalinin, Sergei, Rui Shao, and D. Bonnell (May 2005). "Local Phenomena in Oxides by Advanced Scanning Probe Microscopy". In: *Departmental Papers (MSE)* 88. DOI: 10.1111/j.1551-2916.2005.00383.x.

Kamohara, Toshihiro et al. (Jan. 2007). "Influence of sputtering pressure on polarity distribution of aluminum nitride thin films". In: *Applied Physics Letters* 89, pp. 243507 –243507. DOI: 10.1063/1.2405849.

Karmann, S. et al. (Dec. 1997). "Growth of columnar aluminum nitride layers on Si (111) by molecular beam epitaxy". In: *Materials Science and Engineering B* 50, pp. 228–232. DOI: 10.1016/S0921-5107(97)00168-2.

Keyence (n.d.[a]). *Amplifiez le processus d'analyse en recherche académique*. https://www.keyence.fr/landing/lpc/fr_ed_lp_210311_vh090new.jsp. Microscope brochure.

– (n.d.[b]). *S neox Brochure*. https://www.sensofar.com/wp-content/uploads/2021/03/BR90-05F-EN-Brochure-S-neox.pdf. Microscope brochure.

Kholkin, Andrei et al. (Feb. 2010). "Strong Piezoelectricity in Bioinspired Peptide Nanotubes". In: *ACS nano* 4, pp. 610–4. DOI: 10.1021/nn901327v.

Kim, C. J. et al. (Aug. 1994). "Electrical characteristics of (100), (111), and randomly aligned lead zirconate titanate thin films". In: *Journal of Applied Physics* 76, p. 7478. DOI: 10.1063/1.358467.

Kim, Sung Kyun et al. (Apr. 2016). "Directional dependent piezoelectric effect in CVD grown monolayer MoS_2 for flexible piezoelectric nanogenerators". In: *Nano Energy* 22, pp. 483–489. DOI: 10.1016/j.nanoen.2016.02.046.

Kiser, Jillian et al. (2013). "Stress reconfigurable tunable magnetoelectric resonators as magnetic sensors". In: *Applied Physics Letters* 102 (4), p. 042909. DOI: 10.1063/1.4789500.

Kondo, Masao, K. Maruyama, and K. Kurihara (Jan. 2002). "Epitaxial ferroelectric thin films on silicon substrates for future electronic devices". In: *Fujitsu Scientific and Technical Journal* 38, pp. 46–53.

Kutes, Yasemin et al. (Oct. 2014). "Direct Observation of Ferroelectric Domains in Solution-Processed $CH_3NH_3PbI_3$ Perovskite Thin Films". In: *Journal of Physical Chemistry Letters* 5, pp. 3335–3339. DOI: 10.1021/jz501697b.

Kwok, Chi Kong and Seshu Babu Desu (1992). "Pyrochlore to Perovskite phase-transformation in sol-gel derived lead-zirconate-titanate thin-films". In: *Applied Physics Letters* 60, pp. 1430–1432.

Laurent, Ludovic et al. (2018). "12−μm-Pitch Electromechanical Resonator for Thermal Sensing". In: *Phys. Rev. Applied* 9 (2), p. 024016. DOI: 10.1103/PhysRevApplied.9.024016. URL: https://link.aps.org/doi/10.1103/PhysRevApplied.9.024016.

Le Bourdais, David (Feb. 2015). "Microcapteurs de pression à base de manganites épitaxiées". Theses. Université Paris Sud - Paris XI. URL: https://tel.archives-ouvertes.fr/tel-01726938.

Lee, J. et al. (May 1993). "Effects of crystalline quality and electrode material on fatigue in Pb(Zr,Ti)O_3 thin film capacitors". In: *Applied Physics Letters* 63.1. DOI: 10.1063/1.109739.

Leufke, P. M. et al. (Sept. 2012). "Ferroelectric vs. structural properties of large-distance sputtered epitaxial LSMO/ PZT heterostructures". In: *AIP Advances* 2.032184. DOI: 10.1063/1.4756997.

Li, Jiangyu et al. (2015). "Strain-based scanning probe microscopies for functional materials, biological structures, and electrochemical systems". In: *Journal of Materiomics* 1.1, pp. 3–21. ISSN: 2352-8478. DOI: https://doi.org/10.1016/j.jmat.2015.03.001. URL: https://www.sciencedirect.com/science/article/pii/S2352847815000027.

Lin, Chih-Ming et al. (Feb. 2013). "Surface acoustic wave devices on AlN/ 3C-SiC/ Si multilayer structures". In: *Journal of Micromechanics and Microengineering* 23, p. 025019. DOI: 10.1088/0960-1317/23/2/025019.

Liu, Shuang (Mar. 2013a). "Fabrication et caractérisation électrique et thermique de microbolomètres non refroidis suspendus à base de couches minces La0,7Sr0,3MnO3 sur silicium". Theses. Université de Caen. URL: https://tel.archives-ouvertes.fr/tel-00915819.

– (2013b). "Fabrication et caractérisation électrique et thermique de microbolomètres non refroidis suspendus à base de couches minces $La_{0.7}Sr_{0.3}MnO_3$ sur silicium". Université de Caen. PhD thesis. URL: https://tel.archives-ouvertes.fr/tel-00915819.

– (2019). "Fabrication et caractérisation électrique et thermique de microbolomètres non refroidis suspendus à base de couches minces $La_{0.7}Sr_{0.3}MnO_3$ sur silicium". PhD thesis. Université de Caen.

Liu, Shuang et al. (Apr. 2019). "Free-standing $La_{0.7}Sr_{0.3}MnO_3$ suspended micro-bridges on buffered silicon substrates showing undegraded low frequency noise properties". In: *Journal of Micromechanics and Microengineering* 29. DOI: 10.1088/1361-6439/ab16ac.

Mandal, Snehal, R.J. Choudhary, and Indranil Das (Feb. 2020). "Tuning the magnetotransport properties of epitaxial $Sm_{0.5}Ca_{0.25}Sr_{0.25}MnO_3$ thin films via strain

engineering". In: *Journal of Magnetism and Magnetic Materials* 503, p. 166627. DOI: 10.1016/j.jmmm.2020.166627.

Martin, F et al. (Mar. 2004). "Thickness Dependence of the Properties of Highly c-axis Textured AlN Thin Films". In: *Journal of Vacuum Science & Technology A Vacuum Surfaces and Films* 22. DOI: 10.1116/1.1649343.

Massoud, Hisham Z. (1995). "The onset of the thermal oxidation of silicon from room temperature to $1000^{'C}$". In: *Microelectronic Engineering* 28, pp. 109–116.

Méchin, L. et al. (2012). "Epitaxial $La_{0.7}Sr_{0.3}MnO_3$ thin films grown on $SrTiO_3$ buffered silicon substrates by reactive molecular-beam epitaxy". In: *Physica Status Solidi* 209, 1090–1095. DOI: 10.1002/PSSA.201127712.

Mileham, J. et al. (Sept. 1995). "Wet chemical etching of AlN". In: *Applied Physics Letters* 67, pp. 1119 –1121. DOI: 10.1063/1.114980.

Millis, A. J., T. Darling, and A. Migliori (1998). "Quantifying strain dependence in colossal magnetoresistance manganites". In: *Journal of Applied Physics* 83, p. 1588. DOI: 10.1063/1.367310.

Monk, David J., David S. Soane, and Roger T. Howe (1993). "A review of the chemical reaction mechanism and kinetics for hydrofluoric acid etching of silicon dioxide for surface micromachining applications". In: *Thin Solid Films* 232.1, pp. 1–12. ISSN: 0040-6090. DOI: https://doi.org/10.1016/0040-6090(93)90752-B. URL: https://www.sciencedirect.com/science/article/pii/004060909390752B.

Morresi, Lorenzo (Jan. 2013). *Basics of Molecular Beam Epitaxy (MBE) technique*. Chap. 4. ISBN: 978-1-60805-456-5.

Nascimento, Vanuza et al. (Oct. 2020). "Electro-thermal and optical characterization of an uncooled suspended bolometer based on an epitaxial $La_{0.7}Sr_{0.3}MnO_3$ film grown on $CaTiO_3$/Si". In: *Journal of Physics D: Applied Physics* 54. DOI: 10.1088/1361-6463/abbfca.

Nascimento, Vanuza Marques Do et al. (2021). "Electro-thermal and optical characterization of an uncooled suspended bolometer based on an epitaxial $La_{0.7}Sr_{0.3}MnO_3$ film grown on $CaTiO_3$/Si". In: *Journal of Physics D: Applied Physics* 54 (5), p. 055301. DOI: 10.1088/1361-6463/abbfca.

Ngoc, N. T. et al. (Apr. 2021). "Cantilever magnetoelectric PZT/Tb–Fe–Co resonators for magnetic sensing applications". In: *APL Materials* 9 (041103). DOI: 10.1063/5.0042379.

Nguyen, Minh D. et al. (2017). "Controlling Piezoelectric Responses in $Pb(Zr_{0.52}Ti_{0.48})O_3$ Films through Deposition Conditions and Nanosheet Buffer Layers on Glass". In: *ACS Appl. Mater. Interfaces* 9 (41), 35947–35957. DOI: 10.1021/acsami.7b07428.

Noheda, B. et al. (1999). "A monoclinic ferroelectric phase in the $Pb(Zr_{1-x}Ti_x)O_3$ solid solution". In: *Applied Physics Letters* 74.14, 2059–2061. ISSN: 1077-3118. DOI: 10.1063/1.123756. URL: http://dx.doi.org/10.1063/1.123756.

Nova, T. F. et al. (2019). "Metastable ferroelectricity in optically strained $SrTiO_3$". In: *Science* 364.6445, pp. 1075–1079. DOI: 10.1126/science.aaw4911.

Okano, Hiroshi et al. (Feb. 1994). "Preparation of aluminum nitride thin films by reactive sputtering and their applications to GHz-band surface acoustic wave devices". In: *Applied Physics Letters* 64, pp. 166 –168. DOI: 10.1063/1.111553.

Park, Gun-Tae et al. (2002). "Measurement of piezoelectric coefficients of lead zirconate titanate thin films by strain-monitoring pneumatic loading method". In: *Appl. Phys. Lett.* 80, p. 4606. DOI: 10.1063/1.1487901.

Park, Kwang-Won et al. (Aug. 2014). "Humidity effect of domain wall roughening behavior in ferroelectric copolymer thin films". In: *Nanotechnology* 25, p. 355703. DOI: 10.1088/0957-4484/25/35/355703.

Pawar, Shuvam et al. (2018). "Growth assessment and scrutinize dielectric reliability of c-axis oriented insulating AlN thin films in MIM structures for microelectronics applications". In: *Materials Chemistry and Physics* 219, pp. 74–81. ISSN: 0254-0584. DOI: https://doi.org/10.1016/j.matchemphys.2018.08.013. URL: https://www.sciencedirect.com/science/article/pii/S0254058418306783.

Pellegrino, Luca et al. (2009). "All-Oxide Crystalline Microelectromechanical Systems: Bending the Functionalities of Transition-Metal Oxide Thin Films". In: *Advanced Materials* 21.23, pp. 2377–2381. DOI: https://doi.org/10.1002/adma.200803360. eprint: https://onlinelibrary.wiley.com/doi/pdf/10.1002/adma.200803360. URL: https://onlinelibrary.wiley.com/doi/abs/10.1002/adma.200803360.

Pereira, Vitor M. and A. H. Castro Neto (2009). "Strain Engineering of Graphene's Electronic Structure". In: *Phys. Rev. Lett.* 103 (4), p. 046801. DOI: 10.1103/PhysRevLett.103.046801. URL: https://link.aps.org/doi/10.1103/PhysRevLett.103.046801.

Peter, Frank et al. (2006). "Sample-tip interaction of piezoresponse force microscopy in ferroelectric nanostructures". In: *IEEE Transactions on Ultrasonics, Ferroelectrics, and Frequency Control* 53.12, pp. 2253–2260. DOI: 10.1109/TUFFC.2006.170.

Piller, Markus et al. (2021). *Thermal IR detection with nanoelectromechanical silicon nitride trampoline resonators*. arXiv: 2105.03999 [physics.app-ph].

Pliskin, W.A. (1968). "The evaluation of thin film insulators". In: *Thin Solid Films* 2.1, pp. 1–26. ISSN: 0040-6090. DOI: https://doi.org/10.1016/0040-6090(68)90010-2. URL: https://www.sciencedirect.com/science/article/pii/0040609068900102.

Radhakrishnan, Gouri (Aug. 1995). "Properties of AlN films grown at 350 K by gas-phase excimer laser photolysis". In: *Journal of Applied Physics* 78.6000. DOI: 10.1063/1.360606.

Rajendran, V. et al. (2003). "Anomalies in elastic moduli and ultrasonic attenuation near ferromagnetic transition temperature in $La_{0.67}Sr_{0.33}MnO_3$ perovskite". In: *phys. stat. sol.* 195 (2), 350– 358. DOI: 0.1002/pssa.200305931.

Ramesh, R. et al. (Mar. 1992). "Fatigue and retention in ferroelectric Y-Ba-Cu-O/ Pb-Zr-Ti-O/ Y-Ba-Cu-O heterostructures". In: *Applied Physics Letters* 61.1537. DOI: 10.1063/1.107488.

Ramesh, R. et al. (Dec. 1993). "Ferroelectric La-Sr-Co-O/ Pb-Zr-Ti-O/ La-Sr-Co-O heterostructures on slicion via template growth". In: *Applied Physics Letters* 63.3592. DOI: 10.1063/1.110106.

Remaggi, F. et al. (2016). "Towards Micromechanical Sensors with (La,Sr)MnO_3 Epitaxial Films". In: *Procedia Engineering* 168, 818 – 821.

Reza Ali, Washim and Mahanth Prasad (Dec. 2019). "Piezoelectric MEMS based acoustic sensors A review Elsevier Enhanced Reader". In: *Sensors and Actuators A Physical* 301. DOI: 10.1016/j.sna.2019.111756.

Robisch, V. et al. (2015). "Exchange biased magnetoelectric composites for magnetic field sensor application by frequency conversion". In: *Journal of Applied Physics* 117 (17), 17B513. DOI: 10.1063/1.4913814.

Roy, Kuntal (2014). "Ultra-low-energy straintronics using multiferroic composites". In: *Spintronics VII*. Ed. by Henri-Jean Drouhin, Jean-Eric Wegrowe, and Manijeh Razeghi. Vol. 9167. International Society for Optics and Photonics. SPIE, pp. 164 –175. DOI: 10.1117/12.2066171. URL: https://doi.org/10.1117/12.2066171.

Roy, Kuntal, Supriyo Bandyopadhyay, and Jayasimha Atulasimha (2011). "Hybrid spintronics and straintronics: A magnetic technology for ultra low energy computing and signal processing". In: 99.063108. DOI: 10.1063/1.3624900.

Salary, Mohammad Mahdi et al. (2016). "Mechanical actuation of graphene sheets via optically induced forces". In: *Phys. Rev. B* 94 (23), p. 235403. DOI: 10.1103/PhysRevB.94.235403. URL: https://link.aps.org/doi/10.1103/PhysRevB.94.235403.

Sama, Nossikpendou Yves et al. (July 2008). "On the Influence of the Top and Bottom Electrodes—A Comparative Study between Pt and LNO Electrodes for PZT Thin Films". In: *Journal of Crystal Growth* 310, p. 3299. DOI: 10.1016/j.jcrysgro.2008.04.025.

Saravanan, Solangkili et al. (Jan. 2004). "Surface Micromachining Process for the Integration of AlN Piezoelectric Microstructures". In: *Journal of Materials Processing Technology - J MATER PROCESS TECHNOL*.

Schneider, Dieter and Bernd Schultrich (1998). "Elastic modulus: a suitable quantity for characterization of thin films". In: *Surface and Coatings Technology* 98.1. Papers presented at the Fifth International Conference on Plasma Surface Engineering, pp. 962–970. ISSN: 0257-8972. DOI: https://doi.org/10.1016/S0257-8972(97)00317-4. URL: https://www.sciencedirect.com/science/article/pii/S0257897297003174.

Schwettmann, F. N., R. J. Dexter, and D. F. Cole (1973). "Etch Rate Characterization of Boron-Implanted Thermally Grown SiO[sub 2]". In: *Journal of The Electrochemical Society* 120.11, p. 1566. DOI: 10.1149/1.2403304. URL: https://doi.org/10.1149/1.2403304.

S.Ghosh and J.E.Y.Lee (2016). "Lorentz Force Magnetic Sensor based on a Thin-Film Piezoelectric-on-Silicon Laterally Vibrating Micromechanical Resonator". In: *Eurosensors Conference* 168, pp. 654–657. DOI: 10.1016/j.proeng.2016.11.239.

Shah, Nitinkumar Maheshchandra (2010). "High efficiency thin film copper indium diselenide solar cell". PhD thesis. Maharaja Sayajirao University of Baroda.

Shimizu, Masaru et al. (2000). "Effects of film thickness and grain size on the electrical properties of Pb(Zr,Ti)O_3 thin films prepared by MOCVD". In: *Ferroelectrics* 241.1, pp. 183–190. DOI: 10.1080/00150190008224990. eprint: https://doi.org/10.1080/00150190008224990. URL: https://doi.org/10.1080/00150190008224990.

Shirato, N. (2010). *Colossal Magnetoresistance*.

Shuskus, A., T. Reeder, and E. Paradis (Mar. 1974). "RF-sputtered Aluminum Nitride Films on Sapphire". In: *Applied Physics Letters* 24, pp. 155 –156. DOI: 10.1063/1.1655132.

Sivadasan, A. K. et al. (Apr. 2016). "Piezoelectric domains in the AlGaN hexagonal microrods: Effect of crystal orientations". In: *Journal of Applied Physics* 119.17. DOI: 10.1063/1.4948695.

So, Jin H. et al. (2003). "Measurements of Elastic Constants in Thin Films of Colossal Magnetoresistance Material". In: *Phys. Rev. Lett.* 90 (3), p. 036103. DOI: 10.1103/PhysRevLett.90.036103. URL: https://link.aps.org/doi/10.1103/PhysRevLett.90.036103.

Song, Xiufeng, Renli Fu, and Hong He (2009). "Frequency effects on the dielectric properties of AlN film deposited by radio frequency reactive magnetron sputtering". In: *Microelectronic Engineering* 86.11, pp. 2217–2221. ISSN: 0167-9317. DOI: https://doi.org/10.1016/j.mee.2009.03.036. URL: https://www.sciencedirect.com/science/article/pii/S0167931709002159.

Swann, S. (1988). "Magnetron sputtering". In: 19.2, pp. 67–75. DOI: 10.1088/0305-4624/19/2/304. URL: https://doi.org/10.1088/0305-4624/19/2/304.

Takayama, Ryoichi and Yoshihiro Tomita (1989). "Preparation of epitaxial Pb(Zr_xTi_{1x})O_3 thin films and their crystallographic, pyroelectric, and ferroelectric properties". In: *Journal of Applied Physics* 65, p. 1666. DOI: 10.1063/1.342936.

©, Electronics notes (n.d.). *Capacitor ESR, Dissipation Factor, Loss Tangent & Q*. https://www.electronics-notes.com/articles/basic_concepts/capacitance/esr-dissipation-factor-loss-tangent-q.php. Accessed 23-09-2021.

Thiele, C. et al. (2005). "Voltage-controlled epitaxial strain in $La_{0.7}Sr_{0.3}MnO_3$ / Pb($Mg_{1/3}Nb_{2/3}$)O_3 - $PbTiO_3$ (001) films". In: *Appl. Phys. Lett.* 87.26, p. 262502.

Tong, Q.-Y. et al. (1993). "Hydrophobic silicon wafer bonding". In: *Applied Physics Letters* 64.5, pp. 625–627.

Tonisch, K. et al. (2006a). "Piezoelectric properties of polycrystalline AlN thin films for MEMS application". In: *Sensors and Actuators A: Physical* 132.2, pp. 658–663. ISSN: 0924-4247. DOI: https://doi.org/10.1016/j.sna.2006.03.001.

Tonisch, Katja et al. (June 2006b). "Piezoelectric properties of thin AlN layers for MEMS application determined by piezoresponse force microscopy". In: *physica status solidi (c)* 3, pp. 2274 –2277. DOI: 10.1002/pssc.200565123.

Triscone, J.-M. et al. (1996). "Growth and structural properties of epitaxial $Pb(Zr_xTi_{1-x})O_3$ films and $Pb(Zr_xTi_{1-x})O_3$-cuprate heterostructures". In: *Journal of Applied Physics* 79, p. 4298.

Tsubouchi, Kazuo and Nobuo Mikoshiba (Oct. 1985). "Zero-Temperature-Coefficient SAW Devices on AlN Epitaxial Films". In: *Sonics and Ultrasonics, IEEE Transactions on* 32, pp. 634–644. DOI: 10.1109/T-SU.1985.31647.

Tsuchiya, Tetsuo et al. (Apr. 2007). "Low-temperature growth of epitaxial PZT/ LSMO /LAO film by excimer laser-assisted metal organic deposition (ELAMOD)". In: *Journal of Physics Conference Series* 59, pp. 218–223. DOI: 10.1088/1742-6596/59/1/047.

Urushibara, A. et al. (1995). "Insulator-metal transition and giant magnetoresistance in $La_{1-x}Sr_xMnO_3$". In: *Phys. Rev. B* 51 (20), pp. 14103–14109. DOI: 10.1103/PhysRevB.51.14103. URL: https://link.aps.org/doi/10.1103/PhysRevB.51.14103.

Vacandio, F. et al. (1997). "A study of the physical properties and electrochemical behaviour of aluminium nitride films". In: *Surface and Coatings Technology* 92.3, pp. 221–229. ISSN: 0257-8972. DOI: https://doi.org/10.1016/S0257-8972(97)00103-5. URL: https://www.sciencedirect.com/science/article/pii/S0257897297001035.

Vila-Fungueiriño, J. Manuel et al. (2018). "Epitaxial $La_{0.7}Sr_{0.3}MnO_3$ thin films on silicon with excellent magnetic and electric properties by combining physical and chemical methods". In: *Sci. Technol. Adv. Mater. Natl. Inst. Mater. Sci.* 19, 702–710. DOI: https://doi.org/10.1080/14686996.2018.1520590.

Vilquin, B. et al. (2001). "Orientation control of rhomboedral PZT thin films on Pt/ Ti /SiO_2 /Si substrates". In: *Eur. Phys. J. AP* 15.3, pp. 153–165. DOI: 10.1051/epjap:2001177. URL: https://doi.org/10.1051/epjap:2001177.

Vivien, L. and Lorenzo Pavesi (2013). "Handbook of Silicon Photonics". In: chap. 1.

Vrejoiu, Ionela et al. (2008). "Interfacial strain effects in epitaxial multiferroic heterostructures of $PbZr_xTi_{1x}O_3/La_{0.7}Sr_{0.3}MnO_3$ grown by pulsed-laser deposition". In: *Applied Physics Letters* 92, p. 152506. DOI: 10.1063/1.2908037.

Wang, J. S. and K. M. Lakin (1982). "Low-temperature coefficient bulk acoustic wave composite resonators". In: *Applied Physics Letters* 40.308. DOI: 10.1063/1.93072.

Wang, Y. et al. (Jan. 2002a). "Epitaxial ferroelectric Pb(Zr, Ti)O_3 thin films on Si using $SrTiO_3$ template layers". In: *Applied Physics Letters* 80, pp. 97–99. DOI: 10.1063/1.1428413.

Wang, Y. et al. (2002b). "Epitaxial ferroelectric Pb(Zr,Ti)O_3 thin films on Si using $SrTiO_3$ template layers". In: *Applied Physics Letters* 80.1, pp. 97–99. ISSN: 00036951. DOI: 10.1063/1.1428413.

Wang, Zhiping et al. (Aug. 2011). "Growth of preferentially-oriented AlN films on amorphous substrate by pulsed laser deposition". In: *Physics Letters A* 375, pp. 3007–3011. DOI: 10.1016/j.physleta.2011.06.043.

Weber, Jan et al. (Mar. 2006). "Shear mode FBARs as highly sensitive liquid biosensors". In: *Sensors and Actuators A: Physical* 128, p. 84. DOI: 10.1016/j.sna.2006.01.005.

Wei, Wei, Ying Dai, and Baibiao Huang (2017). "Straintronics in two-dimensional in-plane heterostructures of transition-metal dichalcogenides". In: *Phys. Chem. Chem. Phys.* 19 (1), pp. 663–672. DOI: 10.1039/C6CP07823K. URL: http://dx.doi.org/10.1039/C6CP07823K.

Wong, Chee Wei et al. (2004). "Analog piezoelectric-driven tunable gratings with nanometer resolution". In: *Journal of Microelectromechanical Systems* 13.6, pp. 998–1005. DOI: 10.1109/JMEMS.2004.839592.

Wouters, Dirk J. et al. (1995). "Elements of the leakage current of high-ε ferroelectric PZT films". In: *Integrated Ferroelectrics* 7.1-4, pp. 173–184. DOI: 10.1080/10584589508220230.

Wu, W. et al. (Sept. 2000). "Top-interface-controlled fatigue of epitaxial $Pb(Zr_{0.52}Ti_{0.48})O_3$ ferroelectric thin films on $La_{0.7}Sr_{0.3}MnO_3$ electrodes". In: *Applied Physics Letters* 77.3441. DOI: 10.1063/1.1327279.

Wu, Y., C. Jia, and W. Zhang (May 2012). "Growth of conductive and insulative highly-orientated aluminum nitride thin films using laser molecular beam epitaxy". In: *Diamond and Related Materials* 25, 139–143. DOI: 10.1016/j.diamond.2012.02.022.

Xu, Xiao-Hong et al. (June 2001). "Morphological properties of AlN piezoelectric thin films deposited by DC reactive magnetron sputtering". In: *Thin Solid Films* 388, pp. 62–67. DOI: 10.1016/S0040-6090(00)01914-3.

Yang, Fan, Sangtae Kim, and Yayoi Takamura (2011). "Strain effect on the electrical conductivity of epitaxial $La_{0.67}Sr_{0.33}MnO_3$ thin films". In: *Scripta Materialia* 65 (1), pp. 29–32. DOI: 10.1016/j.scriptamat.2011.03.021.

Yantchev, Ventsislav and Ilia Katardjiev (Mar. 2013). "Thin film Lamb wave resonators in frequency control and sensing applications: A review". In: *Journal of Micromechanics and Microengineering* 23, p. 043001. DOI: 10.1088/0960-1317/23/4/043001.

Ye, Kun Hee et al. (2021). "Atomistic Understanding of the Ferroelectric Properties of a Wurtzite-Structure (AlN)n/(ScN)m Superlattice". In: *physica status solidi (RRL) - Rapid Research Letters* 15.5, p. 2100009. DOI: https://doi.org/10.1002/pssr.202100009.

Yin, S. et al. (2012a). "Epitaxial growth and electrical measurement of single crystalline $Pb(Zr_{0.52}Ti_{0.48})O_3$ thin film on Si(001) for micro-electromechanical systems". In: *Thin Solid Films* 250, pp. 4572–4575. DOI: 10.1016/J.TSF.2011.11.073.

Yin, Shi (2013a). "Integration of epitaxial piezoelectric thin films on silicon". Thèse de doctorat dirigée par Robach, YvesVilquin, Bertrand et Le Rhun, Gwénaël Dispositifs de l'électronique intégrée Ecully, Ecole centrale de Lyon 2013. PhD thesis. URL: http://www.theses.fr/2013ECDL0039.

– (Nov. 2013b). "Integration of epitaxial piezoelectric thin films on silicon". Theses. Ecole Centrale de Lyon. URL: https://tel.archives-ouvertes.fr/tel-01139336.

Yin, Siliang et al. (May 2012b). "Epitaxial growth and electrical measurement of single crystalline $Pb(Zr_{0.52}Ti_{0.48})O_3$ thin film on Si(001) for micro-electromechanical systems". In: *Thin Solid Films* 520, 4572–4575. DOI: 10.1016/j.tsf.2011.11.073.

Zhang, Meng et al. (Sept. 2015). "Research on the Piezoelectric Properties of AlN Thin Films for MEMS Applications". In: *Micromachines* 6, pp. 1236–1248. DOI: 10.3390/mi6091236.

Zhang, Wei et al. (1993). "Heteroepitaxy of AlN on α-Al_2O_3 by electron cyclotron resonance plasma-assisted chemical vapor deposition at low temperatures". In: *Journal of Crystal Growth* 132.1, pp. 337–340. ISSN: 0022-0248. DOI: https://doi.org/10.1016/0022-0248(93)90279-6. URL: https://www.sciencedirect.com/science/article/pii/0022024893902796.

Zhang, Ya et al. (Apr. 2016). "Room temperature, very sensitive thermometer using a doubly clamped microelectromechanical beam resonator for bolometer applications". In: *Applied Physics Letters* 108, p. 163503. DOI: 10.1063/1.4947444.

Zhang, Ya et al. (Apr. 2019). "Fast and sensitive bolometric terahertz detection at room temperature through thermomechanical transduction". In: *Journal of Applied Physics* 125, p. 151602. DOI: 10.1063/1.5045256.

Zheng, Ren-Kui et al. (Mar. 2010). "Effects of substrate-induced strain on transport properties of $LaMnO_{3+\delta}$ and $CaMnO_3$ thin films using ferroelectric poling and converse piezoelectric effect". In: *Phys. Rev. B* 81. DOI: 10.1103/PhysRevB.81.104427.

Zhu, Jing et al. (2008). "Epitaxial growth of cubic AlN films on $SrTiO_3$(100) substrates by pulsed laser deposition". In: *Journal of Crystal Growth* 310, pp. 731–737.

Zibouche, Nourdine et al. (2014). "Transition-metal dichalcogenides for spintronic applications". In: *Annalen der Physik* 526.9-10, pp. 395–401. DOI: https://doi.org/10.1002/andp.201400137. eprint: https://onlinelibrary.wiley.com/doi/pdf/10.1002/andp.201400137. URL: https://onlinelibrary.wiley.com/doi/abs/10.1002/andp.201400137.

Zighem, Fatih et al. (Sept. 2013). "Voltage-induced strain control of the magnetic anisotropy in a Ni thin film on flexible substrate". In: *Journal of Applied Physics* 114. DOI: 10.1063/1.4817645.